Pore Wetting in Desalination of Brine using Membrane Distillation Process

Hooman Chamani

Thesis submitted to the University of Ottawa
in partial fulfillment of the requirements for the
Doctorate in Philosophy degree in Chemical Engineering

Department of Chemical and Biological Engineering
Faculty of Engineering
University of Ottawa

Abstract

It goes without saying that water scarcity is a widespread and increasingly pressing global challenge. One of the methods which can mitigate water shortage is to increase freshwater production via desalination of saline waters. Seawater and saline aquifer sources represent 97.5% of all water on Earth. Hence, treating even a small portion of saline water could significantly reduce water shortage. Although reverse osmosis is one of the state-of-the-art pressure-driven membrane desalination technologies, it is incapable of desalinating high-salinity streams due to the very high osmotic pressure to overcome. Membrane distillation (MD) is one of the emerging methods, which has attracted much attention for desalinating highly saline brines. MD is a thermally driven process in which only vapor molecules pass through the pores of a microporous hydrophobic membrane. This process, however, has not been fully commercialized due to a number of challenges, including "pore wetting". Pore wetting refers to the presence of liquid, instead of just water vapor, inside the membrane pores, which may cause a decrease in MD flux and/or deterioration of distillate quality. Herein, a comprehensive review on pore wetting is presented, and then this phenomenon is investigated from four aspects. In the first phase of this project, a theoretical model is presented according to which the pore size distribution of membrane, a parameter affecting pore wetting risk, is estimated by employing only a few experimental data points in accordance with the wet/dry method, reducing the number of data required to be recorded largely. In the next phase, an equation is presented for the estimation of liquid entry pressure (LEP), a membrane parameter closely related to pore wetting, using computational fluid dynamics (CFD) tools and genetic programming (GP) as an intelligent technique. This equation can estimate LEP in closer agreement to experimental values in comparison to the Young-Laplace equation. In the third phase, movement of liquid-gas interface inside the membrane pore is tracked using a well-founded model, and

consequently, the pressure and velocity at the interface and the required time for replacement are studied. Finally, in the last phase, a model is developed for pore wetting in vacuum MD, considering heat and mass balances at the vapor-liquid interface. This model assumes that heat only enters the pore inlet and is removed due to liquid vaporization at the vapor-liquid interface, with heat transfer through the pore wall neglected. This model shows that partial pore wetting is possible since the vapor-liquid interface might remain within the pore at the steady-state condition. Further, this model can predict the decrease in temperature from the pore inlet to the vapor-liquid interface, a phenomenon that has been reported in the literature without any proof.

Résumé

Il va sans dire que la pénurie d'eau est un problème mondial répandu et de plus en plus pressant. L'une des méthodes permettant d'atténuer la pénurie d'eau consiste à augmenter la production d'eau douce par le biais du dessalement des eaux salines. L'eau de mer et les sources aquifères salines représentent 97,5 % de toute l'eau sur Terre. Par conséquent, le traitement d'une petite quantité d'eau salée pourrait réduire considérablement la pénurie d'eau. Bien que l'osmose inverse soit l'une des technologies de pointe en matière de dessalement par membrane sous pression, elle est incapable de dessaler les flux à forte salinité en raison de la très forte pression osmotique à surmonter. La distillation membranaire (MD) est l'une des méthodes émergentes qui a attiré beaucoup d'attention pour le dessalement des saumures hautement salines. La MD est un processus thermique dans lequel seules les molécules de vapeur passent à travers les pores d'une membrane hydrophobe microporeuse. Ce procédé n'a toutefois pas été pleinement commercialisé en raison d'un certain nombre de difficultés, notamment le "mouillage des pores". Le mouillage des pores fait référence à la présence de liquide, et non pas seulement de vapeur d'eau, à l'intérieur des pores de la membrane, ce qui peut entraîner une diminution du flux de MD et/ou une détérioration de la qualité du distillat.

Ce document présente une revue complète du mouillage des pores, puis étudie ce phénomène sous quatre aspects. Dans la première phase de ce projet, un modèle théorique est présenté selon lequel la distribution de la taille des pores de la membrane, un paramètre affectant le risque de mouillage des pores, est estimée en utilisant seulement quelques points de données expérimentales conformément à la méthode humide/sec. Cela réduit ainsi largement le nombre de données à enregistrer. Dans la phase suivante, une équation est présentée pour l'estimation de la pression d'entrée du liquide (LEP), un paramètre de la membrane étroitement lié au mouillage des pores, en

utilisant des outils de dynamique des fluides numériques (CFD) et la programmation génétique (GP) comme technique intelligente. Cette équation peut estimer la LEP en accord plus étroit avec les valeurs expérimentales par rapport à l'équation de Young-Laplace. Dans la troisième phase, le mouvement de l'interface liquide-gaz à l'intérieur du pore de la membrane est suivi à l'aide d'un modèle bien fondé, et par conséquent, la pression et la vitesse à l'interface ainsi que le temps nécessaire au remplacement sont étudiés. Enfin, dans la dernière phase, un modèle est développé pour le mouillage des pores dans le MD sous vide, en considérant les bilans de chaleur et de masse à l'interface vapeur-liquide. Ce modèle suppose que la chaleur entre uniquement dans l'entrée du pore et est éliminée par la vaporisation du liquide à l'interface vapeur-liquide, le transfert de chaleur à travers la paroi du pore étant négligé. Ce modèle montre que le mouillage partiel des pores est possible puisque l'interface vapeur-liquide peut rester à l'intérieur du pore à l'état d'équilibre. De plus, ce modèle peut prédire la diminution de la température de l'entrée du pore à l'interface vapeur-liquide, un phénomène qui a été rapporté dans la littérature sans aucune preuve.

Statement of Contributions

I hereby declare that I am the author of this thesis. I thoroughly have written chapters 1 and 7, introduction and conclusion, respectively. I have written Chapter 2, which is a comprehensive literature review, with the assistance of Joanne Woloszyn, who was an undergraduate student in Chemical Engineering at the University of Ottawa. Her efforts were appreciated by putting her name as a co-author of the review paper published in the Journal of Progress in Materials Science. Chapters 3, 5, and 6 are related to different models presented in this research. For these chapters, I have developed and validated the models, performed data analysis and written the content of those chapters. Chapter 4 was done in collaboration with Khalifa University of Science and Technology (Prof. Arafat's research group), and CFD modeling of this chapter was done by the mentioned research group. All the chapters of this thesis, except the introduction and conclusion, have been published in scientific peer-reviewed journals, and more detailed authors' contributions can be found at the end of publications. The projects in this thesis have been developed under the supervision of Prof. Lan (Professor) and Prof. Matsuura (Professor Emeritus) of the Department of Chemical and Biological Engineering of the University of Ottawa. I have also revised this thesis according to my supervisors' comments. Also, I have further modified it according to the comments of Dr. Rana (a senior research scientist in our research group at the University of Ottawa), examiners and the reviewers of the publications.

Acknowledgement

I would like to express my deepest gratitude to my supervisors, Prof. Christopher Lan and Prof. Takeshi Matsuura, for their invaluable guidance, encouragement and advice throughout my research and a special thank you goes to Dr. Dipak Rana, who has been a great source of support.

I am grateful to all of those professors with whom I had the privilege of collaborating and those who supported me during this program, Prof. Hassan Arafat (Khalifa University), Prof. John Lienhard (MIT), Prof. Jules Thibault (University of Ottawa), and Prof. Kang Li (Imperial College London).

My sincere thanks must also go to the members of my thesis committee, Prof. Anthony Fane from the University of New South Wales, Prof. Arturo Macchi, Prof. Roberto Narbaitz, and Prof. Jason Zhang from the University of Ottawa, for the time they spent reviewing my thesis.

I cannot forget my friends and colleagues who helped me during this journey, Hassan Hosseini, Mohammadali Baghbanzadeh, Sepehr Ramyar, Joanne Woloszyn, Mostafa Taherian, Arash Fellah Jahromi, Mohammad Reza Askari, Pelin Yazgan-Birgi, Louiza Harkouk, Nima Javanbakht, Morteza Javid, Ata Babakhani, Hamed Mozafari, Aotian Li, Mohammad Amin Sadeghi, and Kefan Jiang.

I would like to thank my wife, **Sepideh Langari**, for her love and great support, for proofreading my thesis and papers, for being the audience of my rehearsals and for being my best friend, and I am forever grateful to her. My heartfelt and profound gratitude goes to my parents and brothers, Hamed and Alireza, for their endless love, help and support. I owe much of my success to my family, and this expedition would not have been possible without their love and support, and I dedicate this major milestone to them.

Table of contents

List of Figures

List of Tables

Abbreviations

AC	Alternating currents
AFM	Atomic force microscopy
AGMD	Air gap membrane distillation
APTES	(3-aminopropyl)-triethoxysilane
CA	Contact angle
CDF	Cumulative distribution function
CFD	Computational fluid dynamics
CTAB	Cetyltrimethylammonium bromide
CTS	Chitosan
CNT	Carbon nanotube
DCMD	Direct contact membrane distillation
DDTI	Detection of dissolved tracer intrusion
DMF	N,N-Dimethylformamide
ECMD	Electrically conducting MD
EDS	Energy-dispersive x-ray spectroscopy
EDX	Energy-dispersive x-ray spectroscopy
EM	Electron microscopy
FAS	Fluorinated alkylsilane
FDTS	(Heptadecafluoro-1,1,2,2-tetrahydrodecyl)trichlorosilane
FDTES	1H,1H,2H,2H-perfluorodecyltriethoxysilane
GO	Graphene oxide
GP	Genetic programming
HFPW	Hydraulic fracturing produced water
I	Internal
iPP	Isotactic polypropylene
IUPAC	International union of pure and applied chemistry
Kn	Knudsen number
LEP	Liquid entry pressure
LIF	Laser-induced fluorescence
LW	Lifshitz-van der Waals
MAE	Mean absolute error
MD	Membrane distillation
MEA	Monoethanol amine
MF	Microfiltration
MHDD	Membrane humidification-dehumidification distillation
MP-PVDF	Micro-pillar PVDF
NF	Nanofiltration
NR	Nanorod
PAN	Polyacrylonitrile
pC6PFA	Poly(1H, 2H, 2H-perfluorooctyl acrylate)
PCTE	Track-etched polycarbonate

PDA	Polydopamine
PDMS	Polydimethylsiloxane
pDVB	Poly(divinyl benzene)
PE	Polyethylene
PEG-co-poly(MAA)	Polyethylene glycol-co-polymethacrylic acid
PEI	Polyethylenimine
PET	Polyethylene terephthalate
PFO	Perfluorooctanoate
PolyDADMAC	Poly(diallyldimethylammonium chloride)
PP	Polypropylene
PPO	Poly(2,6-dimethyl-1,4-phenylene oxide)
PS	Polystyrene
PSD	Pore size distribution
PSF	Polysulfone
PTFE	Polytetrafluoroethylene
PU	Polyurethane
PVA	Polyvinyl alcohol
PVDF	Polyvinylidene fluoride
PVDF-HFP	PVDF-co-hexafluoropropylene
PVSQ	Polyvinylsilsesquioxane
RC	Regenerated cellulose
RGO	Reduced GO
RO	Reverse osmosis
RSM	Response surface methodology
SDS	Sodium dodecyl sulfate
SEM	Scanning electron microscopy
SFE	Surface free energy
SGMD	Sweeping gas membrane distillation
SiNPs	Silica nanoparticles
SiPs	Silica particles
T	Terminal nodes
TEA	Triethanolamine
TEM	Transmission electron microscopy
TMC	Trimesoyl chloride
TPFOS	Trichloro(1H,1H,2H,2H perfluorooctyl)silane
UF	Ultrafiltration
VFW	Volume fraction of water
VMD	Vacuum membrane distillation
VOF	Volume of fluid
VTMOS	Vinyltrimethoxysilane
F-POSS	Fluorinated-decyl polyhedraloligomeric silsesquioxane
V-POSS	Vinyl- Polyhedral oligomeric silsesquioxane
17-FAS	1H, 1H, 2H, 2H-perfluorodecyltrimethoxysilane

Nomenclature

B	Pore geometry (-)
c_p	Heat capacity (J/kg K)
D	Diffusion coefficient (m^2/s)
d_g	Collision diameter (m)
d_p	Pore diameter (m)
F_γ	Body force caused by surface tension (N/m^3)
f	Distribution function
f_s	Fraction of solid surface
g	Gravitational constant (m/s^2)
H	Height of liquid in the liquid reservoir (m)
h	Pressure increment (Pa) in chapter 3; Distance between the floor and the bottom of the fibers (m) in chapter 4
J	Mass flux (kg/m^2 s) in chapter 2; Molar gas flow rate per unit of area (mol/m^2 s) in chapter 3; Velocity (m/s) in chapter 5; Mass flux (kg/m^2 h) in chapter 6
k	Boltzmann constant (J/K)
k_l	Thermal conductivity (W/m K)
Kn	Knudsen number (-)
L_x	Surface dimension in the x-direction
L_y	Surface dimension in the y-direction
l_s	Linear distance between the pore entrance and the liquid-gas interface (m)
M	Molecular weight (kg/mol)
N	Number of pores per unit of area (m^{-2}) in chapter 3; Mass flow rate (kg/s) in chapter 6
N_l	Mass flow rate of liquid (kg/s)
N_T	Total number of pores per unit of area (m^{-2})
N_v	Mass flow rate of vapor (kg/s)
n	Number of pores (-) in chapter 3; Number of pores in 1 m^2 of effective membrane area in chapter 6
n_a	Cumulative distribution of number of pores (-)
n_T	Total number of pores (-)
P	Pressure (Pa)
p	Pressure inside the pore (Pa)
p_0	Initial pressure applied to the membrane (Pa)
p_a	Pressure of the gas trapped in the pore in chapter 2; Unbalanced atmospheric pressure (Pa) in chapter 5
p_c	Capillary pressure (Pa)
p_e	Pressure at pore exit (Pa)
p_f	Final pressure (Pa) in chapter 3; Feed pressure (Pa) in chapters 5 and 6
p_h	Hydrostatic pressure (Pa)
p_i	Pressure at pore inlet (Pa) in chapter 3; Pressure at liquid/gas interface (Pa) in chapter 5
p_p	Pressure at down-stream side of the membrane (Pa)

p_s	Vapor pressure at liquid/vapor interface (Pa)
$\overline{p}$	Average pressure inside the pore (Pa)
Q	Molar gas flow rate (mol/s)
Q_g	Volumetric flow rate of gas (m^3/s)
Q_l	Volumetric flow rate of liquid (m^3/s)
Q_v	Volumetric flow rate (m^3/s)
R	Gas constant (J/mol K) in Eqs. 2.1-2.3 and 2.9 as well as chapters 3 and 6; Radius of fiber (m) in Eqs. 2.15 and 2.16 as well as chapter 4
R_a	Mean value of the membrane surface relative to the center plane
R_q	Standard deviation of z-direction data
R_z	Average difference in height between the five highest peaks and five lowest valleys
r	Pore radius (m)
$r_{critical}$	The *r* value that makes $\Delta p_l = 0$, obtained by Eq. 6.9 (m)
$r_{citical}^{L}$	$r_{critical}$ obtained by the Laplace equation (m)
r_{max}	Maximum pore radius (m)
T	Temperature (K)
T_s	Temperature at liquid/vapor interface (K)
T_f	Feed temperature (K)
t	Time (s)
t_{pass}	Time required for one phase to flow from the pore entrance to pore exit (s)
u	Velocity (m/s)
x	Portion of the pore filled by liquid phase (-)
x_{max}	Maximum value of the variable
x_{min}	Minimum value of the variable
x_{norm}	Normalized value of the variable
x_{org}	Original value of the variable
x_1	Normalized value of contact angle
x_2	Normalized value of pore radius
x_3	Normalized value of membrane thickness
y	Normalized value of LEP in chapter 4; Portion of the pore filled by gas phase (-) in chapter 5
ΔH_v	Heat of vaporization (J/kg)
Δp	Pressure difference (Pa)
Δp_l	Driving force of liquid movement (Pa)
Δp_v	Driving force of gas movement (Pa)

Greek symbols

α	Structural angle (º)
α_i	Phase *i* volume fraction (-)
γ_{LV}	Surface tensions of the liquid-vapor (N/m)
γ_s	Surface energy of the membrane (N/m)
γ_{SL}	Surface tensions of the solid-liquid (N/m)
γ_{SV}	Surface tensions of the solid-vapor (N/m)
δ	Membrane thickness (m)
δ_g	Length of gas phase (m)
δ_l	Length of liquid phase (m)
δ_v	Length of vapor phase (m)
ϵ	Coefficient of slip (m)
ε	Porosity (-)
ε_s	Superficial porosity (-)
η_g	Gas viscosity (Pa s)
η_l	Viscosity of liquid (Pa s)
θ	Contact angle (º)
θ_{eff}	Effective contact angle (º)
λ	Mean free path (m)
μ	Mean of the distribution in chapter 3; Dynamic viscosity (Pa s) in chapter 4
ρ	Density (kg/m^3)
σ	Surface tension (N/m)
ς	Standard deviation
τ	Tortuosity (-)
φ	Angle of capillary tube with respect to the horizontal axis (º)

List of publications

[1] H. Chamani, J. Woloszyn, T. Matsuura, D. Rana, C.Q. Lan, Pore wetting in membrane distillation: A comprehensive review, Prog. Mater. Sci. 122 (2021) 100843. doi: 10.1016/j.pmatsci.2021.100843.

[2] H. Chamani, T. Matsuura, D. Rana, C.Q. Lan, A reverse approach to evaluate membrane pore size distribution by the bubble gas transport method using fewer experimental data points, Desalination. 518 (2021) 115287. doi: 10.1016/j.desal.2021.115287.

[3] H. Chamani, T. Matsuura, D. Rana, C.Q. Lan, Transport characteristics of liquid-gas interface in a capillary membrane pore, J. Membr. Sci. 611 (2020) 118387. doi:10.1016/j.memsci.2020.118387.

[4] H. Chamani, P. Yazgan-Birgi, T. Matsuura, D. Rana, M.I. Hassan Ali, H.A. Arafat, C.Q. Lan, CFD-based genetic programming model for liquid entry pressure estimation of hydrophobic membranes, Desalination. 476 (2020) 114231. doi:10.1016/j.desal.2019.114231.

[5] H. Chamani, T. Matsuura, D. Rana, C.Q. Lan, Modeling of pore wetting in vacuum membrane distillation, J. Membr. Sci. 572 (2019) 332-342. doi:10.1016/j.memsci.2018.11.018.

In addition to the abovementioned publications, I have also been involved in the following research articles during my PhD program:

[1] M.R. Qtaishat, H. Chamani, T. Matsuura, D. Rana, C.Q. Lan, Modeling of the movement of two immiscible liquids in membrane pores, (ready to submit).

[2] Y.S. Khoo, W.J. Lau, H. Chamani, T. Matsuura, A.F. Ismail, Water flux increase by inverting the membrane from its normal position – Is it occurring in FO and PRO?, J. Water Process Eng. 37 (2020) 101366. doi:10.1016/j.jwpe.2020.101366.

Conference presentations

[1] H. Chamani, T. Matsuura, D. Rana, C.Q. Lan, "Determination of membrane pore size distribution using nonlinear regression," AIChE Annual Meeting, Boston, US, November 2021.

[2] H. Chamani, T. Matsuura, D. Rana, C.Q. Lan, "Capillary flow inside the membrane pore: Tracking the interface," MELPRO 2020 Conference, Prague, Czech Republic, November 2020.

[3] H. Chamani, P. Yazgan-Birgi, T. Matsuura, D. Rana, M. Ali, H. Arafat, C.Q. Lan, "Estimation of LEP for MD membranes using CFD-GP model," 69th Canadian Chemical Engineering Conference, Halifax, Canada, October 2019.

Chapter 1

Introduction

Water is an essential resource that sustains life on Earth. Fresh water especially is of great importance since it is required by most plants and mammals, including humans. However, the availability of natural fresh water is relatively small by comprising only 2.5% of the Earth's hydrosphere, with the remaining 97.5% consisting of saline water (Figure 1-1) [1,2]. Another consideration is that this fresh water is not necessarily easily accessible nor potable, thus requiring transport or treatment prior to consumption. Only a mere 0.26% of Earth's fresh water, attributed to surface water such as lakes and rivers, is easily accessible for human needs [1]. Water demands have increased due to the rising population, thus putting a strain on its limited quantity. Meanwhile, human activities such as urbanization and industrialization fuel the problem by polluting available fresh water reserves. In addition, change in weather due to global warming in recent decades is greatly contributing to the global water shortage [2,3]. As a result, there is an increasing necessity for the development, research, and improvement of technologies to ensure water sustainability.

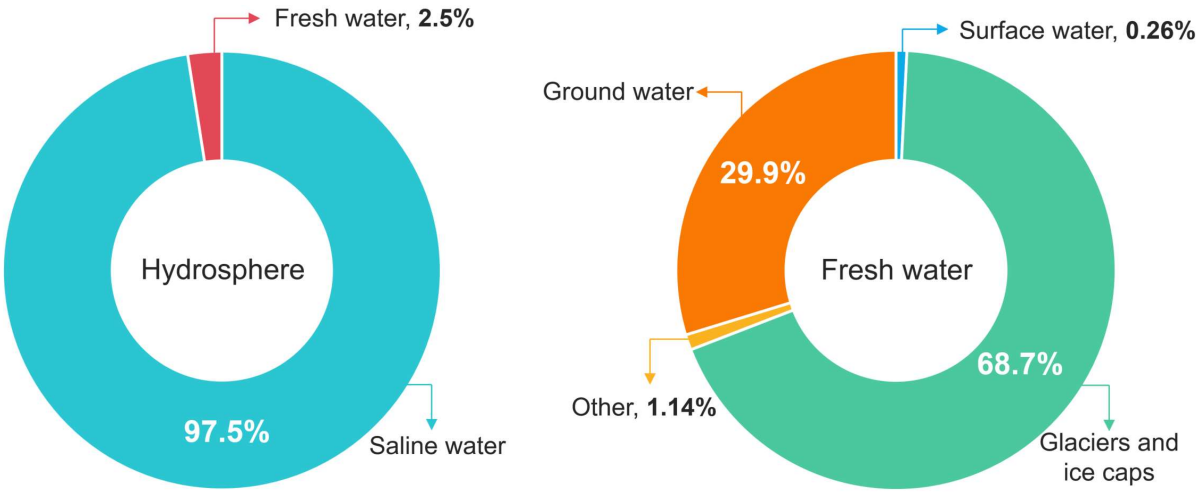

Figure 1-1 Distribution of water in Earth's hydrosphere.

With 97.5% of the Earth's hydrosphere consisting of saline water (Figure 1-1), there is significant potential in obtaining fresh water from saline water by removing its salts and minerals via the process of desalination [4]. Current technologies for water desalination are cost- and energy-intensive, which typically involves a thermal and/or membrane process, with reverse osmosis (RO) and thermal distillation being the major technologies currently in use [4,5]. RO especially has become the dominant process in recent decades due to decreasing costs and advancing technology [5]. In desalination, the mechanism for RO causes the outflow of water through a semipermeable membrane by the application of pressure to the saline feed solution that is greater than its osmotic pressure or the minimum pressure that prevents the inflow of pure water via osmosis [6]. Since RO membranes are designed such that the convective water flow is typically higher than the diffusive flow of salts, there is an accumulation of salts rejected by the membrane at the membrane surface [7]. Because osmotic pressure increases with feed salinity, a major disadvantage of RO is its inability to desalinate highly concentrated salt solutions due to the increased osmotic pressure at the membrane surface [6,7].

An alternative method for desalination, which combines thermal and membrane processes and is better equipped to handle highly saline solutions, especially those with a salinity between 70 to 300 g salt per kg solution, is membrane distillation (MD) [8]. With MD, desalinated water is obtained by the transfer of water vapor due to a vapor pressure difference across a non-wetted, hydrophobic, microporous membrane as a result of an imposed temperature gradient [9]. Various configurations exist for the MD process, including direct contact membrane distillation (DCMD) (Figure 1-2), vacuum membrane distillation (VMD), air gap membrane distillation (AGMD), and sweeping gas membrane distillation (SGMD) [10].

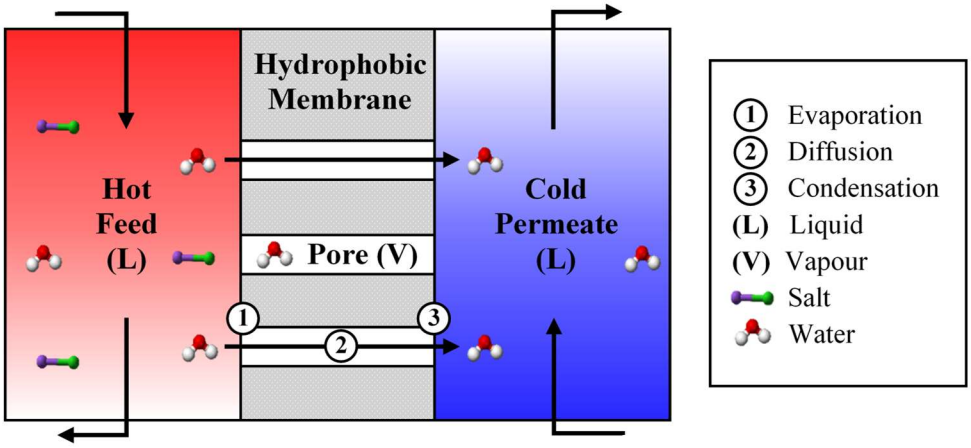

Figure 1-2 Mechanism for desalination by DCMD.

1.1. Problem statement

MD has various advantages over traditional desalination technologies, including operation at lower temperatures than multistage distillation, high salt rejection, and less sensitivity to membrane fouling [11,12]. However, MD has not been commercialized yet mainly due to high thermal energy consumption [13], low permeate flux [14], and of particular relevance, the occurrence of pore wetting [10,15,16]. MD processes require large quantities of thermal energy to preheat the feed, typically in the range of 600 to 9080 kWh/m^3. Various studies have made efforts to decrease energy costs for MD by considering the use of low-grade heat, renewable energy, enthalpy stored in surface seawater, and new configurations [13]. Further, many attempts have been made to increase permeate flux through preparation of appropriate membranes and modification of the MD process [10].

Pore wetting refers to the presence of liquid, instead of vapor, inside the membrane pores. Relative to the two other drawbacks of MD, research on pore wetting phenomena is insufficient. A literature search on the Scopus database (as of October 2020) indicates that out of 1932 publications pertaining to MD and desalination, only 206 articles studied the wetting phenomenon [17].

Although there has been an increase in research about wetting phenomena in recent years, further research is required before MD becomes an industrial technology for desalination.

1.2. Project objectives

Since the wetting phenomenon in MD is poorly understood, and little theoretical research has been done in this field [15], the aim of this research is to tackle this phenomenon in order to provide a better insight into this undesirable phenomenon and consequently mitigate the MD pore wetting. To embark on this expedition, pore wetting is investigated from four aspects to help MD process move towards commercial and sustainable operations. These aspects are as follows:

- Developing a model to estimate membrane pore size distribution (PSD), a significant parameter affecting the pore wetting risk of MD membranes, with a very low number of experimental data points.
- Providing a novel equation for estimating liquid entry pressure (LEP), as a key parameter for measuring membrane wettability potential.
- Tracking the water-air interface inside the membrane pore by developing a well-founded model.
- Modeling of pore wetting in VMD to provide a better understanding and prediction of this important phenomenon.

1.3. Structure of the thesis

This thesis is organized into seven chapters. The second chapter serves as a summary of the current knowledge on wetting phenomena in desalination using MD by providing a comprehensive literature review covering why pore wetting occurs, how it can be modelled, and how it can be prevented. The third chapter presents a mathematical model to evaluate PSD. A unique feature of the proposed model is that much fewer experimental data points are required to find the best fit PSD. In addition, lack of need for a dry test experiment is another advantage of this model. As well, in chapter 4, a single equation is developed by which LEP can be predicted under various conditions, i.e. different pore radii, contact angles and membrane thicknesses. In chapter 5, the movement of liquid-gas interface inside the membrane pore and consequently the pressure and velocity at the interface as well as the required time for the replacement of one phase with another one, are studied. In the next chapter, simulation results for the pore wetting of VMD are reported, considering heat and mass balance at liquid-vapor interface when steady state is achieved, and finally, chapter 7 discusses a conclusion.

1.4. References

[1] I.A. Shiklomanov, Appraisal and Assessment of world water resources, Water Int. 25 (2000) 11–32. doi:10.1080/02508060008686794.

[2] M. Bodzek, K. Konieczny, Membrane techniques in the treatment of geothermal water for fresh and potable water production, Geotherm. Water Manag. (2018) 157–231. doi:10.1201/9781315734972.

[3] M. Elimelech, W.A. Phillip, The future of seawater desalination: Energy, technology, and the environment, Science. 333 (2011) 712–717. doi:10.1126/science.1200488.

[4] M.A. Shannon, P.W. Bohn, M. Elimelech, J.G. Georgiadis, B.J. Mariñas, A.M. Mayes, Science and technology for water purification in the coming decades, Nanosci. Technol. A Collect. Rev. from Nat. Journals. 452 (2009) 337–346. doi:10.1142/9789814287005_0035.

[5] Y. Zhou, R.S.J. Tol, Evaluating the costs of desalination and water transport, Water Resour. Res. 41 (2005) 1–10. doi:10.1029/2004WR003749.

[6] A.B. Riedinger, C.E. Hickman, Considerations of energy consumption in desalination by reverse osmosis, Desalination. 40 (1982) 259–270. doi:10.1016/S0011-9164(00)88694-4.

[7] N. Voutchkov, Pretreatment for Reverse Osmosis Desalination, Elsevier, 2017.

[8] J. Swaminathan, H.W. Chung, D.M. Warsinger, J.H. Lienhard V, Energy efficiency of membrane distillation up to high salinity: Evaluating critical system size and optimal membrane thickness, Appl. Energy. 211 (2018) 715–734. doi:10.1016/j.apenergy.2017.11.043.

[9] R.W. Schofield, A.G. Fane, C.J.D. Fell, Heat and mass transfer in membrane distillation, J. Membr. Sci. 33 (1987) 299–313. doi:10.1016/S0376-7388(00)80287-2.

[10] M.R. Qtaishat, T. Matsuura, Modelling of pore wetting in membrane distillation compared with pervaporation, in: Pervaporation, Vap. Permeat. Membr. Distill. Princ. Appl., Elsevier Ltd, 2015: pp. 385–413. doi:10.1016/B978-1-78242-246-4.00013-1.

[11] T.Y. Cath, Osmotically and thermally driven membrane processes for enhancement of water recovery in desalination processes, Desalin. Water Treat. 15 (2010) 279–286. doi:10.5004/dwt.2010.1760.

[12] S.S. Ray, S.S. Chen, D. Sangeetha, H.M. Chang, C.N.D. Thanh, Q.H. Le, H.M. Ku, Developments in forward osmosis and membrane distillation for desalination of waters, Environ. Chem. Lett. 16 (2018) 1247–1265. doi:10.1007/s10311-018-0750-7.

[13] M. Baghbanzadeh, D. Rana, C.Q. Lan, T. Matsuura, Zero thermal input membrane distillation, a zero-waste and sustainable solution for freshwater shortage, Appl. Energy. 187 (2017) 910–928. doi:10.1016/j.apenergy.2016.10.142.

[14] A. Alkhudhiri, N. Darwish, N. Hilal, Membrane distillation: A comprehensive review, Desalination. 287 (2012) 2–18. doi:10.1016/j.desal.2011.08.027.

[15] E. Guillen-Burrieza, M.O. Mavukkandy, M.R. Bilad, H.A. Arafat, Understanding wetting phenomena in membrane distillation and how operational parameters can affect it, J. Membr. Sci. 515 (2016) 163–174. doi:10.1016/j.memsci.2016.05.051.

[16] F.E. Ahmed, B.S. Lalia, R. Hashaikeh, Membrane-based detection of wetting phenomenon in direct contact membrane distillation, J. Membr. Sci. 535 (2017) 89–93. doi:10.1016/j.memsci.2017.04.035.

[17] Elsevier B.V., Scopus. www.scopus.com (accessed October 15, 2020).

Chapter 2

Research background [1]

[1] The content of this chapter has been published in: Pore wetting in membrane distillation: A comprehensive review, Prog. Mater. Sci. 122 (2021) 100843.

Membrane distillation (MD) is an emerging technology for the desalination of brines. In some cases, liquid penetrates into the pores of the membrane, causing pore wetting. MD's commercialization is hindered largely due to the occurrence of pore wetting phenomena since it results in the reduction of flux and/or permeate quality. Hence, it is of crucial importance for MD to prevent pore wetting from occurring. This chapter reviews different states of pore wetting, methods of detecting this phenomenon, membrane properties related to pore wetting as well as factors causing pore wetting. Moreover, the methods to prepare membranes specifically designed for the mitigation of membrane wetting, such as the design of membrane materials, membrane surface modification, preparation of nanocomposite membranes by the addition of nanoparticles, dual-layered membranes and membranes with the re-entrant structure are discussed. Finally, process-based approaches for wetting mitigation, mainly by the pretreatment of the feed solution, are elucidated, and models for wetting phenomena are also outlined.

2.1. Different states of membrane wetting

The research conducted by Gryta *et al.* appears to be the most insightful in terms of pore wetting [1–3]. Gryta introduced the possibility of partial pore wetting and described pore wetting of DCMD in terms of the following four states (Figure 2-1): non-wetted, surface-wetted, partial-wetted, and wetted [2]. A non-wetted membrane indicates that all membrane pores are filled with vapor (Figure 2-1A). A surface-wetted membrane indicates that membrane pores have been partially filled with liquid, but the liquid does not yet span the entire pore; thus, a vapor layer remains within the pores (Figure 2-1B). At this stage, the distance of the vapor layer has decreased, leading to an increase in membrane flux. This effect was observed in an experiment using polypropylene (PP) hollow fibers where flux increased from 670 to 715 $L/m^2 \cdot d$ in the early stages

of MD [3]. This was attributed to partial liquid intrusion in the pores, leading to the decrease in the distance of the vapor diffusion, which controls the overall flux.

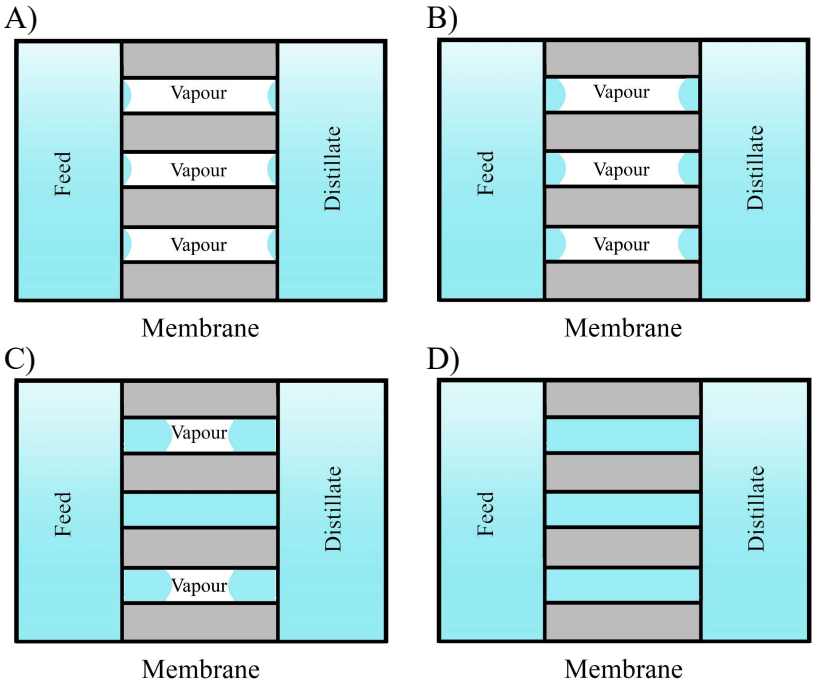

Figure 2-1 Schematic representation of the states of membrane wetting in MD: A) non-wetted, B) surface-wetted, C) partial-wetted, and D) wetted.

Mass transfer across the membrane in MD occurs in three regions depending on the Knudsen number (Kn): Knudsen region (Kn >1), continuum or ordinary-diffusion region (Kn <0.01) and transition or combined Knudsen/ordinary– diffusion region (0.01< Kn <1). Therefore, the flux of the vapor phase, *J*, can be given using the following equations for Knudsen, continuum and transition regions, respectively [4]:

$$J = \frac{2}{3}\frac{\varepsilon r}{\tau\delta}\left(\frac{8M}{\pi RT}\right)^{\frac{1}{2}}\Delta p \tag{2.1}$$

$$J = \frac{\varepsilon}{\tau\delta}\frac{pD}{p_a}\frac{M}{RT}\Delta p \tag{2.2}$$

$$J = \left[\frac{3}{2}\frac{\tau\delta}{\varepsilon r}\left(\frac{\pi RT}{8M}\right)^{\frac{1}{2}} + \frac{\tau\delta}{\varepsilon}\frac{p_a}{pD}\frac{RT}{M}\right]^{-1}\Delta p \tag{2.3}$$

where p_a, p, and D are the pressure of the gas trapped in the pore, total pressure inside the pore (p_a+ vapor pressure of water), and diffusion coefficient, respectively. Moreover, r is pore radius, M is molecular weight, R is the universal gas constant, T is absolute temperature, δ is the length of the vapor phase, ε is membrane porosity, τ is pore tortuosity, and Δp is the difference in the partial pressure of vapor through the membrane matrix. As liquid penetrates the pores, the length of the vapor phase, δ, decreases which may result in an increased flux as suggested by Eqs. 2.1-2.3, thus supporting Gryta's observation. Gryta also suggested that flux might decrease due to a temperature decrease at the vapor-liquid interface which is also supported by Eqs. 2.1-2.3. A decrease in interface temperature on the feed side reduces saturation vapor pressure, thus reducing the driving force and consequently the flux. Moreover, the crystal growth of inorganic salts may lead to a reduction in pore size or the effective membrane area, thus decreasing water production [5].

A partial-wetted membrane indicates that some pores have been filled by liquid (Figure 2-1C). As partial wetting proceeds, permeate quality deteriorates, but maintaining a slightly higher hydraulic pressure on the permeate side is enough to prevent leakage so the MD process may continue [2]. A wetted membrane indicates that all pores have been filled with liquid (Figure 2-1D). Both partial and full wetting result in feed solution leaking into the permeate, which ultimately deteriorates permeate quality and is one of the major disadvantages of pore wetting alongside permeate flux reduction [6].

2.2. Detection of pore wetting

The occurrence of pore wetting greatly inhibits the separation efficiency and continuous operation of MD processes [7]. Detecting and monitoring pore wetting not only helps in understanding the mechanism of the wetting phenomenon but also provides information regarding the appropriate

time for membrane recovery or replacement. Detection processes can be divided into two different approaches: ex-situ and in-situ. First, the ex-situ methods will be explained.

Gryta illustrated partial wetting of PP membrane pores through scanning electron microscopy (SEM) and energy-dispersive x-ray spectroscopy (EDS or EDX) line analyses. Such analyses allowed for salt deposition along the inside of membrane pores to be visualized through changes in calcium and magnesium concentrations following desalination by DCMD (Figure 2-2) [2]. By similar methods, Zhu *et al*. observed partial pore wetting in polyvinylidene fluoride (PVDF) and polyvinyl alcohol (PVA) composite hollow fiber membranes, also following desalination by DCMD [8,9].

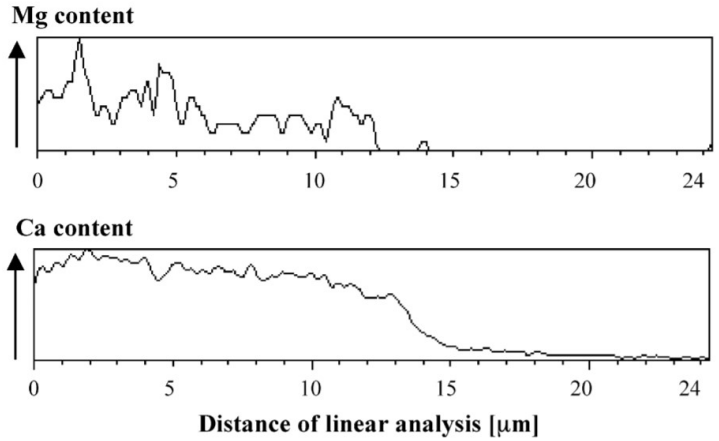

Figure 2-2 SEM-EDS line analysis of Mg and Ca salt deposits inside membrane pore, adapted from [2].

The Detection of Dissolved Tracer Intrusion (DDTI) method has been proposed by Jacob *et al.* [10], which includes the SEM-EDX detection of a tracer (salt), inside or at the surface of membrane pores depending on the extent of wetting in VMD. After desalination, SEM was used to visualize the cross-section of the membrane, and EDX analysis was employed for the required elements. Then the SEM and Cl micrographs were converted into 8-bit images and merged. The gray values (pixel brightness from 0 to 255), which are proportional to the number of chlorine ions, were

measured across the cross-section of the membrane. A potential disadvantage of this method is that it can only study tracers that can be feasibly detected [10]. Although these ex-situ methods of detection illustrate the occurrence of wetting phenomena, they cannot be used during MD operation.

The conventional detection method for pore wetting involves monitoring the electrical conductivity of the permeate because increased diffusion of solutes through the liquid-filled pores results in decreased salt rejection and increased permeate electrical conductivity [3,7,11]. Although advantageous for its simplicity, the conventional method can detect wetting only after the membrane failure takes place due to total wetting [11]. Further, the presence of dissolved gases such as ammonia and carbon dioxide can interfere with detection because they also increase permeate electrical conductivity [3].

Alternatively, another in-situ detection method was developed to detect pore wetting electrolytically. This can be achieved by use of an electrically conductive membrane incorporated into a MD electrochemical cell where the membrane acts as an electrode and a barrier to reject salt. When wetting occurs, the passage of water and salt ions through the membrane completes the circuit, thus increasing the electrolytic conductivity and the current passing through the electrochemical system. In this study, desalination by DCMD was performed using an electrospun PVDF-*co*-hexafluoropropylene (PVDF-HFP) membrane coated with a layer of electrically conductive carbon cloth. The device could detect pore wetting by monitoring the current through the system (Figure 2-3) [7]. This method demonstrated that it is more sensitive than measuring permeate conductivity and provides real-time detection of wetting which is beneficial for industrial use; however, it cannot detect imminent wetting of pores that have not been fully wetted yet [7,11]. Further, consideration must be taken with regards to anodic or cathodic detection since any bias

strongly affects wetting detection [7]. Moreover, the conductive layer on top of the MD membrane will affect the performance of the membrane lying underneath the coated layer.

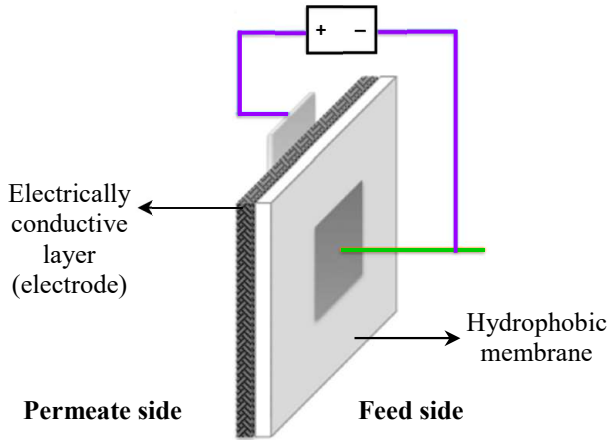

Figure 2-3 Membrane-based MD electrochemical cell for wetting detection, adapted from [7].

Another in-situ method instead detects pore wetting based on the measurement of cross-membrane impedance. Impedance is measured following the application of an alternating current of known frequency and refers to the total opposition, both resistance and reactance, that a circuit exhibits in response to an applied electrical stimulus [12,13]. Impedance varies depending on the presence of electrolyte solution or air in membrane pores [11]. As previously stated, the passage of water and salt ions through a wetted membrane completes the electrical circuit, whereas the air-filled gaps that exist prior to total pore wetting impede the completion of the circuit [7,11]. As wetting proceeds, the air gap diminishes, thus decreasing the overall system impedance. Applying this method for desalination by DCMD, surfactant-induced pore wetting was detected by monitoring cross-membrane impedance and permeate conductivity simultaneously (Figure 2-4) [11]. This method demonstrated the ability to give real-time detection of wetting as well as early detection of imminent wetting-based membrane failure since a decrease in impedance corresponding to partial wetting could be detected prior to an increase in permeate conductivity corresponding to total wetting [11].

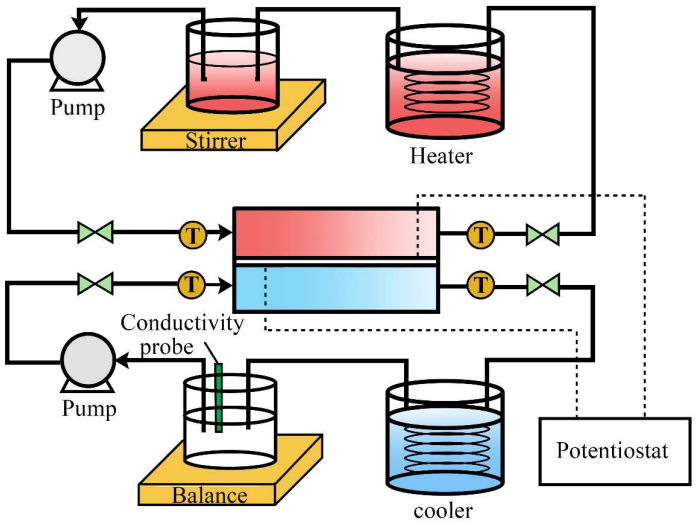

Figure 2-4 DCMD system for cross-membrane impedance measurement, adapted and redrawn from [11].

An optical tool has been developed to detect wetting based on the phenomenon of light transmission for a VMD process with water and saline solutions (Figure 2-5) [14]. This method is based on how the relative amounts of light scattered and transmitted by a material determine its transparency. When light falls on a porous membrane under ambient conditions in an air medium, it appears opaque since a small proportion of the light is transmitted while most of it is scattered. Replacement of the medium from air to the one with a refractive index more similar to that of the membrane material (e.g. water) will increase light transmission, decrease light scattering, and make the membrane appear more translucent. By illuminating the feed-side of a membrane, this phenomenon was shown to monitor the degree of wetting based on the membrane material's shift from opaque towards transparent as captured through pixel or light intensity by a camera or light sensor while all other parameters were constant. In-situ methods are advantageous since there is no destruction of the membrane being studied; however, this optical tool faces some limitations since membranes could not be visualized at the scale of the pores and in practice may be altered by the presence of opaque particles, translucent feed, scaling, and/or fouling [14]. Also, along with

most of the previous methods, this method is not commercially available yet and requires the membrane to be prepared for each study.

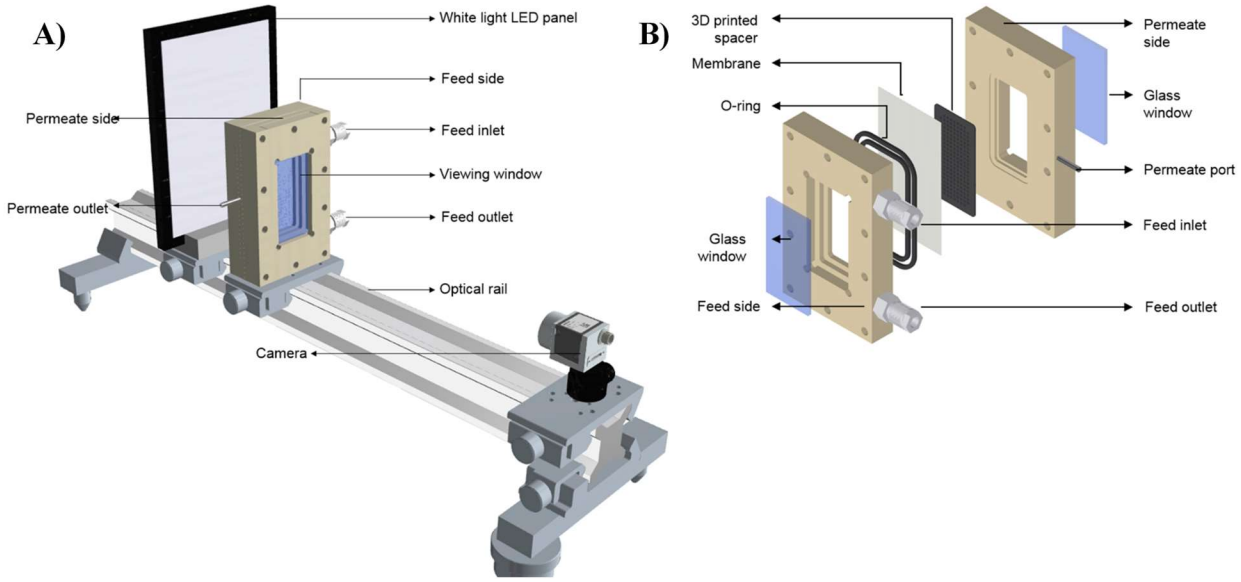

Figure 2-5 A) Optical system for in-situ MD wetting detection and B) the corresponding module design, adapted from [14].

2.3. Membrane properties related to pore wetting

This section discusses surface free energy (SFE), surface morphology, which includes surface roughness and pore size and pore size distribution, contact angle (CA) and liquid entry pressure (LEP). It should be emphasized that SFE and the surface morphology are the intrinsic properties of the membrane, whereas CA and LEP are the parameters that depend on those intrinsic properties.

2.3.1. Surface free energy

Surface properties impact overall material properties and are thus important to many processes such as MD in which the control of membrane surface hydrophobicity is involved [15]. One such property is the SFE (γ) of a membrane which is the energy difference between the bulk and surface of a membrane [16]. The Young equation (Eq. 2.4) describes the thermodynamic equilibrium of

the three interfacial surface tensions of a sessile liquid droplet on an ideal solid surface in relation to its CA [17]. Consequently, the Young equation gives insight into how the relative quantities of the three surface tensions affect CA and wetting behaviour (Table 2-1).

$$\cos\theta_Y = \frac{\gamma_{SV}-\gamma_{SL}}{\gamma_{LV}} \tag{2.4}$$

where θ_Y is the Young CA (°) and γ_{SV}, γ_{SL}, and γ_{LV} are the surface tensions (N/m) of the solid-vapor, solid-liquid, and liquid-vapor interfaces, respectively.

Table 2-1 Relationship between interfacial surface tensions, CA, and wetting characteristics.

Surface Tension Relationship	**CA**	**Predicted Wetting Characteristic**
$\gamma_{SV} - \gamma_{SL} = \gamma_{LV}$	$\theta = 0°$	Perfect wetting
$\gamma_{SV} - \gamma_{SL} > 0$	$0° \leq \theta \leq 90°$	High wetting
$\gamma_{SV} - \gamma_{SL} < 0$	$90° \leq \theta \leq 180°$	Low wetting
$\gamma_{SL} - \gamma_{SV} = \gamma_{LV}$	$\theta = 180°$	Non-wetting

Alternatively, SFE can be calculated from an equation modified from the Young equation, called the Lifshitz-van der Waals (LW) method, which considers LW (apolar), Lewis acid, and Lewis base interactions [18]:

$$(1+\cos\theta)\gamma_L = 2\left(\gamma_S^{LW}\gamma_L^{LW}\right)^{\frac{1}{2}} + 2(\gamma_S^{+}\gamma_L^{-})^{\frac{1}{2}} + 2(\gamma_S^{-}\gamma_L^{+})^{\frac{1}{2}} \tag{2.5}$$

where S and L refer to the solid and liquid phases, and + and – refer to the Lewis acid and Lewis base components of the SFE, respectively [17]. The use of an apolar liquid and/or apolar solid renders the final two terms in Eq. 2.5 negligible [19]. Due to the relationship between CA and SFE, the components of the solid SFE are obtained by measuring the CA with three liquids. Upon obtaining the surface tensions for these liquids (γ_L^{LW}, γ_L^{+}, and γ_L^{-}) from the literature and γ_L from experiments, three equations in the form of Eq. 2.5 (for the three different liquids) can be solved

simultaneously for the three unknowns (γ_S^{LW}, γ_S^+, and γ_S^-) [18,19]. The total surface energy of the membrane (γ_S) is obtained by the following equation [18]:

$$\gamma_S = \gamma_S^{LW} + \gamma_S^{AB} = \gamma_S^{LW} + 2(\gamma_S^+ \gamma_S^-)^{\frac{1}{2}} \quad (2.6)$$

where superscript AB refers to Lewis acid-base interactions.

The SFE of various membrane materials has been given in the literature. For example, typical values for the surface energy of common membrane materials, namely polytetrafluoroethylene (PTFE), PVDF, PP, and polyethylene (PE), are 19.1, 30.3, 30.0, and 33.2 mN/m, respectively [20].

2.3.2. Surface roughness

The apparent CA at the boundary between a liquid and the surface of any solid material is significantly influenced by the surface roughness, which consequently affects processes such as moistening, spreading, and wetting [21]. Since there is a relationship between surface wettability and surface roughness, determination of this parameter is of great importance [22]. Various roughness parameters are used to compare MD membranes, and these parameters can be evaluated by obtaining topographical images of the membrane surfaces with atomic force microscopy (AFM) and analyzing them with the corresponding software. Surface roughness parameters include the mean roughness (R_a), the root mean square of z-direction data (R_q), and the mean difference in the heights of the five highest peaks and five lowest valleys (R_z) [23]. A sample AFM image of a PVDF membrane containing 1% graphene by weight is displayed with its corresponding R_a value in Figure 2-6 [24].

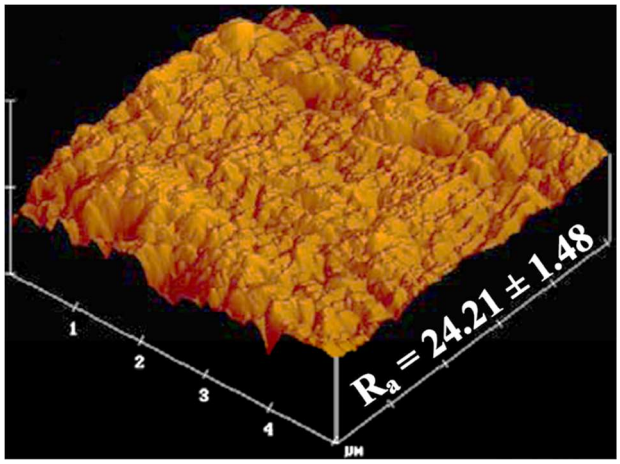

Figure 2-6 AFM image for a graphene-PVDF membrane containing 1 wt% graphene, adapted from [24].

R_a is the mean value of the membrane surface relative to the center plane. The center plane is located such that the volumes enclosed by the images above and below this plane are equal. This parameter is evaluated by the following equation [23]:

$$R_a = \frac{1}{L_x L_y} \int_0^{L_x} \int_0^{L_y} |f(x,y)| dxdy \tag{2.7}$$

where L_x and L_y are the surface dimensions in the x and y directions and f(x,y) is the surface profile relative to the center plane. Meanwhile, R_q is the standard deviation of z-direction data, or Z values, for a specified area and is evaluated by the following equation [23]:

$$R_q = \sqrt{\frac{\sum (Z_i - Z_m)^2}{N_p}} \tag{2.8}$$

where Z_i is the i^{th} Z value, Z_m is the mean Z value, and N_p is the number of points for the specified area. Finally, R_z is the average difference in height between the five highest peaks and five lowest valleys and is calculated relative to the mean plane, or the plane with the minimum variance of image data.

While using the AFM technique to compare the roughness parameters for various membrane surfaces, the data obtained from multiple areas on each membrane sample should be averaged.

Further, the roughness parameters should not be considered absolute since they depend on factors including the curvature and size of the AFM tip, the scanned area, and the data treatment for the imaged surfaces such as plane fitting, flattening, and filtering. Therefore, the same tip should be employed for the comparison of MD membranes using AFM with consistent handling and data treatment of imaged membranes [23].

2.3.3. Pore size and pore size distribution

Membrane pore size is a parameter that significantly affects pore wetting. Since capillary pressure prevents liquid from entering the pore and is inversely proportional to the pore radius, a large pore size reduces capillary pressure and may cause pore wetting. For the purpose of MD, narrowing the pore size distribution reduces pore wetting risk [25]. Pore size and pore size distribution can be measured through a variety of techniques such as the adsorption method, the bubble point method, mercury porosimetry, permporometry, and thermoporometry. The techniques also include methods involving gas or liquid transport and microscopic methods such as SEM, transmission electron microscopy (TEM), and AFM [26].

One of the most prevailing tools to obtain information regarding the pore size, pore shape, morphology, and structure of membranes is electron microscopy (EM), most commonly SEM and TEM [27]. AFM is advantageous due to its high resolution and lack of necessity for special sample preparation like the heavy metal coating required in SEM and TEM, a preparation step that tends to damage the membrane [28]. Although the determination of pore size and pore size distribution is possible using microscopic techniques, the results obtained by these methods are limited to a small surface of the membrane and, therefore, cannot be safely generalized to the whole membrane. To overcome this limitation, some other methods can be employed.

One such method is gas permeation tests which aid in characterizing membranes in terms of the average pore size and the effective porosity by measuring the gas permeation. Effective porosity is the ratio of membrane porosity (ϵ) to effective pore length (L_p), considering the tortuosity of the pores. An apparatus is employed such that the permeation of a gas through a dry membrane is measured with a flow meter at various transmembrane pressures at room temperature. Gas permeance (B) can be expressed by the following linear relation as a function of mean pressure within the membrane pore (P_m) [29,30]:

$$B = \frac{P_m}{8\mu RT}\frac{r^2\epsilon}{L_p} + \frac{4}{3}\left(\frac{2}{\pi MRT}\right)^{0.5}\frac{r\epsilon}{L_p} \tag{2.9}$$

where M is the gas molecular weight, R is the gas constant, T is the absolute temperature, μ is the gas viscosity, and r is the pore radius. Plotting the dependence between B and P_m and evaluating the slope and y-intercept allows for the effective porosity and pore radius to be evaluated [29].

Alternatively, a combination of the bubble point and gas permeation methods, known as the wet/dry flow method, can be employed to determine the maximum pore size, mean pore size, and pore size distribution of membranes. As with the previous method, the wet/dry flow method first evaluates the linear relationship between gas permeation rate and varying transmembrane pressure in a dry membrane. The membrane is subsequently wetted by a liquid with low surface tension and is assumed to be completely wetted by said liquid. The now non-linear dependence of gas permeation rate on varying transmembrane pressure is evaluated at the same temperature.

The bubble point test considered in this method allows for the determination of the largest membrane pore diameter (d_p) since the largest pores are opened at the transmembrane pressure (ΔP_{min}), called the bubble point, as related to d_p through the following Laplace equation [23]:

$$d_p = \frac{4\sigma}{\Delta P_{min}}\cos\theta \tag{2.10}$$

where σ is the surface tension, and θ is the CA between the liquid and membrane surface. Thus, the bubble point corresponds to the minimum ΔP required to force a gas bubble through a wet pore. At values for ΔP higher than the value corresponding to the bubble point, the increased pressure allows smaller pores to become progressively opened until all pores are empty, including the pores of minimum diameter. Therefore, the range of applied ΔP depends on the membrane pore size distribution. The mean pore size can be determined by plotting the ratio of the gas permeation rates in the wetted and dry membranes (J_w/J_d) as a function of pore size (e.g. pore radius) and identifying the size corresponding to a ratio of 0.5 [23].

2.3.4. Contact angle

MD allows for the diffusion of a vapor phase across a non-wettable, hydrophobic, microporous membrane which separates two aqueous liquids with different temperatures [31]. The terms hydrophobicity and hydrophilicity come from Greek origins where hydro means water and philicity and phobicity refer to affinity or lack thereof, respectively [32]. The surface wettability, or affinity of a liquid toward a solid phase like a membrane, is often evaluated using the sessile drop method, which measures CA (Figure 2-7). This method involves the deposition of a liquid droplet on a surface, allowing it to form a solid-liquid interface by displacing another fluid (typically a vapor phase). Competition occurs between cohesive interactions of liquid-phase molecules and adhesive interactions between the solid and liquid phases. CA is measured from the profile of the droplet as the angle between the tangents to the solid-liquid and liquid-vapor interfaces, where a CA less than 90° indicates hydrophilicity and a CA greater than 90° indicates hydrophobicity [33].

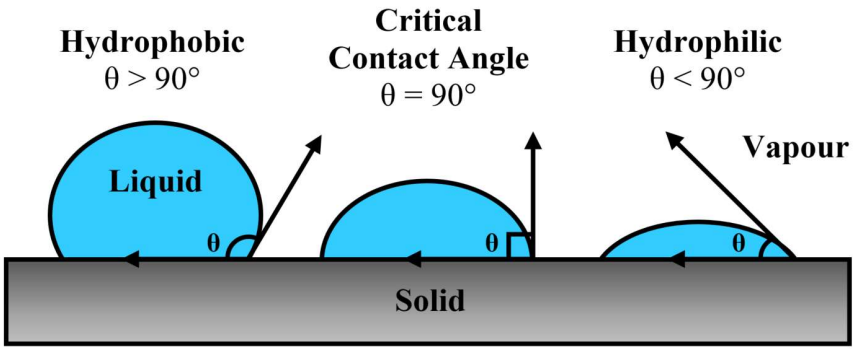

Figure 2-7 Sessile drop CA (θ) measurement for evaluation of surface wettability.

However, the relationship between surface wettability and CA has often come into question. For example, PVDF membranes are commonly used for MD; however, water on a PVDF surface has been shown to result in a CA slightly less than 90°, indicating hydrophilicity. As such, water should theoretically be drawn into the membrane pores, but this is contrary to what is desired for MD and what actually occurs [4]. Therefore, more investigation is required to provide a better understanding of the relationship between CA and wettability.

Various improvements in techniques for the measurement and calculation of CA have been made since the concept of CA was introduced through the work of Thomas Young (Figure 2-8) [33]. Young stated that all capillary phenomena might be explained by a balance of the surface tensions with consideration of the angle of contact [34]. However, the Young equation (Eq. 2.4) is only applicable for determining the macroscopic CA for an ideal solid surface that is perfectly smooth.

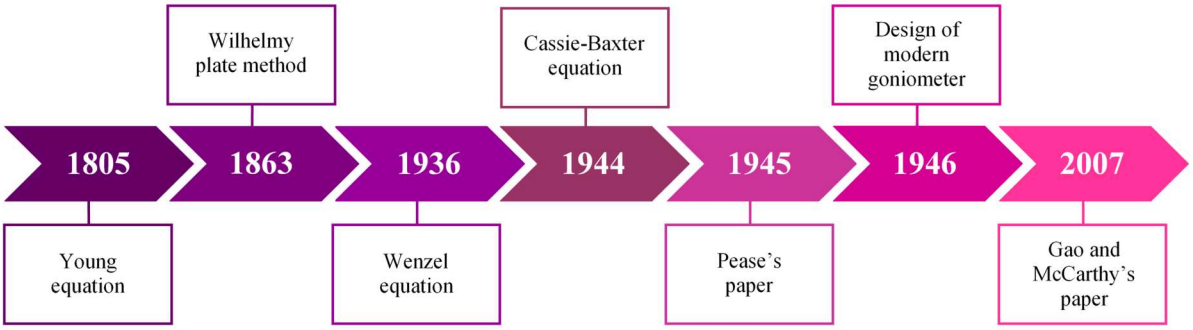

Figure 2-8 Timeline of key equations and methods for CA measurement.

The surface of any real solid will be greater than the geometric surface due to surface roughness. As a result, the experimentally measurable CA is an apparent CA which may differ from the ideal CA for smooth solid surfaces. The Young equation was adapted by Wenzel and then Cassie-Baxter to relate the Young and apparent CAs for rough surfaces depending on the state of surface wetting (Figure 2-9) [33,35]. The following model developed by Wenzel includes a unitless surface roughness factor (r) that considers surface heterogeneity [36]:

$$\cos\theta_W = r\cos\theta_Y \tag{2.11}$$

where θ_W is the apparent CA (°) corresponding to complete surface wetting [33]. Cassie and Baxter sought to extend Wenzel's analysis to rough, porous surfaces [37]. The following is a simplified version of their model for a composite surface [33]:

$$\cos\theta_{CB} = f_s(\cos\theta_Y + 1) - 1 \tag{2.12}$$

where θ_{CB} is the apparent CA (°) of a droplet resting on a composite surface of solid and air, and f_s is the fraction of solid surface that is in contact with the liquid phase.

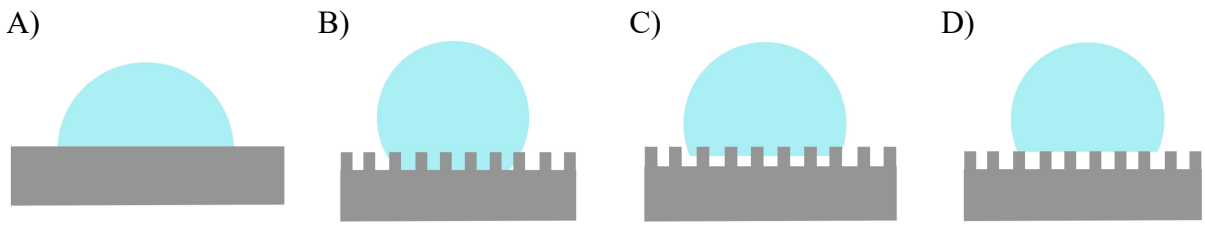

Figure 2-9 Schematic of surface wettability on ideal or rough surfaces according to the A) Young, B) Wenzel, C) intermediate, and D) Cassie-Baxter equations, adapted and redrawn from [33].

The relation between the level of hydrophobicity and membrane surface roughness can be visualized with the preparation of graphs known as Kao diagrams. The CAs on a rough surface (θ_r) and on an ideal smooth surface (θ_s) are measured for numerous liquids with varying surface tension. Kao diagrams are then prepared by plotting $\cos(\theta_r)$ against $\cos(\theta_s)$ (Figure 2-10) [38]. A sample of Kao diagrams for different membrane surfaces can be found in the literature [39,40]. Further, Kao diagrams indicate when the Wenzel or Cassie-Baxter model is applicable. Hydrophilic and highly hydrophilic surfaces are found in the first quadrant, where the soaking of polar solvents is observed due to the hydrophilic surface property. The central area comprises the Wenzel region, for which surfaces are characterized by homogeneous morphology and hydrophobic surface character. The final area, found in the third quadrant, comprises the Cassie-Baxter region, for which surfaces are highly rough and hydrophobic and have developed nano- and micro-structure domains [38,40].

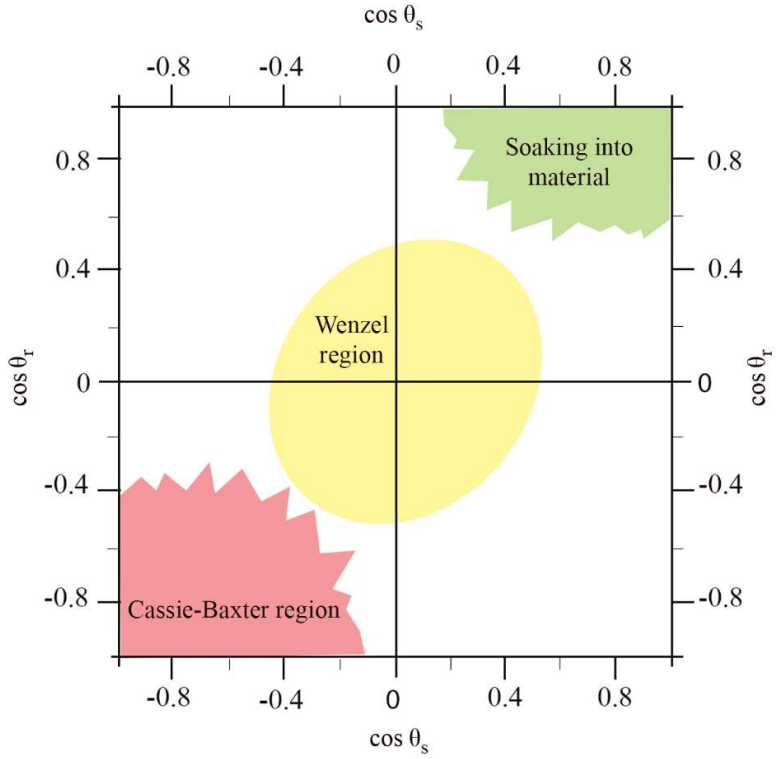

Figure 2-10 Kao diagram outlining the correlation between level of hydrophobicity and membrane surface roughness, adapted and redrawn from [40].

The significance and interpretation of CA have been questioned, so caution must be exercised when considering CA as a wetting parameter. Notably, Pease suggested that the air-liquid interface in contact with the solid is nearly a one-dimensional system where the junction is a line of tension acting on the fluid surface. The three-phase junction line could assume an infinite number of parallel positions on the surface of the solid, thus varying the CA [41]. The preceding equations all predict that CA is dependent on contact area due to differences in surface chemistry or topography; however, experiments by Gao and McCarthy agreed with Pease's assessment that events at the contact line, as opposed to contact area, control CA [42]. Although the Wenzel and Cassie-Baxter models poorly fit experimental data in many scenarios, these equations are still valid if the structure of the contact area reflects the ground-state energies of contact lines and transition states between them and if the distribution of surface defects is spatially uniform [33,42]. In the

case of surfaces with isolated defects, the Cassie-Baxter and Wenzel equations with constant surface fraction and roughness parameters do not hold; however, McHale argued that such surfaces might be described by these models provided that the parameters are reevaluated to local values appropriate to the droplet perimeter [43].

Another consideration is that the CA of an ideal surface depends on the intrinsic surface chemistry, which dictates a minimum in Gibbs energy or a single equilibrium state. Meanwhile, a real surface can exhibit different CAs, which correspond to various possible thermodynamic states due to surface nonuniformity as a result of surface roughness or chemical heterogeneity. In addition, CA appears to be also governed by droplet size. The assumptions of an ideal surface neglect the effect of molecular interactions, but equations have been derived from the Young equation to account for volume through the radius of curvature. Detailed information can be found in the literature [33].

2.3.5. Liquid entry pressure

In the context of membrane wetting characteristics, LEP is the minimum transmembrane pressure that must be applied to a liquid feed before it overcomes the hydrophobicity of a non-wetted membrane, thus penetrating the pores [44]. The most common method for the determination of LEP is Smolder's procedure [45]. The set-up for such LEP measurement consists of a membrane placed in a cell such that the feed side is filled with liquid feed (Figure 2-11A). Pressure is increased gradually by way of pressurized nitrogen from a gas cylinder onto the feed side until a flux through the membrane is observed. This flux is indicated by the first droplet of liquid that appears from the permeate side and occurs at the LEP [46,47].

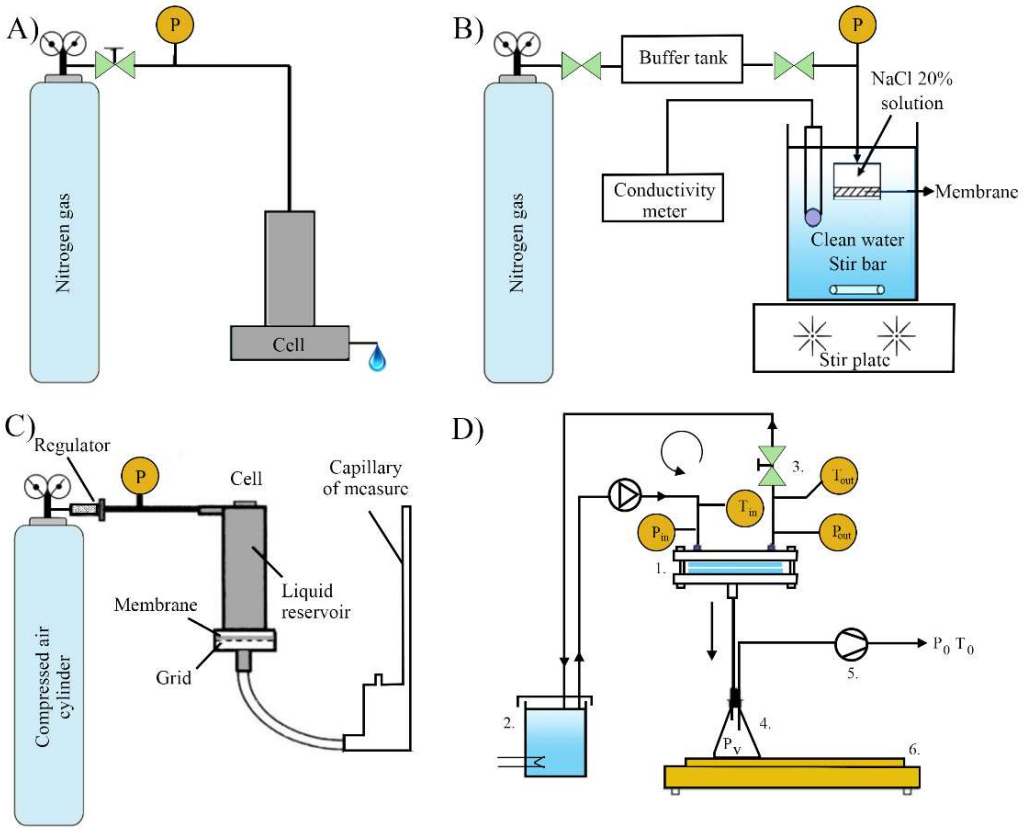

Figure 2-11 Schematic of experimental apparatus used for LEP measurement. Displayed are the apparatus as described by A) Smolders and Franken, adapted and redrawn from [45], B) He et al., adapted and redrawn from [48], C) García-Payo et al., adapted and redrawn from [49], and D) Rácz et al. (1. membrane module, 2. feed, 3. valve, 4. permeate flask, 5. vacuum pump, 6. digital balance), adapted and redrawn from [50].

He *et al*. introduced a similar method in which the feed side is filled with 20 wt% NaCl solution while the cell and membrane are soaked in a tank of pure water whose conductivity is monitored by a conductivity meter (Figure 2-11B). Pressure is applied from a nitrogen cylinder to the feed side until NaCl solution penetrates the membrane, resulting in a quick increase in pure water conductivity. The pressure at which this occurs is considered the LEP [48,50]. García-Payo *et al*. also developed a method which includes a capillary with an inner diameter of 1 mm placed at the outlet of the cell (Figure 2-11C) [49]. This capillary is filled with water and exhibits a stagnant meniscus in the absence of applied pressure. Pressure is applied to the feed side until it exceeds

the value corresponding to the LEP, as indicated by the movement of the meniscus that is measured by a cathetometer [50].

Unlike the preceding methods, which are considered static methods, a dynamic method for LEP determination has been proposed. In this method, the pressure of the recirculating feed is increased stepwise, and simultaneously vacuum is applied on the permeate side. Reaching the LEP corresponds to the movement of a liquid meniscus in the permeate side tube (Figure 2-11D). The permeate flux of the wetted membrane can then be measured at different pressures using a balance placed under the permeate reservoir [50].

The precise estimation of LEP is important since one of the main reasons for pore wetting is exceedance of the LEP, thus causing instability of the MD process [16,51]. Several models have been presented to estimate the LEP, with the following Young-Laplace equation being the classical model for the estimation of LEP for cylindrical pores:

$$\mathrm{LEP} = -\frac{2\sigma\cos\theta}{r_{max}} \tag{2.13}$$

where σ is the surface tension (N/m), θ is the CA (°), and r_{max} is the maximum pore radius (m). However, pores are usually non-cylindrical; therefore, a geometry coefficient is included in the Young-Laplace equation to account for non-cylindrical geometries, thus obtaining the following equation (Franken's model) [31]:

$$\mathrm{LEP} = -\frac{2B\sigma\cos\theta}{r_{max}} \tag{2.14}$$

where B is the unitless pore geometry coefficient which assumes a value of 1 for cylindrical pores. An alternative method for the calculation of LEP was developed by Kim and Harriott by treating the membrane as an array of intersecting cylindrical fibers [52]. The pores of many membranes consist of spaces between individual membrane fibers, and can thus be described as toroidal in

geometry rather than cylindrical (Figure 2-12A-D) [53]. The LEP for such toroidal pores can thus be calculated using the Purcell model [54,55]:

$$\Delta P = \frac{2\sigma}{r} \cdot \frac{\cos(\theta-\alpha)}{1+\left(\frac{R}{r}\right)(1-\cos\ )} = \frac{2\sigma}{r}\cos(\theta_{eff}) \quad (2.15)$$

where R is fiber radius (m), α is structural angle accounting for axial deviation of the pores (°), and θ_{eff} is the effective CA (°). The LEP corresponds to the maximum of Eq. 2.15, so following the differentiation of this equation and setting it equal to zero, α can be determined from the following equation [55]:

$$\sin(\theta - \alpha) = \frac{\sin\theta}{1+\left(\frac{r}{R}\right)} \quad (2.16)$$

In accordance with this model, the effective CA is never below 90°, even for materials with an intrinsic CA of zero. Therefore, spontaneous wetting, or an LEP of zero, requires both an intrinsic CA below 90° and a very small ratio of r/R [55]. However, it has been shown in the literature that spontaneous wetting can occur with a CA greater than zero, regardless of the r/R ratio, ultimately contradicting this model [55,56].

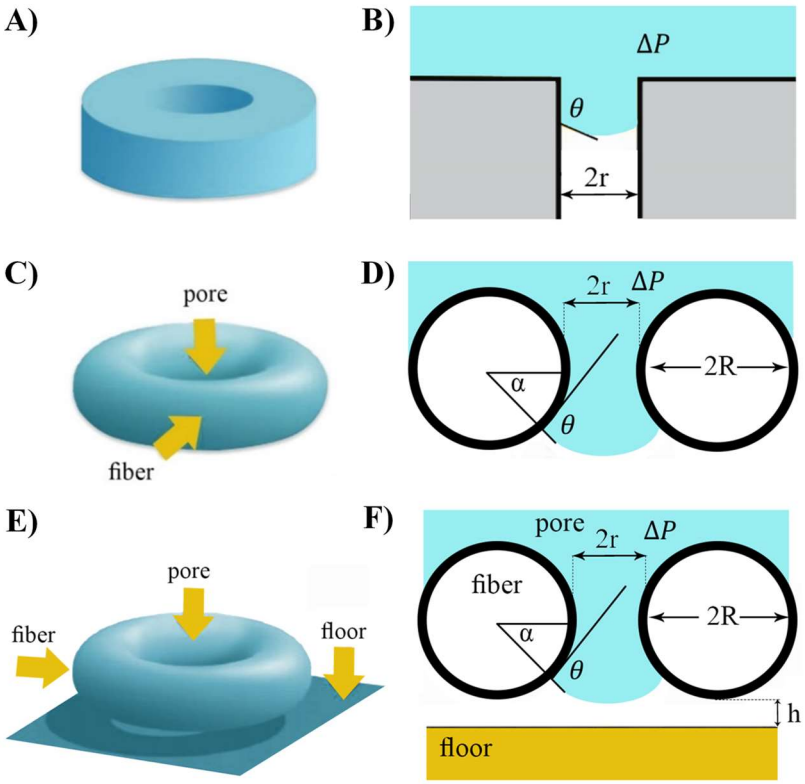

Figure 2-12 Schematic three-dimensional representations and cross-sections of cylindrical and toroidal membrane pores for models of LEP. Displayed are A,B) cylindrical and C-F) toroidal pores, where E,F) pertains to Servi's model, adapted and redrawn from [53].

As an improvement to Kim and Harriott's model, Servi *et al*. included a parameter for the distance between the floor and the bottom of the pore's fibers to consider the importance of interactions between the pores below the initially wetted surface and the liquid (Figure 2-12E-F) [53]. However, the shortcomings of this model are that the estimation r/R is difficult and has only been tested for fibrous nylon membranes [51]. In all previously discussed models, the effect of membrane thickness on LEP was neglected.

Recently, a model was developed using computational fluid dynamics (CFD) tools and validated by estimating LEP for hydrophobic membranes [51]. In this model, pore structure is cylindrical (Figure 2-13A). This model considers membrane thickness and can observe the formation of an air-mixed layer for superhydrophobic membranes, i.e. membranes with a very high CA, at the

water-air interface unlike previous models (Figure 2-13B). This layer causes sliding through the water-air mixed layer on the wall, consequently affecting the LEP. For the estimation of LEP using this model, the transient continuity equation, conservation of momentum balance, and conservation of transport volume fractions balance were simultaneously solved. They found that membrane thickness affects LEP and this finding is supported by a study by Guillen-Burrieza *et al*., which suggests that thicker membranes enhance membrane strength, thus resulting in higher LEP [55]. Although this model provides accurate LEP estimation and can evaluate the progression of wetting in hydrophobic membranes, it is not accompanied by an equation for said LEP estimation.

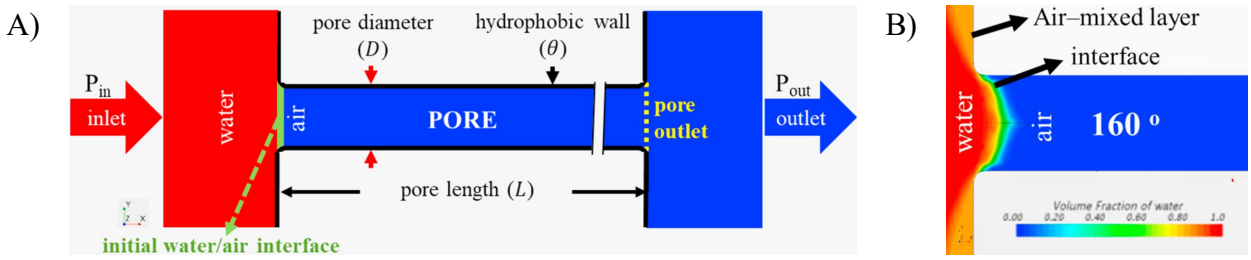

Figure 2-13 A) Schematic of two-dimensional CFD model (Yazgan-Birgi's model) and B) volume fraction of water contour plots for membrane with CA of 160°, adapted from [51]. Red represents 100% water while blue represents 100% air.

Eykens *et al*. suggested that a minimum LEP of 2.5 bar is required for MD, but other values can also be found in the literature as the recommended LEP for MD processes [57,58]. However, employing LEP as an exact parameter for the indication of membrane wetting might be misleading in some cases. For instance, during the MD process, CA might decrease due to several reasons, which will be explained in the following sections. This decrease may reduce LEP and cause liquid to penetrate the pores at a lower pressure than initial LEP, a value which was measured before the MD process, especially for the case when membrane surface hydrophobicity is higher than that of the pore walls. Moreover, during static LEP measurement, the feed side pressure is increased

gradually, which may result in compaction of the membrane, leading to an overestimation of LEP. The extent of the overestimation depends on the membrane structure, e.g. it is more severe for nanofiber membranes. Compaction may also occur during the MD process; however, these two compactions can be very different and liquid may penetrate the pore at a lower pressure than the one obtained by static LEP measurement.

2.4. Factors causing pore wetting

Several explanations behind wetting phenomena in desalination by MD are presented in the literature. In this section, high hydraulic transmembrane pressure (pressure greater than LEP), feed composition, membrane degradation, condensation inside the pore, inappropriate operational parameters, and intermittent operation are presented as reasons for pore wetting.

2.4.1. High transmembrane pressure

Hydrophobic porous membranes do not allow the liquid to pass through the pores until a certain pressure difference is exceeded [49]. Consequently, a high hydraulic transmembrane pressure (pressure greater than LEP) causes pore wetting since high pressures can overcome the hydrophobicity of a non-wetted membrane [16]. When using the phrase "liquid entry pressure (LEP)" caution should be applied. In some cases, there is a considerable difference between LEP values measured by the static and the dynamic (see section 2.3.5) method. To exemplify this issue, Rácz *et al.* investigated the LEP of a flat sheet membrane using oil in water emulsion with different concentrations of oil [59]. For the static method, the LEP value was measured to be 2.3 bar and no considerable influence of oil concentration on LEP was observed up to 3200 ppm. On the other hand, LEP values determined using the dynamic method exhibited a significant dependence on the feed oil content and reduced from 2.0 bar to 0.2 bar in the range 0-250 ppm, respectively. This

means, although a membrane may have a high static LEP value, there is a possibility of failure when used in MD setup. It is noteworthy that most of the LEP values recorded in the literature were measured by the static method.

2.4.2. Feed composition

During the operation of the MD process for desalination, a portion of the membrane pores might be filled with the feed as a result of the interactions between the feed and the membrane [60]. Evaporation of water near the membrane surface increases the salt concentration and causes deposition of salt on the surface [2]. This crystal growth on the surface of the membrane may reduce the hydrophobicity and increase the tendency of the liquid to enter the pore [16]. The temperature and concentration polarization further facilitate salt nucleation at the membrane surface [60]. The reduction of membrane surface hydrophobicity and partial liquid intrusion into the pore will induce crystallization of supersaturated salt solution inside the pore, caused by evaporation of water as well as impeded diffusion of solutes from the liquid-vapor interface into the bulk of the feed. Consequently, the hydrophobicity may decrease inside the pore progressively (Figure 2-14) [60]. The crystal deposition inside the pores hinders a diffusive solute transport from wetted pores to the bulk of the feed; thus, the scale formation rate may be increased [2]. Also, it was suggested that precipitation and growth of inorganic salt crystals might lead to a reduction in the pore sizes or the effective membrane area, consequently reducing water production [5]. Figure 2-14 illustrates the progressive deposition of salts at the entrance and inside of the pore.

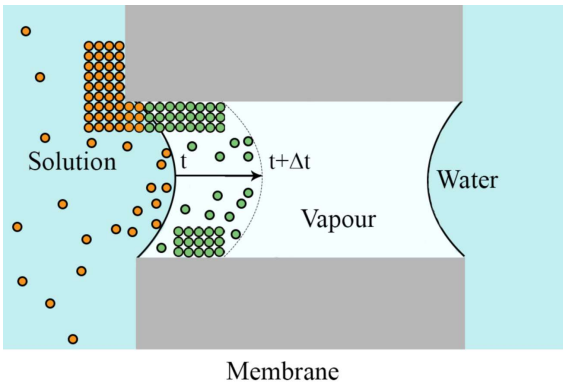

Figure 2-14 Membrane wetting due to the formation of salt deposits inside the pores (orange circles: solutes at time t, green circles: solutes at time t+Δt), adapted and redrawn from [60].

To depict the significance of the influence of salt presence on MD performance and wetting occurrence, the results of a long-term operation carried out by Gryta are worth mentioning. In this experiment, a continuous DCMD was run over three years with the purpose of demineralizing water. Throughout the period of investigation, high salt rejection was maintained, while SEM images suggested that the use of permeate from a RO process as the feed did not cause membrane wetting. However, once tap water was used as the feed, the precipitation of salts was observed on the membrane surface, resulting in wetting [3].

Kiefer *et al*. developed a method using light microscopy with automated image processing and Laser-Induced Fluorescence (LIF) to simultaneously investigate the scaling behaviour of NaCl, $CaSO_4$, $CaCO_3$, and a sea salt mixture and their impact on wetting in VMD [61]. Although it is expected that scale formation triggers wetting in MD because scales are generally hydrophilic and grow into the membrane pores, experiments showed that the size and time of scale growth do not necessarily correspond to wetting. For the feed containing sea salt, rapid growth of NaCl crystals was observed and the crystals covered the membrane surface within several minutes. However, the time required for pore wetting was in the range of several hours. Ex-situ investigations showed calcium content in the wetted area. They came to the conclusion that NaCl crystals did not result

in pore wetting. Also, experiments with sparingly soluble salts illustrated that the time required for crystal growth of $CaCO_3$ and $CaSO_4$ was almost in the same range as that of observed for pore wetting with the feed containing sea salt.

Christie *et al.* compared gypsum and silica scaling for MD purpose and showed that gypsum scaling resulted in pore wetting and earlier water flux reduction [62]. Gypsum crystals were formed inside the membrane matrix and on the membrane surface, while silica was formed only on the membrane surface. The intrusion of gypsum into the membrane pores was attributed to the crystallization pressure caused by rapid and oriented crystal growth, which resulted in pore deformation and consequently wetting. In fact, the crystal growth at the liquid-gas interface results in deforming pore due to the large crystallization pressure exerted. Therefore, the liquid-gas interface moves further into the pore.

The presence of other materials in the salty water may affect the mechanism of pore wetting. For example, it is known that liquids with low surface tension and miscibility in water such as alcohols, and amphiphilic molecules such as surfactants, are effective wetting agents. Wang *et al*. sought to understand the mechanism by which these two agents facilitate wetting using single-frequency transmembrane impedance [63]. The two exhibit different wetting behaviours such that ethanol-induced wetting is instantaneous while surfactant-induced wetting is dynamic and reliant on factors such as vapor flux and bulk concentration of surfactants in the feed. The dynamic behaviour can be attributed to the adsorption of surfactant, e.g. Triton X-100, to the membrane pore surface which removes itself from the wetting frontier and slows down the wetting process, as opposed to ethanol which does not adsorb (Figure 2-15). Organic fouling can also result in reducing surface tension and contact angle, accelerating pore wetting.

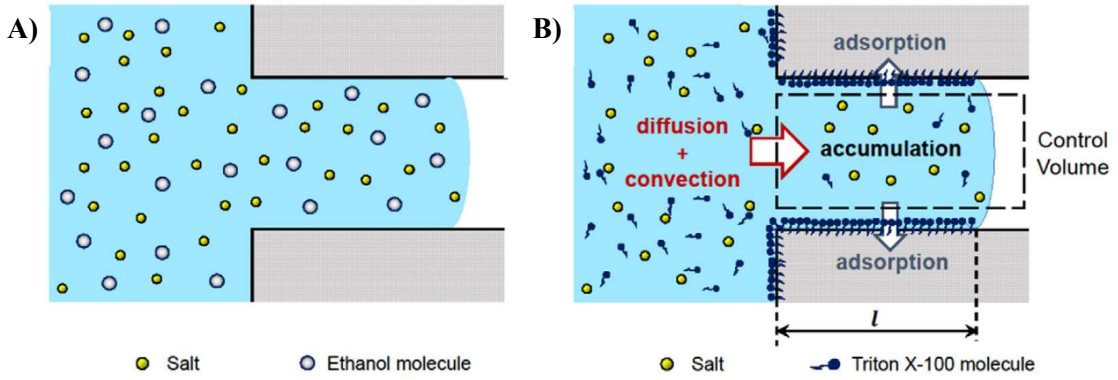

Figure 2-15 Wetting of membrane pores by saline feeds containing A) ethanol or B) Triton X-100 surfactant, adapted from [63].

Contaminants and other materials in the feed may also change the mechanism of wetting phenomena due to different interactions between the membrane and components of wastewater. For example, An *et al*. studied the applicability of MD to treat wastewater from dye processes using PVDF and PTFE membranes [64]. The dye was expected to aggregate into multiple sublayers over time, resulting in concentration polarization due to the increase in dye bulk concentration. However, analysis via SEM showed that dye molecules entered the pores of the PVDF membranes but remained on the surface of the PTFE membranes. This is attributable to PTFE's strong negative charge, which repels the negatively charged dye molecules. Consequently, dye molecules form structures at the membrane surface instead of inside the pores.

2.4.3. Membrane degradation

Another reason for this phenomenon can be attributed to membrane degradation due to physical or chemical changes during long-term operation. In a study performed by McGaughey *et al.*, surface morphology of the two sides of the membrane, contacting either with feed solution or distilled water, was investigated before and after long-term DCMD operation (20 and 100 days) [65]. Table 2-2 illustrates the CAs of virgin and used membranes and shows that the CA of the side contacting the distilled water was decreased, even though there was no scaling on this side.

This means that this reduction was entirely due to the morphology change of the membrane that was caused by the combined effects of shear forces, hydraulic pressure, and temperature. The same trend was also observed for the roughness parameter. Despite noteworthy reduction in feed side hydrophobicity, the quality of distillate was quite high, suggesting that other membrane characteristics, including distillate side or pore wall hydrophobicity, may play a significant role in maintaining rejection during long-term operation.

Table 2-2 Contact angles before and after long-term MD operation [65].

Membrane	**Side**	**Water CA after 20 days***	**Water CA after 100 days****
Virgin	Feed	140°	140°
	Distillate	140°	140°
Used	Feed	49°	61°
	Distillate	114°	104°

*For 20 days of operation: 200 g/L NaCl feed concentration.
**For 100 days of operation: 35 g/L NaCl feed concentration.

Changes in membrane surface chemistry can also facilitate membrane wetting. One such change includes hydrophilization in which some hydrophilic groups are formed on the membrane surface. The presence or absence of these groups determines the hydrophilic character of materials since materials containing more hydrophilic groups have a greater tendency to associate with water. Gryta *et al*. found that hydrophilic groups, e.g. carbonyl or hydroxyl groups, were formed on the PP membrane surface after the membrane was stored in air for nine years [66]. The presence of these groups increased the rate of membrane wettability. Further, chemical reactions between NaCl and the hydrophilic groups on the degraded membrane surface formed sodium carboxylate and caused the membrane to become wetted more quickly.

2.4.4. Condensation inside the pore

Condensation within the pores of MD membrane refers to a phenomenon by which multilayer adsorption of the vapor at the pore wall turns at a certain point into pore filling with the condensed liquid [67]. It is suggested that temperature may decrease inside the pore; therefore, condensation may take place, resulting in liquid water short-circuiting in the pore. However, experimental evidence to support this hypothesis can be scarcely found [68]. In addition, the condition in which this phenomenon may happen was attributed to the sudden reduction in transmembrane temperature difference [68].

2.4.5. Influence of operational parameters

In the research conducted by Guillen-Burrieza *et al*., the effects of operational parameters on pore wetting in DCMD, including the temperature of both hot and cold streams as well as their flow rates, were studied [68]. Based on this study, it was concluded that changing these parameters in a way that enhances the MD flux leads to reduction in pore wetting. In accordance with this research, a high feed temperature delays the occurrence of pore wetting while a higher temperature of the cold stream as well as the flow rates of both feed and permeate streams increases the wetting rate. It is noteworthy that the aim of this study was to investigate the effects of operational parameters, not the effect of scaling. Hence, no low-solubility salts were used in the experiments and feed temperature never exceeded 60 °C. Furthermore, it was suggested that increasing the feed temperature is a good strategy to reduce pore wetting since the higher vapor pressure of liquid at the liquid-vapor interface works against the flow of water in the pore.

From an opposite point of view, increasing temperature reduces surface tension, which turns high feed temperature into a challenge for pore wetting [16]. While studying a DCMD process for RO brine concentration, Ge *et al*. found that a higher-temperature feed corresponded to more

significant membrane wetting, resulting in decreased flux and salt rejection [69]. Saffarini *et al*. also investigated the effect of temperature on the morphology of PTFE membranes, with LEP as a characteristic indicating wetting, and concluded that the increase in temperature changed the membrane morphology and had a negative effect on LEP [44]. Also, the effect of temperature on the CA of PTFE membrane has been studied and it was found that the increase in temperature decreased CA, with the maximum decrease of ca. 6.5° in CA when the temperature was changed from 25 °C to 70 °C [70].

High-salinity feeds introduce an additional concentration boundary layer at the membrane interface. However, it should be noted that an increased flow rate decreases the thickness of boundary layer, which improves the MD performance [71]. Therefore, increasing the flow rate is a double-edged sword since it may increase the performance but on the other hand, may also increase the wetting rate, so caution should be applied in selecting an optimal flow rate.

Other operational parameters that have been cited to influence wetting behaviour include fluid mechanical phenomena such as vibrations, pressure peaks, or uneven flow distribution at the inlet [61].

2.4.6. Intermittent operation

Membranes that are subjected to intermittent operation face long periods of downtime during which they become dried out with surface feed residues. This is the case for many solar-powered MD plants that operate during the hours of the day with sunlight and shut down overnight; however, intermittent operation may also be due to the instability of solar operation conditions. This type of operation can accelerate pore wetting due to the deposition of salts on the membrane surface while the operation is being ceased. Guillen-Burrieza *et al*. observed that two types of hydrophobic membranes commonly used for MD, namely PVDF and PTFE, experienced salt

deposition from intermittent operation which ultimately exacerbated pore wetting. Significant salt deposits were seen within the first week of seawater exposure alongside a progressive decrease in CA, corresponding to a loss in surface hydrophobicity by the second week [72].

2.5. Membrane preparation and design for mitigation of pore wetting

2.5.1. Membrane materials

Ceramic membranes have some advantages, such as high tolerance against harsh conditions; however, high costs have made them less favourable commercially, while polymeric membranes are a better alternative thanks to cheaper costs, ease of modification, and low thermal conductivity. Thus, researchers have focused more on polymeric membranes [73]. Most of the membranes used for MD are made from PVDF, PTFE, or PP [58].

2.5.2. Membrane preparation and modification

There are two ways by which membrane pore wetting can be reduced. They are increase of membrane hydrophobicity and decrease of pore diameter. On the other hand, in order to obtain a high flux, the pore size must be as large as possible [74]. Increasing the hydrophobicity of membranes for MD is achievable through two different approaches, tailoring the whole membrane and/or modification of the membrane surface. In addition, the membrane structure is another factor that should be engineered to reduce pore wetting. Therefore, this section focuses on hydrophobicity and membrane structure.

2.5.2.1. Phase inversion technique

One of the common methods for membrane preparation for MD processes is the phase inversion technique. This technique is a demixing process which involves the removal of solvent from an initially homogeneous cast polymer film to fabricate a porous, solid membrane. The following

four methods are typically employed to achieve the transformation from liquid to solid state [75]: immersion precipitation, thermally-induced phase separation, evaporation-induced phase separation, and vapor-induced phase separation.

Immersion precipitation involves the immersion of a cast polymer film, i.e. polymer in solvent, in a coagulation bath containing non-solvent. The solvent and non-solvent exchange in the film causes precipitation of polymer. Thermally-induced phase separation involves decreasing the temperature of a cast polymer film, which lowers the dissolving power of the solvent. Then, the solvent is removed by extraction, evaporation, or freeze drying, resulting in the formation of porous membrane. Evaporation-induced phase separation also called the solution casting method, involves a polymer dissolved in a solvent or mixture of solvent and non-solvent which upon evaporation of the more volatile solvent causes the polymer to precipitate. Finally, vapor-induced phase separation involves exposing a polymer solution to a vaporous atmosphere of a non-solvent such that absorption of the non-solvent causes precipitation [75].

The structure of a PVDF membrane prepared by the phase inversion process is shown in Figure 2-16 [18]. Evidently, there are two distinct structures observed in this SEM image, a finger-like macrovoid structure and a sponge-like layer. The structure of the membrane affects the wetting resistance to a large extent. For instance, membranes with a finger-like structure can increase MD flux since they display a lower resistance to mass transfer; however, membranes with this structure are prone to become wetted more quickly compared to those comprised of a fully sponge-like structure [76].

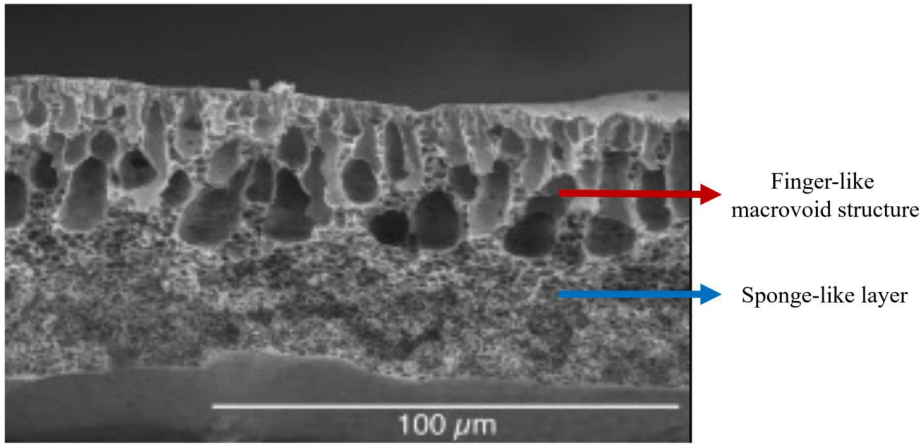

Figure 2-16 SEM image of a PVDF membrane prepared by the phase inversion process, adapted from [18].

Experimental variables pertaining to the phase inversion technique should be carefully optimized to achieve a desired membrane morphology and performance [77]. There are many parameters that need to be considered to have a membrane with desirable wetting properties, such as composition of the coagulation bath, temperature of the bath, concentration of polymer, molecular weight of polymer, etc. This note can be exemplified by a study conducted by Amirilargani *et al*. for the preparation of asymmetric polymeric membranes via phase inversion induced by immersion precipitation in a water coagulation bath, where the influence of coagulation bath temperature was investigated [78]. In accordance with this research, an increase in the size of membrane surface pores and a transition from a spongy structure to a structure with finer-like pores were observed while increasing the coagulation bath temperature from 0 °C to 25 °C. The formation of macrovoid structures appears to occur under rapid precipitation conditions, such as at higher temperatures [79]. Therefore, preparation conditions along with the type of materials (e.g. polymer, solvent, non-solvent) and concentrations used for membrane preparation are of great importance for forming a suitable structure.

In addition, the presence of nanomaterials in the polymer solution can affect membrane structure, membrane surface energy, and roughness, eventually changing the wetting resistance of the membrane. In a study conducted by Murugesan *et al.* for the preparation of nanocomposite membranes for VMD, it was found that a decrease in membrane thickness increased the portion of the finger-like layer in comparison to the spongy-like layer when using hydrophilic inorganic nanoparticles [80].

From another point of view, one of the reasons that facilitate pore wetting is membrane degradation. In long-term operation, increasing the mechanical strength of the membrane can improve its wetting resistance. The use of nanosized materials as additives in a membrane matrix can improve the thermal and mechanical stabilities of the formed composite membrane due to an increase in the interfacial interactions between the particles and polymer matrix [81]. However, the nature of these nano-additives may affect the degree of mechanical strength and a threshold concentration is usually observed. While lower concentrations of nanoparticles have been found to act as cross-linkers by enduring the stress of the load, higher concentrations result in particle aggregation weakening mechanical stability by forming defects and stress convergence points [81–83].

Mechanical characterization of a material such as a membrane requires its response to an applied force. The mechanical properties of polymeric membranes are often evaluated by techniques including uniaxial tensile testing, bending tests, bursting tests, etc. Uniaxial tensile testing is one of the most common methods and allows for the evaluation of mechanical properties such as Young's modulus, yield stress, and ultimate stress among others. This method is performed by gripping opposite ends of the specimen in the loading frame of a testing machine and applying a tensile force until predominant stress, strain, or failure is attained [84]. Woo *et al*. prepared

graphene/PVDF membranes at various graphene loadings with the phase inversion method. Results revealed that the addition of graphene could significantly increase tensile strength (e.g. adding 2 wt% graphene increased membrane tensile strength from 3.5 to 6 MPa) [24]. In this study, tensile properties were measured using a constant elongation velocity of 5 mm/min.

The presence of nanoparticles in the polymer solution can also increase roughness and consequently wetting resistance. In a study carried out by Wu *et al*., super-hydrophobic PVDF membranes were prepared by the phase inversion technique with hydroxyl-rich silica particles (SiPs) added to the polymer solution [85]. The addition of hydroxyl-rich SiPs resulted in the formation of a spherical micro-structure as observed in Figure 2-17 [85].

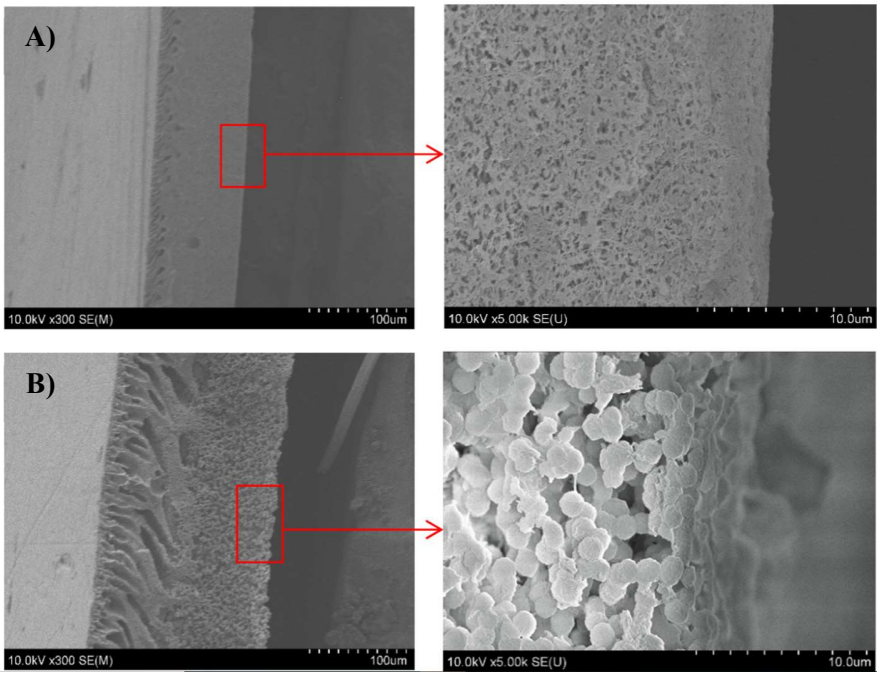

Figure 2-17 SEM images of the cross-sections of PVDF flat sheet membranes A) without silica and B) with 1.5 wt% silica, adapted from [85].

The reason for the increase in hydrophobicity is explained as follows. In this study, the addition of silica increased the surface roughness from 0.423 to 1.715 µm. This roughness was observed by the creation of hills and valley regions on the membrane surface with air pockets in the valley

region, consequently reducing the polymer/water contact area at the surface and increasing CA. At the optimum addition of hydroxyl-rich SiPs of 1.5 wt%, the pure water CA attained its highest value of 153°. SiPs also acted as nuclei for crystallization and enabled the three-dimensional growth of the spherical structures (which is mainly composed of γ type crystals) since the presence of the hydroxyl groups facilitated a transition of the PVDF chains from α to γ type crystals [85]. Moreover, membranes prepared by the phase inversion technique can be modified through different surface modification approaches, including plasma treatment, spray coating, fluorination, etc., which will be discussed in the following sections.

2.5.2.2. Electrospinning technique

In the literature, the fabrication of submicron polymeric nanofibers has been conducted by a variety of techniques including the following [86]: electrospinning, flash spinning, melt-blowing, multi-component spinning, nanolithography, self-assembly, and template synthesis. Among those, electrospinning has attracted much attention for the fabrication of highly porous non-woven nanofibers due to the simplicity of the method. With its ability to carefully control operating conditions and polymer solution properties, electrospinning forms interconnected pores with a uniform pore size and porosities exceeding 90% [87].

The electrospinning apparatus consists of a high-voltage power supply, a syringe pump, and a collector. A polymer solution or melted polymer is loaded into the syringe and the syringe pump drives the liquid to the needle tip resulting in the formation of a droplet, exposed to the electric field. A fiber jet is ejected from the tip when the Coulombic forces overcome the surface tension. Subsequent evaporation of the solvent from the fiber jet produces a randomly deposited solid polymer fiber on the collector, forming a fibrous structure [57].

The structure of nanofibrous membranes is affected by intrinsic properties of the polymer solution (e.g. polymer concentration, type of solvent, etc.), operational conditions, and environmental conditions. Successful nanofibers can be fabricated in relation to a threshold polymer concentration that exists for each combination of polymer and solvent. Lower polymer concentrations and solution viscosities tend to produce beads-on-string structures. These beads lose their spherical shape while increasing polymer concentrations and solution viscosities in favour of producing nanofibers with a uniform diameter. A further increase in polymer concentration would increase the nanofiber diameter [88]. The influence of various solution and process parameters on the morphology of electrospun nanofibers can be found in Table 3 of Tijing's paper [89].

The first attempt of the application of the electrospinning technique for MD occurred in a study by Feng *et al.* in 2008 [90]. Following this research, many attempts have been made to use electrospinning for the preparation of nanofibers for MD [91–95]. High membrane surface roughness created by the structure of the fibers is the main feature of the nanofibrous membrane, leading to high hydrophobicity and, consequently wetting resistance. Efome *et al*. prepared PVDF flat sheet membranes covered by an electrospun PVDF nanofibrous layer to increase the surface hydrophobicity [96]. Adding this nanofibrous layer showed an increase in the roughness and consequently CA.

Unfortunately, the robustness of electrospun polymeric membranes is not guaranteed since they remain susceptible to wetting in long-term operation [97]. Therefore, it is of great importance to improve the wetting characteristics of these membranes through some membrane modification approaches without sacrificing flux. One of the most common methods is heat-press through which higher LEP and mechanical properties are achieved [97,98]. As an example, Yao *et al*. optimized

heat-press conditions for an electrospun PVDF-HFP membrane and found that the best conditions were 150 °C and 6.5 kPa for 8h [97]. Membranes heat-pressed under these optimal conditions achieved a decent permeation flux of 29 LMH and salt rejection of 99.99% while operating a DCMD process with a feed temperature of 60 °C and permeate temperature of 20 °C.

However, some researchers believe that heat-press may fuse the fibers together and decrease the surface roughness, resulting in decreased surface hydrophobicity [99]. To overcome this problem, Shaulsky *et al*. fabricated an electrospun fiber mat with an average pore diameter of approximately 1.2 μm by electrospinning a PVDF-HFP solution in acetone and dimethylacetamide solvent mixture [99]. The PVDF-HFP fibrous mat was further coated with a PVDF layer that was formed through phase inversion technique, filling the empty domains between nanofibers. Finally, an average pore diameter < 0.6 μm was achieved without compromising surface hydrophobicity. With the new membrane design, they could take advantage of the high CA of fibers and simultaneously reduce the wetting potential of nanofibers.

In another study that exemplifies the preparation of wetting resistant nanofibrous membrane, Deng *et al*. proposed a two-tier interlocked composite membrane based on a hierarchical structure of isotactic polypropylene (iPP) coating and an electrospun PVDF nanofibrous support [100]. The resulting superhydrophobic composite membrane achieved high wetting resistance due to increased mechanical strength and hydrophobicity. Superhydrophobicity was achieved through the deformed micro/nanostructured microsphere surface of the coating layer, imparting increased hierarchical roughness and the low surface energy of the material. The iPP/PVDF interlocking zone of the composite membrane provided improved mechanical performance in comparison to PVDF flat sheet or nanofibrous membranes. Further, the iPP/PVDF composite membranes

exhibited robust durability against ultrasonication in isopropanol and resistance against corrosive environments. The structure of the proposed membrane is shown in Figure 2-18.

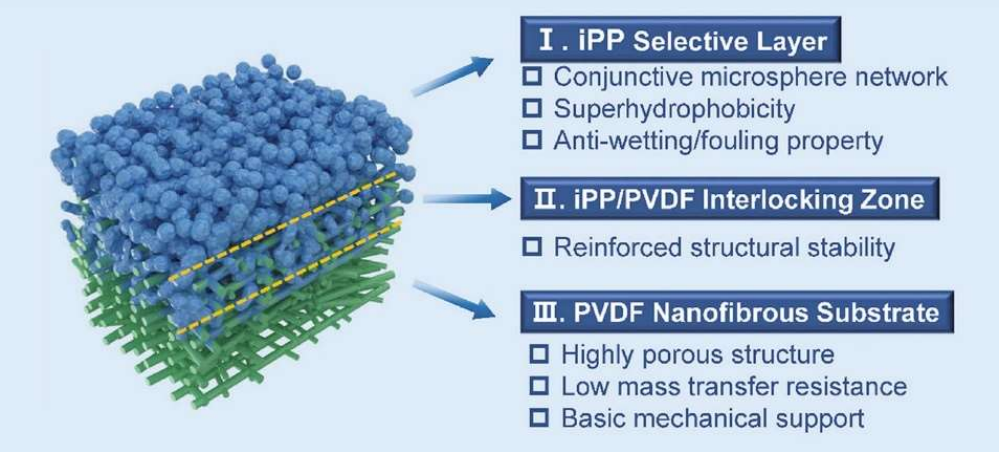

Figure 2-18 Schematic of the proposed two-tier interlocked composite membrane, adapted from [100].

Employing new materials for the preparation of MD membranes is another aspect that is being studied by researchers. For instance, Maab *et al*. synthesized aromatic fluorinated polyoxadiazoles and polytriazoles for the first time for MD membrane preparation both by phase inversion and electrospinning [93]. In this study, an apparent CA of 162° was achieved due to the high polymer hydrophobicity and porosity.

As with the phase inversion technique, embedding nanoparticles within the polymer solution can positively affect the wetting resistance of nanofibrous membranes by increasing roughness and/or lowering surface energy. In accordance with the study by Tijing *et al*., superhydrophobic PVDF-HFP nanofiber membranes containing carbon nanotubes (CNTs) of various concentrations, namely 1 to 5 wt%, were prepared [101]. The CNTs acted as nanofillers which provided enhanced mechanical and hydrophobic properties. The incorporation of 5 wt% CNTs attained a CA of 158.5° because of the membrane's increased roughness and the hydrophobicity of the CNTs.

2.5.2.3. Other membrane preparation techniques

Although there are some researches where membranes are prepared by other methods, including stretching [102,103], track-etching [104–106], etc. for MD process, most studies on anti-wetting membrane preparation for desalination using MD focus on the phase inversion and electrospinning techniques.

The stretching technique is a solvent-free approach applied for semi-crystalline polymers such as PTFE and PE. For this technique, the polymer is heated (higher than the melting point) and extruded in the desired morphology. The stretching perpendicular to the direction of the extrusion yields the porosity of the membrane [57]. Li *et al.* evaluated the influence of stretching conditions on the fabrication of PTFE membrane [102]. It was found that an increase in stretching ratio increased mean pore size, resulting in lower LEP, and consequently, lower wetting resistance. Besides, it was observed that reducing the stretching temperature was a useful approach for pore size control.

Track-etching is another membrane preparation method in which a thin polymeric layer is irradiated using high-energy particles followed by chemical etching [107,108]. Korolkov *et al.* prepared polyethylene terephthalate (PET) membranes track-etched by irradiation with $^{84}Kr^{15+}$ ions having energy of 1.75 MeV/nucleon [104]. Then the membrane was hydrophobized by UV-induced graft polymerization of styrene and CA of 104° was achieved. Although the wetting resistance is thought to increase with an increase in the membrane tortuosity [109], track-etched membranes, which usually possess low tortuosity, are highly beneficial for fundamental studies since most of the models that have been developed for MD assume cylindrical pores of the membrane.

2.5.2.4. Surface modification

One common method that is used to increase the anti-wetting properties of a membrane is surface modification. This modification can be applied to both laboratory-made and commercial membranes. Many attempts have been made to modify the membrane surface such that hydrophobicity of the membrane is increased. In this section, various methods of surface modification are covered.

Plasma surface modification has been widely used in membrane surface modification and has the potential to reduce surface energy, enhance surface roughness, and increase surface hydrophobicity [110]. With plasma technology, a thin hydrophobic layer is formed on the membrane surface through polymerization induced by radicals and fragmented molecules generated during the plasma treatment [57]. Woo *et al*. developed a PVDF membrane by electrospinning and employed CF_4 plasma surface modification [111]. This plasma treatment provided a fluorinated layer to the nanofiber membrane surface, which lowered its surface energy and enhanced wetting resistance to different low surface tension liquids, including ethylene glycol, mineral oil and methanol.

In another study, membrane hydrophobicity was increased by engineering the structure of the surface. A micropillared superhydrophobic PVDF membrane with a CA of $166.0 \pm 2.3°$ was prepared [112]. Its preparation involved the fabrication of a polydimethylsiloxane (PDMS) mold by pre-mixing of oligomer PDMS and curing agent, casting the mixture on a silicon wafer template, curing the PDMS solution and wafer in a vacuum oven, and peeling the PDMS replica off. The micropillared PVDF membrane was then prepared by spreading a PVDF solution on the PDMS replica on top of a glass plate using a casting knife before being exposed to water vapor and immersed in a coagulation bath for precipitation. The schematic of membrane preparation

method and the cross-section SEM image of micropillared superhydrophobic PVDF membrane are displayed in Figure 2-19 [112].

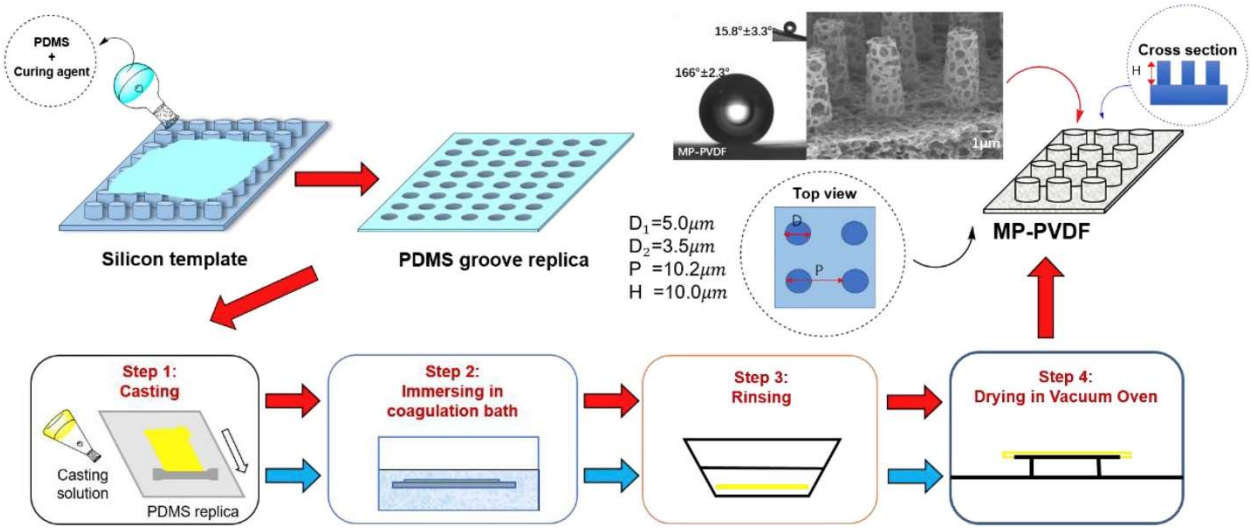

Figure 2-19 The schematic for membrane preparation along with the SEM image of the cross-section of a micropillared PVDF membrane, adapted from [112]. MP-PVDF: Micro-pillar PVDF.

Recently biomimetic superhydrophobic surfaces have attracted much attention. Lotus leaf, butterfly, strider, and gecko are some examples of superhydrophobic surfaces in nature [113]. Inspired by nature and considering lotus leaf structure, Hou *et al.* proposed a biomimetic superhydrophobic PVDF membrane [114]. According to Hou *et al.*, hierarchical micro-, nano-scale morphology was created on the PVDF surface through grafting the spherical polyvinylsilsesquioxane (PVSQ) nanoparticles onto micro-sized SiPs. When vinyltrimethoxysilane (VTMOS) was added to the SiPs suspension, a condensation reaction took place, covering the SiPs surface with polymerized VTMOS of hydrophobic nature. While the condensation and hydrophobization were going on, PVSQ nanoparticles were added and grafted onto the surface-modified SiPs via vinyl polymerization. Thus, the hydrophobic SiPs-PVSQ composite was obtained. Figure 2-20A illustrates the SEM image of SiPs-PVSQ composite

particles. Hydroxyl groups were then added to the membrane surface through treating the commercial PVDF membrane with NaOH solution, and the PVDF membrane containing OH groups was immersed into the SiPs-PVSQ composite solution to absorb the SiPs-PVSQ particles onto the PVDF-OH membrane. The wetting behaviour of the prepared membrane was in Cassie-Baxter state and the surface energy of the membrane could also be decreased thanks to the hydrophobic groups such as vinyls produced by the condensation reaction. Finally, a high water CA of ~160° and LEP of 3.53 bar were achieved. Figure 2-20B displays the schematic of the membrane surface, which was inspired by the lotus leaf.

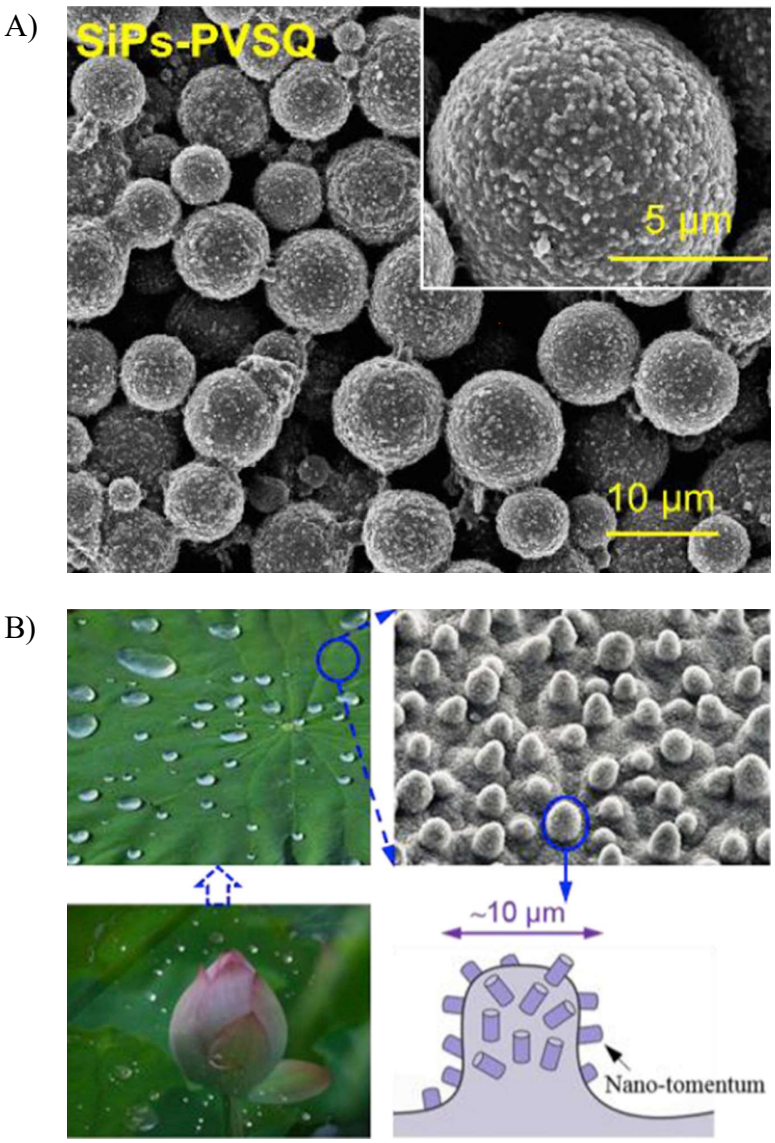

Figure 2-20 A) The SEM image of SiPs-PVSQ composite particles, and B) the schematic of membrane surface inspired by the lotus leaf, adapted from [114].

Another technique used for the modification of membranes is electrospraying. In combination with electrospinning, Attia *et al*. used this technique to develop a superhydrophobic membrane with a hierarchical micro- and nano-structured surface [115]. This was achieved by constructing a beaded structure through spraying nonfluorinated alumina nanoparticles dispersed in a solution of low PVDF concentration on an electrospun PVDF membrane. Membrane surface hydrophobicity was

enhanced such that a CA of 154° was achieved for membranes fabricated with 2 mL spray solution volume and 30 wt% alumina nanoparticles.

Although the increase of CA and LEP via modification of the membrane surface is beneficial, modification of the inside of the pores without pore blockage is also of great significance. In some cases, pore wetting occurs gradually due to membrane degradation and/or scaling; therefore, internal parts of the membrane play an important role in preventing leakage through the pores [65]. This approach can be exemplified by a study done by Servi *et al*. in which track-etched polycarbonate (PCTE) membranes were treated with initiated chemical vapor deposition of (poly(divinyl benzene) (pDVB) and poly(1H, 2H, 2H-perfluorooctyl acrylate) (pC6PFA)) bilayer [116]. The presence of the bilayer on the membrane surface caused the CA to increase compared to an untreated PCTE membrane. While pDVB was present at the pore wall, acting as the cross-linking polymer, the pC6PFA ultrathin (< 10 nm) layer coated on top of the pDVB achieved high CAs with water. Polymerization of the pDVB layer employed DVB monomer and tert-butyl peroxide as an initiator. The pC6PFA layer was then deposited on top of the pDVB layer by employing C6PFA monomer and the same initiator. This method is beneficial for providing an extra resistance against liquid movement inside the pores; however, modification should be applied carefully to prevent pore size reduction and/or blockage.

Dip-coating is also a common method for membrane modification by depositing a thin film of a material of interest on the membrane surface. Parameters including dipping solution, dipping time, and crosslinking agent concentration affect the coating material thickness, membrane pore size, and membrane structural integrity [117]. Jiao *et al*. made use of this technique in the preparation of PVDF electrospun nanofiber membranes that were covered with very low surface energy (~21 mN/m) PDMS by dip-coating [118]. Fabrication of the membranes involved immersion of the

PVDF electrospun nanofiber membranes in a PDMS solution in hexane mixed with triethoxyvinylsilane in the presence of a catalyst. The preparation process that improved the wetting properties of the membrane due to lowered surface energy is displayed in Figure 2-21 [118].

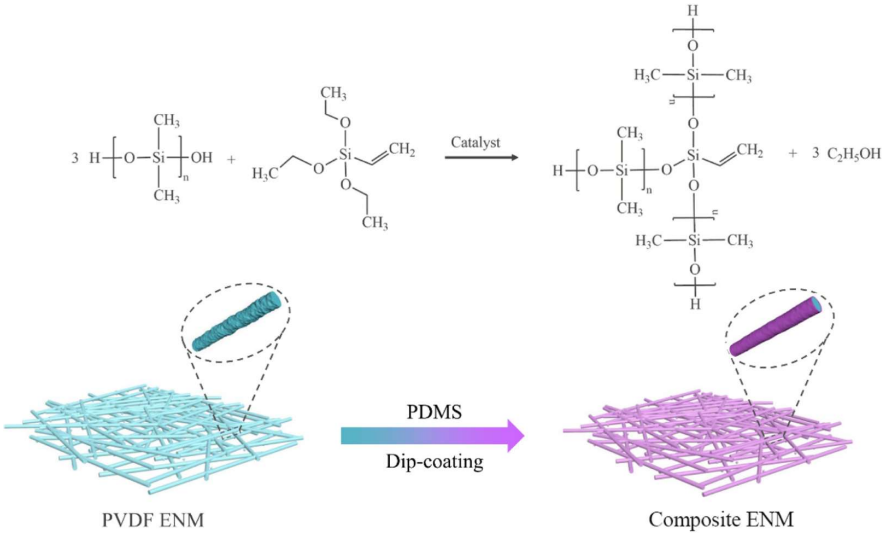

Figure 2-21 Schematic for the preparation of PVDF electrospun nanofiber membranes modified by dip-coating, adapted from [118].

Occasionally, multiple modification methods can be used in combination to improve wetting resistance properties of membranes. For example, in a study by Razmjou *et al*., superhydrophobic PVDF membranes were prepared by depositing TiO_2 nanoparticles by a low-temperature hydrothermal process, which increased the surface roughness, followed by fluorosilanization with 1H, 1H, 2H, 2H-perfluorododecyltrichlorosilane to reduce the surface energy [119]. Interestingly, the TiO_2 nanoparticles were used not only to engineer the hierarchical structure of the membrane but also to provide sites for the hydrolyzed silane coupling agent to be anchored, developing a film that enhanced hydrophobicity. Evidently, the CA of a virgin PVDF membrane increased from 125° to 163° following both modification methods.

For all these surface modification methods, caution should be made for the selection of materials and methods used for modification. Sometimes the release of materials (e.g. nanomaterials) used for modification into the water and wastewater is highly dangerous. This release might occur due to shear force, the cleaning process, etc. Moreover, the modification should be done carefully to prevent pore blockage or pore size reduction.

2.5.3. Membrane design

Mitigation of pore wetting for low surface tension liquids is currently the major concern in MD applications in various separation and purification processes. As well, it has been said by Horseman *et al*. [120] and Christie *et al.* [62] that fouling and scale formation can contribute significantly to membrane pore wetting. Therefore, in this section, methods to mitigate pore wetting by the low surface tension liquids and remove the fouling and scale formation are described.

2.5.3.1. Membranes for low surface tension wastewaters

In spite of the potential of MD to be used for wastewater treatment, contaminants in the feed wastewater may cause serious pore wetting. Thus, wetting is closely related to the composition of industrial wastewater. When MD is applied for the treatment of concentrated brine that comes out from the RO plant, precipitation of salt crystals is the source of the wetting. Surfactant is the major contaminant that induces pore wetting when shale oil-water is treated, while a small amount of oil and grease that are in the wastewater from the chemical plants may cause pore wetting and blockage. Lowering of surface tension in the presence of solvents and acids in the pharmaceutical and semiconductor industries also contributes to pore wetting. Hence, it is essential to develop membranes with non-wetting surfaces to apply MD to the treatment of the above-mentioned wastewaters [121].

Despite the ability of superhydrophobic membranes to strongly repel water, they are still susceptible to wetting by organic contaminants in the wastewaters such as oils, alkanes, and alcohols [122]. Therefore, omniphobic membranes, i.e. membranes which repel both water and low surface tension liquids, have attracted much attention recently to overcome this issue [123].

The role of the Wenzel and Cassie-Baxter state in membrane wetting was discussed in section 2.3.4. Obviously, the Cassie-Baxter state is more favourable for keeping the inside of the pore non-wetted while holding air in the pore when the membrane is brought into contact with water. The transition from the Wenzel to Cassie-Baxter state will occur at a threshold contact angle θ_c which can be calculated by equating the Wenzel and Cassie-Baxter relations:

$$\cos\theta_c = \frac{f_s - 1}{r - f_s} \tag{2.17}$$

where r is surface roughness factor and f_s is the fraction of solid surface which is in contact with the liquid phase.

Since $f_s < 1 < r$, $\cos\theta_c < 0$ and θ_c should be greater than 90°. In other words, when the contact angle is less than 90°, it is inevitably less than the contact angle required to enable the transition, and the Wenzel status is always preferred. Thus, it is difficult to maintain the Cassie-Baxter status when the contact angle is less than 90°. Lack of natural or artificial surfaces with sufficiently low surface energy to enable equilibrium contact angles of greater than 90° for low surface tension liquids makes it difficult to repel these types of liquids [124].

Nevertheless, it has been known for a long time that highly non-wetting status can still be achieved in nature even when the leaves are slightly hydrophilic [125]. Recently, it has been revealed that the surface is not wetted if the membrane surface has a re-entrant structure, i.e. concave topography such that the cross-section of the solid fraction decreases towards the base of the surface, enabling a thermodynamically metastable Cassie-Baxter state for the liquid-solid-vapor interface [126]. The

principle to allow the Cassie-Baxter status for the material of intrinsically low contact angle is well demonstrated by Figure 2-22.

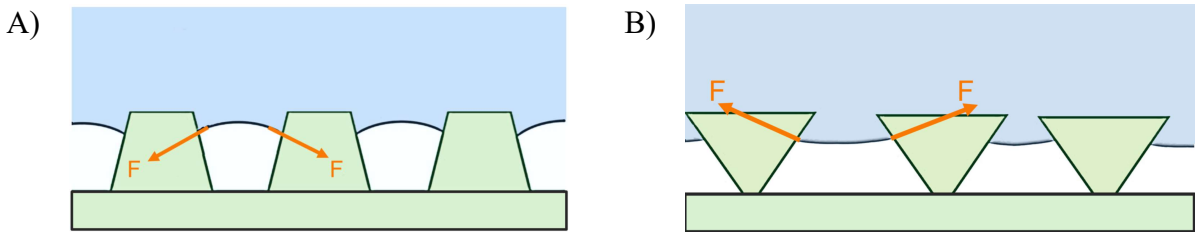

Figure 2-22 Liquid-air interfaces formed at A) pointed and B) re-entrant structure, adapted and redrawn from [121].

Figure 2-22A shows that the capillary force works downwards, promoting the occurrence of the Wenzel status, while in Figure 2-22B, the force works upwards, preventing the occurrence of the Wenzel status. Thus, the space between the solid walls may be kept non-wetted. Since the development of omniphobic membranes that exhibit non-wetting properties not only for water but also for non-aqueous liquid is very important for the treatment of wastewater by MD, many omniphobic membranes have been developed based on this principle to prevent pore wetting. Some of the examples are shown below.

2.5.3.1.1. Membranes made by the phase inversion technique

Boo *et al*. developed omniphobic membranes based on a commercial flat sheet PVDF membrane [127]. The surface of the PVDF membrane was made positively charged by alkaline treatment, followed by modification with electropositive (3 aminopropyl)-triethoxysilane (APTES). Then, negatively charged silica nanoparticles (SiNPs) were deposited onto the modified PVDF surface so that the particles could be bound firmly to the membrane surface by electrostatic interaction. The membrane surface was further treated by coating of (Heptadecafluoro-1,1,2,2-tetrahydrodecyl)trichlorosilane (FDTS) via vapor phase silanization. The re-entrant structure was formed by the presence of the nanoparticles. The membrane was tested for DCMD using the feeds

such as the solution containing sodium dodecyl sulfate (SDS), mineral oil added feed solution, and pre-filtered shale gas produced water. In each case, substantial improvement of the performance stability was observed with the surface-modified membranes compared to the pristine PVDF membrane.

In a study conducted by Li *et al*., omniphobic PVDF composite membranes were prepared through coating with SiNPs by electrostatic adsorption or chemical bonding followed by fluorination [128]. As confirmed by SEM, the SiNPs created a re-entrant structure which enhanced surface roughness. Further, the membranes achieved high CAs greater than 150° when measured with water, diiodomethane, and ethylene glycol. By comparing the two methods used to coat the membranes with SiNPs, it was determined that chemical bonding was more stable than electrostatic adsorption. The preparation method for these membranes is outlined in Figure 2-23 [128].

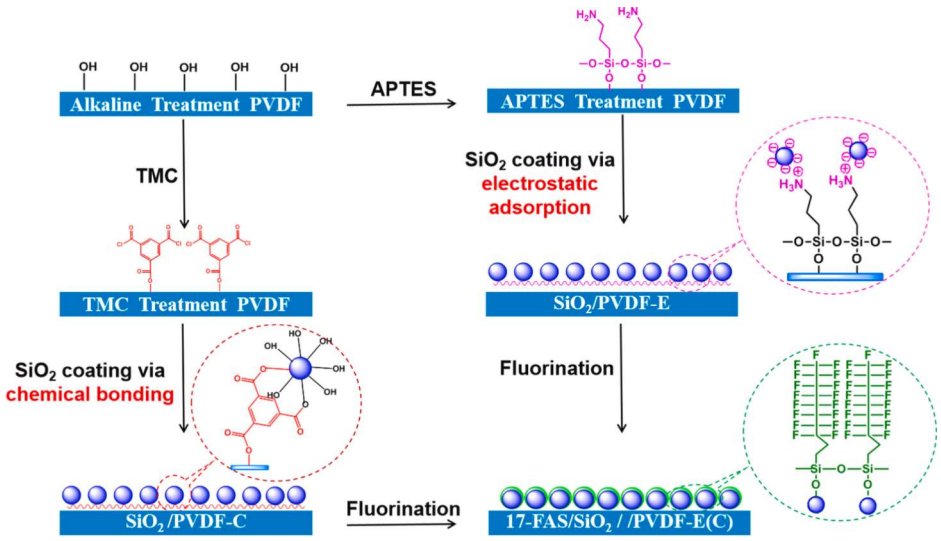

Figure 2-23 Preparation of omniphobic membranes using SiO_2 coating via electrostatic adsorption (17-FAS/SiO_2/PVDF-E) and chemical bonding (17-FAS/SiO_2/PVDF-C), adapted from [128]. TMC: trimesoyl chloride, 17-FAS: 1H, 1H, 2H, 2H-perfluorodecyltrimethoxysilane.

Woo *et al*. modified a flat sheet PVDF membrane by the layer-by-layer technique [129]. The surface of the PVDF membrane was modified by the following steps: 1) Coating of 5 wt%

poly(diallyldimethylammonium chloride)(polyDADMAC) solution, 2) Coating of 5 wt% silica aerogel dispersed in ethanol, 3) Coating of 5 wt% polyDADMAC solution, and 4) Fluorination with 1*H*,1*H*,2*H*,2*H*-perfluorodecyltriethoxysilane (FDTES) solution. Thus, the membrane had low surface energy and high surface roughness with a re-entrant structure. The membrane exhibited a remarkably high water CA of 177°. The membrane also exhibited high CAs for ethylene glycol mineral oil and methanol. The membrane was further tested for AGMD of RO brine produced from coal seam gas to which SDS and humid acid were added. Although the modified membrane showed lower flux than the unmodified membrane, the performance was more stable, and the rejection was improved.

Zheng *et al*. modified the surface of a PVDF membrane by the following steps [130]: 1) The alkaline-treated PVDF membrane was immersion-coated with APTES solution, 2) Synthesis of polystyrene (PS) microspheres by free radical dispersion polymerization of styrene monomer followed by coating of SiNPs on PS microspheres (SiNPs@PS), 3) Spray coating of 2 % SiNPs@PS dispersed in alcohol onto APTES modified PVDF membrane, where polymer 3-methacryloxypropyltrimethoxysilane (PA174) was added to make the bond between the SiNPs@PS and membrane surface stronger, and 4) Fluorination with 17-FAS. The membrane exhibited water and hexane CA of 176 and 138.4°, respectively. The membrane was subjected to DCMD with SDS stabilized hexadecane emulsion as the feed. The modified membrane showed very stable DCMD performance with high salt rejection compared to the other benchmark membranes. The results exhibited that the re-entrant, omniphobic structure was highly resistant to emulsion wetting.

Lu *et al*. modified PVDF hollow fiber membranes by the following steps [131]: 1) Alkaline-treated PVDF nanofiber was immersed in 1.5 wt% APTES solution in ethanol to coat APTES of positive

charge, 2) Immersion of APTES coated hollow fibers in 0.5 wt% SiNPs dispersed in deionized water, and 3) Dip-coating with 0.025 wt% Teflon AF 2400 dissolved in Galden heat-transfer fluid. The membrane repelled liquids of different surface tensions, including water, ethylene glycol, cooking oil and ethanol. When tested for VMD with a feed solution containing 0.6 mM of SDS, the surface-modified hollow fiber showed excellent stability for 7 h. They have also studied the effect of the size of the SiNPs and concluded that a particle size of 60 nm was better than the other nanoparticles of larger sizes.

2.5.3.1.2. Inorganic membranes

The attempts have also been made to fabricate omniphobic membranes from inorganic materials. Although the focus of this work is on organic polymeric membranes, some examples of inorganic membranes are shown below.

Lin *et al*. modified the surface of glass fibers (from the picture they have shown the fibers look like nanofibers) for DCMD with feed solutions of low surface tension [123]. The following five-step method was applied to prepare an omniphobic membrane: 1) Negatively charged borosilicate glass fibers were treated with APTES to make the surface positively charged, 2) The APTES coated glass fibers were immersed in an aqueous suspension of SiNPs, where the negatively charged SiNPs were electrostatically bound to the positively charged modified glass fibers, 3) To strengthen the binding between the glass fibers and the nanoparticles, SiNPs coated membrane was briefly treated with a toluene solution of silicon tetrachloride ($SiCl_4$). $SiCl_4$ hydrolyzed in the presence of a small amount of water fuses the contact region between SiNPs and glass fibers, 4) The glass fibers were then treated with fluorinated alkylsilane (FAS) solution in N,N-Dimethylformamide (DMF), and 5) The glass fibers were then subjected to heat treatment at 130^{o}C. The membrane so prepared showed high CAs for all liquids tested, including water, mineral

oil, decane and ethanol. The membrane was then subjected to DCMD experiments with SDS added NaCl solution of 1.0 M to compare with a commercial PTFE membrane. The PTFE membrane was wetted in the presence of SDS, but the prepared membrane was not wetted.

Similarly, Chen *et al*. developed omniphobic membranes by depositing either ZnO nanorods or nanoparticles on alumina hollow fiber membranes using the chemical deposition method followed by surface fluorination and polymer coating [132]. The method consists of the following steps: 1) For the deposition of ZnO nanorods, the $KMnO_4$ treated alumina hollow fiber was further treated with aqueous zinc sulfate solution containing monoethanol amine (MEA) and NH_4OH. For the deposition of ZnO nanoparticles, the $KMnO_4$ treated alumina hollow fiber was further treated with aqueous zinc nitrate solution containing triethanolamine (TEA) and NH_4OH, and 2) The ZnO deposited membranes were immersed into 1% v/v fluoroalkylsilane (17-FAS)/n-hexane solution. The self-assembled FAS was covalently bonded on metal oxide (ZnO or Al_2O_3). The ZnO nanorods and ZnO nanoparticles deposited hollow fibers had CA of 128.7° and 138.1°, respectively, for a 90 v/v% ethanol/water mixture, both of which were higher than the 114.8° of the pristine hollow fiber. The membranes were subjected to DCMD with a feed solution of 1 M NaCl solution with successive addition of SDS from 0.2 to 2.0 mM. The membrane deposited with ZnO nanoparticles exhibited the best non-wetting performance, maintaining the initial flux for 24 h, when 2.0 mM SDS was added.

Chen *et al*. also applied the same technique on glass fibers using ZnO nanoparticles and obtained the CAs of 152.8 and 110.3° for water and ethanol, respectively [133]. When the membrane was subjected to DCMD experiments with the feed solution of 1M NaCl containing 0.3 mM SDS at 60°C, the flux was maintained for 8 h showing excellent omniphobicity of the membrane.

2.5.3.1.3. Electrospun nanofibers

The bottom part of the nanofiber constitutes a re-entrant structure that opposes pore wetting. Therefore, many works have been done to fabricate omniphobic membranes based on electrospun nanofibers. However, the omniphobicity of nanofibers is usually not high enough, and the coating with low surface energy material is often applied.

A hydrothermal technique was used to develop omniphobic membranes consisting of titanium dioxide nanorods (NRs) on PVDF-HFP nanofibers [134]. The NRs constituted pine-needle-like hierarchical re-entrant nanostructures which enabled a Cassie-Baxter state due to the accumulation of air in the nanostructures, thus enhancing anti-wetting behaviour in combination with low-surface-energy fluorination, which was evidenced by the high CA for water (168°) and mineral oil (153°). SEM images of the nanofiber membrane before and after modification are displayed in Figure 2-24 [134]. In addition, Figure 2-25 compares pristine and modified membranes in terms of CAs and surface wetting behaviours [134].

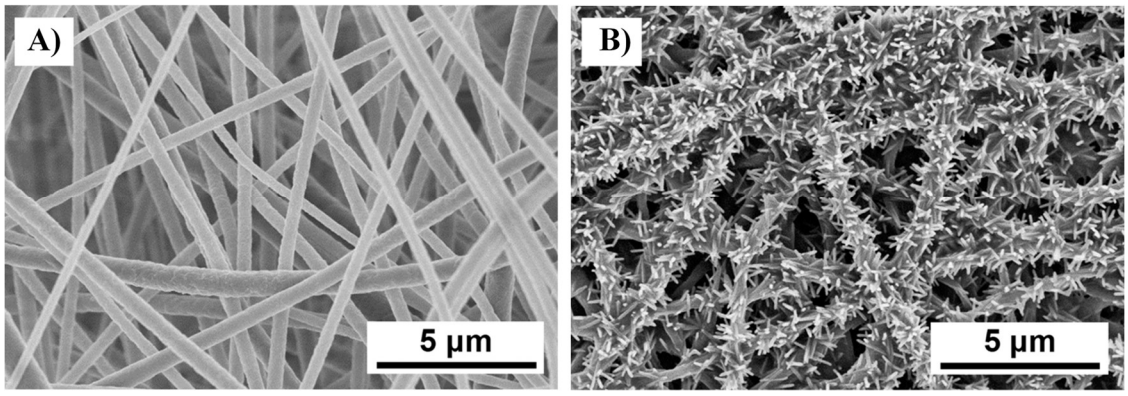

Figure 2-24 SEM images of A) pristine PVDF-HFP nanofibers and B) fluorinated PVDF-HFP/TiO_2 nanofibers with NRs, adapted from [134].

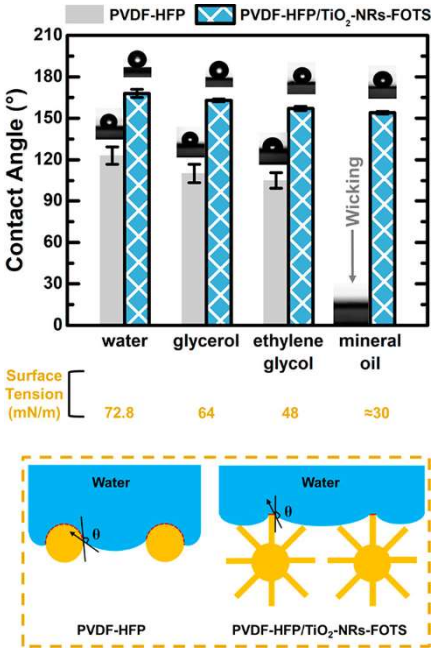

Figure 2-25 Comparison between PVDF-HFP nanofibers and fluorinated PVDF-HFP/TiO_2 nanofibers with NRs in terms of CAs and surface wetting behaviours, adapted from [134].

Woo *et al*. applied CF_4 plasma surface modification on electrospun PVDF nanofibers to fabricate membranes for AGMD [111]. The performance of the membrane was evaluated using RO brine produced from coal seam gas water containing a small amount of SDS. The plasma treatment was effective in lowering the surface energy due to the formation of $–CF_2$-CF_2- and $–CF_3$ groups at the nanofiber surface. After 15 min of plasma treatment, high CAs (147-149°) were observed for low surface tension liquids such as ethylene glycol, mineral oil and methanol, along with a high CA for water (160.6°). LEP increased from 142 kPa for the neat PVDF nanofiber to 187 kPa for the 15 min plasma-treated nanofibers. In AGMD experiments, the initial flux of plasma-treated nanofibers (15.3 L/m^2 h) was maintained for 10 h up to 0.7 mM addition of SDS with almost complete salt rejection, while the pristine PVDF nanofiber membrane underwent pore wetting at the SDS addition of 0.3 mM.

Instead of surface treatment of electrospun nanofibers, Lu *et al*. developed a one-step electro-spinning fabrication of nanofiber membranes of high omniphobicity from PVDF-HFP and fluorinated-decyl polyhedraloligomeric silsesquioxane (F-POSS) colloidal suspension [135]. The nanofiber membrane so produced showed high CAs of 148.8 and 128.2^{o} for mineral oil and ethanol, respectively. The membrane was subjected to DCMD experiments using 1 M NaCl solution as the feed with successive addition of SDS from 0.1 to 0.3 mM. While the F-POSS incorporated membrane could maintain the initial flux and nearly complete salt rejection for 8 h, the performance of the pristine PVDF-HFP membrane started to drop after 4 h.

Another omniphobic membrane was fabricated by Lee *et al*. by the following steps [122]: 1) Electrospinning of PVDF-HFP nanofibers in which cationic surfactant (benzyltriethylammonium) is blended, 2) The nanofibers were then grafted with negatively charged SiNPs via dip-coating. The electrostatic force binds the SiNPs to the nanofiber surface, and 3) SiNPs coated nanofibers were further coated with fluoroalkylsilane to lower the surface energy. Thus, the resultant membrane had a multi-level re-entrant structure. The resultant membrane showed CAs from about 110 to above 130^{o} for mineral oil, decane and ethanol, while pristine PVDF-HFP nanofiber membranes failed to sustain the liquid droplet on the surface. The membrane was subjected to DCMD for 8 h using 1 M NaCl solution with progressive SDS addition (0.1 mM at 2 h, 0.2 mM at 4 h, 0.3 mM at 6 h) as feed. While the initial flux of the surface-modified PVDF-HFP nanofiber membrane was about one half of the pristine PVDF-HFP nanofiber, the former could maintain the initial flux during the entire period of 8 h with near 100 % salt rejection, while the performance of the latter deteriorated at the first addition of SDS at 2 h due to the pore wetting.

Deng *et al*. developed omniphobic nanofiber membranes by dipping electrospun PVDF membranes into FDTES solutions with different FDTES concentrations (0.5, 2.0 and 3.5 wt% in

n-hexane) [136]. FDTES was hydrolyzed and became polyFDTES by polycondensation and was deposited on the nanofiber surface, forming a structure similar to budding willow twigs with tiny bumps contributing high omniphobicity to the modified PVDF nanofiber membrane. The CAs for mineral oil were above 115°, and the CAs for ethanol were 73.4°, 89.7°, and 94.7°, corresponding to FDTES concentrations of 0.5, 2.0, and 3.5 wt%, respectively. The membrane coded PVDF-F-2-60 (meaning dip-coating was made with 2 wt% FDTES solution and the membrane thickness was 60 μm) was subjected to DCMD with 3.5 wt% NaCl solution with progressive SDS addition (0.05 and 0.1 mM at 2 and 4 h). While the pristine PVDF nanofiber membrane started to deteriorate at 2 h, the modified PVDF nanofiber maintained the initial performance for an entire period of 6 h.

2.5.3.1.4. Janus membrane

Janus membrane is a two-faced membrane (hydrophilic/omniphobic or hydrophilic/superhydrophobic). Omniphobic membranes have good resistance to wetting agents and surfactants; however, they still suffer from fouling in oil-polluted wastewaters. Oil droplets can result in quick fouling and consequently decrease in flux, clogging and pore wetting. Janus membrane, which can comprise a bottom omniphobic layer and a top hydrophilic layer, has a high omniphobicity in the air as well as high oleophobicity (i.e. oil repelling ability) in water [137].

Huang *et al*. fabricated a Janus nanofiber membrane. The fabrication procedure consists of three steps [138]: 1) Electrospinning of PVDF-HFP nanofibers blended with cetyltrimethylammonium bromide (CTAB, 98%), 2) Dip coating of nanofibers with SiNPs, 3) Fluorination by FAS (97%) via vapor deposition, and 4) Further coating of a layer of nanoparticle polymer composite made of SiNPs, chitosan (CTS), and perfluorooctanoate (PFO) (SiNPs-CTS/PFO). They compared the wettability of the following three membranes; a) pristine PVDF-HFP nanofiber membrane, called

conventional hydrophobic membrane, b) the membrane after step 3) called *Janus bottom membrane* and c) the membrane after step 4) called *Janus membrane.* As expected, *conventional hydrophobic membrane* was hydrophobic showing high water CA in air and Janus bottom membrane was omniphobic showing high CAs for all water, mineral oil and ethanol in air. But oil CA under water was low for both the *conventional hydrophobic membrane* and *Janus bottom membrane.* Only *Janus membrane* showed high CA of oil in water, possibly due to the formation of a hydration layer at the hydrophilic SiNPs-CTS/PFO surface. The membranes were then subjected to DCMD experiments with NaCl solution in which SDS was added progressively (0.1 mM at 1.5 h, 0.2 mM at 2.5 h and 0.4 mM at 3.5 h). While the performance of *conventional hydrophobic membrane* and *Janus bottom membrane,* started to deteriorate at 1.5 and 2.5 h, respectively, *Janus membrane*'s performance was stable during the entire experimental period of more than 6 h.

Makanjuola *et al*. developed a dual-layered electrospun PVDF-HFP/cellulose membrane whose schematic is shown in Figure 2-26 [139]. The cellulose-modified PVDF-HFP electro-spun nanofiber membrane contains hydroxyl groups on its surface which can hydrogen bond with water, forming a hydration layer. Therefore, the low surface tension oil phase in the feed is prevented from penetrating the hydrophilic cellulose-modified layer and wetting the hydrophobic layer underneath. The hydration layer repels the oil phase due to its positive interfacial free energy [140]. Meanwhile, saline water may penetrate the hydrophilic layer, but only the water evaporates and enters the pores of the hydrophobic layer [139].

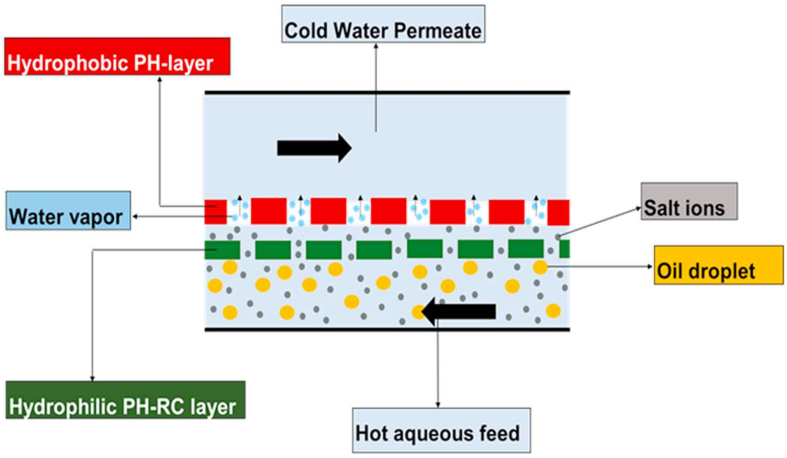

Figure 2-26 Schematic for a DCMD process with dual-layered membranes, adapted from [139]. PH: PVDF-HFP and RC: regenerated cellulose.

In very recent research, a Janus membrane was prepared through layer-by-layer deposition of catechol/CTS and polyethylenimine (PEI) over a PVDF membrane for the treatment of saline waters containing surfactant and oil-in-water emulsion by DCMD [141]. The hydration barrier effect caused by hydrophilic properties and hierarchical cauliflower-like morphology of the top surface layer prevented the attachment of the surfactant and oil. In addition, the electrostatic repulsion between the cationic surfactant and protonated amino groups on the membrane surface improved DCMD performance in terms of fouling and wetting phenomena.

A Janus membrane was prepared by Zhu *et al.* via the following three steps [142]: 1) Electrospinning of PVDF nanofiber, 2) Electrospraying of PVDF-HFP/PS blend solution containing SiNPs coated with trimethoxy (heptadecafluorotetrahydrodecyl)-triethoxysilane (FAS), and 3) Electrospraying of polyacrylonitrile (PAN) solution containing SiNPs. Thus, the first PVDF layer provided a necklace-like structure, the second F-SiNPs@ PVDF-HFP/PS (hydrophobic) layer and the third SiNPs@PAN (hydrophilic) layer provided the Janus skin. According to the CA measurement, the second layer surface exhibited superhydrophobicity with water in air CA of 164°, while the third layer exhibited surperoleophobicity with an oil ($CHCl_3$) in

water CA of 166°. The membrane was then subjected to DCMD with a feed solution containing 3.5 wt% of sodium chloride and 1000 ppm of lubricating oil at a temperature difference of 40 °C. The membrane maintained the water flux of 25 L/m^2 h with nearly perfect salt rejection for 50 h, while the commercial PVDF membrane's flux was only 17 L/m^2 h, and the conductivity of the permeate quickly increased.

Chew *et al.* fabricated another Janus membrane by applying the following two steps on a commercial hollow fiber membrane [143]: 1) Coating of the outer surface of the hollow fiber with polydopamine (PDA) via oxidant-induced polymerization, and 2) Further dip-coating of AgNPs on the PDA coated hollow fiber. The water CA in air for pristine PVDF hollow fiber, after PDA coating and after AgNPs coating was 109.5°, 13.2° and 7.6°, respectively, showing the hydrophobic/hydrophilic Janus structure of the hollow fiber. On the other hand, underwater petroleum CA was very high after AgNPs coating, showing its underwater oleophobicity. The membranes were further subjected to DCMD experiments using saline water (3.5 wt% NaCl) with Tween-20 (500 ppm) stabilized petroleum emulsion at a transmembrane temperature difference of 40 °C. While initial flux of the pristine PVDF hollow fiber was 14 L/m^2 h, it went up quickly together with increasing permeate conductivity. The multilayer Janus hollow fiber exhibited a slightly lower initial flux of 13 L/m^2 h; however, it maintained the initial flux and nearly complete salt rejection for 72 h.

Li *et al*. fabricated a Janus membrane by the following steps [144]: 1) Quartz fiber functionalization with ATPES, 2) Attachment of SiNPs, 3) Coating of PVDF-HFP/DMF solution blended with FDTES, and 4) Grafting of the zwitterionic polymer brush layer [2-(methacryloyloxy)-ethyl]dimethyl-(3-sulfopropyl) ammonium hydroxide (PSBMA). Oil-fouling MD experiment was carried out using saline water as the feed (1 M NaCl, containing oil). The

omniphobic membrane without a hydrophilic layer (zwitterionic polymer brush layer), obtained before step 4, was prone to severe fouling and wetting. In contrast, Janus membrane with hydrophilic layer (after step 4) exhibited constant water flux and nearly complete salt rejection over the entire MD testing period.

Wang and Lin fabricated a composite membrane by the following steps [145]: 1) Synthesis of PFO-CTS/SiNPs nanoparticles, and 2) Spray coating of PFO-CTS/SiNPs nanoparticles on PVDF membrane. The composite membrane had the Janus structure with the hydrophobic PVDF layer and the CTS layer, whose hydrophilicity was enhanced by the presence of PFO. Besides, the surface roughness of the composite membrane was increased by the presence of SiNPs. The composite membrane exhibited hydrophilicity with a water in air CA of 15^{o}. It also exhibited oleo- and superoleophilicity with the transition of in-air oil CA from 55 to 0^{o} in 10 min. On the other hand, the composite membrane was found highly oleophobic with an oil in water CA of 139.3^{o}. In DCMD experiments, the composite membrane was stable during 20 h of operation when the feed was oil in water emulsion without surfactant. However, the performance of the composite membrane deteriorated after 0.2 h when 100 mM of Triton-X was added as a surfactant. Table 2-3 summarizes recent publications on omniphobic and oleophobic membranes.

Table 2-3 Recent publications on omniphobic and oleophobic membranes.

MD configuration	Preparation method	Contact angle (°)	MD performance	Ref.
Phase inversion				
DCMD	PVDF membrane coated with APTES, followed by deposition of SiNPs and silanization with FDTS	Water; ca 160 1 M NaCl solution with 0.1 mM SDS; ca 140 Mineral oil; ca 150	1 M NaCl solution with SDS up to 0.2 mM; stable performance for 8 h	[127]
DCMD	PVDF membranes coated with SiNPs by electrostatic adsorption or chemical bonding followed by fluorination	Water, diiodomethane, ethylene glycol; above 150	Coking wastewater; 6.2 % decrease in flux for membrane prepared with chemical bonding method and 15 % decrease for electrostatic adsorption method after 120 h	[128]
AGMD	PVDF membrane coated with polyDADMAC and silica aerogel by layer-by-layer assembly technique and fluorinated	Water; 177 Ethylene glycol, mineral oil and methanol; high	RO brine produced from coal seam gas, SDS added; stable flux and high rejection	[129]

DCMD	PVDF membrane coated with APTES and SiNPs@PS then fluorinated with FAS 17	Water; 176 Hexane; 138.4	SDS stabilized hexadecane emulsion; stable operation with high rejection	[130]
VMD	PVDF hollow fiber coated with APTES and SiNPs and further coated with Teflon AF2400	Water, ethylene glycol, cooking oil, and ethanol; repelled	SDS containing solution; stable for 7 h	[131]
Inorganic membrane				
DCMD	Glass fiber coated with APTES and SiNPs, treated with $SiCl_4$, fluorinated with FAS and heat treated	Water, mineral oil decane and ethanol; high	1.0 M NaCl solution containing SDS; stable operation without wetting	[123]
DCMD	Alumina hollow fiber deposited by ZnO nanorod or ZnO nanoparticle and fluorinated by 17-FAS	Ethanol/water mixture; 128.7 for nanorod 138.1 for nanoparticle	1.0 M NaCl solution with 2.0 mM SDS; stable for ZnO nanoparticles	[132]
DCMD	Same technique as above but on glass fibers with ZnO nanoparticles	Water; 152.8 Ethanol; 110.3	1.0 M NaCl solution with 0.3 mM SDS; stable operation for 8 h	[133]
Electrospun nanofibers				

DCMD	PVDF-HFP nanofibers deposited by TiO_2 NRs	Water; 168 Mineral oil; 153	35 g/L NaCl solution with up to 0.5 mM SDS and up to 400 ppm mineral oil; stable for 5 h	[134]
AGMD	PVDF nanofibers plasma-treated	Ethylene glycol, mineral oil and methanol; 147-149 Water; 160.6	RO brine produced from coal seam gas water; stable for 10 h up to 0.7 mM SDS addition	[111]
DCMD	Electrospinning of PVDF-HFP/FPOSS mixture	Mineral oil; 148.8 Ethanol; 128.2	1 M NaCl solution with 0.1 to 0.3 mM addition of SDS; stable for 8 h	[135]
DCMD	PVDF-HFP blended with benzyltriethylammonium electrospun and coated with SiNPs and fluoroalkylsilane	Mineral oil, decane, ethanol; 110 to >130	1 M NaCl solution with 0.1 to 0.3 mM of SDS; flux about half of pristine nanofibers but stable 8 h operation	[122]
DCMD	PVDF nanofiber deposited by polyFDTES	Mineral oil; above 115 Ethanol; 73.4 to 94.7	3.5 wt% NaCl solution with 0.05 to 0.1 mM SDS; stable for 6 h	[136]
Janus membrane				
DCMD	Electro-spinning of PVDF-HFP/CTAB blend, SiNPs coating,	Water, mineral oil, ethanol; high Oil under water CA; high	NaCl solution with 0.1 to 0.4 mM SDS; stable for more than 6 h	[138]

	fluorination by FAS, coating of SiNPs-CTS/PFO			
DCMD	Electro-spun PVDF-HFP nanofiber coated with RC	Oil under water; Up to 150.1	35 g/L NaCl solution with 1000 ppm mineral oil; stable for 15 h	[139]
DCMD	PVDF membrane plasma etched and catechol/CTS and PEI coated by layer-by-layer assembly	Water in air; PVDF 160 Janus 0 Oil under water; Janus superoleophobic	500 mg/L Tween-20 stabilized n-hexadecane emulsion in water; slight decrease in flux and increase in EC in 90 h	[141]
DCMD	PVDF nanofiber coated with F-SiNPs@ PVDF-HFP/PS and then with SiNPs@PAN	Water in air; F-SiNPs@ PVDF-HFP/PS coated 164 CH_3Cl under water; SiNPs@PAN coated 166	3.5 wt% NaCl with 1000 ppm lubricating oil; stable performance for 50 h	[142]
DCMD	PVDF-HF coated with PDA and then with AgNPs	Water in air; PVDF HF 109.5, after 2 layer coating 7.6 Petroleum under water; 2 layer coating high	3.5 wt% NaCl with 500 ppm Tween-20; performance stable for 72 h	[143]

DCMD	Quartz fiber functionalized with ATPES, attachment of SiNPs, coating of PVDF-HFP/DMF blended with FDTES, coating of PSBMA	Water; high for both hydrophobic and omniphobic membrane Crude oil, hexadecane, ethanol; hydrophobic membrane wetted, omniphobic membrane high	1 M NaCl containing up to 0.2 mM SDS; Janus membrane stable for 10 h Saline oil-in-water emulsion containing 1 M NaCl, 0.5 g L−1 crude oil, and 0.03 g L−1 TWEEN 20; Janus membrane stable for 12 h	[144]
DCMD	PVDF membrane spray-coated with PFO-CTS/SiNPs nanoparticles	Water in air; 15 Oil in air; 55 to 0 Oil in water; 139.3	Oil in water emulsion; stable for 20 h Oil in water with surfactant; deteriorated in 0.2 h	[145]

2.5.3.2. Self-cleaning membrane

Superhydrophobic membrane surfaces possessing self-cleaning properties can be protected from contamination, and consequently, pore wetting [146]. Herein, some examples are presented according to which membranes can eliminate foulants. It should be noted that there are different compounds in wastewaters, resulting in deposition of, for instance, dye, silica, etc. Depending on the nature of wastewater, a membrane needs to be designed in a way such that it can clean its own surface.

In a study by Liang *et al*., the self-cleaning properties of PTFE nanofiber membranes modified with SiO_2 nanoparticles were studied [147]. Self-cleaning tests involved the immersion and subsequent removal of a pure PTFE fibrous membrane and a 7.3 wt% SiO_2-modified PTFE membrane in water containing ink dye. Wetting was observed only for the pure PTFE membrane. Furthermore, both membrane surfaces were covered in graphite and dust and subsequently cleaned with running water, showing that only the pure PTFE membrane was wet while the 7.3 wt% SiO_2-modified PTFE membrane became clean quickly and remained dry.

Huang *et al*. prepared PTFE/ZnO ultrafine fibrous porous membranes by a combination of electrospinning and sintering techniques and evaluated their VMD performance in the treatment of saline wastewater containing organic dye [148]. Following the sintering process, the photocatalyst-ZnO particles were homogeneously immobilized on the surface of ultrafine PTFE fibers. UV irradiation in the presence of ZnO photocatalysis demonstrated superior photocatalytic properties thanks to production of hydroxyl radicals that can degrade most of the complex organic compounds. After a 6-h VMD operation, the fouled membranes were immersed in distilled water and subjected to UV irradiation for 3 h to destroy the foulant. The self-cleaning property of the membrane with ZnO photocatalysis is shown in Figure 2-27, which displays SEM images of fouled

PTFE/ZnO membrane prior to and following UV irradiation [148]. Further experiments in this study showed that UV irradiation during VMD operation with the modified membrane could effectively degrade dye from the feed.

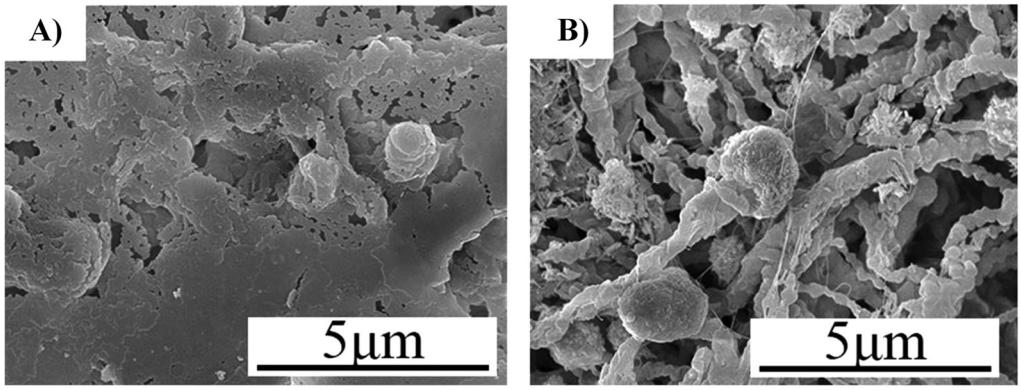

Figure 2-27 SEM images of PTFE/ZnO membrane fouling A) before and B) after UV irradiation, adapted from [148].

An additional approach for cleaning silicate scaling is electrochemical cleaning using a membrane coated with CNTs. Tang *et al*. evaluated this approach with CNT-coated polymeric membranes for the treatment of geothermal brines by DCMD [149]. The feed employed in this study led to silicate scaling; however, silicate salt deposits could be redissolved and diffused back into the bulk water under high pH conditions. A cathodic electric potential was applied to the CNT-coated membranes to increase pH at the membrane surface due to water splitting based on the following chemical reaction:

$$H_2O + e^- \leftrightarrow \frac{1}{2} H_2 + OH^- \quad (2.18)$$

In this case, the membrane acted as the cathode while a titanium counter electrode was used as the anode with a constant current of 20 mA. This process ultimately allows cleaning to be confined to a very thin water layer at the membrane surface instead of modifying the bulk solution chemistry. This electrochemical cleaning process is shown in Figure 2-28 [149].

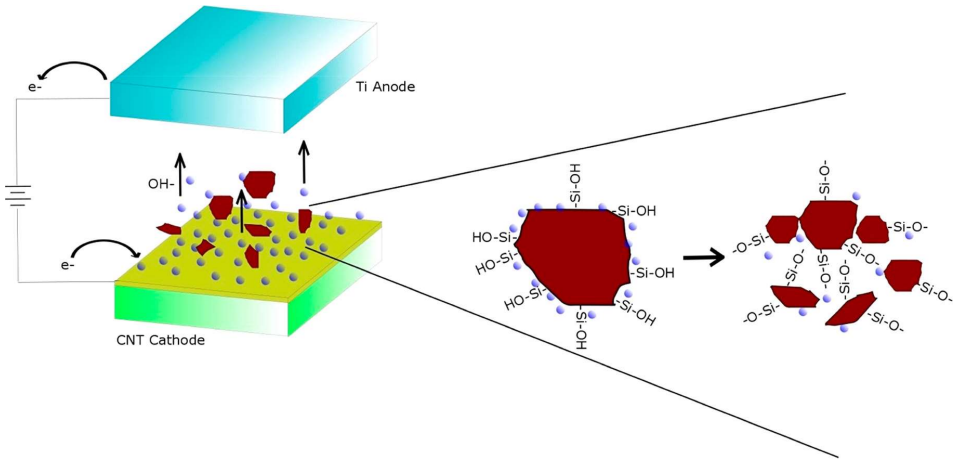

Figure 2-28 Schematic of proposed electrochemical cleaning mechanism for silicate scaling, adapted from [149].

2.5.3.3. Self-heating *membrane*

Localized heating of the membrane with the aim of mitigating vapor condensation within the pores, which is one of the reasons for pore wetting, was proposed by Li *et al.* [67]. In this study, Joule-heating was employed for AGMD, with an ultrathin layer of graphene oxide (GO) on the air gap side of the membrane that was heated by electric current (not the feed side to avoid degradation of membrane in ionizable environment). With this design, 90% of heat passed into the feed side with the temperature gradient opposite to the conventional AGMD, reducing capillary condensation and consequently pore wetting. Figure 2-29 displays the schematic of the proposed setup and direction of the temperature gradient. A similar idea was developed in 2017, where CNT/polymer composite heater was used and the degradation of CNT was prevented by controlling the frequency of alternating current applied [150]. Wu *et al.* proposed a solar-driven MD using PDA-coated PVDF photo-thermal membrane [151]. Coating of PDA with large light absorption capacity and excellent photo-thermal conversion properties enabled higher temperature difference across the membrane and, consequently, higher driving force for the vapor movement. Also, fluoro-silanization was employed to increase hydrophobicity. Figure 2-30 shows the schematic of solar-driven DCMD

setup used in this study. For the membrane which was immersed in water, after 600 seconds of illumination, the temperature of the top surface of membrane was increased from 20 °C to 26 °C (with 0.75 kW m^{-2} of solar irradiation) and to 32 °C (with 7 kW m^{-2} of solar irradiation), while the temperature of the membrane without the PDA layer was increased to 22 °C and 24 °C, respectively, with the same amounts of solar irradiation. This approach can be studied with the aim of pore wetting mitigation since temperature polarization outside of the membrane can negatively affect pore wetting, which can be controlled using this approach.

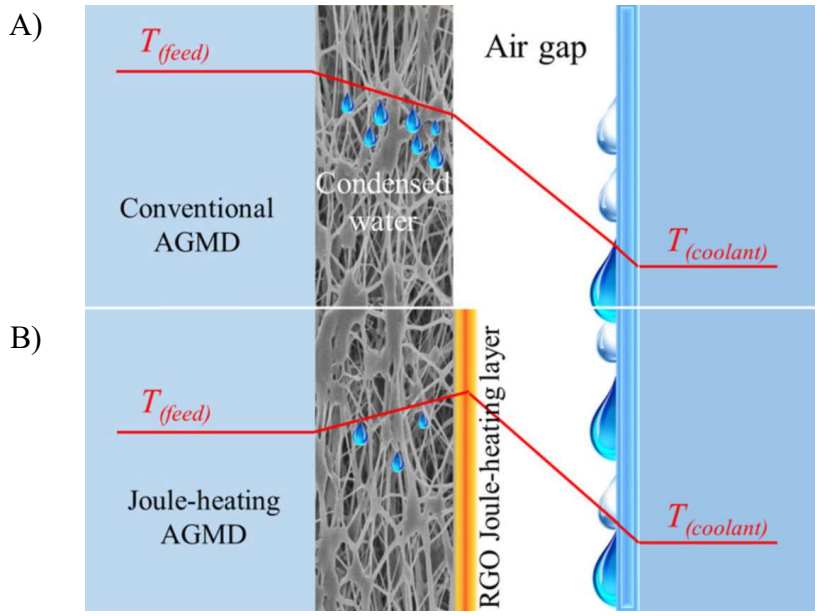

Figure 2-29 Schematic of proposed setup for mitigating capillary condensation, A) Conventional AGMD and B) Joule-heating AGMD, adapted from [67]. RGO: Reduced GO.

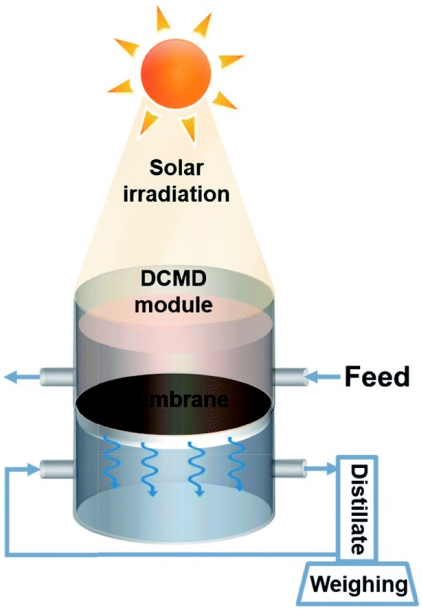

Figure 2-30 Schematic of solar-driven DCMD setup, adapted from [151].

2.5.3.4. Membrane with the potential of removing concentration polarization layer

Recently, an electrically conducting MD (ECMD) process was developed in which membrane was composed of a CNT layer deposited on a PP support and cross-linked by PVA. Alternating currents (AC) were applied to the membrane resulting in electrophoretic mixing of the stagnant concentration polarization layer and minimizing of mineral scale formation and consequently pore wetting [152]. Figure 2-31 illustrates the schematic of the proposed membrane with which the concentration polarization layer was stirred. Also, another membrane parameter affecting concentration polarization is membrane roughness. It has been suggested that membranes with rough surfaces have higher hydrodynamic effects causing lower concentration polarization [153].

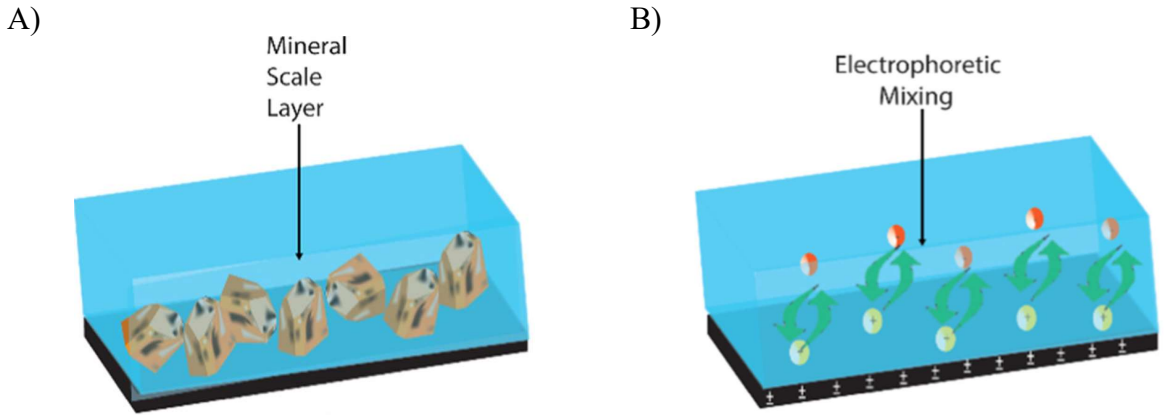

Figure 2-31 Schematic of proposed ECMD process in which a CNT layer was deposited on membrane surface: A) without potential, B) with alternating currents, adapted from [152].

2.5.3.5. Antibacterial membrane

Metal nanoparticles are one type of material that shows strong antibacterial activity [154]. TiO_2 is a metal oxide excellent for environmental engineering operations, thanks to catalytic activity, high stability, and low cost. Titanium cations demolish the microorganism cell wall, and therefore, the growth of biofilm is delayed [155]. Ray *et al.* prepared an anti-wetting and anti-biofouling PVDF membrane through a facile approach, in which trichloro(1H,1H,2H,2H perfluorooctyl)silane (TPFOS) was employed to increase hydrophobicity and also an antibacterial layer containing TiO_2 nanoparticles was added through the dip-coating method [155]. The PVDF membrane was initially dip-coated with polyethylene glycol-co-polymethacrylic acid (PEG-co-poly(MAA)) and then plasma treated to form a large amount of -COOH/-OH groups that promote the coordinate bonding of TiO_2 on the membrane surface. Figure 2-32 shows the schematic of the membrane preparation, followed by a hydrophobization process using TPFOS. The membrane was tested using *Escherichia coli*, a gram-negative bacterium, and also *Staphylococcus aureus*, a gram-positive bacterium, and for both of them, the membrane exhibited a ~99% reduction in bacteria concentration, thus proving the ability of the membrane to reduce biofouling and consequently

mitigate wetting. Table 2-4 summarizes some other recent publications on the methods applied to increase membrane wetting resistance.

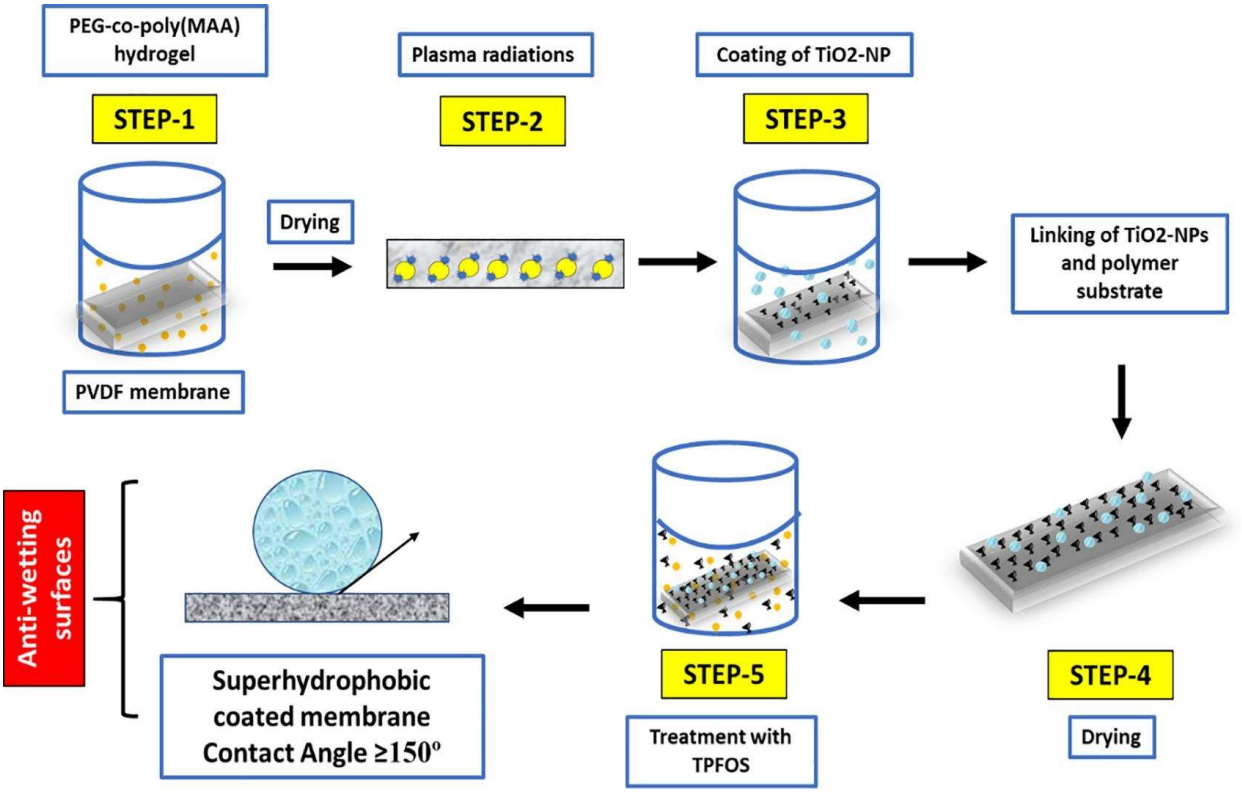

Figure 2-32 The schematic of preparation of antibacterial PVDF membrane, adapted from [155]. NP: Nanoparticle

Table 2-4 Recent publications on high wetting resistant membranes.

Membrane	Configuration	Water CA (°)	LEP_w (bar)	Contribution to wetting resistance	Ref.
PVDF	DCMD	173.2	2.16	Solvent-thermal induced roughening (Due to the combined effect of solvent and heating, the shells of nanofibers were swelled (partially) and undergone more considerable thermal expansion in comparison to the non-swelled cores, causing the deformation of the shells relative to the cores to form surface roughness) followed by 1H,1H,2H,2H perfluorooctyltrichlorosilane coating	[156]
PTFE/PP	DCMD	145.1	2.24	Layer-by-layer coating: Teflon and PDA on a plasma-treated PTFE/PP membrane, resulting in enhanced wetting resistance toward different liquids, including pure water, surfactant, ethanol, and crude oil	[157]
PVDF-HFP	AGMD	154.5	2.17	Incorporation of boron nitride nanosheets in PVDF-HFP electrospun membrane resulting in forming a favourable polymer phase, creating a superhydrophobic surface, and improving mechanical strength	[158]
PVDF	DCMD	170	0.72	Electrospraying PVDF/PDMS/silica layer over a nanofibrous PVDF support layer resulting in hierarchically micro/nano-rough topology	[159]
PVDF-HFP/PET	DCMD	136	0.383	Providing hierarchical structure and increasing the mechanical strength for electrospun membranes comprising the interconnected PVDF-HFP nanofibers and PET microfibers	[160]

PVDF	DCMD	166	-	Creating superhydrophobic hierarchical coating with cauliflower-shaped beads via electrospraying method using a dope solution containing V-POSS and PDMS	[161]
PVDF	VMD	140.5	2.339	Incorporation of 1H, 1H, 2H, 2H - perfluorooctyltriethoxysilane functionalized GO nanosheets in PVDF nanofiber layer fabricated by electrospinning process	[162]
PPO	DCMD	138	1.26	Application of new material, i.e. PPO, for membrane preparation using electrospinning: Smooth surface of this membrane reduces adhesion of inorganic salts, and therefore increases anti-scaling behaviour	[163]
PVDF	DCMD	159	1.89	Electrospraying PVDF-HFP/ZnO/DMF solution onto fluorinated PVDF membrane creating spherical micro/nano hierarchical structure and stabilizing Cassie-Baxter state	[164]
PVDF	DCMD	164.4	4.09	Fabrication of an omniphobic membrane with low surface energy and re-entrant structure through spraying a solution containing fluorocarbon surfactant, fluorinated alkyl silane, and SiO_2 nano-particles onto PVDF membrane (electrostatic adsorption)	[165]
PET	DCMD	155.6	-	Fabrication of an omniphobic membrane through creating hierarchical re-entrant structure induced by adding an electrospinning layer (cellulose acetate and SiNPs) onto PET membrane, followed by surface fluorination using 1H, 1H, 2H, 2H-perfluorodecyl-triethoxysilane	[166]
PSF	DCMD	154.1	1.08	Incorporation of fluorinated PU into the PSF dope solution and preparation of membrane using electrospinning, during which a spontaneous fluorinated PU additive segregation to the nanofiber surface occurred. This resulted in rendering the nanofibers heterogeneous with rougher and corrugated surfaces.	[167]

PVDF	MHDD	145.2	1.05	Fabrication of GO-PVP layer over PVDF membrane followed by hydrophobization using hexadecyltrimethoxysilane	[168]
PP	VMD	158.49	-	Coating SiO_2 nanoparticles on PP membrane followed by fluorination using 1H,1H,2H,2H-perfluorodecyltriethoxysilane, resulting in increasing the interface roughness and superhydrophobicity	[169]
PVDF	DCMD	131.7	0.68	Incorporation of silanized-TiO_2 into the PVDF dope solution to reduce the membrane surface energy	[170]
PVDF	DCMD	156.4	0.842	Electrospinning PVDF dope solution containing modified SiNPs (with silane reagent, N-octadecyltrichlorosilane) to increase hydrophobicity	[171]
PVDF	DCMD	75.7	1.4	Incorporation of graphene into PVDF dope solution and preparation of membrane by immersion precipitation. Tuning pore structure without aggregation thanks to the structure of graphene	[172]
PTFE	VMD	Pristine PTFE: 134 Modified PTFE: 59	3.6	Coating hydrophilic dopamine over PTFE to separate oily saline stream	[173]
PVDF	DCMD	Pristine PVDF: 109.5 Modified PVDF: 13.2	-	Deposition of a hydrophilic layer over PVDF membrane via oxidant-induced dopamine polymerization, making the membrane appropriate for low surface tension feed	[174]
PVDF	DCMD	164	-	Fabrication of hierarchically superhydrophobic PVDF membrane by casting over stainless-steel mesh template, resulting in creating lotus leave structure	[175]

V-POSS: Vinyl- Polyhedral oligomeric silsesquioxane, PPO: Poly(2,6-dimethyl-1,4-phenylene oxide), PSF: Polysulfone, PU: Polyurethane, MHDD: Membrane humidification-dehumidification distillation.

2.5.4. Membrane recovery

Several methods have been proposed for the recovery and dewetting of wetted MD membranes, including rinsing, cleaning, drying, and employing pressurized air. Although recovery and dewetting of the membrane is important, it should be performed carefully. Some of the methods may damage the structure and/or reduce the hydrophobicity of the membrane. Herein, the research carried out for dewetting of MD membranes is presented.

Shin *et al*. explored the dewetting of membranes used for desalination by immersing the membranes in an ethanol solution to replace the air in the pores, then immersing the membranes in deionized water to replace the ethanol in the pores, and finally applying a hot air flow to the surface of the wetted membranes [176]. To optimize the dewetting conditions, namely hot air temperature and dewetting time, response surface methodology (RSM) was employed. Applying hot air was found to be effective for dewetting with optimal conditions being 70.6 °C and 7 min. However, the effectiveness of dewetting was found to be sensitive to these conditions and should therefore be adjusted to minimize membrane damage and maximize membrane recovery. In contrast, Gryta found that a similar method of rinsing membranes wetted by NaCl solution with distilled water followed by drying was insufficient for their regeneration [177]. Following drying, these membranes experienced rapid partial rewetting likely due to remaining salt deposits in the pores.

In another study, Guillen-Burrieza *et al*. evaluated the ability to restore pieces of fouled PTFE membranes by immersing them in beakers of several cleaning agents under continuous agitation, followed by rinsing with deionized water and drying at room temperature [178]. The cleaning protocol with a solution of 0.1 wt% oxalic acid and 0.8 wt% citric acid was found to remove a significant amount of the scale layer that covered the fouled membrane surface, leading to the

greatest CA recovery. However, this protocol also caused structural damage to the membrane which was at least in part a consequence of the operation and chemical treatment. Therefore, selection of cleaning protocol should be conducted in a way that the protocol removes scale effectively while avoiding damage to the membrane structure.

Alternatively, Warsinger *et al*. proposed an approach that entails the application of pressurized air from the permeate side for several seconds to remove water from the pores before it evaporates [179]. One advantage of this technique is the short time required for the dewetting process which has been proved theoretically in the literature [180]. This approach is also advantageous since it does not separate water and salts by vaporization, contrary to the dryout method where water evaporates, leaving crystalline solutes inside the pore, which may later facilitate pore rewetting. The air backwashing approach was shown to be consistently more effective than the standard dryout method by achieving a higher restoration of LEP. However, air backwashing has the potential to cause superficial tears.

2.6. Process-based approach for mitigation of pore wetting

Depending on the composition of wastewater, a pretreatment process can be employed to decrease fouling and wetting in MD. As previously discussed, the presence of some materials, e.g. organic materials, may accelerate pore wetting. Therefore, using an appropriate pretreatment process to remove these harmful materials before they come into contact with membranes is one of the effective approaches for mitigating pore wetting. Various processes have been employed as pretreatment for MD including filtration [1,181,182], chemical treatment [183,184], biological treatment [185], thermal process [186], fenton oxidation [187], dissolved air floatation [188], etc. Most of these studies have placed the focus on the reduction of fouling and scaling on the

membrane surface and inside the pores. Herein, some examples of this type of research are presented.

In the study of fouling and wetting caused by crystal formation in seawater MD, Kim *et al*. suggested NaOH/Na_2CO_3 softening as a pretreatment [189]. This method captures and reduces the concentrations of Ca and Mg ions, thus preventing fouling and wetting caused by potential scalants. However, it was suggested that a low concentration of these two ions should be maintained for better control of fouling and wetting (in comparison to the complete removal of these ions). Also, the addition of Mg in feed solution was suggested to delay scale formation (Ca-based), resulting in retardation of wetting in the MD process [189]. Meanwhile, Sardari *et al*. investigated membrane fouling as a result of treating high salinity hydraulic fracturing produced water (HFPW), a feed stream containing high total dissolved solids and a significant amount of dissolved organics, surfactants, and low surface tension contaminants [190]. This study suggested that combined electrocoagulation and DCMD may be used to improve water recovery from HFPWs and found that this pretreatment method was effective in reducing suspended solids and the organic content of raw HFPW samples resulting in membrane fouling mitigation and, consequently, lowering of the permeate flux decline. On the other hand, Yan *et al.* suggested that with respect to membrane scaling control, organic removal by pretreatment is not necessarily essential for high-salinity wastewater treatment with MD. In addition, a biological pretreatment, with which the amounts of biopolymers increases, may be beneficial to decrease gypsum scaling. They observed that the presence of dissolved organics in the feed delayed rather than accelerated gypsum scaling and pore wetting [191]. Therefore, it is necessary to take into account the interactions among components of wastewater when designing the pretreatment systems.

From another point of view, it is expected that smaller-sized crystals on a membrane surface facilitate the deposition of crystals within the membrane pores, resulting in partial wetting. In accordance with the research conducted by Wang *et al*., coagulation was shown to be a beneficial pretreatment method since it could increase the size of crystal particles, decreasing the chance of membrane partial wetting and resulting in a higher permeate flux [192]. As another pretreatment system, foam fractionation was employed to reduce pore wetting during MD treatment of municipal wastewater RO brines. Foam fractionation is an adsorptive process utilizing air bubbles for removing hydrophobic and surface-active materials. This pretreatment was carried out using a protein skimmer put in a beaker containing saltwater [193]. Also, Suwaileh *et al.* employed forward osmosis as MD pretreatment to prevent fouling and wetting [194]. Shin *et al.* proposed a new design for MD by employing Ohmic heating, where electrochemical oxidation and DCMD were carried out sequentially. This setup could destroy the organic compounds anodically, and consequently, combining these two processes made MD resistant toward pore wetting. Also, it should be mentioned that the temperature of the aqueous sulfate solution was increased to 70 °C via resistive heating [195].

In addition to pretreatment, Rezaei *et al.* developed a novel technique of air recharging on the feed side. In this study, MD was employed for the desalination of a feed containing surfactant. This method could decrease the contact area of membrane with feed solution and reduce the adhesion of surfactant to the membrane by replacing the liquid tending to penetrate into the pore with air molecules [196]. Also, Chen *et al.* reported that the introduction of gas bubbles into the DCMD process reduced temperature polarization and also increased the surface shear rate resulting in postponing scale formation on the membrane surface and consequently reducing the pore wetting [197].

2.7. Modeling of pore wetting

A definition for MD was published by the International Union of Pure and Applied Chemistry in 1996 to eliminate conflicting terminology regarding membranes and membrane processes. As such, MD was defined as a "distillation process in which the liquid and gas phases are separated by a porous membrane, the pores of which are not wetted by the liquid phase" [198]. This definition has since shaped MD transport theory.

The well-known theory by Schofield *et al*. associates concentration polarization with the hydrodynamic condition of the feed [23,199], but neglects the polarization within the pores. This is important to note because the concentration polarization in the pores can be more significant due to the absence of liquid turbulence. Further, rapid evaporation inside the membrane results in an increased salt concentration. Once the salt concentration exceeds its solubility limit, the deposition of salt in the pores occurs, as evidenced by some researches [2].

Likewise, liquid phase temperature polarization has been limited to the feed and permeate boundary phase. However, heat transfer in the liquid is mostly neglected in the pores. This is important to note since severe temperature polarization can occur from the reduced temperature at the vapor-liquid interface as a result of slow heat conduction through the liquid and fast evaporation of water which absorbs a significant amount of energy. Ultimately, a model that considers the behaviour of liquid inside membrane pores is necessary.

Minimal research exists in the literature which attempts to model pore wetting. An early model was developed by Peña *et al*. while assuming two opposing fluxes occur in the membrane: a vapor flux from feed to permeate side through dry pores and a liquid flux from permeate to feed side through liquid-filled pores as a result of a pressure difference between the two sides [200]. This model explains the decrease in flux during progressive membrane wetting while considering a new

parameter, the percentage of pores filled with liquid water. However, in this model, pores were either small and completely nonwetted or large and totally wetted and no pores were considered as partially filled with both gas/vapor and liquid phases.

Another model proposed by Qtaishat *et al*. sought to model pore wetting in VMD [4]. This model was developed with an assumption that the liquid is transported by Poiseuille flow followed in series by the vapor transport via Knudsen flow. Although this model provides insight into wetting phenomena, it is limited to VMD and predicts unreasonably high fluxes. Further, it assumes that the system is isothermal, so heat transfer is not considered.

More recently, Wang *et al*. developed a kinetic model to predict the propagation rate of the vapor-liquid interface in a progressively and partially wetted membrane pore induced by surfactant (SDS) in the feed [201]. This model assumes 1) a balance of forces at the vapor-liquid interface, 2) pseudo-steady state transport of surfactants, and 3) pseudo-equilibrium surfactant adsorption. This model considers three major mechanisms for mass transport of surfactants in membrane pores: convection, diffusion, and adsorption. In accordance with this model, pore wetting kinetics is dependent on SDS concentration and vapor flux. This model provided insight into pore wetting in MD such as indicating that surfactants promote pore wetting by reducing feed surface tension (however, not through making the pore wall hydrophilic) and, for this reason, adsorption of surfactants on the pore wall deters pore wetting by continuously removing surfactant from the vapor-liquid interface. However, this model can only predict kinetics for active agents that can significantly change aqueous solution surface tension and can strongly adsorb onto the pore surface. Further, heat transfer is not considered despite its significant effect on MD performance as well as pore wetting.

2.8. Conclusion

It is needless to talk about the importance of MD for the desalination process. However, it is of considerable significance to tackle pore wetting phenomena in order to resolve this issue and help MD become commercialized, resulting in moving one step closer to making safe drinking water accessible to everyone. Hitherto, several factors have been identified as the possible sources of pore wetting, including transmembrane pressure, feed composition, membrane degradation, condensation within the pores, operational parameters and intermittent operation.

In spite of many other membrane processes such as RO, concentration polarization (inside and outside the pore) does not affect the driving force of MD process directly. However, it can accelerate scaling and, consequently, pore wetting. Regarding temperature polarization, not only does it reduce driving force, but it also facilitates scaling and, consequently, pore wetting. Also, it affects condensation inside the pores. To avoid temperature and concentration polarization, some of the following methods can be employed: providing an appropriate mixing on the feed side; engineering the membrane surface to provide a better mixing; preventing feed from penetrating into the pore and consequently avoiding temperature and concentration polarization inside the pore; incorporation of CNT or other similar nanomaterials into the membrane and providing an electrical circuit in order to control temperature and concentration polarization outside the membrane and even inside the pores, etc.

There are two main approaches for the mitigation of pore wetting: membrane-based and process-based approaches. Regarding the membrane-based approaches, some notes should be considered:

- High wetting resistance of some membranes relies on air pockets available on the membrane surface. These types of membranes have shown excellent performance.

However, for these types of membranes, long-term operation tests are highly recommended since air molecules may escape from the surface of the membrane.

- Mitigation of pore wetting includes air pockets on the membrane surface. However, the presence of air in the pores might provide potentially significant resistance to vapor diffusion. Therefore, caution should be applied in this regard.
- Membranes should be prepared in a way to be resistant to changes in chemical and physical structure during long-term operations or cleaning processes to make sure that they do not lose wetting resistance.
- Also, membranes should be prepared with a facile method at a low cost in order to be scalable.
- Release of harmful materials from the membrane may contaminate the environment. Therefore, it is preferred to use environmentally friendly materials for membrane preparation and modification.
- Re-entrant morphology can provide a Cassie-Baxter state for even low surface tension liquids resulting in high wetting resistance. Rigorous theoretical studies are required to optimize this effect for various pore shapes. As well, the technologies have to be developed to fabricate the membranes of the most favourable architecture.
- Dual-layered membranes are appropriate for oily saline waters where the hydrophilic layer repulses the oil phase.
- Regarding the membranes containing CNT or GO layer, where this layer completes an electrical circuit, cautions should be applied to avoid membrane damage in ionizable environments.

Most of these approaches in membrane material and membrane design are based on enhancement and maintenance of high hydrophobicity of the membrane surface. The other aspects concerning the pore geometry, such as angle of cone-shaped pore entry, pore size distribution in the longitudinal direction of the pore, pore length, etc. are largely neglected. Further researches, both experimental and theoretical, seem to be necessary to prevent membrane pores from wetting and to make the MD process commercially feasible.

Although membrane recovery is a method for reusing a wetted membrane, it should be performed carefully since some of the recovery methods damage the structure or reduce the hydrophobicity. Process-based approaches primarily have concentrated on pretreatment of MD feed solution. It seems that pretreatment can be considered as a suitable approach for removing materials that accelerate pore wetting.

In addition, developing models describing the wetting process can provide a better insight into this phenomenon. Modeling is highly recommended since measurement (e.g. concentration and temperature measurement) at the pore scale is challenging. Modeling of pore wetting can be tackled from different aspects:

1) Modifying the available models used to determine effective parameters on wetting phenomena such as pore size distribution.
2) Providing a more efficient equation for estimation of LEP.
3) Focusing on the movement of liquid/gas interface in the pore in terms of interfacial pressure and velocity.
4) Developing a model dealing with pore wetting considering heat and mass balance.

2.9. References

[1] K. Karakulski, M. Gryta, Water demineralisation by NF/MD integrated processes, Desalination. 177 (2005) 109–119. doi:10.1016/j.desal.2004.11.018.

[2] M. Gryta, Influence of polypropylene membrane surface porosity on the performance of membrane distillation process, J. Membr. Sci. 287 (2007) 67–78. doi:10.1016/j.memsci.2006.10.011.

[3] M. Gryta, Long-term performance of membrane distillation process, J. Membr. Sci. 265 (2005) 153–159. doi:10.1016/j.memsci.2005.04.049.

[4] M.R. Qtaishat, T. Matsuura, Modelling of pore wetting in membrane distillation compared with pervaporation, in: Pervaporation, Vap. Permeat. Membr. Distill. Princ. Appl., Elsevier Ltd, 2015: pp. 385–413. doi:10.1016/B978-1-78242-246-4.00013-1.

[5] K.G. Nayar, J. Swaminathan, D. Panchanathan, D.E.M. Warsinger, G.H. McKinley, J.H. Lienhard, Effect of scale deposition on surface tension of seawater and membrane distillation, Proc. 2015 Int. Desalin. Assoc. World Congr. Desalin. Water Reuse. (2015) 1–11.

[6] H. Chamani, P. Yazgan-Birgi, T. Matsuura, D. Rana, M.I. Hassan Ali, H.A. Arafat, C.Q. Lan, CFD-based genetic programming model for liquid entry pressure estimation of hydrophobic membranes, Desalination. 476 (2020) 114231. doi:10.1016/j.desal.2019.114231.

[7] F.E. Ahmed, B.S. Lalia, R. Hashaikeh, Membrane-based detection of wetting phenomenon in direct contact membrane distillation, J. Membr. Sci. 535 (2017) 89–93. doi:10.1016/j.memsci.2017.04.035.

[8] J. Zhu, L. Jiang, T. Matsuura, New insights into fabrication of hydrophobic/hydrophilic

composite hollow fibers for direct contact membrane distillation, Chem. Eng. Sci. 137 (2015) 79–90. doi:10.1016/j.ces.2015.05.064.

[9] X. Feng, L.Y. Jiang, T. Matsuura, P. Wu, Fabrication of hydrophobic/hydrophilic composite hollow fibers for DCMD: Influence of dope formulation and external coagulant, Desalination. 401 (2017) 53–63. doi:10.1016/j.desal.2016.07.026.

[10] P. Jacob, S. Laborie, C. Cabassud, Visualizing and evaluating wetting in membrane distillation: New methodology and indicators based on Detection of Dissolved Tracer Intrusion (DDTI), Desalination. 443 (2018) 307–322. doi:10.1016/j.desal.2018.06.006.

[11] Y. Chen, Z. Wang, G.K. Jennings, S. Lin, Probing pore wetting in membrane distillation using impedance: Early detection and mechanism of surfactant-induced wetting, Environ. Sci. Technol. Lett. 4 (2017) 505–510. doi:10.1021/acs.estlett.7b00372.

[12] H.G.L. Coster, T.C. Chilcott, A.C.F. Coster, Impedance spectroscopy of interfaces, membranes and ultrastructures, Bioelectrochemistry Bioenerg. 40 (1996) 79–98. doi:10.1016/0302-4598(96)05064-7.

[13] J.M. Kavanagh, S. Hussain, T.C. Chilcott, H.G.L. Coster, Fouling of reverse osmosis membranes using electrical impedance spectroscopy: Measurements and simulations, Desalination. 236 (2009) 187–193. doi:10.1016/j.desal.2007.10.066.

[14] P. Jacob, B. Dejean, S. Laborie, C. Cabassud, An optical in-situ tool for visualizing and understanding wetting dynamics in membrane distillation, J. Membr. Sci. 595 (2020) 117587. doi:10.1016/j.memsci.2019.117587.

[15] J. Kujawa, A. Rozicka, S. Cerneaux, W. Kujawski, The influence of surface modification on the physicochemical properties of ceramic membranes, Colloids Surfaces A Physicochem. Eng. Asp. 443 (2014) 567–575. doi:10.1016/j.colsurfa.2013.10.044.

[16] M. Rezaei, D.M. Warsinger, J.H. Lienhard V, M.C. Duke, T. Matsuura, W.M. Samhaber, Wetting phenomena in membrane distillation: Mechanisms, reversal, and prevention, Water Res. 139 (2018) 329–352. doi:10.1016/j.watres.2018.03.058.

[17] H. Yildirim Erbil, Surface energetics of films of poly(vinyl acetate-butyl acrylate) emulsion copolymers, Polymer (Guildf). 37 (1996) 5483–5491. doi:10.1016/S0032-3861(96)00385-0.

[18] Z. Chen, D. Rana, T. Matsuura, Y. Yang, C.Q. Lan, Study on the structure and vacuum membrane distillation performance of PVDF composite membranes: I. Influence of blending, Sep. Purif. Technol. 133 (2014) 303–312. doi:10.1016/j.seppur.2014.07.015.

[19] W. Wu, R.F. Giese, C.J. van Oss, Evaluation of the Lifshitz-van der waals/acid-base approach to determine surface tension components, Langmuir. 11 (1995) 379–382.

[20] A. Alkhudhiri, N. Darwish, N. Hilal, Membrane distillation: A comprehensive review, Desalination. 287 (2012) 2–18. doi:10.1016/j.desal.2011.08.027.

[21] N. Hilal, A. Fauzi Ismail, T. Matsuura, D. Oatley-Radcliffe, Membrane Characterization - 1st Edition, Elsevier. (2017).

[22] J. Lee, B. He, N.A. Patankar, A roughness-based wettability switching membrane device for hydrophobic surfaces, J. Micromechanics Microengineering. 15 (2005) 591–600. doi:10.1088/0960-1317/15/3/022.

[23] M. Khayet Souhaimi, T. Matsuura, Membrane Distillation: Principles and Applications, Elsevier, 2011.

[24] Y.C. Woo, Y. Kim, W.G. Shim, L.D. Tijing, M. Yao, L.D. Nghiem, J.S. Choi, S.H. Kim, H.K. Shon, Graphene/PVDF flat-sheet membrane for the treatment of RO brine from coal seam gas produced water by air gap membrane distillation, J. Membr. Sci. 513 (2016) 74–

84. doi:10.1016/j.memsci.2016.04.014.

[25] B.S. Lalia, E. Guillen, H.A. Arafat, R. Hashaikeh, Nanocrystalline cellulose reinforced PVDF-HFP membranes for membrane distillation application, Desalination. 332 (2014) 134–141. doi:10.1016/j.desal.2013.10.030.

[26] K.C. Khulbe, C.Y. Feng, T. Matsuura, Pore Size, Pore Size Distribution, and Roughness at the Membrane Surface, in: Synth. Polym. Membr. Charact. by At. Force Microsc., Springer, 2008.

[27] G.R. Guillen, Y. Pan, M. Li, E.M.V. Hoek, Preparation and characterization of membranes formed by nonsolvent induced phase separation: A review, Ind. Eng. Chem. Res. 50 (2011) 3798–3817. doi:10.1021/ie101928r.

[28] M. Khayet, K.C. Khulbe, T. Matsuura, Characterization of membranes for membrane distillation by atomic force microscopy and estimation of their water vapor transfer coefficients in vacuum membrane distillation process, J. Membr. Sci. 238 (2004) 199–211. doi:10.1016/j.memsci.2004.03.036.

[29] M. Khayet, T. Matsuura, Preparation and characterization of polyvinylidene fluoride membranes for membrane distillation, Ind. Eng. Chem. Res. 40 (2001) 5710–5718. doi:10.1021/ie010553y.

[30] P.C. Carman, Flow of Gases Through Porous Media, Butterworth Publications, London, 1956.

[31] A.C.M. Franken, J.A.M. Nolten, M.H.V. Mulder, D. Bargeman, C.A. Smolders, Wetting criteria for the applicability of membrane distillation, J. Membr. Sci. 33 (1987) 315–328. doi:10.1016/S0376-7388(00)80288-4.

[32] K.Y. Law, Definitions for hydrophilicity, hydrophobicity, and superhydrophobicity:

Getting the basics right, J. Phys. Chem. Lett. 5 (2014) 686–688. doi:10.1021/jz402762h.

[33] C.H. Kung, P.K. Sow, B. Zahiri, W. Mérida, Assessment and interpretation of surface wettability based on sessile droplet contact angle measurement: Challenges and opportunities, Adv. Mater. Interfaces. 6 (2019) 1900839. doi:10.1002/admi.201900839.

[34] T. Young, An essay on the cohesion of fluids, Philos. Trans. R. Soc. London. 95 (1805) 65–87. doi:10.1098/rstl.1805.0005.

[35] M. Yao, L.D. Tijing, G. Naidu, S.H. Kim, H. Matsuyama, A.G. Fane, H.K. Shon, A review of membrane wettability for the treatment of saline water deploying membrane distillation, Desalination. 479 (2020) 114312. doi:10.1016/j.desal.2020.114312.

[36] R.N. Wenzel, Resistance of solid surfaces to wetting by water, Ind. Eng. Chem. 28 (1936) 988–994. doi:10.1021/ie50320a024.

[37] S. Cassie, A. B. D.; Baxter, Wettability of porous surfaces, Trans. Faraday Soc. 40 (1944) 546–551.

[38] J. Kujawa, W. Kujawski, Functionalization of ceramic metal oxide powders and ceramic membranes by perfluoroalkylsilanes and alkylsilanes possessing different reactive groups: Physicochemical and tribological properties, ACS Appl. Mater. Interfaces. 8 (2016) 7509–7521. doi:10.1021/acsami.5b11975.

[39] J. Kujawa, S. Al-Gharabli, W. Kujawski, K. Knozowska, Molecular grafting of fluorinated and nonfluorinated alkylsiloxanes on various ceramic membrane surfaces for the removal of volatile organic compounds applying vacuum membrane distillation, ACS Appl. Mater. Interfaces. 9 (2017) 6571–6590. doi:10.1021/acsami.6b14835.

[40] J. Kujawa, W. Kujawski, S. Cerneaux, G. Li, S. Al-Gharabli, Zirconium dioxide membranes decorated by silanes based-modifiers for membrane distillation – Material chemistry

approach, J. Membr. Sci. 596 (2020) 117597. doi:10.1016/j.memsci.2019.117597.

[41] D.C. Pease, The significance of the contact angle in relation to the solid surface, J. Phys. Chem. 49 (1945) 107–110. doi:10.1021/j150440a007.

[42] L. Gao, T.J. McCarthy, How Wenzel and Cassie were wrong, Langmuir. 23 (2007) 3762–3765. doi:10.1021/la062634a.

[43] G. McHale, Cassie and Wenzel: Were they really so wrong?, Langmuir. 23 (2007) 8200–8205. doi:10.1021/la7011167.

[44] R.B. Saffarini, B. Mansoor, R. Thomas, H.A. Arafat, Effect of temperature-dependent microstructure evolution on pore wetting in PTFE membranes under membrane distillation conditions, J. Membr. Sci. 429 (2013) 282–294. doi:10.1016/j.memsci.2012.11.049.

[45] K. Smolders, A.C.M. Franken, Terminology for membrane distillation, Desalination. 72 (1989) 249–262. doi:10.1016/0011-9164(89)80010-4.

[46] M. Baghbanzadeh, D. Rana, T. Matsuura, C.Q. Lan, Effects of hydrophilic CuO nanoparticles on properties and performance of PVDF VMD membranes, Desalination. 369 (2015) 75–84. doi:10.1016/j.desal.2015.04.032.

[47] Z. Chen, D. Rana, T. Matsuura, D. Meng, C.Q. Lan, Study on structure and vacuum membrane distillation performance of pvdf membranes: II. influence of molecular weight, Chem. Eng. J. 276 (2015) 174–184. doi:10.1016/j.cej.2015.04.030.

[48] K. He, H.J. Hwang, I.S. Moon, Air gap membrane distillation on the different types of membrane, Korean J. Chem. Eng. 28 (2011) 770–777. doi:10.1007/s11814-010-0415-0.

[49] M.C. García-Payo, M.A. Izquierdo-Gil, C. Fernández-Pineda, Wetting study of hydrophobic membranes via liquid entry pressure measurements with aqueous alcohol solutions, J. Colloid Interface Sci. 230 (2000) 420–431. doi:10.1006/jcis.2000.7106.

[50] G. Rácz, S. Kerker, Z. Kovács, G. Vatai, M. Ebrahimi, P. Czermak, Theoretical and experimental approaches of liquid entry pressure determination in membrane distillation processes, Period. Polytech. Chem. Eng. 58 (2014) 81–91. doi:10.3311/PPch.2179.

[51] P. Yazgan-Birgi, M.I. Hassan Ali, H.A. Arafat, Estimation of liquid entry pressure in hydrophobic membranes using CFD tools, J. Membr. Sci. 552 (2018) 68–76. doi:10.1016/j.memsci.2018.01.061.

[52] B.S. Kim, P. Harriott, Critical entry pressure for liquids in hydrophobic membranes, J. Colloid Interface Sci. 115 (1987) 1–8. doi:10.1016/0021-9797(87)90002-6.

[53] A.T. Servi, J. Kharraz, D. Klee, K. Notarangelo, B. Eyob, E. Guillen-Burrieza, A. Liu, H.A. Arafat, K.K. Gleason, A systematic study of the impact of hydrophobicity on the wetting of MD membranes, J. Membr. Sci. 520 (2016) 850–859. doi:10.1016/j.memsci.2016.08.021.

[54] W.R. Purcell, Interpretation of capillary pressure data, J. Pet. Technol. 2 (1950) 11–12. doi:10.2118/950369-g.

[55] E. Guillen-Burrieza, A. Servi, B.S. Lalia, H.A. Arafat, Membrane structure and surface morphology impact on the wetting of MD membranes, J. Membr. Sci. 483 (2015) 94–103. doi:10.1016/j.memsci.2015.02.024.

[56] T. Franken, Membrane Distillation: a new approach using composite membranes, University of Twente, 1988.

[57] L. Eykens, K. De Sitter, C. Dotremont, L. Pinoy, B. Van der Bruggen, Membrane synthesis for membrane distillation: A review, Sep. Purif. Technol. 182 (2017) 36–51. doi:10.1016/j.seppur.2017.03.035.

[58] L. Eykens, K. De Sitter, C. Dotremont, L. Pinoy, B. Van Der Bruggen, How to optimize the membrane properties for membrane distillation: A review, Ind. Eng. Chem. Res. 55 (2016)

9333–9343. doi:10.1021/acs.iecr.6b02226.

[59] G. Rácz, S. Kerker, O. Schmitz, B. Schnabel, Z. Kovács, G. Vatai, M. Ebrahimi, P. Czermak, Experimental determination of liquid entry pressure (LEP) in vacuum membrane distillation for oily wastewaters, Membr. Water Treat. 6 (2015) 237–249. doi:10.12989/mwt.2015.6.3.237.

[60] M. Gryta, Concentration of NaCl solution by membrane distillation integrated with crystallization, Sep. Sci. Technol. 37 (2002) 3535–3558. doi:10.1081/SS-120014442.

[61] F. Kiefer, A. Präbst, K.S. Rodewald, T. Sattelmayer, Membrane scaling in Vacuum Membrane Distillation - Part 1: In-situ observation of crystal growth and membrane wetting, J. Membr. Sci. 590 (2019) 117294. doi:10.1016/j.memsci.2019.117294.

[62] K.S.S. Christie, Y. Yin, S. Lin, T. Tong, Distinct behaviors between gypsum and silica scaling in membrane distillation, Environ. Sci. Technol. 54 (2020) 568-576. doi:10.1021/acs.est.9b06023.

[63] Z. Wang, Y. Chen, X. Sun, R. Duddu, S. Lin, Mechanism of pore wetting in membrane distillation with alcohol vs. surfactant, J. Membr. Sci. 559 (2018) 183–195. doi:10.1016/j.memsci.2018.04.045.

[64] A.K. An, J. Guo, S. Jeong, E.J. Lee, S.A.A. Tabatabai, T.O. Leiknes, High flux and antifouling properties of negatively charged membrane for dyeing wastewater treatment by membrane distillation, Water Res. 103 (2016) 362–371. doi:10.1016/j.watres.2016.07.060.

[65] A.L. McGaughey, R.D. Gustafson, A.E. Childress, Effect of long-term operation on membrane surface characteristics and performance in membrane distillation, J. Membr. Sci. 543 (2017) 143–150. doi:10.1016/j.memsci.2017.08.040.

[66] M. Gryta, J. Grzechulska-Damszel, A. Markowska, K. Karakulski, The influence of

polypropylene degradation on the membrane wettability during membrane distillation, J. Membr. Sci. 326 (2009) 493–502. doi:10.1016/j.memsci.2008.10.022.

[67] K. Li, Y. Zhang, Z. Wang, L. Liu, H. Liu, J. Wang, Electrothermally driven membrane distillation for low-energy consumption and wetting mitigation, Environ. Sci. Technol. 53 (2019) 13506–13513. doi:10.1021/acs.est.9b04861.

[68] E. Guillen-Burrieza, M.O. Mavukkandy, M.R. Bilad, H.A. Arafat, Understanding wetting phenomena in membrane distillation and how operational parameters can affect it, J. Membr. Sci. 515 (2016) 163–174. doi:10.1016/j.memsci.2016.05.051.

[69] J. Ge, Y. Peng, Z. Li, P. Chen, S. Wang, Membrane fouling and wetting in a DCMD process for RO brine concentration, Desalination. 344 (2014) 97–107. doi:10.1016/j.desal.2014.03.017.

[70] R. Saffarini, H. Arafat, R. Thomas, Influence of pore structure on membrane wettability in membrane distillation, in: Sixth Jordan Int. Chem. Eng. Conf., Amman, 2012.

[71] M. Safavi, T. Mohammadi, High-salinity water desalination using VMD, Chem. Eng. J. 149 (2009) 191–195. doi:10.1016/j.cej.2008.10.021.

[72] E. Guillen-Burrieza, R. Thomas, B. Mansoor, D. Johnson, N. Hilal, H. Arafat, Effect of dry-out on the fouling of PVDF and PTFE membranes under conditions simulating intermittent seawater membrane distillation (SWMD), J. Membr. Sci. 438 (2013) 126–139. doi:10.1016/j.memsci.2013.03.014.

[73] J. Ravi, M.H.D. Othman, T. Matsuura, M. Ro'il Bilad, T.H. El-badawy, F. Aziz, A.F. Ismail, M.A. Rahman, J. Jaafar, Polymeric membranes for desalination using membrane distillation: A review, Desalination. 490 (2020) 114530. doi:10.1016/j.desal.2020.114530.

[74] J. Zhang, Z. Song, B. Li, Q. Wang, S. Wang, Fabrication and characterization of

superhydrophobic poly (vinylidene fluoride) membrane for direct contact membrane distillation, Desalination. 324 (2013) 1–9. doi:10.1016/j.desal.2013.05.018.

[75] B.S. Lalia, V. Kochkodan, R. Hashaikeh, N. Hilal, A review on membrane fabrication: Structure, properties and performance relationship, Desalination. 326 (2013) 77–95. doi:10.1016/j.desal.2013.06.016.

[76] M. Gryta, M. Barancewicz, Influence of morphology of PVDF capillary membranes on the performance of direct contact membrane distillation, J. Membr. Sci. 358 (2010) 158–167. doi:10.1016/j.memsci.2010.04.044.

[77] M. Khayet, C. Cojocaru, M.C. García-Payo, Experimental design and optimization of asymmetric flat-sheet membranes prepared for direct contact membrane distillation, J. Membr. Sci. 351 (2010) 234–245. doi:10.1016/j.memsci.2010.01.057.

[78] M. Amirilargani, E. Saljoughi, T. Mohammadi, M.R. Moghbeli, Effects of coagulation bath temperature and polyvinylpyrrolidone content on flat sheet asymmetric polyethersulfone membranes, Polym. Eng. Sci. 50 (2010) 885–893. doi:10.1002/pen.21603.

[79] V. Ghaffarian, S.M. Mousavi, M. Bahreini, H. Chamani, Poly (butylene succinate)/polyethersulfone/poly (ethylene glycol) membrane: influence of additive molecular weight and concentration on morphology, properties, and performance of the membrane, Desalin. Water Treat. 57 (2016) 16800–16809. doi:10.1080/19443994.2015.1084597.

[80] V. Murugesan, D. Rana, T. Matsuura, C.Q. Lan, Optimization of nanocomposite membrane for vacuum membrane distillation (VMD) using static and continuous flow cells: Effect of nanoparticles and film thickness, Sep. Purif. Technol. 241 (2020) 116685. doi:10.1016/j.seppur.2020.116685.

[81] M. Baghbanzadeh, D. Rana, C.Q. Lan, T. Matsuura, Effects of inorganic nano-additives on properties and performance of polymeric membranes in water treatment, Sep. Purif. Rev. 45 (2016) 141–167. doi:10.1080/15422119.2015.1068806.

[82] J. Lee, H.R. Chae, Y.J. Won, K. Lee, C.H. Lee, H.H. Lee, I.C. Kim, J. min Lee, Graphene oxide nanoplatelets composite membrane with hydrophilic and antifouling properties for wastewater treatment, J. Membr. Sci. 448 (2013) 223–230. doi:10.1016/j.memsci.2013.08.017.

[83] G. Wu, S. Gan, L. Cui, Y. Xu, Preparation and characterization of PES/TiO2 composite membranes, Appl. Surf. Sci. 254 (2008) 7080–7086. doi:10.1016/j.apsusc.2008.05.221.

[84] K. Wang, A.A. Abdala, N. Hilal, M.K. Khraisheh, Mechanical Characterization of Membranes, in: Membr. Charact., Elsevier B.V., 2017: pp. 259–306. doi:10.1016/B978-0-444-63776-5.00013-9.

[85] C. Wu, W. Tang, J. Zhang, S. Liu, Z. Wang, X. Wang, X. Lu, Preparation of super-hydrophobic PVDF membrane for MD purpose via hydroxyl induced crystallization-phase inversion, J. Membr. Sci. 543 (2017) 288–300. doi:10.1016/j.memsci.2017.08.066.

[86] X. Wang, B.S. Hsiao, Electrospun nanofiber membranes, Curr. Opin. Chem. Eng. 12 (2016) 62–81. doi:10.1016/j.coche.2016.03.001.

[87] F.E. Ahmed, B.S. Lalia, R. Hashaikeh, A review on electrospinning for membrane fabrication: Challenges and applications, Desalination. 356 (2015) 15–30. doi:10.1016/j.desal.2014.09.033.

[88] Y. Liao, C.H. Loh, M. Tian, R. Wang, A.G. Fane, Progress in electrospun polymeric nanofibrous membranes for water treatment: Fabrication, modification and applications, Prog. Polym. Sci. 77 (2018) 69–94. doi:10.1016/j.progpolymsci.2017.10.003.

[89] L.D. Tijing, J.S. Choi, S. Lee, S.H. Kim, H.K. Shon, Recent progress of membrane distillation using electrospun nanofibrous membrane, J. Membr. Sci. 453 (2014) 435–462. doi:10.1016/j.memsci.2013.11.022.

[90] C. Feng, K.C. Khulbe, T. Matsuura, R. Gopal, S. Kaur, S. Ramakrishna, M. Khayet, Production of drinking water from saline water by air-gap membrane distillation using polyvinylidene fluoride nanofiber membrane, J. Membr. Sci. 311 (2008) 1–6. doi:10.1016/j.memsci.2007.12.026.

[91] J.A. Prince, G. Singh, D. Rana, T. Matsuura, V. Anbharasi, T.S. Shanmugasundaram, Preparation and characterization of highly hydrophobic poly(vinylidene fluoride) - Clay nanocomposite nanofiber membranes (PVDF-clay NNMs) for desalination using direct contact membrane distillation, J. Membr. Sci. 397–398 (2012) 80–86. doi:10.1016/j.memsci.2012.01.012.

[92] C.I. Su, J.H. Shih, M.S. Huang, C.M. Wang, W.C. Shih, Y. sheng Liu, A study of hydrophobic electrospun membrane applied in seawater desalination by membrane distillation, Fibers Polym. 13 (2012) 698–702. doi:10.1007/s12221-012-0698-3.

[93] H. Maab, L. Francis, A. Al-saadi, C. Aubry, N. Ghaffour, G. Amy, S.P. Nunes, Synthesis and fabrication of nanostructured hydrophobic polyazole membranes for low-energy water recovery, J. Membr. Sci. 423–424 (2012) 11–19. doi:10.1016/j.memsci.2012.07.009.

[94] Z. Li, Y. Liu, J. Yan, K. Wang, B. Xie, Y. Hu, W. Kang, B. Cheng, Electrospun polyvinylidene fluoride/fluorinated acrylate copolymer tree-like nanofiber membrane with high flux and salt rejection ratio for direct contact membrane distillation, Desalination. 466 (2019) 68–76. doi:10.1016/j.desal.2019.05.005.

[95] C. Su, T. Horseman, H. Cao, K.S.S. Christie, Y. Li, S. Lin, Robust superhydrophobic

membrane for membrane distillation with excellent scaling resistance, Environ. Sci. Technol. 53 (2019) 11801–11809. doi:10.1021/acs.est.9b04362.

[96] J.E. Efome, D. Rana, T. Matsuura, C.Q. Lan, Enhanced performance of PVDF nanocomposite membrane by nanofiber coating: A membrane for sustainable desalination through MD, Water Res. 89 (2016) 39–49. doi:10.1016/j.watres.2015.11.040.

[97] M. Yao, Y.C. Woo, L.D. Tijing, W.G. Shim, J.S. Choi, S.H. Kim, H.K. Shon, Effect of heat-press conditions on electrospun membranes for desalination by direct contact membrane distillation, Desalination. 378 (2016) 80–91. doi:10.1016/j.desal.2015.09.025.

[98] Y. Liao, R. Wang, M. Tian, C. Qiu, A.G. Fane, Fabrication of polyvinylidene fluoride (PVDF) nanofiber membranes by electro-spinning for direct contact membrane distillation, J. Membr. Sci. 425–426 (2013) 30–39. doi:10.1016/j.memsci.2012.09.023.

[99] E. Shaulsky, S. Nejati, C. Boo, F. Perreault, C.O. Osuji, M. Elimelech, Post-fabrication modification of electrospun nanofiber mats with polymer coating for membrane distillation applications, J. Membr. Sci. 530 (2017) 158–165. doi:10.1016/j.memsci.2017.02.025.

[100] L. Deng, K. Liu, P. Li, D. Sun, S. Ding, X. Wang, B.S. Hsiao, Engineering construction of robust superhydrophobic two-tier composite membrane with interlocked structure for membrane distillation, J. Membr. Sci. 598 (2020) 117813. doi:10.1016/j.memsci.2020.117813.

[101] L.D. Tijing, Y.C. Woo, W.G. Shim, T. He, J.S. Choi, S.H. Kim, H.K. Shon, Superhydrophobic nanofiber membrane containing carbon nanotubes for high-performance direct contact membrane distillation, J. Membr. Sci. 502 (2016) 158–170. doi:10.1016/j.memsci.2015.12.014.

[102] K. Li, Y. Zhang, L. Xu, F. Zeng, D. Hou, J. Wang, Optimizing stretching conditions in

fabrication of PTFE hollow fiber membrane for performance improvement in membrane distillation, J. Membr. Sci. 550 (2018) 126–135. doi:10.1016/j.memsci.2017.12.070.

[103] H. Wang, S. Ding, H. Zhu, F. Wang, Y. Guo, H. Zhang, J. Chen, Effect of stretching ratio and heating temperature on structure and performance of PTFE hollow fiber membrane in VMD for RO brine, Sep. Purif. Technol. 126 (2014) 82–94. doi:10.1016/j.seppur.2014.02.027.

[104] I. V. Korolkov, A.B. Yeszhanov, M. V. Zdorovets, Y.G. Gorin, O. Güven, S.S. Dosmagambetova, N.A. Khlebnikov, K. V. Serkov, M. V. Krasnopyorova, O.S. Milts, D.A. Zheltov, Modification of PET ion track membranes for membrane distillation of low-level liquid radioactive wastes and salt solutions, Sep. Purif. Technol. 227 (2019) 115694. doi:10.1016/j.seppur.2019.115694.

[105] I. V. Korolkov, Y.G. Gorin, A.B. Yeszhanov, A.L. Kozlovskiy, M. V. Zdorovets, Preparation of PET track-etched membranes for membrane distillation by photo-induced graft polymerization, Mater. Chem. Phys. 205 (2018) 55–63. doi:10.1016/j.matchemphys.2017.11.006.

[106] I. V. Korolkov, A.B. Yeszhanov, Y.G. Gorin, M. V. Zdorovets, N.A. Khlebnikov, K. V. Serkov, Hydrophobization of PET track-etched membranes for direct contact membrane distillation, Mater. Res. Express. 5 (2018) 065317. doi:10.1088/2053-1591/aacc39.

[107] A.K. Pabby, S.S.H. Rizvi, A.M. Sastre, Handbook of Membrane Separations: Chemical, Pharmaceutical, Food, and Biotechnological Applications, Taylor & Francis, 2009.

[108] T.A. Saleh, V.K. Gupta, Nanomaterial and Polymer Membranes, Elsevier, 2016.

[109] J. Zuo, T.S. Chung, PVDF hollow fibers with novel sandwich structure and superior wetting resistance for vacuum membrane distillation, Desalination. 417 (2017) 94–101.

doi:10.1016/j.desal.2017.05.022.

[110] X. Wei, B. Zhao, X.M. Li, Z. Wang, B.Q. He, T. He, B. Jiang, CF4 plasma surface modification of asymmetric hydrophilic polyethersulfone membranes for direct contact membrane distillation, J. Membr. Sci. 407–408 (2012) 164–175. doi:10.1016/j.memsci.2012.03.031.

[111] Y.C. Woo, Y. Chen, L.D. Tijing, S. Phuntsho, T. He, J.S. Choi, S.H. Kim, H.K. Shon, CF4 plasma-modified omniphobic electrospun nanofiber membrane for produced water brine treatment by membrane distillation, J. Membr. Sci. 529 (2017) 234–242. doi:10.1016/j.memsci.2017.01.063.

[112] Z. Xiao, R. Zheng, Y. Liu, H. He, X. Yuan, Y. Ji, D. Li, H. Yin, Y. Zhang, X.M. Li, T. He, Slippery for scaling resistance in membrane distillation: A novel porous micropillared superhydrophobic surface, Water Res. 155 (2019) 152–161. doi:10.1016/j.watres.2019.01.036.

[113] W.A.F. Wae AbdulKadir, A.L. Ahmad, O.B. Seng, N.F. Che Lah, Biomimetic hydrophobic membrane: A review of anti-wetting properties as a potential factor in membrane development for membrane distillation (MD), J. Ind. Eng. Chem. 91 (2020) 15–36. doi:10.1016/j.jiec.2020.08.005.

[114] D. Hou, K.S.S. Christie, K. Wang, M. Tang, D. Wang, J. Wang, Biomimetic superhydrophobic membrane for membrane distillation with robust wetting and fouling resistance, J. Membr. Sci. 599 (2020) 117708. doi:10.1016/j.memsci.2019.117708.

[115] H. Attia, D.J. Johnson, C.J. Wright, N. Hilal, Robust superhydrophobic electrospun membrane fabricated by combination of electrospinning and electrospraying techniques for air gap membrane distillation, Desalination. 446 (2018) 70–82.

doi:10.1016/j.desal.2018.09.001.

[116] A.T. Servi, E. Guillen-Burrieza, D.M. Warsinger, W. Livernois, K. Notarangelo, J. Kharraz, J.H. Lienhard V, H.A. Arafat, K.K. Gleason, The effects of iCVD film thickness and conformality on the permeability and wetting of MD membranes, J. Membr. Sci. 523 (2017) 470–479. doi:10.1016/j.memsci.2016.10.008.

[117] L.N. Nthunya, L. Gutierrez, S. Derese, E.N. Nxumalo, A.R. Verliefde, B.B. Mamba, S.D. Mhlanga, A review of nanoparticle-enhanced membrane distillation membranes: membrane synthesis and applications in water treatment, J. Chem. Technol. Biotechnol. 94 (2019) 2757–2771. doi:10.1002/jctb.5977.

[118] L. Jiao, K. Yan, J. Wang, S. Lin, G. Li, F. Bi, L. Zhang, Low surface energy nanofibrous membrane for enhanced wetting resistance in membrane distillation process, Desalination. 476 (2020) 114210. doi:10.1016/j.desal.2019.114210.

[119] A. Razmjou, E. Arifin, G. Dong, J. Mansouri, V. Chen, Superhydrophobic modification of TiO2 nanocomposite PVDF membranes for applications in membrane distillation, J. Membr. Sci. 415–416 (2012) 850–863. doi:10.1016/j.memsci.2012.06.004.

[120] T. Horseman, Y. Yin, K.S. Christie, Z. Wang, T. Tong, S. Lin, Wetting, scaling, and fouling in membrane distillation: State-of-the-art insights on fundamental mechanisms and mitigation strategies, Environ. Sci. Technol. Engg. 1 (2021) 117–140. doi:10.1021/acsestengg.0c00025.

[121] K.J. Lu, Y. Chen, T.S. Chung, Design of omniphobic interfaces for membrane distillation – A review, Water Res. 162 (2019) 64–77. doi:10.1016/j.watres.2019.06.056.

[122] J. Lee, C. Boo, W.H. Ryu, A.D. Taylor, M. Elimelech, Development of omniphobic desalination membranes using a charged electrospun nanofiber scaffold, ACS Appl. Mater.

Interfaces. 8 (2016) 11154–11161. doi:10.1021/acsami.6b02419.

[123] S. Lin, S. Nejati, C. Boo, Y. Hu, C.O. Osuji, M. Elimelech, Omniphobic membrane for robust membrane distillation, Environ. Sci. Technol. Lett. 1 (2014) 443–447. doi:10.1021/ez500267p.

[124] A. Tuteja, W. Choi, J.M. Mabry, G.H. McKinley, R.E. Cohen, Robust omniphobic surfaces, Proc. Natl. Acad. Sci. U. S. A. 105 (2008) 18200–18205. doi:10.1073/pnas.0804872105.

[125] Y.T. Cheng, D.E. Rodak, Is the lotus leaf superhydrophobic?, Appl. Phys. Lett. 86 (2005) 1–3. doi:10.1063/1.1895487.

[126] A. Tuteja, W. Choi, M. Ma, J.M. Mabry, S.A. Mazzella, G.C. Rutledge, G.H. McKinley, R.E. Cohen, Designing superoleophobic surfaces, Science. 318 (2007) 1618–1622. doi:10.1126/science.1148326.

[127] C. Boo, J. Lee, M. Elimelech, Omniphobic polyvinylidene fluoride (PVDF) membrane for desalination of shale gas produced water by membrane distillation, Environ. Sci. Technol. 50 (2016) 12275–12282. doi:10.1021/acs.est.6b03882.

[128] J. Li, S. Guo, Z. Xu, J. Li, Z. Pan, Z. Du, F. Cheng, Preparation of omniphobic PVDF membranes with silica nanoparticles for treating coking wastewater using direct contact membrane distillation: Electrostatic adsorption vs. chemical bonding, J. Membr. Sci. 574 (2019) 349–357. doi:10.1016/j.memsci.2018.12.079.

[129] Y.C. Woo, Y. Kim, M. Yao, L.D. Tijing, J.S. Choi, S. Lee, S.H. Kim, H.K. Shon, Hierarchical composite membranes with robust omniphobic surface using layer-by-layer assembly technique, Environ. Sci. Technol. 52 (2018) 2186–2196. doi:10.1021/acs.est.7b05450.

[130] R. Zheng, Y. Chen, J. Wang, J. Song, X.M. Li, T. He, Preparation of omniphobic PVDF

membrane with hierarchical structure for treating saline oily wastewater using direct contact membrane distillation, J. Membr. Sci. 555 (2018) 197–205. doi:10.1016/j.memsci.2018.03.041.

[131] K.J. Lu, J. Zuo, J. Chang, H.N. Kuan, T.S. Chung, Omniphobic hollow-fiber membranes for vacuum membrane distillation, Environ. Sci. Technol. 52 (2018) 4472–4480. doi:10.1021/acs.est.8b00766.

[132] L.H. Chen, Y.R. Chen, A. Huang, C.H. Chen, D.Y. Su, C.C. Hsu, F.Y. Tsai, K.L. Tung, Nanostructure depositions on alumina hollow fiber membranes for enhanced wetting resistance during membrane distillation, J. Membr. Sci. 564 (2018) 227–236. doi:10.1016/j.memsci.2018.07.011.

[133] L.H. Chen, A. Huang, Y.R. Chen, C.H. Chen, C.C. Hsu, F.Y. Tsai, K.L. Tung, Omniphobic membranes for direct contact membrane distillation: Effective deposition of zinc oxide nanoparticles, Desalination. 428 (2018) 255–263. doi:10.1016/j.desal.2017.11.029.

[134] X. Li, W. Qing, Y. Wu, S. Shao, L.E. Peng, Y. Yang, P. Wang, F. Liu, C.Y. Tang, Omniphobic nanofibrous membrane with pine-needle-like hierarchical nanostructures: Toward enhanced performance for membrane distillation, ACS Appl. Mater. Interfaces. 11 (2019) 47963–47971. doi:10.1021/acsami.9b17494.

[135] C. Lu, C. Su, H. Cao, X. Ma, F. Duan, J. Chang, Y. Li, F-POSS based omniphobic membrane for robust membrane distillation, Mater. Lett. 228 (2018) 85–88. doi:10.1016/j.matlet.2018.05.126.

[136] L. Deng, H. Ye, X. Li, P. Li, J. Zhang, X. Wang, M. Zhu, B.S. Hsiao, Self-roughened omniphobic coatings on nanofibrous membrane for membrane distillation, Sep. Purif. Technol. 206 (2018) 14–25. doi:10.1016/j.seppur.2018.05.035.

[137] M. Afsari, H.K. Shon, L.D. Tijing, Janus membranes for membrane distillation: Recent advances and challenges, Adv. Colloid Interface Sci. 289 (2021) 102362. doi:10.1016/j.cis.2021.102362.

[138] Y.X. Huang, Z. Wang, J. Jin, S. Lin, Novel Janus membrane for membrane distillation with simultaneous fouling and wetting resistance, Environ. Sci. Technol. 51 (2017) 13304–13310. doi:10.1021/acs.est.7b02848.

[139] O. Makanjuola, F. Ahmed, I. Janajreh, R. Hashaikeh, Development of a dual-layered PVDF-HFP/cellulose membrane with dual wettability for desalination of oily wastewater, J. Membr. Sci. 570–571 (2019) 418–426. doi:10.1016/j.memsci.2018.10.028.

[140] G. Zuo, R. Wang, Novel membrane surface modification to enhance anti-oil fouling property for membrane distillation application, J. Membr. Sci. 447 (2013) 26–35. doi:10.1016/j.memsci.2013.06.053.

[141] S. Zhao, Z. Tao, M. Han, Y. xi Huang, B. Zhao, L. Wang, X. Tian, F. Meng, Hierarchical Janus membrane with superior fouling and wetting resistance for efficient water recovery from challenging wastewater via membrane distillation, J. Membr. Sci. 618 (2021) 118676. doi:10.1016/j.memsci.2020.118676.

[142] Z. Zhu, Z. Liu, L. Zhong, C. Song, W. Shi, F. Cui, W. Wang, Breathable and asymmetrically superwettable Janus membrane with robust oil-fouling resistance for durable membrane distillation, J. Membr. Sci. 563 (2018) 602–609. doi:10.1016/j.memsci.2018.06.028.

[143] N.G.P. Chew, Y. Zhang, K. Goh, J.S. Ho, R. Xu, R. Wang, Hierarchically structured Janus membrane surfaces for enhanced membrane distillation performance, ACS Appl. Mater. Interfaces. 11 (2019) 25524–25534. doi:10.1021/acsami.9b05967.

[144] C. Li, X. Li, X. Du, T. Tong, T.Y. Cath, J. Lee, Antiwetting and antifouling Janus membrane

for desalination of saline oily wastewater by membrane distillation, ACS Appl. Mater. Interfaces. 11 (2019) 18456–18465. doi:10.1021/acsami.9b04212.

[145] Z. Wang, S. Lin, Membrane fouling and wetting in membrane distillation and their mitigation by novel membranes with special wettability, Water Res. 112 (2017) 38–47. doi:10.1016/j.watres.2017.01.022.

[146] H. Li, S. Yu, A robust superhydrophobic surface and origins of its self-cleaning properties, Appl. Surf. Sci. 420 (2017) 336–345. doi:10.1016/j.apsusc.2017.05.131.

[147] Y. Liang, J. Ju, N. Deng, X. Zhou, J. Yan, W. Kang, B. Cheng, Super-hydrophobic self-cleaning bead-like SiO_2@PTFE nanofiber membranes for waterproof-breathable applications, Appl. Surf. Sci. 442 (2018) 54–64. doi:10.1016/j.apsusc.2018.02.126.

[148] Q.L. Huang, Y. Huang, C.F. Xiao, Y.W. You, C.X. Zhang, Electrospun ultrafine fibrous PTFE-supported ZnO porous membrane with self-cleaning function for vacuum membrane distillation, J. Membr. Sci. 534 (2017) 73–82. doi:10.1016/j.memsci.2017.04.015.

[149] L. Tang, A. Iddya, X. Zhu, A. V. Dudchenko, W. Duan, C. Turchi, J. Vanneste, T.Y. Cath, D. Jassby, Enhanced flux and electrochemical cleaning of silicate scaling on carbon nanotube-coated membrane distillation membranes treating geothermal brines, ACS Appl. Mater. Interfaces. 9 (2017) 38594–38605. doi:10.1021/acsami.7b12615.

[150] A. V. Dudchenko, C. Chen, A. Cardenas, J. Rolf, D. Jassby, Frequency-dependent stability of CNT Joule heaters in ionizable media and desalination processes, Nat. Nanotechnol. 12 (2017) 557–563. doi:10.1038/nnano.2017.102.

[151] X. Wu, Q. Jiang, D. Ghim, S. Singamaneni, Y.S. Jun, Localized heating with a photothermal polydopamine coating facilitates a novel membrane distillation process, J. Mater. Chem. A. 6 (2018) 18799–18807. doi:10.1039/c8ta05738a.

[152] U. Rao, A. Iddya, B. Jung, C.M. Khor, Z. Hendren, C. Turchi, T. Cath, E.M.V. Hoek, G.Z. Ramon, D. Jassby, Mineral scale prevention on electrically conducting membrane distillation membranes using induced electrophoretic mixing, Environ. Sci. Technol. 54 (2020) 3678–3690. doi:10.1021/acs.est.9b07806.

[153] M.M. Damtie, B. Kim, Y.C. Woo, J.S. Choi, Membrane distillation for industrial wastewater treatment: Studying the effects of membrane parameters on the wetting performance, Chemosphere. 206 (2018) 793–801. doi:10.1016/j.chemosphere.2018.05.070.

[154] Y.N. Slavin, J. Asnis, U.O. Häfeli, H. Bach, Metal nanoparticles: Understanding the mechanisms behind antibacterial activity, J. Nanobiotechnology. 15 (2017) 65. doi:10.1186/s12951-017-0308-z.

[155] S. Sinha Ray, R. Dangayach, Y.N. Kwon, Surface engineering for anti-wetting and antibacterial membrane for enhanced and fouling resistant membrane distillation performance, Chem. Eng. J. 405 (2021) 126702. doi:10.1016/j.cej.2020.126702.

[156] W. Qing, Y. Wu, X. Li, X. Shi, S. Shao, Y. Mei, W. Zhang, C.Y. Tang, Omniphobic PVDF nanofibrous membrane for superior anti-wetting performance in direct contact membrane distillation, J. Membr. Sci. 608 (2020) 118226. doi:10.1016/j.memsci.2020.118226.

[157] M. Li, K.J. Lu, L. Wang, X. Zhang, T.S. Chung, Janus membranes with asymmetric wettability via a layer-by-layer coating strategy for robust membrane distillation, J. Membr. Sci. 603 (2020) 118031. doi:10.1016/j.memsci.2020.118031.

[158] D. Lee, Y.C. Woo, K.H. Park, S. Phuntsho, L.D. Tijing, M. Yao, W.G. Shim, H.K. Shon, Polyvinylidene fluoride phase design by two-dimensional boron nitride enables enhanced performance and stability for seawater desalination, J. Membr. Sci. 598 (2020) 117669. doi:10.1016/j.memsci.2019.117669.

[159] Y. Liao, G. Zheng, J.J. Huang, M. Tian, R. Wang, Development of robust and superhydrophobic membranes to mitigate membrane scaling and fouling in membrane distillation, J. Membr. Sci. 601 (2020) 117962. doi:10.1016/j.memsci.2020.117962.

[160] X. An, Y. Bai, G. Xu, B. Xie, Y. Hu, Fabrication of interweaving hierarchical fibrous composite (iHFC) membranes for high-flux and robust direct contact membrane distillation, Desalination. 477 (2020) 114264. doi:10.1016/j.desal.2019.114264.

[161] W. Jia, J.A. Kharraz, P.J. Choi, J. Guo, B.J. Deka, A.K. An, Superhydrophobic membrane by hierarchically structured PDMS-POSS electrospray coating with cauliflower-shaped beads for enhanced MD performance, J. Membr. Sci. 597 (2020) 117638. doi:10.1016/j.memsci.2019.117638.

[162] H. Li, W. Shi, X. Zeng, S. Huang, H. Zhang, X. Qin, Improved desalination properties of hydrophobic GO-incorporated PVDF electrospun nanofibrous composites for vacuum membrane distillation, Sep. Purif. Technol. 230 (2020) 115889. doi:10.1016/j.seppur.2019.115889.

[163] Y. Du, D. Wang, W. Wang, J. Fu, X. Chen, L. Wang, W. Yang, X. Zhang, Electrospun nanofibrous polyphenylene oxide membranes for high-salinity water desalination by direct contact membrane distillation, ACS Sustain. Chem. Eng. 7 (2019) 20060–20069. doi:10.1021/acssuschemeng.9b05805.

[164] B.J. Deka, J. Guo, N.K. Khanzada, A.K. An, Omniphobic re-entrant PVDF membrane with ZnO nanoparticles composite for desalination of low surface tension oily seawater, Water Res. 165 (2019) 114982. doi:10.1016/j.watres.2019.114982.

[165] X. Li, H. Shan, M. Cao, B. Li, Facile fabrication of omniphobic PVDF composite membrane via a waterborne coating for anti-wetting and anti-fouling membrane distillation, J. Membr.

Sci. 589 (2019) 117262. doi:10.1016/j.memsci.2019.117262.

[166] D. Hou, C. Ding, C. Fu, D. Wang, C. Zhao, J. Wang, Electrospun nanofibrous omniphobic membrane for anti-surfactant-wetting membrane distillation desalination, Desalination. 468 (2019) 114068. doi:10.1016/j.desal.2019.07.008.

[167] M. Khayet, C. García-Payo, T. Matsuura, Superhydrophobic nanofibers electrospun by surface segregating fluorinated amphiphilic additive for membrane distillation, J. Membr. Sci. 588 (2019) 117215. doi:10.1016/j.memsci.2019.117215.

[168] Q.W. Su, H. Lu, J.Y. Zhang, L.Z. Zhang, Fabrication and analysis of a highly hydrophobic and permeable block GO-PVP/PVDF membrane for membrane humidification-dehumidification desalination, J. Membr. Sci. 582 (2019) 367–380. doi:10.1016/j.memsci.2019.04.023.

[169] Y. Shao, M. Han, Y. Wang, G. Li, W. Xiao, X. Li, X. Wu, X. Ruan, X. Yan, G. He, X. Jiang, Superhydrophobic polypropylene membrane with fabricated antifouling interface for vacuum membrane distillation treating high concentration sodium/magnesium saline water, J. Membr. Sci. 579 (2019) 240–252. doi:10.1016/j.memsci.2019.03.007.

[170] N.S.M. Yatim, O.B. Seng, K.A. Karim, Fluorosilaned-TiO_2 /PVDF membrane distillation with improved wetting resistance for water recovery from high solid loading wastewater, J. Membr. Sci. Res. 5 (2019) 55–64. doi:10.22079/JMSR.2018.89172.1202.

[171] L.N. Nthunya, L. Gutierrez, A.R. Verliefde, S.D. Mhlanga, Enhanced flux in direct contact membrane distillation using superhydrophobic PVDF nanofibre membranes embedded with organically modified SiO_2 nanoparticles, J. Chem. Technol. Biotechnol. 94 (2019) 2826–2837. doi:10.1002/jctb.6104.

[172] C. Athanasekou, A. Sapalidis, I. Katris, E. Savopoulou, K. Beltsios, T. Tsoufis, A.

Kaltzoglou, P. Falaras, G. Bounos, M. Antoniou, P. Boutikos, G.E. Romanos, Mixed matrix PVDF/graphene and composite-skin PVDF/graphene oxide membranes applied in membrane distillation, Polym. Eng. Sci. 59 (2019) 262–278. doi:10.1002/pen.24930.

[173] W. Sun, F. Shen, Z. Wang, Y. Zhang, Y. Wan, An ultrathin, porous and in-air hydrophilic/underwater oleophobic coating simultaneously increasing the flux and antifouling property of membrane for membrane distillation, Desalination. 445 (2018) 40–50. doi:10.1016/j.desal.2018.07.026.

[174] N.G.P. Chew, S. Zhao, C. Malde, R. Wang, Polyvinylidene fluoride membrane modification via oxidant-induced dopamine polymerization for sustainable direct-contact membrane distillation, J. Membr. Sci. 563 (2018) 31–42. doi:10.1016/j.memsci.2018.05.035.

[175] F. Zhao, Z. Ma, K. Xiao, C. Xiang, H. Wang, X. Huang, S. Liang, Hierarchically textured superhydrophobic polyvinylidene fluoride membrane fabricated via nanocasting for enhanced membrane distillation performance, Desalination. 443 (2018) 228–236. doi:10.1016/j.desal.2018.06.003.

[176] Y. Shin, H. Cho, J. Choi, Y. Sun Jang, Y.J. Choi, J. Sohn, S. Lee, J. Choi, Application of response surface methodology (RSM) in the optimization of dewetting conditions for flat sheet membrane distillation (MD) membranes, Desalin. Water Treat. 57 (2016) 10020–10030. doi:10.1080/19443994.2015.1038114.

[177] M. Gryta, Direct contact membrane distillation with crystallization applied to NaCl solutions, Chem. Pap. 56 (2002) 14–19.

[178] E. Guillen-Burrieza, A. Ruiz-Aguirre, G. Zaragoza, H.A. Arafat, Membrane fouling and cleaning in long term plant-scale membrane distillation operations, J. Membr. Sci. 468

(2014) 360–372. doi:10.1016/j.memsci.2014.05.064.

[179] D.M. Warsinger, A. Servi, G.B. Connors, M.O. Mavukkandy, H.A. Arafat, K.K. Gleason, J.H. Lienhard, Reversing membrane wetting in membrane distillation: Comparing dryout to backwashing with pressurized air, Environ. Sci. Water Res. Technol. 3 (2017) 930–939. doi:10.1039/c7ew00085e.

[180] H. Chamani, T. Matsuura, D. Rana, C.Q. Lan, Transport characteristics of liquid-gas interface in a capillary membrane pore, J. Membr. Sci. 611 (2020) 118387. doi:10.1016/j.memsci.2020.118387.

[181] X. Du, Z. Zhang, K.H. Carlson, J. Lee, T. Tong, Membrane fouling and reusability in membrane distillation of shale oil and gas produced water: Effects of membrane surface wettability, J. Membr. Sci. 567 (2018) 199–208. doi:10.1016/j.memsci.2018.09.036.

[182] F.X. Kong, Z.P. Wang, Z. Ji, J.F. Chen, C.M. Guo, G.D. Sun, Y.F. Xie, Organic fouling of membrane distillation for shale gas fracturing flowback water desalination: A special interest in the feed properties by pretreatment, Environ. Sci. Water Res. Technol. 5 (2019) 1339–1348. doi:10.1039/c9ew00334g.

[183] M. Gryta, Chemical pretreatment of feed water for membrane distillation, Chem. Pap. 62 (2008) 100–105. doi:10.2478/s11696-007-0085-5.

[184] J. Li, J. Wu, H. Sun, F. Cheng, Y. Liu, Advanced treatment of biologically treated coking wastewater by membrane distillation coupled with pre-coagulation, Desalination. 380 (2016) 43–51. doi:10.1016/j.desal.2015.11.020.

[185] S. Goh, J. Zhang, Y. Liu, A.G. Fane, Fouling and wetting in membrane distillation (MD) and MD-bioreactor (MDBR) for wastewater reclamation, Desalination. 323 (2013) 39–47. doi:10.1016/j.desal.2012.12.001.

[186] E.J. Hull, K.R. Zodrow, Acid rock drainage treatment using membrane distillation: Impacts of chemical-free pretreatment on scale formation, pore wetting, and product water quality, Environ. Sci. Technol. 51 (2017) 11928–11934. doi:10.1021/acs.est.7b02957.

[187] F. Ricceri, M. Giagnorio, G. Farinelli, G. Blandini, M. Minella, D. Vione, A. Tiraferri, Desalination of produced water by membrane distillation: Effect of the feed components and of a pre-treatment by fenton oxidation, Sci. Rep. 9 (2019) 14964. doi:10.1038/s41598-019-51167-z.

[188] J. Guo, B.J. Deka, K.J. Kim, A.K. An, Regeneration of superhydrophobic TiO2 electrospun membranes in seawater desalination by water flushing in membrane distillation, Desalination. 468 (2019) 114054. doi:10.1016/j.desal.2019.06.020.

[189] H.W. Kim, T. Yun, S. Hong, S. Lee, S. Jeong, Retardation of wetting for membrane distillation by adjusting major components of seawater, Water Res. 175 (2020) 115677. doi:10.1016/j.watres.2020.115677.

[190] K. Sardari, P. Fyfe, D. Lincicome, S. Ranil Wickramasinghe, Combined electrocoagulation and membrane distillation for treating high salinity produced waters, J. Membr. Sci. 564 (2018) 82–96. doi:10.1016/j.memsci.2018.06.041.

[191] Z. Yan, F. Qu, H. Liang, H. Yu, H. Pang, H. Rong, G. Fan, B. Van der Bruggen, Effect of biopolymers and humic substances on gypsum scaling and membrane wetting during membrane distillation, J. Membr. Sci. 617 (2021) 118638. doi:10.1016/j.memsci.2020.118638.

[192] J. Wang, D. Qu, M. Tie, H. Ren, X. Peng, Z. Luan, Effect of coagulation pretreatment on membrane distillation process for desalination of recirculating cooling water, Sep. Purif. Technol. 64 (2008) 108–115. doi:10.1016/j.seppur.2008.07.022.

[193] K. Rajwade, A.C. Barrios, S. Garcia-Segura, F. Perreault, Pore wetting in membrane distillation treatment of municipal wastewater desalination brine and its mitigation by foam fractionation, Chemosphere. 257 (2020) 127214. doi:10.1016/j.chemosphere.2020.127214.

[194] W. Suwaileh, D. Johnson, D. Jones, N. Hilal, An integrated fertilizer driven forward osmosis- renewables powered membrane distillation system for brackish water desalination: A combined experimental and theoretical approach, Desalination. 471 (2019) 114126. doi:10.1016/j.desal.2019.114126.

[195] Y.U. Shin, E.T. Yun, J. Kim, H. Lee, S. Hong, J. Lee, Electrochemical oxidation-membrane distillation hybrid process: utilizing electric resistance heating for distillation and membrane defouling through thermal activation of anodically formed persulfate, Environ. Sci. Technol. 54 (2020) 1867–1877. doi:10.1021/acs.est.9b05141.

[196] M. Rezaei, D.M. Warsinger, J.H. Lienhard V, W.M. Samhaber, Wetting prevention in membrane distillation through superhydrophobicity and recharging an air layer on the membrane surface, J. Membr. Sci. 530 (2017) 42–52. doi:10.1016/j.memsci.2017.02.013.

[197] G. Chen, X. Yang, R. Wang, A.G. Fane, Performance enhancement and scaling control with gas bubbling in direct contact membrane distillation, Desalination. 308 (2013) 47–55. doi:10.1016/j.desal.2012.07.018.

[198] W.J. Koros, Y.H. Ma, T. Shimidzu, Terminology for membranes and membrane processes, Pure Appl. Chem. 68 (1996) 1479–1489. doi:10.1351/pac199668071479.

[199] R.W. Schofield, A.G. Fane, C.J.D. Fell, Heat and mass transfer in membrane distillation, J. Membr. Sci. 33 (1987) 299–313. doi:10.1016/S0376-7388(00)80287-2.

[200] L. Peña, J.M.O. De Zárate, J.I. Mengual, Steady states in membrane distillation: Influence of membrane wetting, J. Chem. Soc. Faraday Trans. 89 (1993) 4333–4338.

doi:10.1039/FT9938904333.

[201] Z. Wang, Y. Chen, S. Lin, Kinetic model for surfactant-induced pore wetting in membrane distillation, J. Membr. Sci. 564 (2018) 275–288. doi:10.1016/j.memsci.2018.07.010.

Chapter 3

A novel model to evaluate membrane pore size distribution by bubble gas transport method [1]

[1] The content of this chapter has been published in: A reverse approach to evaluate membrane pore size distribution by the bubble gas transport method using fewer experimental data points, Desalination. 518 (2021) 115287.

3.1. Abstract

Membrane technologies have been successfully developed as a promising approach for separation and purification in chemical engineering fields. Membrane distillation (MD), reverse osmosis (RO), nanofiltration (NF), ultrafiltration (UF) and microfiltration (MF) are some of the common separation processes for all of which membrane pore size plays a critical role in the efficiency of process. Besides, pore size distribution (PSD) is another parameter significantly affecting the separation performance. For instance, narrowing PSD mitigates pore wetting risk in MD membranes, a phenomenon that can result in the failure of MD. In this study, a novel mathematical model is presented to evaluate PSD. Unlike the conventional approach, this method starts from the assumption of a distribution function, typically Gaussian normal distribution, for the PSD, based on which a flow rate versus pressure curve is drawn theoretically. Then, the mean pore size and standard deviation of the PSD are optimized by the best fit of the theoretical curve to the experimental data by nonlinear regression. A unique feature of the proposed model is that much fewer experimental data points are required to find the best fit PSD. In addition, lack of need for a dry test experiment is another advantage of this model. The PSDs estimated by this model for three different membranes were compared with those presented in the literature, and a close agreement was observed.

3.2. Introduction

Membranes have found their own place in chemical technologies and can be utilized in a wide range of applications. Separation is one of the membrane applications where the objective is to allow one component of a mixture to pass through the membrane whereas preventing the penetration of other components [1]. The pressure-driven membrane separation processes are

usually classified into reverse osmosis (RO), nanofiltration (NF), ultrafiltration (UF) and microfiltration (MF), according to the pore size at the active surface layer of the membrane. The range of the pressure applied to the feed solution and the size of the solute rejected by the membrane largely depend on the pore size [2]. As well, in membrane distillation (MD), the flux and liquid entry pressure (LEP) are governed by the pore size of the MD membrane. Depending on the Knudsen number, Kn, (or in other words, pore size) the vapor transport inside the pore follows the Knudsen flow, viscous model, ordinary-diffusion model, or combination thereof [3]. In addition to determining the governing equation, pore radius can affect the flow rate of vapor passing through a membrane in a specific flow region. For instance, the vapor transport governed by Knudsen flow (with the unit of kg/s) is proportional to pore radius with the power of 3 [4]. Besides, LEP can be estimated by the Young-Laplace model, according to which pore size has an inverse relationship with LEP [5,6]. Also, it is worth mentioning that narrowing the pore size distribution (PSD) mitigates pore wetting risk, a phenomenon that is not desirable in MD [7]. To sum up, it is extremely important to measure the membrane pore size and PSD.

A number of methods to measure the pore size have been so far proposed, including microscopic method [8], gas permeability method [9], bubble gas transport method [10], mercury porosimetry [11], evapoporometry [12], and thermoporometry [13]. Each technique has its own benefits and drawbacks.

Amongst those, the bubble gas transport method is often used due to its simplicity. This method was first invented by Bechhold in 1908 [14] as the bubble point method to measure the largest pore of the membrane. It was later modified as the bubble gas transport method that allowed the measurement of PSD, described in detail by Kesting in his book of 1972 [15]. Currently, it is known as ASTM F316-03,2011 [16], and the equipment has been commercialized [17,18].

In this technique, the pressure required to blow gas through a wet membrane is measured. When the membrane is wetted, the top of the membrane is in contact with a liquid that fills all the pores of the membrane. The other side of the membrane, on the other hand, is in contact with gas. When the pressure of gas is progressively increased, the gas flow rate increases [2]. Figure 3-1 illustrates the schematic of the setup used for this method for measuring the PSD of hollow fiber membranes. By using this technique, the trend of change in flow rate versus gas pressure, typically shown in Figure 3-2, is obtained experimentally. Often, the gas flow rate through the dry membrane (all pores are unfilled with liquid) is also obtained. Figure 3-2 illustrates gas permeation through pores of a wet membrane: (a) all pores are wetted, and no gas molecule passes through the pores, (b) only gas bubble passes through the largest pore; this point is called bubble point, (c) in this stage, gas flows through some pores, and still some small pores are filled with liquid, and (d) from this point, the gas passes through all the pores. Figure 3-3 exhibits these four stages schematically.

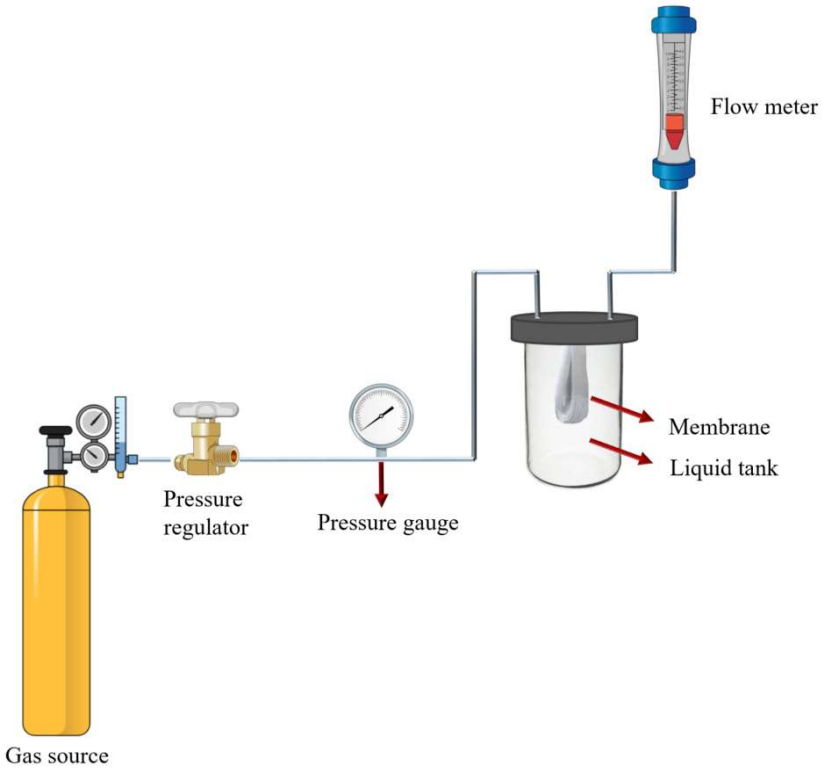

Figure 3-1 The schematic of the setup used for measuring the PSD of hollow fiber membranes.

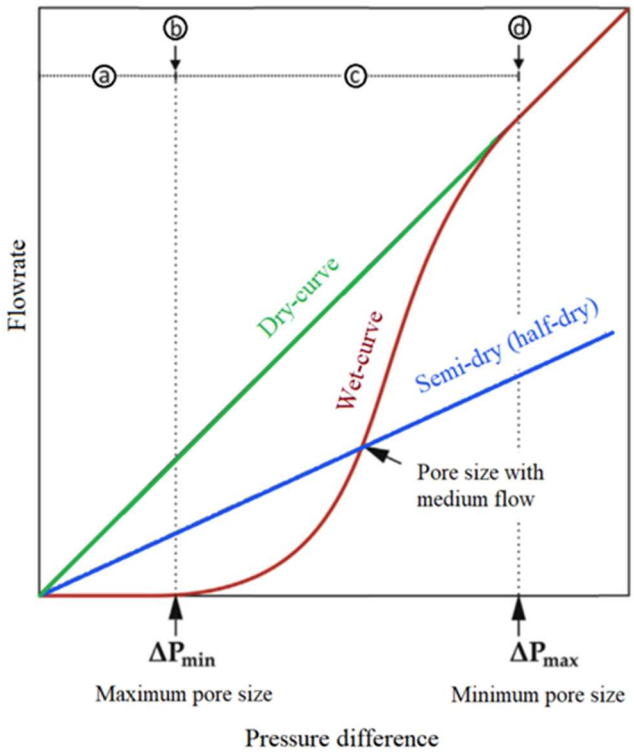

Figure 3-2 Flow rate versus gas pressure curve obtained by the bubble gas transport method.

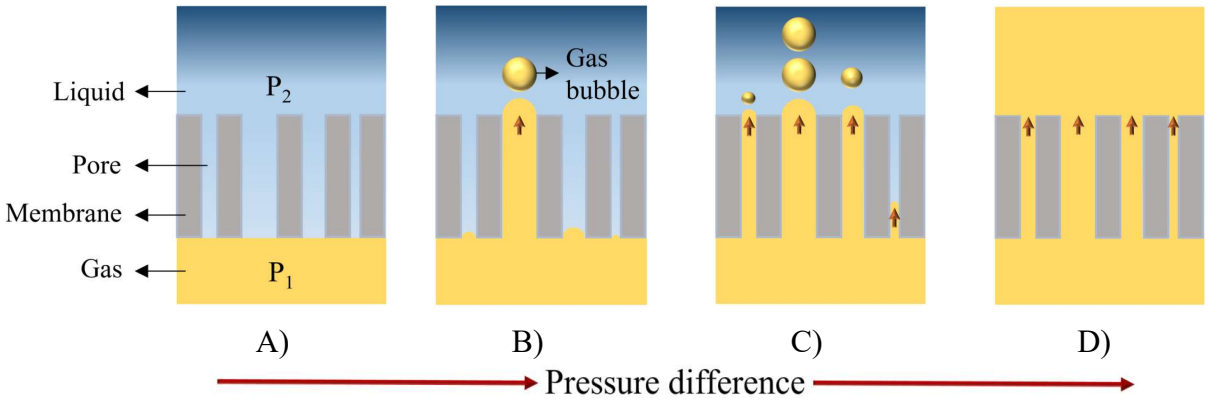

Figure 3-3 Different stages of gas permeation through a membrane using the bubble gas transport method, corresponding to the steps of Figure 3-2: A) all pores are wet, B) only gas passes through the largest pore, C) some pores are wet, while others contain gas, and D) from this point, gas passes through all the pores.

The flow rate versus applied pressure curve is then analyzed as follows [19]. The molar gas flow rate, J (mol/m^2 s), through a single circular pore, considering both Knudsen and viscous flows, is given by:

$$J(r) = \frac{1}{RT\tau\delta}\left[\frac{2}{3}r\left(\frac{8RT}{\pi M}\right)^{1/2} + \frac{\bar{p}r^2}{8\eta_g}\right]\Delta p \tag{3.1}$$

where R (J/mol K), T (K), τ (-), and δ (m) are gas constant, temperature, tortuosity, and membrane thickness, respectively. Also, r (m), $\bar{p}$ (Pa), η_g (Pa s), Δp (Pa) are pore radius, average pressure in the pore, gas viscosity, pressure difference across the membrane pore, respectively. M (kg/mol) is molecular weight.

Approximating the PSD function by a discrete distribution with m classes, the ith class has a radius of:

$$\Delta r(i) = r(i-1) - r(i) \tag{3.2}$$

where $r(i)$ is the smallest open pore radius when pressure $\Delta p(i)$ is applied, both related to each other by the Young-Laplace equation:

$$r(i) = \frac{2\sigma\cos}{\Delta p(i)} \tag{3.3}$$

where σ (N/m) is surface tension, and θ (°) is the contact angle. Taking account Eq. 3.1, the molar flux at pressure $\Delta p(j)$ is given by:

$$\frac{J(j)}{\Delta p(j)} = \frac{\pi}{RT\tau\delta}\sum_{i=1}^{j}\left[\frac{2}{3}r(i)^3N(i)\left(\frac{8RT}{\pi M}\right)^{1/2} + \frac{r(i)^4N(i)\bar{p}(j)}{8\eta_g}\right] \tag{3.4}$$

Hence, the number of pores per unit of area, $N(j)$ (m^{-2}), with radius between $r(j-1)$ and $r(j)$ is expressed as:

$$\frac{N(j)}{\tau\delta} = \frac{\frac{J(j)}{\Delta p(j)} - \sum_{i=1}^{j-1}\left[\frac{2\pi}{3RT}\left(\frac{8RT}{\pi M}\right)^{1/2} r(i)^3 + \frac{\pi r(i)^4 \bar{p}(j)}{8\eta_g RT}\right]\frac{N(i)}{\tau\delta}}{\frac{2\pi}{3R}\left(\frac{8RT}{\pi M}\right)^{1/2} r(j)^3 + \frac{\pi r(j)^4 \bar{p}(j)}{8\eta_g RT}} \tag{3.5}$$

where $j = 1 \ldots$ m.

Using $\frac{N(j)}{\tau\delta}$ so obtained, PSD, total number of pores and superficial porosity can be calculated.

1) The PSD is calculated by:

$$\frac{1}{\tau\delta}\frac{dN(j)}{dr(j)} = \frac{\frac{N(j)}{\tau\delta}}{r(j-1) - r(j)} \tag{3.6}$$

2) The total number of pores per unit of area, N_T (m^{-2}):

$$\frac{N_T}{\tau\delta} = \sum_{i=1}^{m} \frac{N(i)}{\tau\delta} \tag{3.7}$$

3) The superficial porosity, ε_s (-):

$$\frac{\varepsilon_s}{\tau\delta} = \sum_{i=1}^{m} \pi r(i)^2 \frac{N(i)}{\tau\delta} \tag{3.8}$$

An improved procedure was proposed by Khayet *et al*. [20]. By their method, flow rate versus pressure curve is generated at dry and wet conditions. The ratio of the wet and dry flow rates (J_w and J_d, respectively) through the pores that are smaller than the pore diameter $d_p(j)$ is used to define g_a function:

$$g_a(j) = 1 - g'_a(j) = 1 - \frac{J_w(j)}{J_d(j)} \tag{3.9}$$

The incremental flow rate ratio occurring through the j^{th} pore is:

$$g_d(j) = \frac{g'_a(j+1) - g'_a(j-1)}{2} \tag{3.10}$$

Since the flow rate through a pore is proportional to the cross-sectional area of this particular pore, the number of the j^{th} pore with the diameter of $d_p(j)$ is:

$$n(j) = K \frac{g_d(j)}{d_p(j)^2} \tag{3.11}$$

where

$$K = \frac{g_a(n)}{\sum_{j=1}^{n} \frac{g_d(j)}{d_p(j)^2}} \tag{3.12}$$

And the cumulative distribution of number of pores is:

$$n_a(j) = \sum_{k=1}^{j} n_d(k) \tag{3.13}$$

The PSD so obtained is further fitted to an appropriate distribution function. Often, a line with a half slope of the dry experiment is drawn and its intersection with the wet experiment (see Figure 3-2) is used to obtain the pore size that corresponds to the medium flow rate.

Thus, both methods are based on drawing the flow rate versus pressure curve and further mathematical manipulation. Therefore, schematically, these techniques are described from top to bottom in Figure 3-4A.

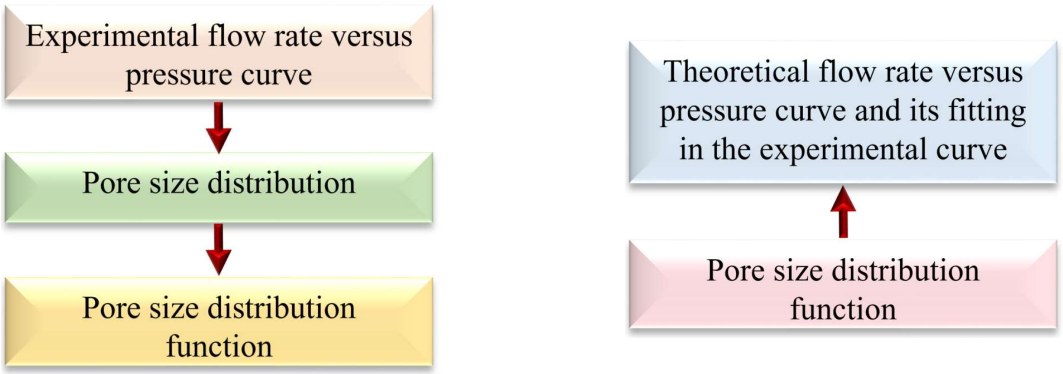

Figure 3-4 Comparison between the steps of A) the conventional and B) the proposed approach.

Even though the bubble gas transport technique is fast, simple, repeatable, and inexpensive, it is not free from criticisms. While Piatkiewicz *et al*. reported that contact angle does not influence the determination of PSD [21], other researchers detected the effect of the contact angle and said that by ignoring its effect, the pore sizes are overestimated [2,22]. Some commercial products were therefore developed to solve this problem. For example, Coulter Porofilm forms a meniscus of zero contact angle for many materials, so that cos $\theta = 1$ and the following Cantor's equation can be used instead of the Young-Laplace equation [2]:

$$\Delta p = \frac{2\sigma}{r} \tag{3.14}$$

Cantor's equation then tells that the pressure required for the displacement of liquid by gas is lowered by lowering the surface tension of the liquid, which protects the membrane from compaction and damage. Coulter Porofilm has a surface tension of only 16 mN/m compared to 72.8 mN/m of water [19].

The rate of pressure increase in the bubble gas transport experiment is another factor that may influence the evaluation of the pore size. A slow pressure increase is desirable to minimize such effect. One of the most serious criticisms is the mechanism of gas transport in the capillary pore. It is known that the capillary flow mechanism depends on the Knudsen number, Kn, which is the ratio of the mean free path, λ (m), to the pore size, d_p (m), where λ is the average distance that a molecule travels between two successive collisions, given by [20,23,24]:

$$\lambda = \frac{1}{\pi\sqrt{2}} \frac{kT}{p d_g^2} \tag{3.15}$$

where k (J K^{-1}) is Boltzmann constant, p (pa) is pressure inside the pore, and d_g (m) is collision diameter.

A novel approach is proposed in this work. Unlike the conventional approach, this approach is from the bottom to the top as described in Figure 3-4B, i.e. we first assume a distribution function for the PSD and then produce a flow rate versus pressure curve theoretically based on such a distribution. Typically, the distribution function is either Gaussian normal distribution or log-normal distribution with the mean value and standard deviation as two characterizing parameters, but any other models, including multimodal distributions, can be used. The theoretical curve fitting in the experimental data is examined by changing the PSD parameters (i.e. mean pore size and standard deviation), and the parameters that allow the best fit are chosen by the nonlinear regression analysis. Finally, PSD curves, either in the probability density or cumulative form, can be drawn. The new approach has several advantages over the conventional methods, including i) This approach eliminates the necessity of the dry permeation experiment that is required in the method proposed by Khayet *et al*. [20]. ii) This approach reduces the number of experimental points required to draw the PSD curves. A small number of experimental points are enough to achieve the PSD function according to the new approach. iii) The new approach allows the comparison of different membranes by the mean pore size and the standard deviation generated for a given distribution function.

The objective of this work is, therefore, to develop a mathematical model that allows producing the theoretical flow rate versus pressure curve and then examine the theoretical curve fitting, by nonlinear regression, in the experimental data that were recorded in the literature. As a result, the best fit PSD can be found.

3.3. Model development

Assuming Poiseuille equation, the volumetric flow rate (m^3/s) of a compressible ideal gas in the isothermal condition is calculated by [25, 26]:

$$Q_v = \frac{\pi r^4}{16\eta_g \delta} \times \frac{(p_i^2 - p_e^2)}{p_e} \tag{3.16}$$

where η_g (Pa s), and δ (m) are viscosity of gas (air in this work), and membrane thickness, respectively. p_i (Pa) and p_e (Pa) are the pressures at the pore inlet and exit, respectively. The molar flow rate (mol/s) at pore exit is calculated by:

$$Q = Q_v \times \frac{p_e}{RT} \tag{3.17}$$

Therefore,

$$Q = \frac{\pi r^4}{16\eta_g \delta} \times \frac{(p_i^2 - p_e^2)}{p_e} \times \frac{p_e}{RT} = \frac{\pi r^4}{16\eta_g \delta} \times \frac{(p_i^2 - p_e^2)}{RT} \tag{3.18}$$

where R (J mol^{-1} K^{-1}) and T (K) are universal gas constant and temperature, respectively. Between the applied air pressures p_0 and $p_1 = p_0 + h$, where h is small increment of pressure, the pores of radii between r_0 and r_1 are opened. r_0 and r_1 can be calculated by the following equations:

$$r_0 = \frac{2\sigma \cos}{p_0} \tag{3.19}$$

$$r_1 = \frac{2\sigma \cos}{p_1} \tag{3.20}$$

It should be noted that the pore of radius r_0 is opened when the pressure drop across the membrane becomes p_0. Therefore, p_0 is a gauge pressure and so is p_1.

The number of those pores, n_1, is equal to:

$$n_1 = n_T \int_{r_1}^{r_0} f\,(r)dr \tag{3.21}$$

where $f(r)$ is a distribution function such as normal distribution function and n_T (-) is the total number of pores. The integral form of the distribution function is called cumulative distribution function (CDF) and $\int_{r_1}^{r_0} f\,(r)dr$ is estimated by:

$$\int_{r_1}^{r_0} f\,(r)dr = CDF(r_0) - CDF(r_1) \tag{3.22}$$

Therefore, combining Eq. 3.21 and Eq. 3.22:

$$n_1 = n_T\big(CDF(r_0) - CDF(r_1)\big) \tag{3.23}$$

Considering the effect of tortuosity, τ (-), the rate of gas flow through these pores at pressure p_1 is therefore approximated by:

$$Q(p_1) = n_1 \times \frac{\pi(\frac{2\sigma}{p_0+h/2})^4}{16\eta_g\delta\tau RT} \times (p_i - p_e)(p_i + p_e) \tag{3.24}$$

$p_i - p_e$ is the pressure difference across the membrane pore, and both p_i and p_e are absolute pressure. Since p_0 and p_1 are gauge pressures and p_e is atmospheric pressure, $p_i - p_e$ is approximately equal to:

$$p_i - p_e = \frac{(p_0+p_1)}{2} = p_0 + \frac{h}{2} \tag{3.25}$$

Consequently $p_i + p_e$ is:

$$p_i + p_e = p_0 + \frac{h}{2} + 2p_e \tag{3.26}$$

Therefore,

$$Q_{n1}(p_1) = n_T\big(CDF(r_0) - CDF(r_1)\big) \times \frac{\pi(\frac{2\sigma}{p_0+h/2})^4}{16\eta_g\delta\tau RT} \times (p_0 + \frac{h}{2})(p_0 + \frac{h}{2} + 2p_e) \quad (3.27)$$

When the pressure is further increased from p_1 to $p_2 = p_1 + h$, the flow rate in the n_1 pores is:

$$Q_{n1}(p_2) = n_T\big(CDF(r_0) - CDF(r_1)\big) \times \frac{\pi(\frac{2\sigma}{p_0+h/2})^4}{16\ _g\delta\tau RT} \times (p_1 + \frac{h}{2})(p_1 + \frac{h}{2} + 2p_e) \quad (3.28)$$

Furthermore, the pores of radii from r_1 to r_2 are newly opened and their number, n_2, is:

$$n_2 = n_T\big(CDF(r_1) - CDF(r_2)\big) \quad (3.29)$$

The flow rate through n_2 pores is:

$$Q_{n2}(p_2) = n_T\big(CDF(r_1) - CDF(r_2)\big) \times \frac{\pi(\frac{2\sigma}{p_1+h/2})^4}{16\eta_g\delta\tau RT} \times (p_1 + \frac{h}{2})(p_1 + \frac{h}{2} + 2p_e) \quad (3.30)$$

Therefore, the total flow rate at pressure p_2 is calculated by:

$$Q(p_2) = Q_{n1}(p_2) + Q_{n2}(p_2) = n_T\big(CDF(r_0) - CDF(r_1)\big) \times \frac{\pi(\frac{2\sigma}{p_0+h/2})^4}{16\eta_g\delta\tau RT} \times (p_1 + \frac{h}{2})(p_1 + \frac{h}{2} +$$

$$2p_e) + n_T\big(CDF(r_1) - CDF(r_2)\big) \times \frac{\pi(\frac{2\sigma}{p_1+h/2})^4}{16\ _g\delta\tau RT} \times (p_1 + \frac{h}{2})(p_1 + \frac{h}{2} + 2p_e) = n_T\Big\{\big(CDF(r_0) -$$

$$CDF(r_1)\big) \times \frac{\pi(\frac{2\sigma}{p_0+h/2})^4}{16\eta_g\delta\tau RT} + \big(CDF(r_1) - CDF(r_2)\big) \times \frac{\pi(\frac{2\sigma}{p_1+h/2})^4}{16\eta_g\delta\tau RT}\Big\} \times (p_1 + \frac{h}{2})(p_1 + \frac{h}{2} + 2p_e) \quad (3.31)$$

With a similar approach, $Q(p_n)$ is estimated by:

$$Q(p_n) = n_T \sum_{i=1}^{n}\Big\{\big(CDF(r_{i-1}) - CDF(r_i)\big) \times \frac{\pi(\frac{2\sigma}{p_{i-1}+h/2})^4}{16\eta_g\delta\tau RT}\Big\} \times (p_{n-1} + \frac{h}{2})(p_{n-1} + \frac{h}{2} + 2p_e) \quad (3.32)$$

In the probability theory, a normal distribution (Laplace–Gauss or Gaussian distribution) is a type of continuous probability distribution according to which the probability density function is given as follows [27]:

$$f(r) = \frac{1}{\varsigma\sqrt{2\pi}} e^{-\frac{1}{2}(\frac{r-\mu}{\varsigma})^2} \tag{3.33}$$

where μ (m) is the mean of the distribution, and ς (m) is the standard deviation.

Let us assume there are *m* experimental data points, $(Q_1)_{exp}, (Q_2)_{exp}, \ldots, (Q_m)_{exp}$, corresponding to applied gauge pressures $p_1, p_2, \ldots, p_m$. To find the optimum μ and ς, mean absolute error (MAE) is minimized by nonlinear regression.

$$MAE = \frac{\sum_{i=1}^{m-1} \left| \left(\frac{Q_i}{Q_m}\right)_{model} - \left(\frac{Q_i}{Q_m}\right)_{exp} \right|}{m-1} \tag{3.34}$$

To calculate $(Q_1)_{model}, (Q_2)_{model}, \ldots, (Q_m)_{model}$, Eq. 3.32 is used. However, $\frac{n_T}{\delta\tau}$ is unknown in Eq. 3.32; therefore, Eq. 3.32 is rearranged to:

$$Q(p_n) = \frac{n_T}{\delta\tau} A(p_n) \tag{3.35}$$

where

$$A(p_n) = \sum_{i=1}^{n} \left\{ \left(CDF(r_{i-1}) - CDF(r_i)\right) \times \frac{\pi(\frac{2\sigma}{p_{i-1}+h/2})^4}{16\ gRT} \right\} \times (p_{n-1} + \frac{h}{2})(p_{n-1} + \frac{h}{2} + 2p_e) \tag{3.36}$$

Considering that $\frac{n_T}{\delta\tau}$ is constant:

$$\left(\frac{Q_i}{Q_m}\right)_{model} = \left(\frac{A_i}{A_m}\right)_{model} \tag{3.37}$$

From Eqs. 3.34 and 3.37, MAE is rearranged to:

$$MAE = \frac{\sum_{i=1}^{m-1}\left|\left(\frac{A_i}{A_m}\right)_{model} - \left(\frac{Q_i}{Q_m}\right)_{exp}\right|}{m-1} \tag{3.38}$$

After optimization of the distribution parameters, A_i is calculated using Eq. 3.36 and $\left(\frac{n_T}{\delta\tau}\right)_i$ is further calculated by dividing $(Q_i)_{exp}$ by A_i. The $\left(\frac{n_T}{\delta\tau}\right)_i$ values so calculated are averaged to obtain $\frac{n_T}{\delta\tau}$. Then, by knowing $\frac{n_T}{\delta\tau}$, μ and ς, flow rate, Q, as a function of pressure, p, is calculated, and Q versus p curve is drawn. In addition, the number of pores corresponding to each pore radius range can be calculated using the following equation:

$$\frac{n_i}{\delta\tau} = \frac{n_T}{\delta\tau}\left(CDF(r_{i-1}) - CDF(r_i)\right) \tag{3.39}$$

Hitherto, the model was developed considering the Poiseuille flow, i.e. only the second term of Eq. 3.1. In the following step, the model is built considering both terms of Eq. 3.1. The molar gas flow rate, Q (mol/s), through a single circular pore is calculated by multiplying Eq. 3.1 by the pore area (πr^2):

$$Q = \frac{\pi r^2}{RT\tau\delta}\left[\frac{2}{3}r\left(\frac{8RT}{\pi M}\right)^{1/2} + \frac{\bar{p}r^2}{8\eta_g}\right]\Delta p \tag{3.40}$$

With the same approach as that used for developing Eq. 3.32, $Q(p_n)$ is estimated by:

$$Q(p_n) = n_T\sum_{i=1}^{n}\left\{\left(CDF(r_{i-1}) - CDF(r_i)\right) \times \frac{2}{3}\frac{\pi\left(\frac{2\sigma}{p_{i-1}+h/2}\right)^3}{\delta\tau}\left(\frac{8}{\pi MRT}\right)^{1/2}\right\} \times \left(p_{n-1} + \frac{h}{2}\right) +$$

$$n_T\sum_{i=1}^{n}\left\{\left(CDF(r_{i-1}) - CDF(r_i)\right) \times \frac{\pi\left(\frac{2\sigma}{p_{i-1}+h/2}\right)^4}{16\eta_g\delta\tau RT}\right\} \times \left(p_{n-1} + \frac{h}{2}\right)\left(p_{n-1} + \frac{h}{2} + 2p_e\right) \tag{3.41}$$

When the Knudsen flow term is also considered.

It is obvious that at a particular pressure difference across the membrane, different pores of a membrane may face different flow types depending on the *Kn* number. Therefore, modeling should be carried out in accordance with selection of an appropriate equation for estimation of $Q(p_n)$ for each pore (selection between Eqs. 3.32 and 3.41) depending on the *Kn* number. Therefore, the final equation for estimation of flow rate using the developed model is the following piecewise function. The first sub-function of the following bracket corresponds to the transition region when Knudsen and Poiseuille flows take place simultaneously, while the second one corresponds to the Poiseuille (viscous) flow and the selection between these two sub-functions depends on the *Kn* number, which will be discussed in detail in the next section.

$$Q(p_n) = n_T \sum_{i=1}^{n} \begin{cases} \{B_i\} \times (p_{n-1} + \frac{h}{2}) + \{C_i\} \times (p_{n-1} + \frac{h}{2})(p_{n-1} + \frac{h}{2} + 2p_e), & 0.01 < Kn < 1 \\ \{C_i\} \times (p_{n-1} + \frac{h}{2})(p_{n-1} + \frac{h}{2} + 2p_e), & Kn < 0.01 \end{cases}$$

(3.42)

where

$$B_i = \left(CDF(r_{i-1}) - CDF(r_i)\right) \times \frac{2}{3} \frac{\pi(\frac{2\sigma}{p_{i-1}+h/2})^3}{\delta\tau} \left(\frac{8}{\pi MRT}\right)^{1/2} \tag{3.43}$$

$$C_i = \left(CDF(r_{i-1}) - CDF(r_i)\right) \times \frac{\pi(\frac{2\sigma}{p_{i-1}+h/2})^4}{16\eta_g \delta\tau RT} \tag{3.44}$$

Figure 3-5 illustrates the flowchart of the modeling algorithm.

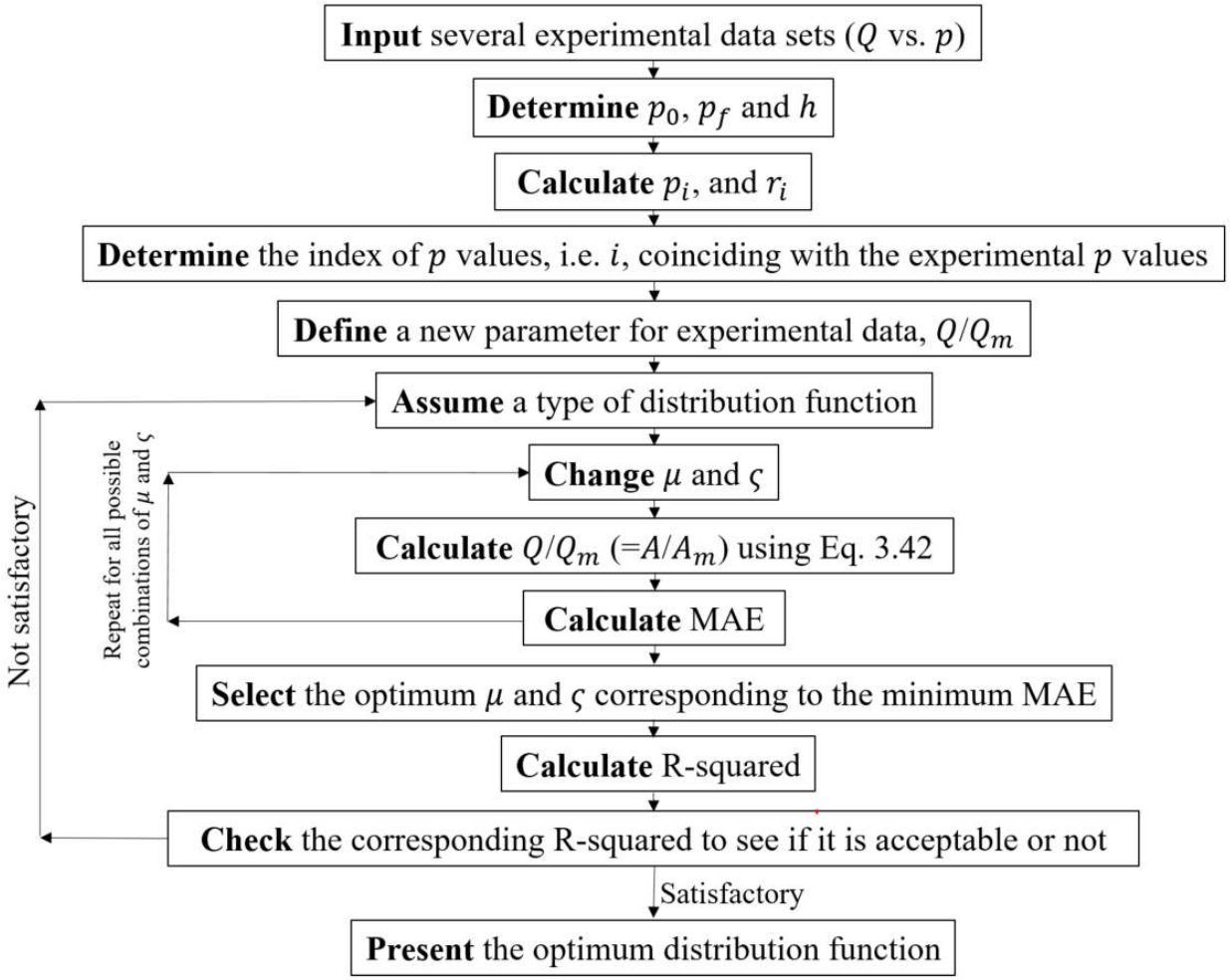

Figure 3-5 Flowchart of the proposed model for estimation of PSD.

3.4. Results and discussion

3.4.1. Nature of gas flow

To develop an appropriate model for the estimation of PSD, determining the nature of gas flow inside the pores is of great importance. The nature of flow inside the pore can be determined by comparing the membrane pore size with the mean free path of the gas molecule. A pressure difference across the membrane results in Poiseuille (in other words, viscous) flow, while the ordinary-diffusion flow becomes negligible, and if the molecule-molecule collisions exceed the

molecule-pore wall collisions, Poiseuille flow can justify the behaviour of the mass transfer inside the pore [28]. This type of flow, i.e. Poiseuille flow, is determined by $Kn < 0.01$ [29]. On the other hand, if the pore size of the membrane is smaller in comparison to the mean free path of the gas molecules ($Kn = \lambda/d_p > 1$), molecule-pore wall collisions surpass molecule-molecule collisions and the flow of gas inside the pores can be described using Knudsen flow [3]. For Kn numbers between those two mentioned ranges, both Knudsen and viscous flows contribute to the mass transfer of gas molecules through the pores.

The kinetic diameter of air molecules was calculated as the average value from the corresponding individual gases by Sonnick *et al*. as 0.36 nm [30]. Therefore, the mean free path of air molecules at the temperature of 25 ºC is calculated by:

$$\lambda = \frac{k_B T}{\sqrt{2}\pi {d_k}^2 p} = \frac{1.38064852\times10^{-23}\times298.15}{\sqrt{2}\pi(0.36\times10^{-9})^2 p} \tag{3.45}$$

where p (Pa) is the average and absolute pressure inside the pore. Since p_e is atmospheric pressure:

$$p = \frac{p_i + p_e}{2} = \frac{p_i + (1.013\times10^5)}{2} \tag{3.46}$$

Therefore, Kn is calculated by:

$$Kn = \frac{\lambda}{d_p} = \frac{1.38064852\times10^{-23}\times298.15}{\sqrt{2}\pi(0.36\times10^{-9})^2 p d_p} = \frac{7.1490457\times10^{-3}}{\frac{p_i + (1.013\times10^5)}{2} d_p} \tag{3.47}$$

As a result, pore diameter and the gas pressure at the pore entrance determine the behaviour of gas flow within the membrane pore when using the bubble gas transport method.

3.4.2. Comparison with the conventional approach

In order to evaluate the performance of the proposed model, the experimental results presented by Martinez *et al*. [19] have been employed, and the outcome of the developed model was compared with that of the conventional method of PSD determination using the bubble gas transport method. In the mentioned study [19], a Coulter Porometer II (produced by Coulter Electronics Ltd.) has been used. For this purpose, membranes were initially wetted by a liquid, Coulter Porofilm, with a very low surface tension of 0.016 Pa m, and assuming $\theta = 0\,°$ with nearly all types of material. Therefore, cos θ = 1 and Cantor's equation can be used instead of the Young-Laplace equation (Eq. 3.14 instead of Eqs. 3.19 and 3.20). In the next step, pressure (with the use of dry air at 25 ^{o}C) was gradually applied to the membranes which were wetted. The orientation of the membrane was selected in a way to have air flow from the active layer to the support layer. Three different hydrophobic membranes (commercial membranes), including TF1000, TF450 and TF200 were tested in terms of PSD. These membranes had two layers, an active layer made of Polytetrafluoroethylene (PTFE), and a support layer made of Polypropylene (PP). Since the pores of the support layer were very large (around 500 μm) in comparison to the active layer, the pressure drop across the support layer was neglected.

According to Eq. 3.47, Kn was between 0.01 and 1 under all circumstances considered in this work, with the minimum Kn of 0.04 that corresponds to the maximum pressure and pore diameter. Therefore, only the first sub-function of Eq. 3.42 was employed. However, considering that the minimum Kn is close to 0.01, further increase in pressure or pore diameter may result in passing into the Poiseuille flow region.

The modeling was carried out in MATLAB environment in accordance with Figure 3-5, showing the modeling algorithm. For each membrane, the modeling was performed using only four data

sets, one of which is related to zero flow rate ($Q = 0$). Each data set contained pressure and the corresponding flow rate ([*p, Q*]). The data sets were chosen randomly from Q versus p graphs of the reference paper. p_0 and p_f refer to the initial and final pressure, respectively, between which the modeling was carried out. $p_0=0$ and $p_f=5$ bar can be considered a good choice for many membranes. However, in the case of membranes with very small pores that need high pressure, p_f can be increased to the desired pressure. Given the numerical nature of this modeling, continuous functions, equations and variables were transferred into discrete counterparts. Discretization of pressure, p, was done with the mesh size of h. h should be small enough in a way that the discretized pressures close enough to the experimental pressures can be found in the range between p_0 and p_f. Also, h should be small enough not to affect the computed results. On the other hand, it is obvious that reduction in the mesh size of h increases the time required for calculation largely.

The distribution function parameters, i.e. mean of the distribution (μ), and standard deviation (ς), were determined by minimizing the MAE through nonlinear regression, which is widely employed in optimization processes in chemical engineering fields [31, 32]. In statistics, the 68- 95- 99.7 rule (three-sigma rule) expresses that 68%, 95% and 99.7% of the values obtained by a normal distribution are within $\mu \pm \varsigma$, $\mu \pm 2\varsigma$ and $\mu \pm 3\varsigma$, respectively [33, 34]. Considering that all pore radii should have a positive value, $\mu - 3\varsigma > 0$. This constriction reduced the number of μ and ς combinations to a large extent, decreasing the time of calculations. In addition to the mentioned method, other optimization algorithms such as genetic algorithm can be applied for this purpose. Table 3-1 illustrates the specifications of the optimum distribution functions fitted to experimental data. As shown in this table, the values of R^2 are almost equal to 1, meaning that the predicted data points agree with the experimental ones very well.

Table 3-1 Mean of the distribution (μ) and standard deviation (ς) of the optimum distribution functions.

Membrane	**TF1000**	**TF450**	**TF200**
Mean of the distribution (μ)	3.3×10^{-7} m	2.4×10^{-7} m	1.6×10^{-7} m
Standard deviation (ς)	1.7×10^{-8} m	1.1×10^{-8} m	1.2×10^{-8} m
R^2	0.9964	0.9998	0.9962
MAE	0.0184	0.0046	0.0179

By knowing the values of μ and ς, and employing Eq. 3.33, the probability density can be calculated at different pore radii. Figure 3-6 shows the probability density function for these three membranes obtained by μ and ς values presented in Table 3-1.

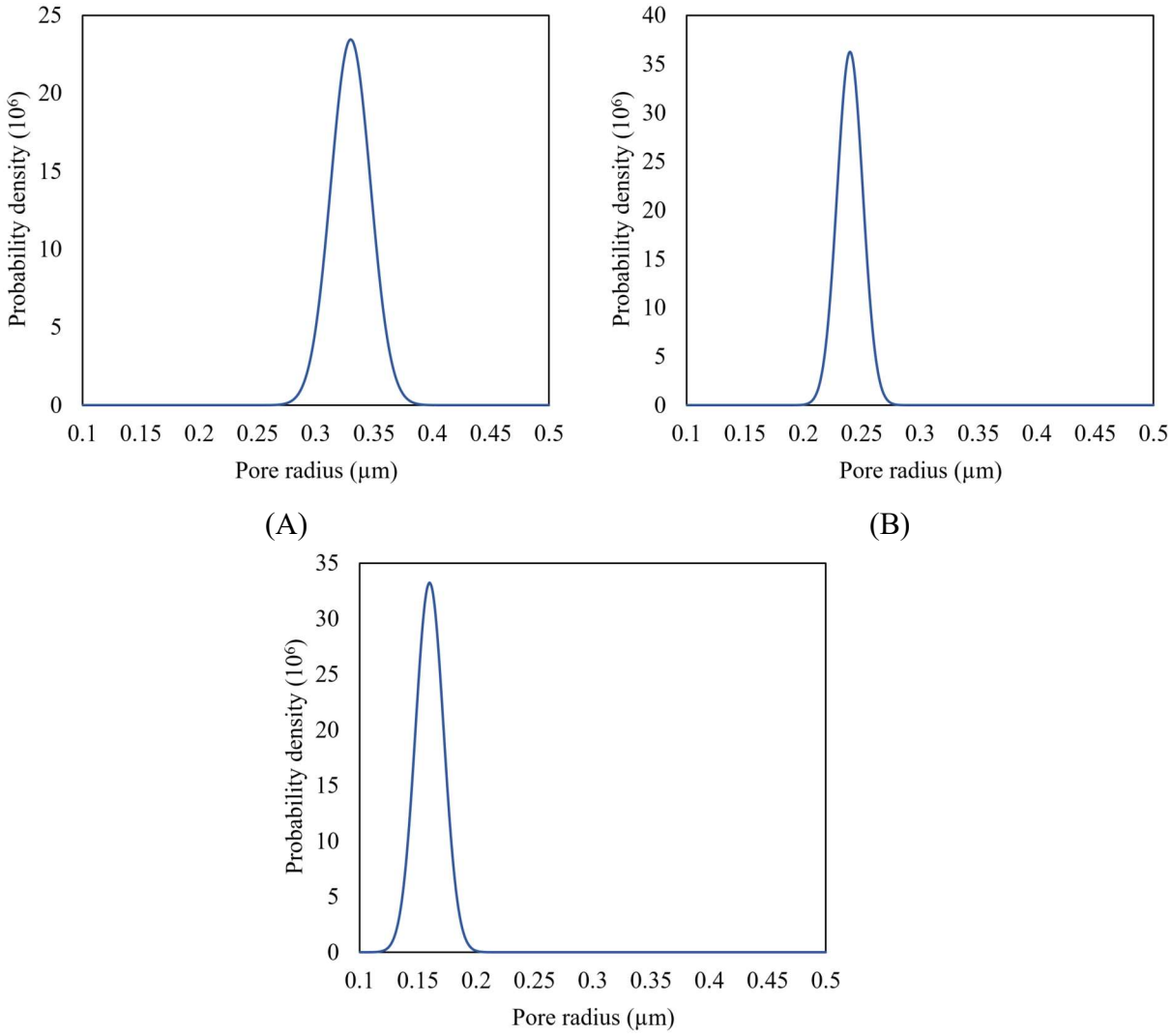

Figure 3-6 Probability density function for A) TF1000, B) TF450 and C) TF200.

The area trapped under all three figures (Figure 3-6) is equal to 1. However, in the reference paper, $\frac{dN}{dr}\frac{1}{\tau\delta}$ (m^{-4}) was used instead of the probability density function for y-axis. To reproduce the y-axis data, the following equation was used:

$$\frac{dN}{dr}\frac{1}{\tau\delta} = \left(\frac{N}{\delta\tau}\right)_m \frac{\left(CDF(r_{i-1}) - CDF(r_i)\right)}{r_{i-1} - r_i} \tag{3.48}$$

where $(\frac{N}{\delta\tau})_m$ is the number of pores per unit of area (m^{-2}) divided by membrane thickness (m) times tortuosity (-), provided by the manufacturer of membranes. The values of this parameter are 3.35×10^{16}, 5.1×10^{16}, and 10.5×10^{16} m^{-3} for TF1000, TF450, and TF200, respectively. Figure 3-7 illustrates the distribution of membrane pore radii in terms of $\frac{dN}{dr}\frac{1}{\tau\delta}$ versus pore radius for both experimental and calculated values. Their agreement is excellent. Again, it is worth mentioning that the dash-line graphs were reproduced by the model, and the model was developed using only four experimental data points, whereas the conventional one was based on many experimental data points. Figure 3-8 displays the flow rate versus pressure graphs obtained by the model calculation and the experiments. Again, their agreement is excellent. The unit of flow rate obtained by the model was mol/s and was converted to l(STP)/min (22.4 l(STP) ~ 1mol).

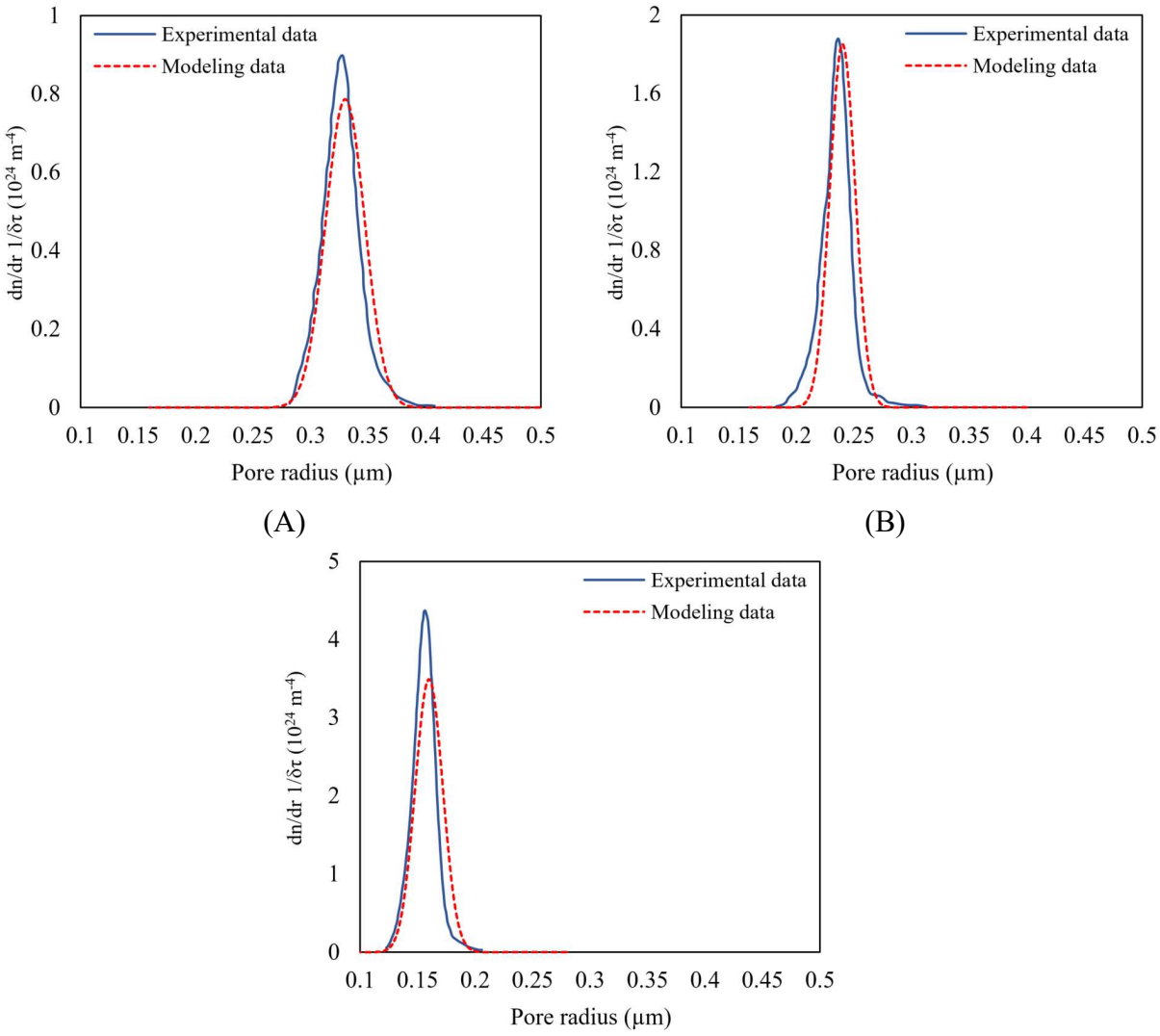

Figure 3-7 Comparison between the PSD obtained by the conventional method [19] and the ones reproduced by the developed model for A) TF1000, B) TF450 and C) TF200.

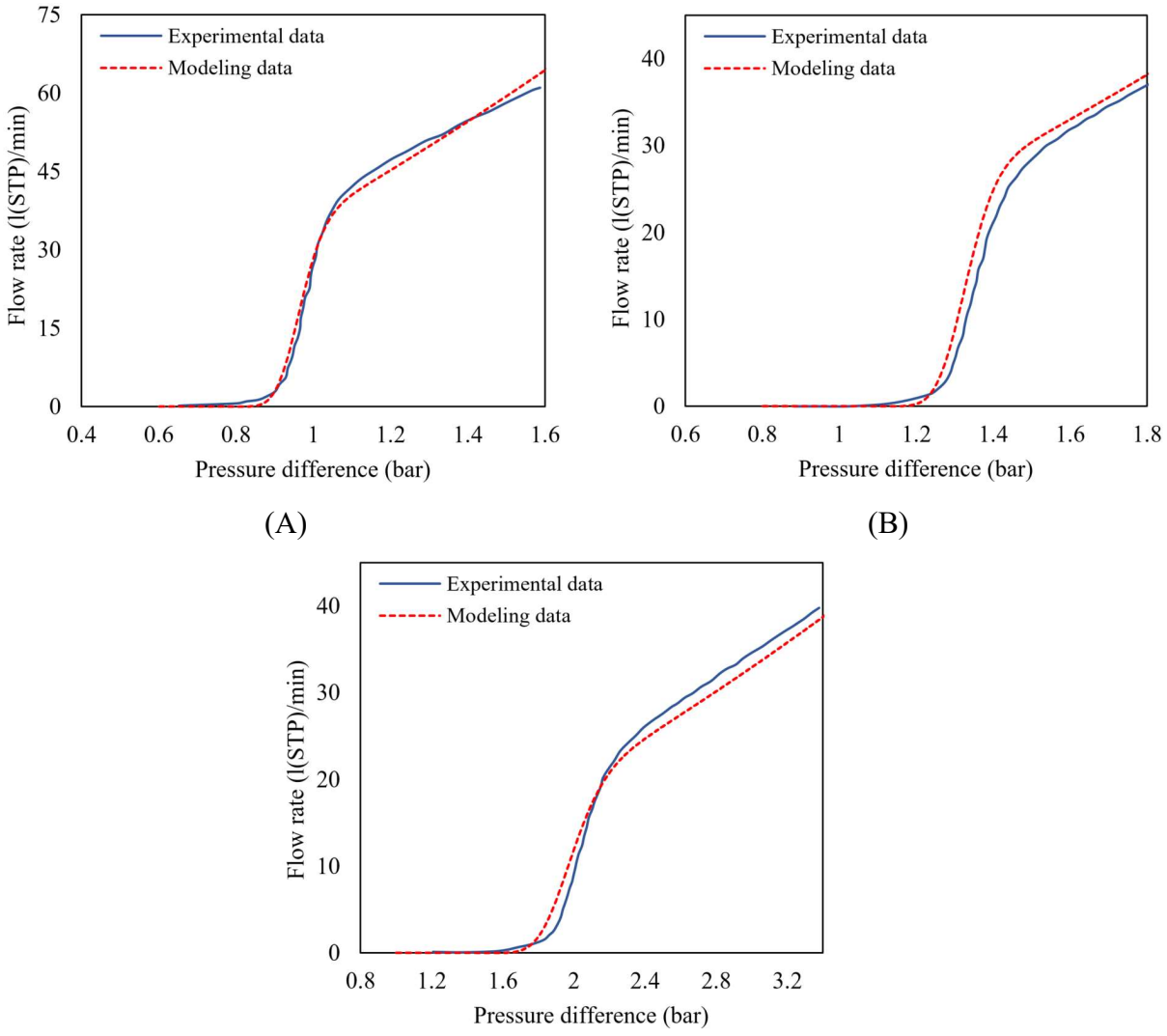

Figure 3-8 Gas flow rate versus pressure difference obtained by Coulter Porometer [19] and the developed model for A) TF1000, B) TF450 and C) TF200.

Herein, the most common distribution function for membrane PSD, i.e. normal distribution, was employed, and the results were satisfactory. In the case of unsuccessful modeling with normal distribution, other distribution functions such as log-normal distribution or even bimodal distribution can be tested. The modeling procedure is exactly the same as that of normal distribution, and the only difference is related to the distribution function itself. For instance, the

log-normal distribution, which is a function whose logarithm has a normal distribution, is as follows:

$$f(r) = \frac{1}{r\varsigma\sqrt{2\pi}} e^{-\frac{1}{2}\left(\frac{\log r-\mu}{\varsigma}\right)^2} \tag{3.49}$$

3.4.3. Advantages of the proposed model

The main advantage of the proposed model for the estimation of PSD is the small number of data points required to be recorded. As already stated, only with four experimental data points, the PSD of membranes was estimated with a very close agreement with that of the conventional technique, which usually requires many data points [19, 20]. Let us express its importance with an example. In the adsorption process of an aqueous solution, researchers usually collect only a few data sets ([adsorption capacity, time]), not all data sets, and try to fit those few data sets to kinetic equations. The kinetic equation, which has the best fitting to the experimental data, is used to describe the kinetic behaviour of the adsorption process. This reduces the time, energy and cost of recoding unnecessary data sets. Besides, unlike the previous technique [19], this model selects the governing equation of gas flow based on the *Kn* number for each individual pore diameter and pressure combination. As another advantage, this technique does not require data of gas flux through dry membrane.

3.5. Conclusion

Estimation of membrane PSD is of great significance in the membrane processes. For instance, in MD membranes, even a small portion of large pores may result in pore wetting and failure of MD. Therefore, evaluation of PSD for MD membrane and selection of a membrane with narrow PSD is desired. In this study, a model (a piecewise function with two sub-functions) was developed for

the estimation of PSD. The basis of this model is minimizing the mean absolute error using nonlinear regression. PSD of three commercial membranes was estimated by this method in a very close agreement with the conventional approach. This model is intelligent and selects the appropriate sub-function of the developed piecewise function by calculation of Knudsen number, Kn, for all pore size and pressure combinations, although, for these three membranes, the minimum Kn was more than 0.01 and only the first sub-function was employed. Therefore, the behaviour of gas flow inside the pores of these membranes could be predicted by the combination of Knudsen and Poiseuille flows. A low number of data points required to be recorded and lack of need for a dry test experiment are advantages of this method in comparison to the conventional techniques. In this study, the focus was placed on the liquid-gas systems of PSD. As future research, a model can be developed for other systems, including liquid-liquid systems.

3.6. References

[1] R.W. Baker, Membrane Technology and Applications, 2nd ed., Wiley, 2004.

[2] I.G. Wenten, K. Khoiruddin, A.N. Hakim, N.F. Himma, The Bubble Gas Transport Method, in: N. Hilal, A.F. Ismail, T. Matsuura (Eds.), Membr. Charact., Elsevier, Amsterdam, 2017: pp. 199–218.

[3] M.R. Qtaishat, T. Matsuura, Modelling of pore wetting in membrane distillation compared with pervaporation, in: Pervaporation, Vap. Permeat. Membr. Distill. Princ. Appl., Elsevier Ltd, 2015: pp. 385–413. doi:10.1016/B978-1-78242-246-4.00013-1.

[4] H. Chamani, T. Matsuura, D. Rana, C.Q. Lan, Modeling of pore wetting in vacuum membrane distillation, J. Membr. Sci. 572 (2019) 332–342. doi:10.1016/j.memsci.2018.11.018.

[5] H. Chamani, P. Yazgan-Birgi, T. Matsuura, D. Rana, M.I. Hassan Ali, H.A. Arafat, C.Q. Lan, CFD-based genetic programming model for liquid entry pressure estimation of hydrophobic membranes, Desalination. 476 (2020) 114231. doi:10.1016/j.desal.2019.114231.

[6] B.-S. Kim, P. Harriott, Critical entry pressure for liquids in hydrophobic membranes, J. Colloid Interface Sci. 115 (1987) 1–8.

[7] B.S. Lalia, E. Guillen, H.A. Arafat, R. Hashaikeh, Nanocrystalline cellulose reinforced PVDF-HFP membranes for membrane distillation application, Desalination. 332 (2014) 134–141. doi:10.1016/j.desal.2013.10.030.

[8] L. Zeman, L. Denault, Characterization of microfiltration membranes by image analysis of electron micrographs. Part I. Method development, J. Membr. Sci. 71 (1992) 221–231. doi:10.1016/0376-7388(92)80207-Z.

[9] H. Yasuda, J.T. Tsai, Pore size of microporous polymer membranes, J. Appl. Polym. Sci. 18 (1974) 805–819. doi:10.1002/app.1974.070180316.

[10] G. Capannelli, F. Vigo, S. Munari, Ultrafiltration membranes - characterization methods, J. Membr. Sci. 15 (1983) 289–313. doi:10.1016/S0376-7388(00)82305-4.

[11] J.I. Calvo, A. Hernández, P. Prádanos, L. Martínez, W.R. Bowen, Pore size distributions in microporous membranes II. Bulk characterization of track-Etched filters by air porometry and mercury porosimetry, J. Colloid Interface Sci. 176 (1995) 467–478. doi:10.1006/jcis.1995.9944.

[12] E. Akhondi, F. Zamani, J. W. Chew, W. B. Krantz, A. G. Fane, Improved design and protocol for evapoporometry determination of the pore-size distribution, J. Membr. Sci. 496 (2015) 334-343. doi: 10.1016/j.memsci.2015.09.013.

[13] M. Brun, A. Lallemand, J.F. Quinson, C. Eyraud, A new method for the simultaneous determination of the size and shape of pores: the thermoporometry, Thermochim. Acta. 21 (1977) 59–88. doi:10.1016/0040-6031(77)85122-8.

[14] H. Bechhold, Durchlässigkeit von ultrafiltern, Zeitshrift Fűr Phys. Chemie. 64 (1908) 328.

[15] R.E. Kesting, Synthetic Polymer Membranes, McGraw Hill, New York, NY, 1972.

[16] ASTM, Standard test methods for pore size characteristics of membrane filters by bubble point and mean flow pore test, 2011.

[17] https://www.medisca.com/Pages/ProductDetails.aspx?StockCode=7110&C=EQ&C4=197.

[18] https://www.utwente.nl/en/tnw/emi/characterisation/porometry/.

[19] L. Martínez, F.J. Florido-Díaz, A. Hernández, P. Prádanos, Characterisation of three hydrophobic porous membranes used in membrane distillation: Modelling and evaluation of their water vapor permeabilities, J. Membr. Sci. 203 (2002) 15–27. doi:10.1016/S0376-7388(01)00719-0.

[20] M. Khayet, A. Velázquez, J.I. Mengual, Modelling mass transport through a porous partition: Effect of pore size distribution, J. Non-Equilibrium Thermodyn. 29 (2004) 279–299. doi:10.1515/JNETDY.2004.055.

[21] W. Piatkiewicz, S. Rosiński, D. Lewińska, J. Bukowski, W. Judycki, Determination of pore size distribution in hollow fibre membranes, J. Membr. Sci. 153 (1999) 91–102. doi:10.1016/S0376-7388(98)00243-9.

[22] C. Cosentino, F. Amato, M. Ferrari, Characterization Methods for Quality Control of Nanopore and Nanochannel Membranes, in: BioMEMS Biomed. Nanotechnol., Springer US, 2007: pp. 203–225. doi:10.1007/978-0-387-25842-3_7.

[23] A.K. Thakur, I.M. Hsieh, M.R. Islam, B. Lin, C.C. Chen, M. Malmali, Performance of sweeping gas membrane distillation for treating produced water: Modeling and experiments, Desalination. 492 (2020) 114597. doi:10.1016/j.desal.2020.114597.

[24] K.H. Lee, S.T. Hwang, The transport of condensible vapors through a microporous vycor glass membrane, J. Colloid Interface Sci. 110 (1986) 544–555. doi:10.1016/0021-9797(86)90407-8.

[25] H. Chamani, T. Matsuura, D. Rana, C.Q. Lan, Transport characteristics of liquid-gas interface in a capillary membrane pore, J. Membr. Sci. 611 (2020) 118387. doi:10.1016/j.memsci.2020.118387.

[26] J.D. Current, Physics Related to Anesthesia, Pedia Press, 2010.

[27] S. Du, W. Yu, Two-dimensional network simulation of structural plane in rock mass and its engineering application, Electron. J. Geotech. Eng. 5 (2015) 1779–1789.

[28] M. Khayet, T. Matsuura, Membrane Distillation: Principles and Applicationss, Elsevier, 2011.

[29] W. Xie, Thermal Atomic Layer Etching and Vapor Phase Infiltration for Carbon Material Synthesis, North Carolina State University, 2019.

[30] S. Sonnick, M. Meier, G. Ünsal-Peter, L. Erlbeck, H. Nirschl, M. Rädle, Thermal accommodation in nanoporous silica for vacuum insulation panels, Int. J. Thermofluids. 1–2 (2020) 100012. doi:10.1016/j.ijft.2019.100012.

[31] Z. Mokhtari-Shourijeh, S. Langari, L. Montazerghaem, N.M. Mahmoodi, Synthesis of porous aminated PAN/PVDF composite nanofibers by electrospinning: Characterization and Direct Red 23 removal, J. Environ. Chem. Eng. 8 (2020) 103876. doi:10.1016/j.jece.2020.103876.

[32] Y.S. Khoo, W.J. Lau, H. Chamani, T. Matsuura, A.F. Ismail, Water flux increase by inverting the membrane from its normal position – Is it occurring in FO and PRO?, J. Water Process Eng. 37 (2020) 101366. doi:10.1016/j.jwpe.2020.101366.

[33] L.C. Edomwonyi-Otu, B.O. Aderemi, O. Edomwonyi-Otu, A. Simo, M. Maaza, Alum production from some Nigerian kaolinite deposits, Int. J. Eng. Res. Africa. 7 (2012) 13–19. doi:10.4028/www.scientific.net/JERA.7.13.

[34] G. Gallego, C. Cuevas, R. Mohedano, N. García, On the mahalanobis distance classification criterion for multidimensional normal distributions, IEEE Trans. Signal Process. 61 (2013) 4387–4396. doi:10.1109/TSP.2013.2269047.

Chapter 4

CFD-based genetic programming model for liquid entry pressure estimation of hydrophobic membrane [1]

[1] The content of this chapter has been published in: CFD-based genetic programming model for liquid entry pressure estimation of hydrophobic membranes, Desalination. 476 (2020) 114231.

4.1. Abstract

Wetting phenomenon inside the pore is a significant obstacle hindering membrane distillation (MD) from being fully industrialized. Herein, a new equation is provided for the users, using the combination of computational fluid dynamics (CFD) and genetic programming (GP) tools for estimation of liquid entry pressure (LEP), a parameter closely related to pore wetting. CFD was applied to model the wetting process inside the pore during the gradual increase in feed pressure at different scenarios in which contact angle, pore radius and membrane thickness were changed. Afterwards, GP as an intelligent method was employed to provide a computer program estimating LEP in the whole ranges in which CFD modeling was carried out. Moreover, validation was done using experimental data and then the influence of effective parameters on LEP was studied. This work provides an explicit formula for estimation of LEP in closer agreement with the experimental data in comparison to the Young-Laplace equation. In addition, the influence of the membrane thickness was added to the equation, providing a more realistic formula for LEP estimation.

4.2. Introduction

More than two billion individuals all over the world do not have access to safe drinking water and this number is prone to increase as a result of population growth, increased living standards, and development of industrial and agricultural activities [1,2]. One of the methods which can mitigate water shortage is to increase freshwater production via desalination of saline waters [3]. Seawater and saline aquifer sources represent 97.5% of all water on Earth. Hence, treating even a small portion of saline water could significantly reduce water shortage [4]. Although reverse osmosis (RO) is one of the state-of-the-art pressure-driven membrane desalination technologies, it is incapable of desalinating high-salinity streams (70-300 g salt/kg solution) due to the very high

osmotic pressure to overcome and the only means of treating hypersaline waters is desalination by thermal evaporation [5,6]. Membrane distillation (MD) is one of the emerging methods, which has attracted much attention for desalinating highly saline brines [7].

MD is a thermally driven process in which only vapor molecules pass through the pores of a microporous hydrophobic membrane [8]. This process, however, has not been fully commercialized due to a number of challenges, including "pore wetting" [9-13]. Pore wetting refers to the penetration of liquid feed, instead of just water vapor, into the membrane pores, causing a significant decrease in MD flux [14-27] and/or deterioration of distillate quality [10,11,28,29]. Liquid entry pressure (LEP), as a parameter showing wetting characteristics of a membrane, can be defined as the minimum transmembrane pressure which causes the liquid feed to overcome the hydrophobic forces and enter the pores [14]. It is noteworthy that Smolder's procedure is the experimental procedure applied in most cases for the determination of LEP [30]. Figure 4-1 illustrates a schematic of a setup used for LEP measurement in which the membrane sample is mounted in the cell filled with water and the pressure is increased gradually using nitrogen gas. The pressure at which the first droplet of water appears on the permeate side of the membrane is recorded as LEP [31,32].

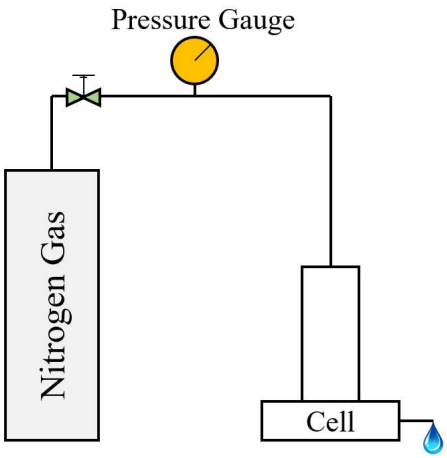

Figure 4-1 Schematic of an experimental setup used for LEP measurement.

Since exceedance of LEP is one of the principal reasons for wetting phenomena [28], precise estimation of LEP is essential in order to assess the membrane wetting potential. Hitherto, several models have been presented to estimate LEP. The Young-Laplace model is the classic model for estimation of LEP for cylindrical pores, given as:

$$LEP = \frac{-2\sigma cos\theta}{r_{max}} \tag{4.1}$$

where σ (N/m), θ (°) and r_{max} (m) are surface tension, contact angle between wetting liquid and membrane, and maximum pore radius, respectively. Franken's model [33], which considers an additional parameter, B (-), as a pore geometry coefficient, is shown in Eq. 4.2.

$$LEP = \frac{-2B\sigma cos\theta}{r_{max}} \tag{4.2}$$

where the value of B depends on the shape of the pore cross-section and for a circular cross-section pore it is equal to unity.

Kim *et al*. [34] developed a model for LEP, in which membranes were considered as arrays of uniform fibers which intersect at constant angles. In fact, the pores are described as tori instead of cylinders that are assumed in the Young-Laplace model (see Figure 4-2) [35]. They presented Eq. 4.3 as the difference of pressure across the liquid–gas interface at the membrane surface [36]:

$$\Delta P = \frac{2\sigma}{r}\frac{\cos(\theta-\alpha)}{1+(R/r)(1-cos\alpha)} = \frac{2\sigma}{r}\cos\theta_{eff} \tag{4.3}$$

where σ (N/m) is surface tension, θ (°) is contact angle and r (m) is pore radius. Furthermore, R (m) and θ_{eff} (°) are radius of fiber and effective contact angle, respectively. α (°) is the structural angle which accounts for the axial deviation of the pores and can be obtained using the following equation [36]:

$$Sin(\theta-\alpha) = \frac{sin\theta}{1+(r/R)} \tag{4.4}$$

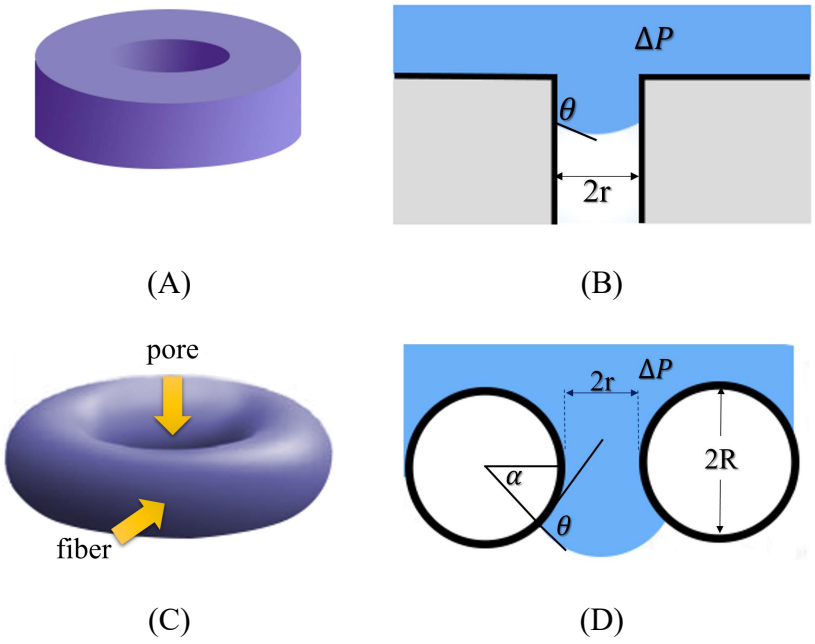

Figure 4-2 Schematic presentation of a single pore: A) and B) cylindrical pore (Young-Laplace model), C) and D) toroidal pore (Kim model). θ and r are contact angle and pore radius, respectively. R is radius of fiber and α is the structural angle.

As a drawback for this model, the effective contact angle (θ_{eff}) cannot be lower than 90° even for materials possessing low contact angle near zero and based on this model, spontaneous wetting occurs when the contact angle is below 90 ° and *r/R* is very small, which contradicts the experimental results that showed the occurrence of spontaneous wetting at a contact angle of greater than zero, regardless of *r/R* [36].

Servi *et al*. modified Kim *et al*.'s model to improve its ability for prediction of the experimental data by introducing a new parameter, *h*, the distance between the floor and the bottom of the fibers (see Figure 4-3) [35]. Their model accounts for interactions between the pores below the initially wetted surface and the liquid [35]. However, in this model, estimation of *r/R* is difficult. Moreover, this model was tested only for fibrous nylon membrane and the effect of membrane thickness on LEP was neglected in all previous equations.

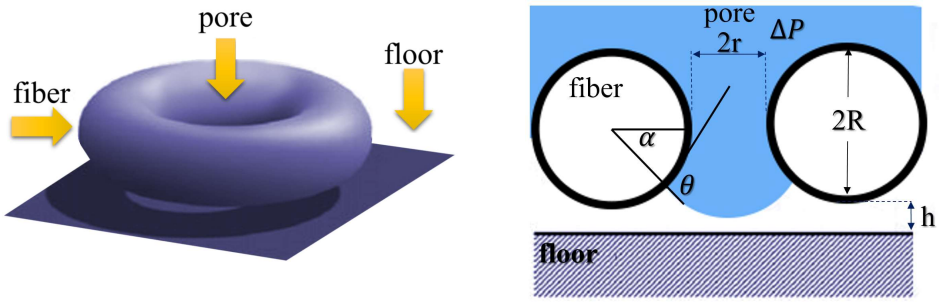

(A) (B)

Figure 4-3 The schematic of a pore for Servi's model: A) 3D and B) cross-section. θ and r are contact angle and pore radius, respectively. R and α are radius of fiber and structural angle, respectively. h is the distance between the floor and bottom of the fibers.

In order to predict LEP precisely, recently a model was developed using computational fluid dynamics (CFD) tools and validation was carried out using experimental LEP data [37]. The unique feature of the model is that the effect of membrane thickness was considered. Although this model allows very accurate prediction of LEP, it is impossible to put the model into few equations since it is based on CFD. If a mathematical formula can be built allowing the same prediction as that of the CFD, it would be beneficial for the user of the model.

Genetic programming (GP), as a genetic algorithm branch, has been proved powerful to capture the nonlinear relationship existing among the variables in different fields [38]. The principal idea behind the GP is evolution theory according to which the population is improved progressively by disregarding the not-so-fit population and generating new children from better populations [39]. GP has been used for modeling of membrane processes in a few studies. Okhovat *et al*. [40] employed GP to deliver a mathematical function for the membrane rejection of nanofiltration process, considering the influence of feed concentration as well as transmembrane pressure. The proposed model exhibited satisfactory accuracy and proved the ability of GP as a powerful

prediction tool for the nanofiltration process. Fouladitajar *et al*. [41] compared the GP model to the individual and combined blocking laws for assessing membrane fouling of the microfiltration process with oil-in-water emulsion. As a result, the process was predicted more accurately by the GP model. Suh *et al*. [42] developed a model in order to estimate the membrane damage degree by applying GP. The model predicted satisfactorily the area of membrane breach as a function of mass of the permeated particle, particle concentration, transmembrane pressure, and permeate water flux. Shokrkar *et al*. [43] used GP for estimating the membrane flux in the separation process of oily wastewaters by ceramic microfiltration membranes. Moreover, GP has been applied for estimation of pervaporation separation index with high accuracy (R^2=0.9722) [44].

The objective of this work is to present a single equation by which LEP can be predicted under various conditions. It should be noted that the effect of membrane thickness on LEP is predicted for the first time by a single equation in this work. To this end, the CFD tool is combined with the GP model for the evaluation of LEP. In this attempt, LEP modeling is carried out by the CFD model for different sets of variables including contact angle, pore radius and membrane thickness. Then, an explicit formula is generated by applying GP to reproduce the results of CFD model as accurately as possible. Moreover, after the validation of the newly developed formula, the effect of different parameters on LEP is assessed.

4.3. Model Development

4.3.1. CFD model

As mentioned, the LEP values were calculated for the sets of variables (contact angle, pore radius and membrane thickness) by the CFD model.

For this purpose, a two dimensional CFD model was developed by applying the volume of fluid (VOF) approach with the following assumptions:

- The pore structure is straight and cylindrical.
- The pore tortuosity is negligible.
- Heat does not transfer through the pore wall.
- Water and air are considered incompressible and immiscible.
- The physical properties are constant, corresponding to the temperature of 25 °C.
- At the wall of the pore, a no-slip condition is considered.

The stagnant water pressure on the feed side was increased systematically and VOF modeling strategy was performed to follow the interface between two immiscible fluids (water and air) affected by surface tension force. Static contact angle values were used, so the value was constant in each simulation whether the flow was advancing or receding. When the water/air interface reaches permeate side (pore exit), it indicates that complete pore wetting occurred.

The model equations, i.e., Eq. 4.5 (transient form of continuity), Eq. 4.6 (momentum conservation) and Eq. 4.7 (the transport volume fractions conservation) were solved simultaneously by employing Star-CCM+ solver [45] via finite volume numerical discretization scheme.

$$\frac{\partial \rho}{\partial t} + \nabla.(\rho u) = 0 \tag{4.5}$$

$$\frac{\partial \rho u}{\partial t} + \nabla.(\rho u u) = -\nabla P + \nabla.(\mu \nabla u) + \rho g + F_{\gamma} \tag{4.6}$$

$$\frac{\partial (\alpha_i)}{\partial t} + \nabla.(\alpha_i u) = 0 \tag{4.7}$$

where ρ (kg/m^3), t (s) and u (m/s) are density, time and velocity, respectively. Furthermore, P (Pa), μ (Pa s), g (m/s^2), F_γ (N/m^3) and α_i represent pressure, dynamic viscosity, gravitational constant, body force caused by surface tension and phase i volume fraction, respectively. The surface tension force term was calculated by using the continuum surface force method and further details could be found in reference [37].

4.3.2. GP model

GP, as a machine learning algorithm inspired by biological evolution, was introduced by Koza [46]. Computer programs are developed for problem solution by employing the Darwinian natural selection principle [47]. In fact, GP is an extension of genetic algorithm with a principal difference such that the GP solutions are computer programs in the form of tree structures, while genetic algorithm represents the solutions as a string of numbers [48]. For instance, Figure 4-4 illustrates a GP tree. The sub-tree located on the right-hand side which contains "*v*", "×" and "*6*" represents "$v\times6$". Therefore, the right side is "*cos (v×6)*" and the figure as a whole represents "$f(u,v) = log(u+3) - cos\,(v\times6)$".

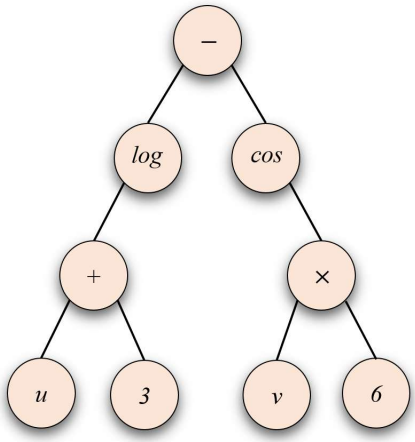

Figure 4-4 Representation of $log(u+3) - cos(v\times6)$ in form of tree structure. An example of a tree structure function used in GP.

In Figure 4-4, the connections are called nodes and these nodes can be divided into two groups [42]: i) internal (I) nodes or functions, consuming one or more input(s) and producing one output. "+", "-", and "log" are examples of these types of nodes. ii) terminal (T) or leaf nodes are nodes at the end of points of tree, representing external inputs, constants as well as zero augment functions.

In the beginning, initial population of programs is generated. For this purpose, three techniques were specified by Koza for creating random initial population, namely full, grow, and Ramped Half-and-Half method [49]. Ramped Half-and-Half method combines the full and grow initialization methods. In this study, Ramped Half-and-Half method was applied for initialization of the population as this method increases the variation in the structure of initial population. The main difference between the grow and full method is that if the maximum depth of tree is larger than the depth of tree, for grow method, a node can be selected randomly from both sets of terminal and nonterminal nodes while for the full method, the node can be selected only from nonterminal ones. Figure 4-5 shows two trees generated using grow and full methods with the maximum depth of tree 2 [50]. For the maximum depth of tree D, Half-and-Half method separates the population size into D-1 classes with different maximum depths of tree, i.e., from 2 to D, and fifty percent of each class is generated using grow method and the other fifty percent using full method. This technique results in enough diversity in the population since the results are the mixture of irregular trees with different depths which were generated by grow method and more regular ones created by the full method [50].

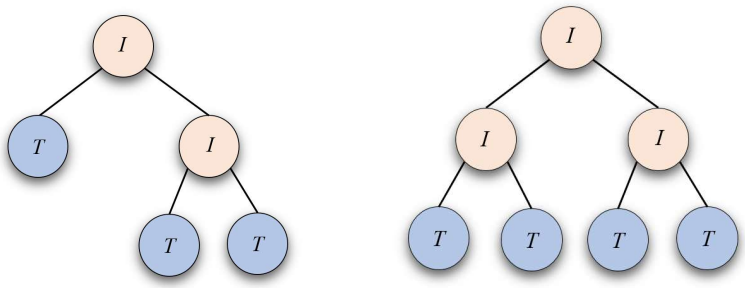

(A) (B)

Figure 4-5 Schematic of methods of initializing the population for GP modeling: A) grow and B) full methods, I: internal node and T: terminal node.

Afterwards, for each program fitness value is calculated. Herein, the fitness value is the sum of absolute differences between LEP obtained by CFD and LEP estimated by GP modeling. Then, a new generation of programs (offspring) will be produced in accordance with fitness values of parents, i.e. previous programs, by breeding them using genetic operators. Genetic operators can be divided into three categories: crossover, mutation as well as reproduction [41]. In order to produce a superior generation, genetic operators should be applied appropriately. The definition of these operators are as follows [40,42]: i) Crossover: this operator swaps the sub-trees between parents (two tree structure programs), resulting in generation of two offspring (Figure 4-6A). ii) Mutation: although the crossover operator provides many new children, it does not introduce any new information to the population and consequently, the population tends to be homogeneous. Therefore, by applying the mutation operator, this issue can be solved because the mutation operator randomly exchanges a sub-tree of a tree structure with a new sub-tree. In Figure 4-6B, the selected sub-tree is mutated. iii) Reproduction: this operator transfers the most excellent tree structure programs to the future generation.

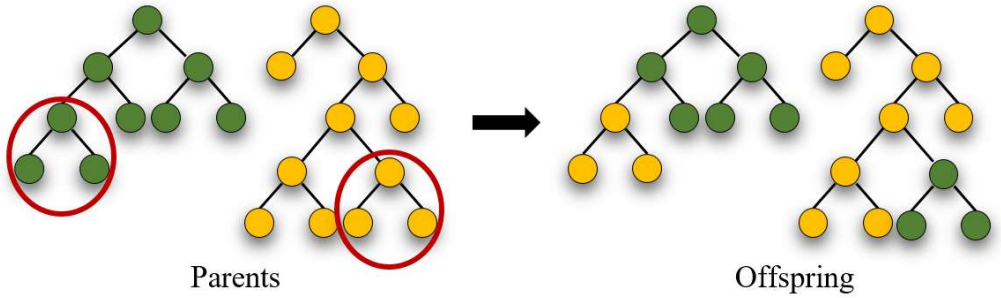

(A)

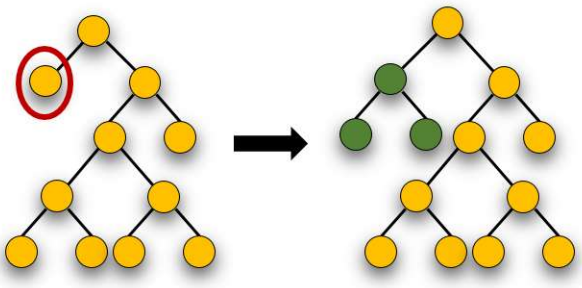

(B)

Figure 4-6 Genetic operators used during producing offspring: A) crossover and B) mutation.

The programs tend to improve in quality during consecutive generations owing to selecting superior individuals and passing their most desirable characteristics to the next generation and this evolutionary model continues until a termination criterion is reached [41]. The flowchart of the proposed GP model, applied in this study, is shown in Figure 4-7.

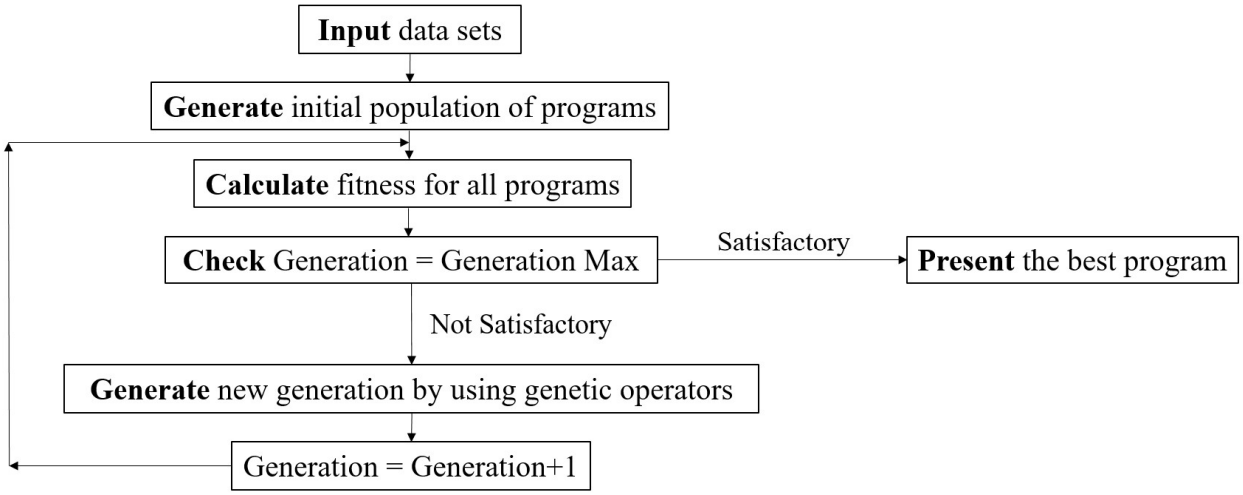

Figure 4-7 Flowchart of the proposed GP model (each input data set contains the values of several parameters including pore radius, contact angle, membrane thickness as well as corresponding LEP obtained by CFD modeling).

4.3.3. Modeling procedure

Herein, 40 sets of parameters were provided. Each set contained the values of several variables including contact angle (θ), pore radius (r), membrane thickness (δ) and corresponding LEP at pore exit which was computed for each data set by CFD modeling. The ranges of the parameters were 90-150^o, 0.05-1.35 μm and 10-50 μm, for θ, r and δ, respectively, as given in Table 4-1. Afterward, an explicit formula was developed for LEP as the function of the above three parameters by GP using the data obtained from CFD modeling. The domains of all input (θ, r and δ) and output (LEP) variables were changed using Eq. 4.8 (all parameters were normalized between 0.1 and 0.9). This model was developed using MATLAB R2017a software.

$$x_{norm} = 0.8\frac{x_{orig}-x_{min}}{x_{max}-x_{min}} + 0.1 \quad (4.8)$$

where x_{orig} and x_{norm} are original and normalized values of the variable, respectively. x_{max} and x_{min} are extreme values of x_{orig}.

Table 4-1 The parameters used for the CFD model.

Parameter	Values
Contact angle, θ (°)	90, 110, 130 and 150
Pore radius, r (μm)	0.05, 0.15, 0.45 and 1.35
Membrane thickness, δ (μm)	10, 30 and 50

4.4. Results and discussion

4.4.1. Model development

A two-dimensional solver mesh was generated through an automated mesh operation in Star-CCM+ software and optimization of the mesh size was performed by changing the mesh size gradually until LEP no longer was changed. Figure 4-8 illustrates the mesh structure of a pore as well as the schematic of the CFD model geometry for a single pore. The feed pressure was increased linearly with a constant rate of 10^{-8} bar s^{-1} and as soon as the liquid entered the pore, the way of pressure increase was changed so that after increasing the pressure (0.01 bar increase), the pressure remained unchanged for 1.2×10^{-5} s.

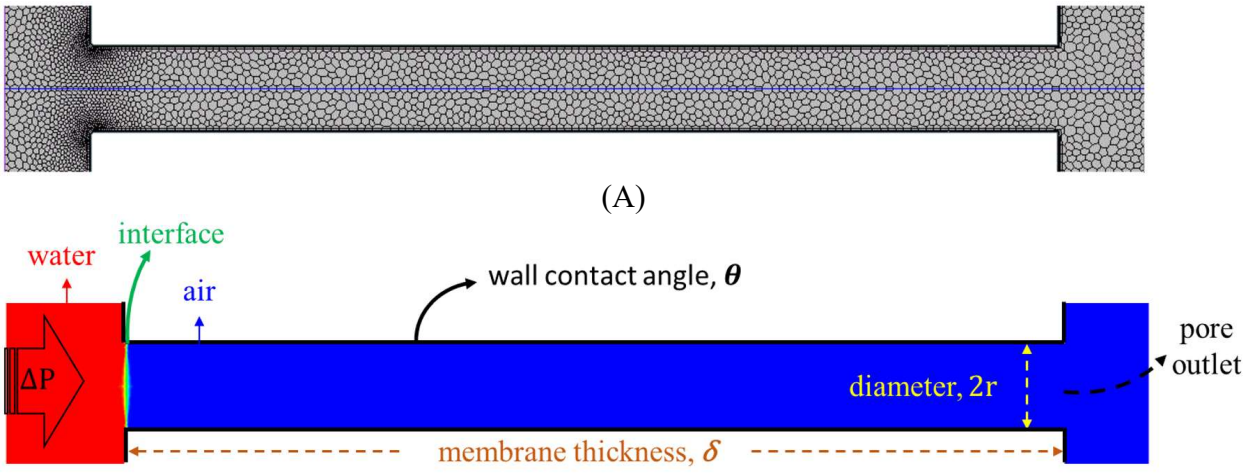

Figure 4-8 A) The structure of the mesh (where pore radius (r)= 0.45 μm and membrane thickness (δ)= 10 μm) and B) the schematic of geometry of the CFD model for a single pore.

The LEP data obtained by CFD model were divided randomly into two groups; i) Testing data which contains 10% of all data sets and ii) Training data which contains the remaining data sets. The GP model was carried out using the training data and as a result, the following equation was generated:

$$y = ln(abs(cos(cos(cos((ln(abs(cos(cos(cos(sin(((ln(x_2) - (x_1 - x_2))\dots \\ +((2 * x_1) - x_2))))))) * (((ln(x_2) - (x_1 - x_2)) + sin(x_2)) - cos((\dots \\ ((ln(x_2) - (sin(cos(x_2)) - x_2)) + (cos(x_3) * (x_3 * (x_2 - x_1))))\dots \\ -\cos(x_2))))))))) * (((\ln(x_2) - (x_1 - x_2)) + \sin((x_2 * x_1) - x_2)) \dots \\ -cos((ln(abs(sin(x_2))) - cos(x_2))))$$

(4.9)

where x_1, x_2, and x_3 are normalized contact angle, normalized pore radius, and normalized membrane thickness, respectively and y is normalized LEP. It should be noted that the LEP obtained by this equation is the normalized LEP and in order to convert LEP to the original scale, the minimum and maximum LEP which were obtained by the CFD model are required; $LEP_{min} = 0.09$ bar and $LEP_{max} = 14.04$ bar.

4.4.2. Model validation

By plotting the data obtained by the CFD-GP model against the data obtained by CFD, it can be seen that all data are located in a narrow region along the diagonal line (Figure 4-9), which means that the GP predictions are in good agreement with the CFD data. Moreover, the coefficient of determination parameter, R^2, which has the values close to unity for both groups of data (0.9815 and 0.9993 for the training and testing data sets, respectively), proves the reliability of the proposed equation provided by GP over the whole range of data, as the testing data were selected randomly. In fact, it shows that the proposed model is fitted to all CFD data points, even the ones which were not used for training the model (i.e., the testing data set).

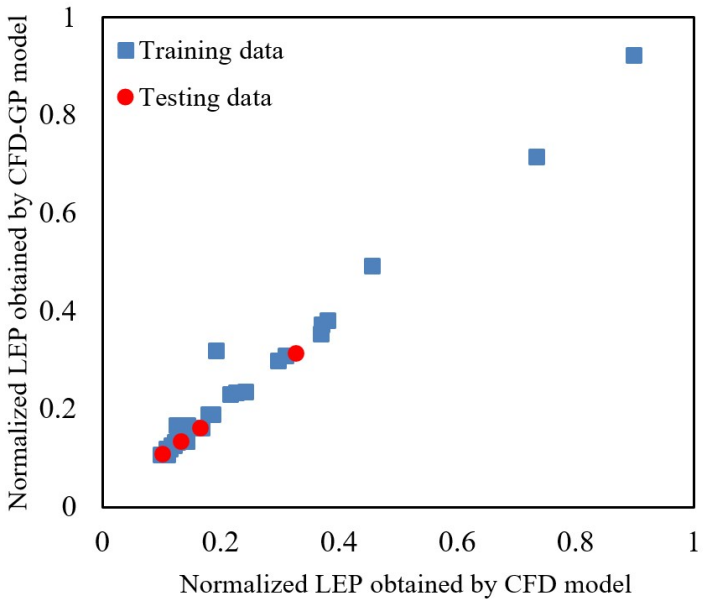

Figure 4-9 Normalized LEP estimated by CFD-GP model vs. normalized LEP obtained by CFD model, for both training and testing sets.

Table 4-2 shows the comparison between the experimental LEP values and those obtained by CFD-GP and Young-Laplace models. The experimental LEP values were obtained from the literature for membranes with cylindrical pores formed by the track-etched method [51-53]. The contact angle, pore radius and thickness of each membrane along with the corresponding LEP values ($LEP^{\text{exp.}}$, $LEP^{\text{Young-Laplace}}$ and $LEP^{\text{CFD-GP}}$) are presented in Table 4-2. According to this table, the agreement of the proposed model with the experimental data is far superior to the Young-Laplace model.

Table 4-2 Comparison between the experimental LEP values and those obtained by CFD-GP and Young-Laplace models.

Membrane type	θ (°)	r (μm)	δ (μm)	$LEP^{\mathrm{CFD-GP}}$ (bar)	$LEP^{\mathrm{Young-Laplace}}$ (bar)	$LEP^{\mathrm{exp.}}$ (bar)	Ref.
Modified polycarbonate	124	0.18	24	2.51	4.47	2.76	[51]
Modified polyethylene terephthalate	91	0.134	12	1.54	0.18	1.4	[52]
Modified polyethylene terephthalate	109	0.105	12	3.66	4.46	3.4	[53]

4.4.3. Influence of effective parameters on LEP

The effects of the contact angle, pore radius and membrane thickness on LEP are further illustrated in this section for both the proposed and the Young-Laplace model.

The capillary pressure is caused by surface tension and prevents the liquid from penetrating the pore [54]. Based on the Young-Laplace equation, the LEP is equal to the capillary pressure and is proportional to $Cos\theta$. It is thus obvious that increasing the contact angle increases the LEP (Figure 4-10). The same increasing trend for LEP can be seen for the newly proposed model (Figure 4-11).

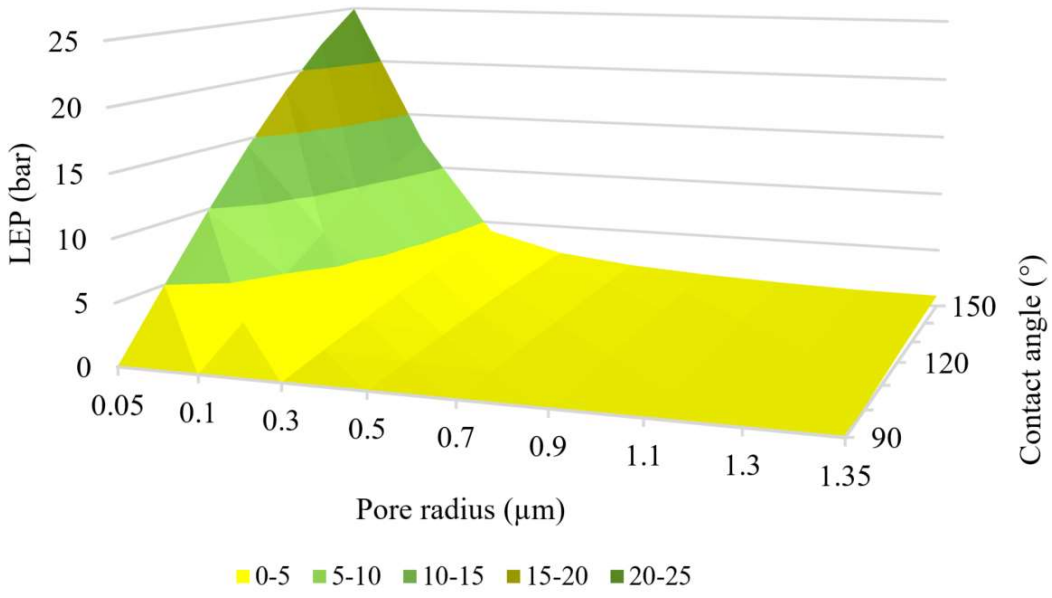

Figure 4-10 The effect of contact angle and pore radius on LEP according to the Young-Laplace model.

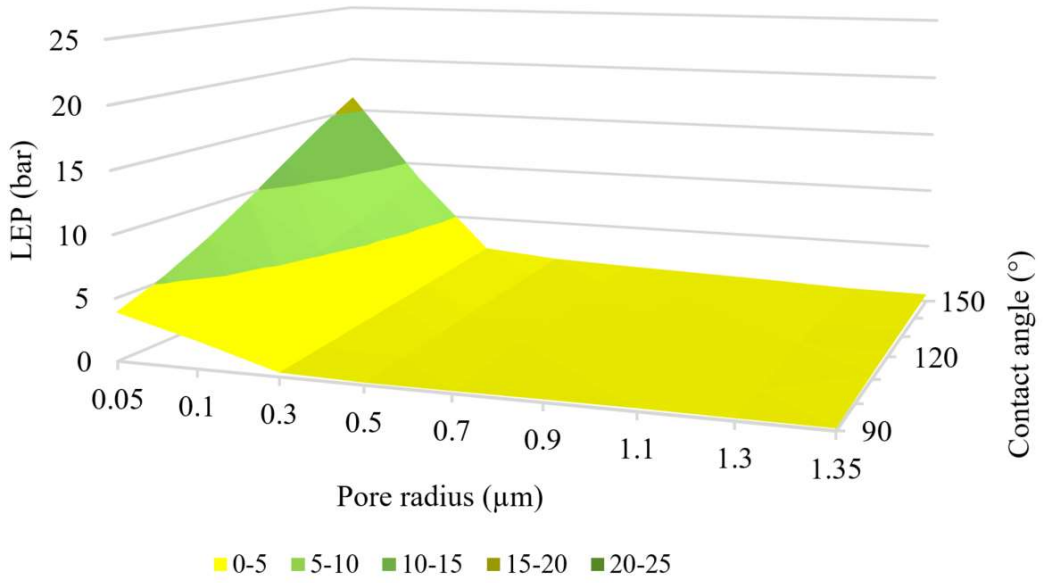

Figure 4-11 The effect of contact angle and pore radius on LEP according to the CFD-GP model (membrane thickness (δ)= 30 µm).

For high contact angles, the LEP values predicted by the new model are less than those expected from the Young-Laplace equation. This difference can be attributed to the overestimation of Young-Laplace equation which has been reported in many cases [36,37,51].

On the other hand, the LEP corresponding to $\theta = 90°$ is zero for the Young-Laplace model, regardless of pore radius, while the LEP obtained by the proposed model is more than zero. E.g., according to the CFD-GP model, for pore radius of 0.1 micron, contact angle of 90°, and thickness of 30 micron, LEP is ca 2 bar, which seems to be more realistic as in many cases, membranes with contact angle near 90° have much higher LEP than 0. For instance, the LEP value corresponding to the modified polyethylene terephthalate with contact angle of 91° was measured as 1.4 bar [52]. As another example, the measured LEP for PVDF membrane containing 2 percent CuO with contact angle of 91.6 ° was around 3 bar [31].

The CFD modeling approach takes the behavior of both water and air phases into account. Figure 4-12 represents a volume fraction of water (VFW) contour plot which was generated by using the CFD model result when θ = 150° and r = 0.15 μm. The area in red color is full of water (VFW = 1) and the blue colored area represents 100% air region (VFW = 0). Also, the color transition (0 < VFW < 1) indicates water/air interface or air/water mixed layer. Since the VOF approach is mostly appropriate for free surface flow problems modeling (where each phase has a discrete structure), nanometer-scale air pockets and thin layers nearby the wall cannot be captured individually in the simulations [45]. For this reason, the VOF model results just represent the averaged region as a water/air mixed layer on the VFW contour plots. In the literature, it was previously reported that water/air mixed layer formation is proportional to contact angle (θ) and the interaction between water and air can be observed only at very high θ values (super-hydrophobic material) [37]. Therefore, air/water mixed layer formation was not observed when θ is less than 150°. At 150°,

the layer was very thin, as shown in Figure 4-12. For the super-hydrophobic surface case ($\theta \geq 150°$), there is a limited contact area between a water droplet and the surface. Thus, the air phase has the potential to slide through and create an air/water mixed layer nearby the pore entrance region. The air/water mixed layer might slightly reduce the resistance (which is due to the surface tension), and this can create a very small slip length. Finally, the whole process might trigger an earlier water flow through the pore. However, Young-Laplace model does not account the effect of air/water mixed layer. For this reason, at higher θ values, the actual LEP values are further lower than the LEP values calculated from the Young-Laplace equation.

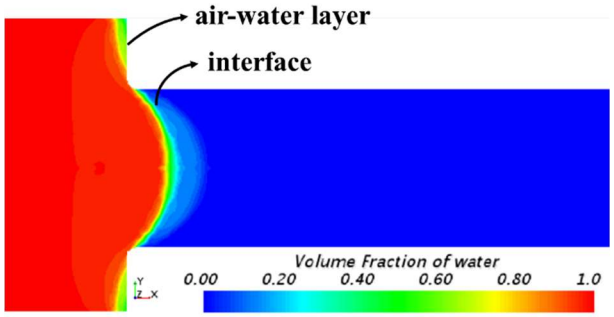

Figure 4-12 The air/water layer formed on the membrane pore wall (where contact angle (θ) = 150° and pore radius (r) = 0.15 µm; red color represents 100% water and blue color shows 100% air).

Again, based on the Young-Laplace equation, the LEP is equal to the capillary pressure which is inversely proportional to the pore radius. Therefore, increasing the pore radius decreases the LEP (Figure 4-10). The same decreasing trend can be seen for the proposed model with lower LEP values, which is more obvious at the low pore radii (Figure 4-11).

Since the hydrophobicity of the pore wall plays an important role in the rejection of liquid water from the pore and consequently preventing leakage [55], it could be useful to take the effect of

membrane thickness on LEP into account. As shown in Figure 4-13, the newly proposed equation predicts the increase of LEP with membrane thickness, in contrast to the Young-Laplace model, according to which LEP is not a function of membrane thickness. The literature states that the increase in thickness reduces the vapor flux in MD due to the higher mass transfer resistance [56]. Although in pore wetting it is not vapor but liquid water that passes through the pore, the resistance should similarly affect the movement of liquid. The presented equation could successfully capture the effect of membrane thickness on LEP, which was not considered by the previous LEP equations. The effect of membrane thickness on LEP had previously been evaluated in several research articles. Guillen-Burrieza *et al*. suggested that the membrane thickness, a characteristic which is normally not considered influential in membrane hydrophobicity, clearly affects the LEP, meaning that the thicker membranes, the higher LEPs [36]. Also, Yazgan-Birgi *et al*. mentioned that the wetting process takes place gradually through the membrane pore, and the applied pressure during LEP measurement should be increased to push the water through the membrane pore after its initial entry into it, resulting in a significant effect of thickness on LEP, with longer pores having higher LEPs [37]. Since it has been believed for a long time that LEP is not a function of membrane thickness, further research should be carried out to verify the effect of thickness on LEP. For this purpose, it is recommended to prepare several membranes with the same pore radius, pore density, and contact angle (e.g. modified with initiated chemical vapor deposition), with different thicknesses using the track-etched method to evaluate the influence of pore length on LEP experimentally.

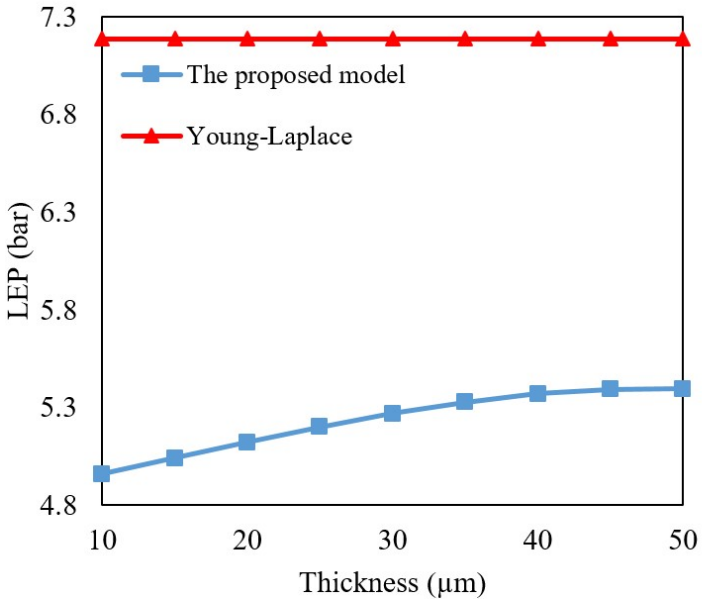

Figure 4-13 The effect of membrane thickness on LEP (contact angle $(\theta) = 120°$ and pore radius $(r) = 0.1\ \mu m$).

4.5. Conclusion

In this study, a new equation was presented for estimation of LEP using a CFD-based GP model. After validation of the model, the influence of effective parameters, including contact angle, pore radius and membrane thickness on LEP was discussed. Moreover, the difference between the estimated LEP using the newly proposed model and Young-Laplace model at different conditions was studied. Considerable differences in the LEP values were noticed between these two models. In particular, even though the same trends are found in LEP vs. contact angle and LEP vs. pore radius, the newly proposed model predicts the increase of LEP with the membrane thickness, in contrast to the Young-Laplace model according to which LEP is not a function of membrane thickness.

Therefore, the combined CFD-GP model could effectively capture the pattern of LEP changes and provide an explicit formula for this purpose. This technique, i.e., the combination of CFD and GP tools, seems to be a powerful method for other chemical engineering processes and as future research, providing an equation for LEP which considers the presence of salt in feed is suggested, as it might affect surface tension as well as air/water mixture layer.

4.6. References

[1] S.J. Kim, S.H. Ko, K.H. Kang, J. Han, Direct seawater desalination by ion concentration polarization, Nat. Nanotechnol. 5 (2010) 297–301. doi:10.1038/nnano.2010.34.

[2] H. Wang, Low-energy desalination, Nat. Nanotechnol. 13 (2018) 273–274. doi:10.1038/s41565-018-0118-y.

[3] A. Deshmukh, M. Elimelech, Understanding the impact of membrane properties and transport phenomena on the energetic performance of membrane distillation desalination, J. Membr. Sci. 539 (2017) 458–474. doi:10.1016/j.memsci.2017.05.017.

[4] M.A. Shannon, P.W. Bohn, M. Elimelech, J.G. Georgiadis, B.J. Mariñas, A.M. Mayes, Science and technology for water purification in the coming decades, Nature. 452 (2008) 301–310. doi:10.1038/nature06599.

[5] C. Boo, M. Elimelech, Thermal desalination membranes: Carbon nanotubes keep up the heat, Nat. Nanotechnol. 12 (2017) 501–503. doi:10.1038/nnano.2017.114.

[6] J. Swaminathan, H.W. Chung, D.M. Warsinger, J.H. Lienhard V, Energy efficiency of membrane distillation up to high salinity: Evaluating critical system size and optimal membrane thickness, Appl. Energy. 211 (2018) 715–734. doi:10.1016/J.APENERGY.2017.11.043.

[7] P.G. S. Leaper, A. Abdel-Karim, T. A. Gad-Allah, Air-gap membrane distillation as a one-step process for textile wastewater treatment, Chem. Eng. J. 360 (2019) 1330–1340. doi:10.1016/J.CEJ.2018.10.209.

[8] R.X. M. Ren, P. Ning, J. Xu, G. Qu, Concentration and treatment of ceric ammonium nitrate wastewater by integrated electrodialysis-vacuum membrane distillation process, Chem. Eng. J. 351 (2018) 721–731. doi:10.1016/J.CEJ.2018.06.155.

[9] E. Guillen-Burrieza, M.O. Mavukkandy, M.R. Bilad, H.A. Arafat, Understanding wetting phenomena in membrane distillation and how operational parameters can affect it, J. Membr. Sci. 515 (2016) 163–174. doi:10.1016/J.MEMSCI.2016.05.051.

[10] M.R. Qtaishat, T. Matsuura, Modelling of pore wetting in membrane distillation compared with pervaporation, in: Pervaporation, Vap. Permeat. Membr. Distill., Elsevier, 2015: pp. 385–413. doi:10.1016/B978-1-78242-246-4.00013-1.

[11] F.E. Ahmed, B.S. Lalia, R. Hashaikeh, Membrane-based detection of wetting phenomenon in direct contact membrane distillation, J. Membr. Sci. 535 (2017) 89–93. doi:10.1016/J.MEMSCI.2017.04.035.

[12] H. Chamani, T. Matsuura, D. Rana, C.Q. Lan, Modeling of pore wetting in vacuum membrane distillation, J. Membr. Sci. 572 (2019). doi:10.1016/j.memsci.2018.11.018.

[13] P. Jacob, T. Zhang, S. Laborie, C. Cabassud, Influence of operating conditions on wetting and wettability in membrane distillation using Detection of Dissolved Tracer Intrusion (DDTI), Desalination. 468 (2019) 114086. doi:10.1016/J.DESAL.2019.114086.

[14] R.B. Saffarini, B. Mansoor, R. Thomas, H.A. Arafat, Effect of temperature-dependent microstructure evolution on pore wetting in PTFE membranes under membrane distillation conditions, J. Membr. Sci. 429 (2013) 282–294. doi:10.1016/J.MEMSCI.2012.11.049.

[15] L. Camacho, L. Dumée, J. Zhang, J. Li, M. Duke, J. Gomez, S. Gray, Advances in Membrane Distillation for Water Desalination and Purification Applications, Water. 5 (2013) 94–196. doi:10.3390/w5010094.

[16] A.M. Alklaibi, N. Lior, Membrane-distillation desalination: Status and potential, Desalination. 171 (2005) 111–131. doi:10.1016/J.DESAL.2004.03.024.

[17] C.M. Tun, A.G. Fane, J.T. Matheickal, R. Sheikholeslami, Membrane distillation crystallization of concentrated salts—flux and crystal formation, J. Membr. Sci. 257 (2005) 144–155. doi:10.1016/J.MEMSCI.2004.09.051.

[18] F. He, J. Gilron, H. Lee, L. Song, K.K. Sirkar, Potential for scaling by sparingly soluble salts in crossflow DCMD, J. Membr. Sci. 311 (2008) 68–80. doi:10.1016/J.MEMSCI.2007.11.056.

[19] M. Gryta, Long-term performance of membrane distillation process, J. Membr. Sci. 265 (2005) 153–159. doi:10.1016/J.MEMSCI.2005.04.049.

[20] K. Karakulski, M. Gryta, Water demineralisation by NF/MD integrated processes, Desalination. 177 (2005) 109–119. doi:10.1016/J.DESAL.2004.11.018.

[21] M. Gryta, Influence of polypropylene membrane surface porosity on the performance of membrane distillation process, J. Membr. Sci. 287 (2007) 67–78. doi:10.1016/J.MEMSCI.2006.10.011.

[22] E. Guillen-Burrieza, R. Thomas, B. Mansoor, D. Johnson, N. Hilal, H. Arafat, Effect of dry-out on the fouling of PVDF and PTFE membranes under conditions simulating intermittent seawater membrane distillation (SWMD), J. Membr. Sci. 438 (2013) 126–139. doi:10.1016/J.MEMSCI.2013.03.014.

[23] P. Peng, A.G. Fane, X. Li, Desalination by membrane distillation adopting a hydrophilic membrane, Desalination. 173 (2005) 45–54. doi:10.1016/J.DESAL.2004.06.208.

[24] Y. Peng, Y. Dong, H. Fan, P. Chen, Z. Li, Q. Jiang, Preparation of polysulfone membranes via vapor-induced phase separation and simulation of direct-contact membrane distillation by measuring hydrophobic layer thickness, Desalination. 316 (2013) 53–66. doi:10.1016/J.DESAL.2013.01.021.

[25] M. Qtaishat, M. Khayet, T. Matsuura, Novel porous composite hydrophobic/hydrophilic polysulfone membranes for desalination by direct contact membrane distillation, J. Membr. Sci. 341 (2009) 139–148. doi:10.1016/J.MEMSCI.2009.05.053.

[26] L. Peña, J.M.O. de Zárate, J.I. Mengual, Steady states in membrane distillation: influence of membrane wetting, J. Chem. Soc., Faraday Trans. 89 (1993) 4333–4338. doi:10.1039/FT9938904333.

[27] M. Rezaei, W. Samhaber, Wetting Behaviour of Superhydrophobic Membranes Coated with Nanoparticles in Membrane Distillation, Chem. Eng. Trans. 47 (2016) 373–378. doi:10.3303/CET1647063.

[28] Z. Wang, Y. Chen, X. Sun, R. Duddu, S. Lin, Mechanism of pore wetting in membrane distillation with alcohol vs. surfactant, J. Membr. Sci. 559 (2018) 183–195, https://doi.org/10.1016/J.MEMSCI.2018.04.045.

[29] Y. Chen, Z. Wang, G.K. Jennings, S. Lin, Probing Pore Wetting in Membrane Distillation Using Impedance: Early Detection and Mechanism of Surfactant-Induced Wetting, Environ. Sci. Technol. Lett. 4 (2017) 505–510. doi:10.1021/acs.estlett.7b00372.

[30] K. Smolders, A.C.M. Franken, Terminology for Membrane Distillation, Desalination. 72 (1989) 249–262. doi:10.1016/0011-9164(89)80010-4.

[31] M. Baghbanzadeh, D. Rana, T. Matsuura, C.Q. Lan, Effects of hydrophilic CuO nanoparticles on properties and performance of PVDF VMD membranes, Desalination. 369 (2015) 75–84. doi:10.1016/J.DESAL.2015.04.032.

[32] C.Q.L. Z. Chen, D. Rana, T. Matsuura, D. Meng, Study on structure and vacuum membrane distillation performance of PVDF membranes: II. Influence of molecular weight, Chem. Eng. J. 276 (2015) 174–184. doi:10.1016/J.CEJ.2015.04.030.

[33] A.C.M. Franken, J.A.M. Nolten, M.H.V. Mulder, D. Bargeman, C.A. Smolders, Wetting criteria for the applicability of membrane distillation, J. Membr. Sci. 33 (1987) 315–328. doi:10.1016/S0376-7388(00)80288-4.

[34] B.-S. Kim, P. Harriott, Critical entry pressure for liquids in hydrophobic membranes, J. Colloid Interface Sci. 115 (1987) 1–8. doi:10.1016/0021-9797(87)90002-6.

[35] A.T. Servi, J. Kharraz, D. Klee, K. Notarangelo, B. Eyob, E. Guillen-Burrieza, A. Liu, H.A. Arafat, K.K. Gleason, A systematic study of the impact of hydrophobicity on the wetting of MD membranes, J. Membr. Sci. 520 (2016) 850–859. doi:10.1016/J.MEMSCI.2016.08.021.

[36] E. Guillen-Burrieza, A. Servi, B.S. Lalia, H.A. Arafat, Membrane structure and surface morphology impact on the wetting of MD membranes, J. Membr. Sci. 483 (2015) 94–103. doi:10.1016/J.MEMSCI.2015.02.024.

[37] P. Yazgan-Birgi, M.I. Hassan Ali, H.A. Arafat, Estimation of liquid entry pressure in hydrophobic membranes using CFD tools, J. Membr. Sci. 552 (2018) 68–76. doi:10.1016/J.MEMSCI.2018.01.061.

[38] A. Asadi Tashvigh, F. Zokaee Ashtiani, M. Karimi, A. Okhovat, A novel approach for estimation of solvent activity in polymer solutions using genetic programming, Calphad. 51 (2015) 35–41. doi:10.1016/J.CALPHAD.2015.07.005.

[39] M. Bagheri, A. Akbari, S.A. Mirbagheri, Advanced control of membrane fouling in filtration systems using artificial intelligence and machine learning techniques: A critical review, Process Saf. Environ. Prot. 123 (2019) 229–252. doi:10.1016/J.PSEP.2019.01.013.

[40] A. Okhovat, S.M. Mousavi, Modeling of arsenic, chromium and cadmium removal by nanofiltration process using genetic programming, Appl. Soft Comput. 12 (2012) 793–799. doi:10.1016/J.ASOC.2011.10.012.

[41] A. Fouladitajar, F. Zokaee Ashtiani, A. Okhovat, B. Dabir, Membrane fouling in microfiltration of oil-in-water emulsions; a comparison between constant pressure blocking laws and genetic programming (GP) model, Desalination. 329 (2013) 41–49. doi:10.1016/J.DESAL.2013.09.003.

[42] C. Suh, B. Choi, S. Lee, D. Kim, J. Cho, Application of genetic programming to develop the model for estimating membrane damage in the membrane integrity test using fluorescent nanoparticle, Desalination. 281 (2011) 80–87. doi:10.1016/J.DESAL.2011.07.045.

[43] H. Shokrkar, A. Salahi, N. Kasiri, T. Mohammadi, Prediction of permeation flux decline during MF of oily wastewater using genetic programming, Chem. Eng. Res. Des. 90 (2012) 846–853. doi:10.1016/J.CHERD.2011.10.002.

[44] A. Dashti, M. Asghari, M. Dehghani, M. Rezakazemi, A.H. Mohammadi, S.K. Bhatia, Molecular dynamics, grand canonical Monte Carlo and expert simulations and modeling of water–acetic acid pervaporation using polyvinyl alcohol/tetraethyl orthosilicates membrane, J. Mol. Liq. 265 (2018) 53–68. doi:10.1016/J.MOLLIQ.2018.05.078.

[45] Siemens Product Lifecycle Management Software Inc., Star-CCM+, 2018.

[46] J.R. Koza, Genetic programming : on the programming of computers by means of natural selection, MIT Press, 1992.

[47] A.H. Gandomi, D. Mohammadzadeh S., J.L. Pérez-Ordóñez, A.H. Alavi, Linear genetic programming for shear strength prediction of reinforced concrete beams without stirrups, Appl. Soft Comput. 19 (2014) 112–120. doi:10.1016/J.ASOC.2014.02.007.

[48] S.K. Babanajad, A.H. Gandomi, D. Mohammadzadeh S., A.H. Alavi, Numerical modeling of concrete strength under multiaxial confinement pressures using linear genetic programming, Autom. Constr. 36 (2013) 136–144. doi:10.1016/J.AUTCON.2013.08.016.

[49] H. Khayyam, A. Jamali, H. Assimi, R.N. Jazar, Genetic Programming Approaches in Design and Optimization of Mechanical Engineering Applications, in: Nonlinear Approaches Eng.

Appl., Springer International Publishing, Cham, 2020: pp. 367–402. doi:10.1007/978-3-030-18963-1_9.

[50] J. Eggermont, Data Mining using Genetic Programming: Classification and Symbolic Regression, Leiden University, 2005.

[51] A.T. Servi, E. Guillen-Burrieza, D.M. Warsinger, W. Livernois, K. Notarangelo, J. Kharraz, J.H. Lienhard V, H.A. Arafat, K.K. Gleason, The effects of iCVD film thickness and conformality on the permeability and wetting of MD membranes, J. Membr. Sci. 523 (2017) 470–479. doi:10.1016/J.MEMSCI.2016.10.008.

[52] I. V. Korolkov, A.B. Yeszhanov, M. V. Zdorovets, Y.G. Gorin, O. Güven, S.S. Dosmagambetova, N.A. Khlebnikov, K. V. Serkov, M. V. Krasnopyorova, O.S. Milts, D.A. Zheltov, Modification of PET ion track membranes for membrane distillation of low-level liquid radioactive wastes and salt solutions, Sep. Purif. Technol. 227 (2019). doi:10.1016/j.seppur.2019.115694.

[53] I. V. Korolkov, A.B. Yeszhanov, Y.G. Gorin, M. V. Zdorovets, N.A. Khlebnikov, K. V. Serkov, Hydrophobization of PET track-etched membranes for direct contact membrane distillation, Mater. Res. Express. 5 (2018). doi:10.1088/2053-1591/aacc39.

[54] M. Rezaei, D.M. Warsinger, J.H. Lienhard V, M.C. Duke, T. Matsuura, W.M. Samhaber, Wetting phenomena in membrane distillation: Mechanisms, reversal, and prevention, Water Res. 139 (2018) 329–352. doi:10.1016/J.WATRES.2018.03.058.

[55] A.L. McGaughey, R.D. Gustafson, A.E. Childress, Effect of long-term operation on membrane surface characteristics and performance in membrane distillation, J. Membr. Sci. 543 (2017) 143–150. doi:10.1016/J.MEMSCI.2017.08.040.

[56] A. Alkhudhiri, N. Darwish, N. Hilal, Membrane distillation: A comprehensive review, Desalination. 287 (2012) 2–18. doi:10.1016/J.DESAL.2011.08.027.

Chapter 5

Transport characteristics of liquid-gas interface in a capillary membrane pore [1]

[1] The content of this chapter has been published in: Transport characteristics of liquid-gas interface in a capillary membrane pore, J. Membr. Sci. 611 (2020) 118387.

5.1. Abstract

Interface displacement of two phases mainly caused by replacement of one fluid with another one can occur inside the membrane pore during membrane preparation and characterization. This phenomenon is exemplified by measurement of liquid entry pressure (LEP) in membrane distillation, measurement of pore size and pore size distribution by the bubble point method, measurement of pore size and pore size distribution by porometry, wetting of dry membrane and also drying of wet membrane. In most of the theoretical studies, focus was on the transmembrane pressure required for one phase to enter into the membrane pores filled with another phase and little attention was paid to the movement of interface in the capillary. This paper attempts to discuss quantitatively the movement of interface, water/air interface in particular. Therefore, movement of the interface was tracked using a well-founded model and consequently, the pressure and velocity at the interface and the required time for replacement were studied. In addition, the influence of different parameters, including pore radius, contact angle, and membrane thickness, was assessed. It was found that the low resistance for the air flow, assumed in Washburn's equation, can be justified as an approximation. Moreover, the model proposed in this work can predict that the pressure at the air/water interface (when air replaces liquid water) may become significantly lower than the atmospheric pressure at the pore exit, causing pore shrinkage. As well, the pressure at the water/air interface (when liquid water replaces air) may become significantly higher than the feed pressure applied at the pore entrance, causing pore expansion.

5.2. Introduction

The capillary flow in which the interface of two phases moves from one end of capillary to the other end can occur in membrane preparation and characterization. Examples are 1) measurement

of liquid entry pressure (LEP) in membrane distillation [1,2], 2) measurement of pore size and pore size distribution by the bubble point method [1,3], 3) measurement of pore size and pore size distribution by porometry [4], 4) wetting of dry membrane, 5) drying of wet membrane, etc.

In examples 1) and 4), i.e. LEP measurement and wetting of dry membrane, liquid (water in most cases) enters into the air-filled pore and the water/air interface moves from the pore entrance to the pore exit. In example 2), i.e. bubble point method, air enters into the liquid (not necessarily water)-filled pore and the air/liquid interface moves from the pore entrance to the pore exit. In example 3), i.e. porometry, liquid enters into the pore filled with another liquid and the liquid/liquid interface moves from pore entrance to the pore exit. In example 5), i.e. drying of wet membrane, liquid (water in most cases) in the liquid-filled pore is vaporized and the water/vapor interface moves from the pore exit to the pore entrance.

In all these examples, focus was mostly placed on the transmembrane pressure that is required for one phase to enter into the pore which is filled with another phase [5-7] and little attention has been paid to the movement of the phase boundary in the pore.

Imbibition of liquid into the capillary was dealt with by the classical theory of Washburn and Lucas [8,9]. In his paper of 1921, Washburn discussed the liquid motion in a cylindrical tube. According to the equation he derived, the velocity of the front of the liquid column, $\frac{d\delta_l}{dt}$, can be given as:

$$\frac{d\delta_l}{dt} = \frac{\sum p}{8r^2\eta_l\delta_l}(r^4 + 4\epsilon r^3) \tag{5.1}$$

where δ_l is the length of the liquid column, t is time, $\sum p$ is the sum over the external pressure such as unbalanced atmospheric pressure, p_a (zero if both ends of capillary are open), hydrostatic pressure, p_h, and capillary pressure, p_c. η_l is the viscosity of the liquid, r is the radius of the

cylindrical pore, and ϵ is the coefficient of slip, which can be assumed to be zero when the pore has a wettable surface.

The pressures are written as:

$$p_h = Hg\rho - l_s g\rho \sin\varphi \tag{5.2}$$

$$p_c = \frac{2\sigma\cos\theta}{r} \tag{5.3}$$

where H is the height of liquid in the liquid reservoir, g is acceleration by gravity, ρ is the liquid density, and l_s is the linear distance between the pore entrance and the liquid/gas interface. φ is the angle of capillary tube with respect to the horizontal axis, σ is the surface tension of the liquid and θ is the contact angle of the liquid on the surface of the capillary material. Combination of all forces yields:

$$\frac{d\delta_l}{dt} = \frac{\left[p_a + (Hg\rho - l_s g\rho\sin\varphi) + \frac{2\sigma\cos\theta}{r}\right](r^4 + 4\epsilon r^3)}{8r^2\eta_l\delta_l} \tag{5.4}$$

Further, when p_f is applied at the pore entry and p_p is maintained at the pore exit, p_a can be replaced by $p_f - p_p$. For a horizontal capillary tube hydrostatic pressure (p_h) can usually be ignored. Then, for the wettable capillary tube, Eq. 5.4 can be simplified to:

$$\frac{d\delta_l}{dt} = \frac{\left[(p_f - p_p) + \frac{2\sigma\cos\theta}{r}\right](r^2)}{8\eta_l\delta_l} \tag{5.5}$$

Integration of Eq. 5.5 with $\delta_l = 0$ at $t = 0$ results in:

$$\delta_l = \sqrt{\frac{\left[(p_f - p_p) + \frac{2\sigma\cos\theta}{r}\right](r^2)}{4\eta_l}}\, t^{1/2} \tag{5.6}$$

when both ends of the capillary are open to the atmosphere:

$$\delta_l = \sqrt{\frac{r\sigma\cos\theta}{2\eta_l}}\, t^{1/2} \tag{5.7}$$

Hitherto, many applications and discussions have been made about this equation [10-14]. Bosanquet later improved Washburn's equation by taking the changes of the momentum of liquid into consideration [15]. The equation is written as [16]:

$$\frac{d}{dt}\left(\pi r^2 \rho \delta_l \frac{d\delta_l}{dt}\right) + 8\pi\eta_l \delta_l \frac{d\delta_l}{dt} = p_e \pi r^2 + 2\pi r\sigma\cos\theta \tag{5.8}$$

where p_e is the external pressure. Szekely *et al*. also tried to modify Washburn's equation by considering energy balance at the initial liquid intake and derived the following equation [17]:

$$\left(\delta_l + \frac{7}{6}r\right)\frac{d^2\delta_l}{dt^2} + 1.225\left(\frac{d\delta_l}{dt}\right)^2 + \frac{8\eta_l}{\rho r^2}\delta_l\left(\frac{d\delta_l}{dt}\right) = \frac{1}{\rho}\left(\frac{2\sigma\cos\theta}{r} - \rho g\delta_l\right) \tag{5.9}$$

Obviously, their equation includes the gravitational potential term when applicable. Ridgway *et al*. compared the results predicted by the above equations [16]. In all the above equations, focus is on the liquid flow without taking account of the gas flow in the front of the moving liquid.

The objective of this research is to derive equations in which both the liquid and the gas transport are taken into account for the movement of the liquid/gas (or gas/liquid) interface inside the membrane pore, especially for the water/air (or air/water) interface. The equations derived are applied for different scenarios, including i) water enters into an air-filled pore and the water/air interface moves toward the pore exit and ii) air enters into a water-filled pore and the air/water interface moves toward the pore exit. In both scenarios, the transport in the membrane pore is considered for both hydrophobic and hydrophilic membranes. Furthermore, the pressure and velocity at the interface as well as the time required for passing the pore are studied. The effect of

membrane parameters including pore radius, contact angle and membrane thickness is assessed as well.

5.3. Model Development

Figure 5-1 shows schematically the presence of cylindrical pores in a membrane. In this study, for a single pore of a membrane, considered as a straight and cylindrical pore, liquid water replacement with air (and vice versa) is studied for both hydrophobic and hydrophilic materials. Thus, model development and results are divided into four cases:

(1) liquid water replaces air (hydrophobic, contact angle (θ) $\geq 90^{o}$) (Figure 5-2A)

(2) air replaces liquid water (hydrophobic, contact angle (θ) $\geq 90^{o}$) (Figure 5-2B)

(3) liquid water replaces air (hydrophilic, contact angle (θ) $\leq 90^{o}$) (Figure 5-2C)

(4) air replaces liquid water (hydrophilic, contact angle (θ) $\leq 90^{o}$) (Figure 5-2D)

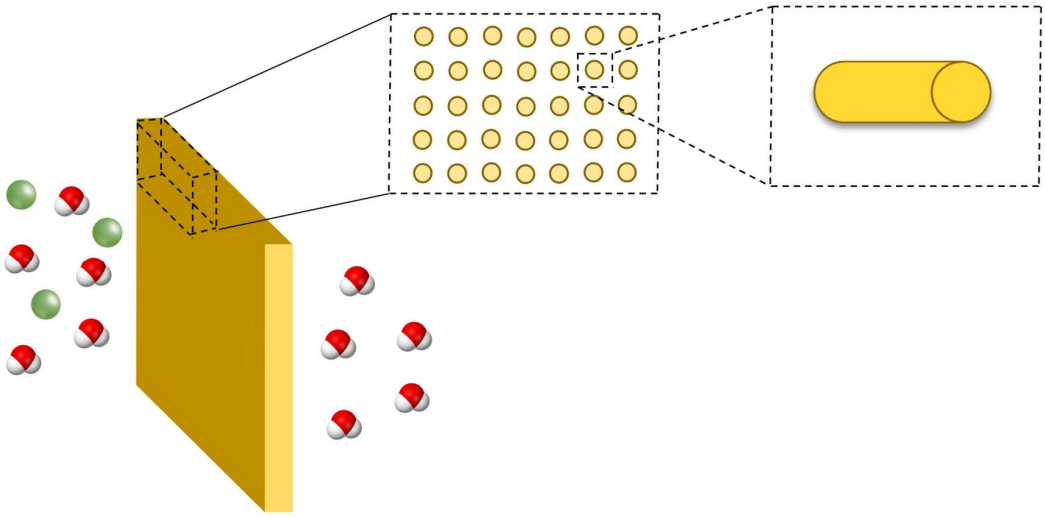

A) B) C)

Figure 5-1 Schematic of a A) membrane, B) network of pores, and C) cylindrical pore.

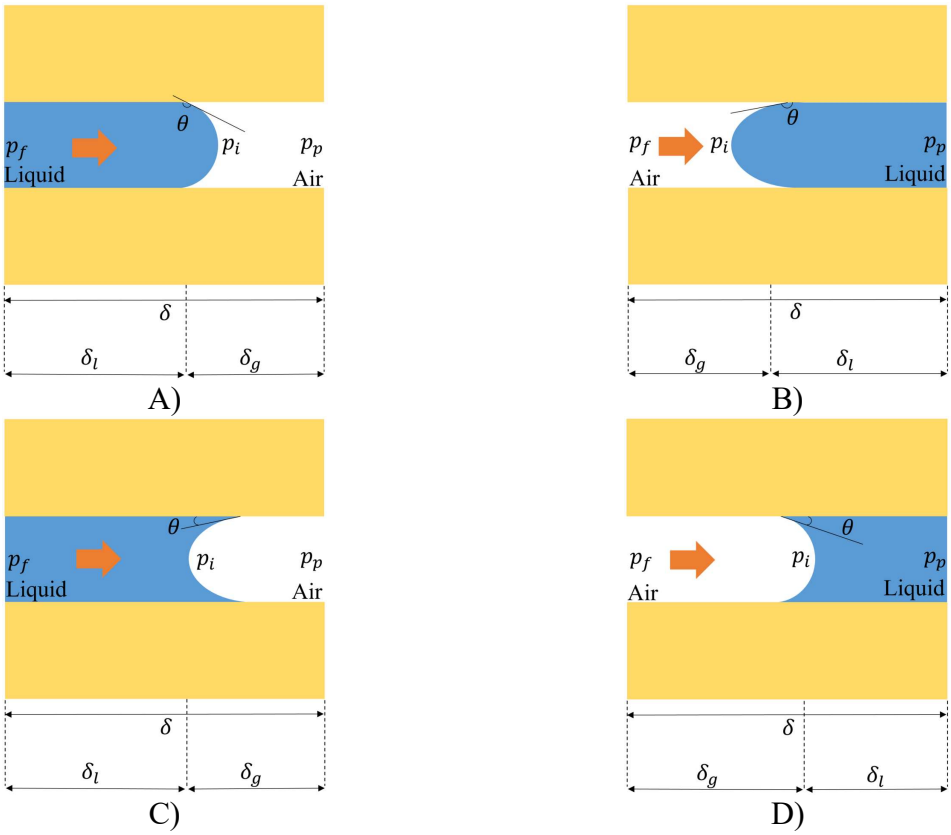

Figure 5-2 Different cases studied: A) case (1): liquid water replaces air (contact angle (θ) $\geq$ 90°), B) case (2): air replaces liquid water (contact angle (θ) $\geq$ 90 °), C) case (3): liquid water replaces air (contact angle (θ) $\leq$ 90 °) and D) case (4): air replaces liquid water (contact angle (θ) $\leq$ 90°) in a single pore.

First, the model development is described for cases (1) and (3), i.e. liquid water replaces air in the pore. Note that for case (1), $\theta \geq 90°$, and for case (3), $\theta < 90°$. Water flow inside a uniform cylindrical pore can be described by the Poiseuille model when the concentration gradient across the membrane is not significant [18]. This assumption is justified since in this study, we are dealing with pure water and there is no concentration gradient. Thus, volumetric flow rate, Q_l (m^3/s), of water can be given by Eq. 5.10 [19,20]:

$$Q_l = \frac{\pi r^4}{8\eta_l \delta_l} \Delta p_l \tag{5.10}$$

where r (m), η_l (Pa s), δ_l (m), Δp_l (Pa) are pore radius, viscosity of water, length of liquid phase, and the driving force for the movement of water, respectively. The driving force can be calculated using Eq. 5.11, obtained from force balance [19]:

$$\Delta p_l = p_f - p_i + p_c \tag{5.11}$$

where p_f (Pa) and p_i (Pa) are the feed pressure and the pressure at the water/air interface, respectively, and p_c (Pa) is the capillary pressure given by Eq. 5.3, with σ and θ in (N/m) and (°), respectively.

The assumption of Poiseuille flow (liquid phase) for the pore sizes studied in this work can be justified since the minimum pore radius with which the modeling was carried out was 10^{-7} m. In accordance with a work by Huang *et al*. [21], NSG-GO nanochannels with uniform pore size distribution of 3-5 nm showed a typical viscous flow obeying Poiseuille's law. In addition, there are several classical examples of using the Poiseuille flow for moving liquid in the capillary [8,9].

On the other hand, transport of gasses through the membrane pores can be described by several mechanisms, including Poiseuille flow, Knudsen diffusion, Surface diffusion, Slip flow, etc., depending on the pore radius of the membrane (r) and mean free path of the molecules (λ) [22]. When the pore radius is much greater than λ, the transport of gasses through the pore obeys Poiseuille flow [22]. Since under the standard atmospheric conditions, the value of λ for air molecules is 65 nm [23], which is much smaller than the minimum pore radius studied in this research, Poiseuille equation is safely applicable. Hence, the volumetric flow rate (m^3/s) of a compressible ideal gas in the isothermal condition is given by [24]:

$$Q_g = \frac{\pi r^4}{16 \eta_g \delta_g} \times \frac{\left(p_i^2 - p_p^2\right)}{p_p} \tag{5.12}$$

where η_g (Pa s), δ_g (m), and p_p (Pa) are viscosity of air, length of air phase, and pressure at pore exit, respectively. It should be mentioned that for the temperature of 298 K and pressure below 2.5 atm, with which this study was done, the assumption of ideal gas can be justified. In addition, the meniscus of liquid/vapor interface does not affect the pressure at the interface. The applicability of this assumption was checked by calculating the ratio of pressure divided by the affected pressure using the Kelvin equation (ratio of pressure divided by the affected pressure was equal to 1, meaning that the meniscus of liquid/vapor interface does not affect pressure). It should also be noted that the above equation calculates the volumetric flow rate of ideal gas at the pore exit. The molar flow rate is $Q_g \times \frac{p_p}{RT}$, which is also the same as the molar flow rate at the water/air interface. Then, the volumetric flow rate at the interface is:

$$Q_g \times \frac{p_p}{RT} \times \frac{RT}{p_i} = \frac{\pi r^4}{16\eta_g \delta_g} \times \frac{\left(p_i^2 - p_p^2\right)}{p_i} \tag{5.13}$$

The velocity, J (m/s), can be calculated using Eq. 5.14:

$$J = \frac{Q}{\pi r^2} \tag{5.14}$$

Considering that the velocity of water and air are equal at the water/air interface [25],

$$J_i = \frac{r^2}{8\eta_l \delta_l} \times \left(p_f - p_i + \frac{2\sigma \cos\theta}{r}\right) = \frac{r^2}{16\eta_g \delta_g} \times \frac{\left(p_i^2 - p_p^2\right)}{p_i} \tag{5.15}$$

where J_i (m/s) is the interfacial velocity. Rearranging Eq. 5.15, the ratio of water to air length is:

$$\frac{\delta_l}{\delta_g} = \frac{\frac{2r^2}{\eta_l} \times \left(p_f - p_i + \frac{2\sigma \cos\theta}{r}\right)}{\frac{r^2}{\eta_g} \times \frac{\left(p_i^2 - p_p^2\right)}{p_i}} \tag{5.16}$$

Since the total pore length, δ (m) is equal to:

$$\delta = \delta_l + \delta_g \tag{5.17}$$

and by setting x (-), as the fraction of the length of water, Eq. 5.19 is obtained.

$$x = \frac{\delta_l}{\delta} \tag{5.18}$$

$$x = \frac{\dfrac{\dfrac{2r^2}{\eta_l} \times \left(p_f - p_i + \dfrac{2\sigma\cos\theta}{r}\right)}{\dfrac{r^2}{\eta_g} \times \dfrac{\left(p_i^2 - p_p^2\right)}{p_i}}}{1 + \dfrac{\dfrac{2r^2}{\eta_l} \times \left(p_f - p_i + \dfrac{2\sigma\cos\theta}{r}\right)}{\dfrac{r^2}{\eta_g} \times \dfrac{\left(p_i^2 - p_p^2\right)}{p_i}}} \tag{5.19}$$

Eq. 5.19 allows the calculation of p_i as a function of x (and vice versa), for a given set of parameters such as p_f, θ and r. For η_l and σ, viscosity of water and surface tension (0.89×10^{-3} Pa s [26] and 72×10^{-3} N/m [27], respectively, at 25°C) and for η_g, the viscosity of air (18.4×10^{-6} Pa s at 25°C [28]) are used. Upon knowing p_i and x, interfacial velocity, J_i, can be calculated using Eq. 5.15. Furthermore, the time required for liquid water to flow from the pore entrance to the pore exit, t_{pass} (s), is calculated by:

$$t_{pass} = \delta \times \int_0^1 \frac{dx}{J_i} \tag{5.20}$$

For cases (2) and (4), where air replaces liquid water, Eqs. 5.21 and 5.22 are used instead of Eqs. 5.10 (together with Eqs. 5.11 and 5.3) and 5.12 to calculate the volumetric flow rate of water and air (m^3/s), respectively.

$$Q_l = \frac{\pi r^4}{8\eta_l\delta_l} \times \left(p_i - p_p - \frac{2\sigma\cos\theta}{r}\right) \tag{5.21}$$

$$Q_g = \frac{\pi r^4}{16\eta_g \delta_g} \times \frac{\left(p_f^2 - p_i^2\right)}{p_i} \tag{5.22}$$

Interfacial velocity is therefore,

$$J_i = \frac{r^2}{8\eta_l \delta_l} \times \left(p_i - p_p - \frac{2\sigma\cos\theta}{r}\right) = \frac{r^2}{16\eta_g \delta_g} \times \frac{\left(p_f^2 - p_i^2\right)}{p_i} \tag{5.23}$$

Furthermore, by defining y as the fraction of air length, Eq. 5.25 is obtained.

$$y = \frac{\delta_g}{\delta} \tag{5.24}$$

$$y = \frac{1}{1 + \frac{\frac{2r^2}{\eta_l} \times \left(p_i - p_p - \frac{2\sigma\cos\theta}{r}\right)}{\frac{r^2}{\eta_g} \times \frac{\left(p_f^2 - p_i^2\right)}{p_i}}} \tag{5.25}$$

The pressure at the interface, p_i, can be calculated as the function of y, and then the interfacial velocity, J_i, is calculated by using Eq. 5.23. The time required for air to flow from pore entrance to pore exit is calculated by:

$$t_{pass} = \delta \times \int_0^1 \frac{dy}{J_i} \tag{5.26}$$

5.4. Results and discussion

Figure 5-3 shows the results of the calculation for a set of parameters given in the caption (case (1)). Figure 5-3 (p_i vs. x) shows that interfacial pressure, p_i, decreases quickly as the interface moves toward the pore exit, approaching the permeate pressure, p_p, of 101325 Pa (1 atm). Also, in Figure 5-3 (J_i vs. x), interfacial velocity, J_i, also decreases quickly, approaching near zero at the pore outlet.

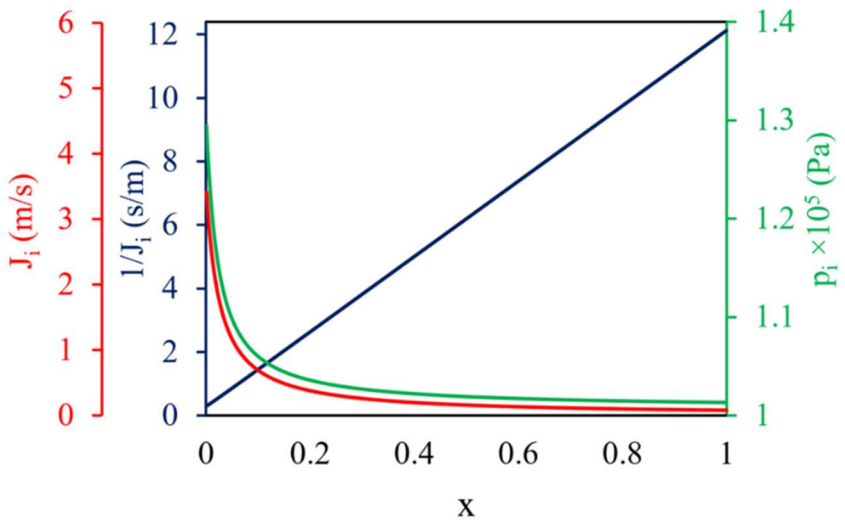

Figure 5-3 Simulation results for case (1), liquid water replaces the air, pore radius (r) = 10^{-6} m, contact angle (θ) = 120°, membrane thickness (δ) = 50×10^{-6} m, and feed pressure (p_f) = 202650 Pa, p_i vs. x, J_i vs. x and $1/J_i$ vs. x.

Interestingly, $1/J_i$ has a linear relationship versus x (Figure 5-3). The meaning of the linear relationship is as follows. Since $p_i \cong p_p$ in most of x, Eq. 5.15 can be approximated by:

$$J_i = \frac{\left[(p_f - p_p) + \frac{2\sigma\cos\theta}{r}\right](r^2)}{8\eta_l\delta_l} \tag{5.27}$$

Hence,

$$\frac{1}{J_i} = \frac{8\eta_l\delta}{\left[(p_f - p_p) + \frac{2\sigma\cos\theta}{r}\right](r^2)}x = \alpha x \tag{5.28}$$

where α is the slope of $\frac{1}{J_i}$ versus x, which is constant.

$$\alpha = \frac{8\eta_l\delta}{\left[(p_f - p_p) + \frac{2\sigma\cos\theta}{r}\right](r^2)} \tag{5.29}$$

On the other hand,

$$J_i = \frac{d\delta_l}{dt} = \frac{\delta dx}{dt} \tag{5.30}$$

Combining Eq. 5.28 and Eq. 5.30 and rearranging:

$$xdx = \frac{1}{\alpha\delta} dt \tag{5.31}$$

Integrating with $x = 0$ at $t = 0$,

$$x^2 = \frac{2}{\alpha\delta} t \tag{5.32}$$

$$x = \sqrt{\frac{2}{\alpha\delta}} t^{1/2} \tag{5.33}$$

And combining Eq. 5.29 and Eq. 5.33:

$$\delta_l = \sqrt{\frac{2\delta}{\alpha}} t^{1/2} = \sqrt{\frac{\left[(p_f - p_p) + \frac{2\sigma\cos\theta}{r}\right](r^2)}{4\eta_l}} t^{1/2} \tag{5.34}$$

which is the same as Eq. 5.6. Therefore, Washburn's equation is considered to be an approximation by assuming $p_i = p_p$. This is allowed since air can move with much smaller driving force (pressure difference) than water.

The linear relationship of $\frac{1}{J_i}$ versus x (Figure 5-3) has another merit. $\int_0^1 \frac{dx}{J_i}$ is the area below the linear straight line, which can readily be obtained, and t_{pass} can be calculated by multiplying $\int_0^1 \frac{dx}{J_i}$ by δ. It is 3.09×10^{-4} s for this particular case.

Figure 5-4A shows the effect of pore radius, r, on $J_{i,ave}$ that is defined as $1/\int_0^1 \frac{dx}{J_i}$. From figure $J_{i,ave}$ increases as r increases. Figure 5-4A also shows that t_{pass} diminishes as r increases. Water reaches the pore exit almost instantly since the thickness of the membrane is as small as 50×10^{-6} m. However, t_{pass} should obviously depend on the feed pressure, p_f. t_{pass} will increase as p_f decreases and become the maximum when p_f is just above the pressure required for the liquid entry to the pore, which is $p_p - \frac{2\sigma\cos}{r}$. Under the conditions given in Figure 5-3 caption, $p_p - \frac{2\sigma\cos\theta}{r} =$ 173325 Pa. It was found that at p_f = 173600 Pa, t_{pass} was 0.03 s. Hence, t_{pass} is, at most, a fraction of a second. This short time coincides with the results of several pieces of research suggesting that the fluid would pass the pore very fast [16,29].

According to Smolder *et al.*'s method to measure the LEP of water [1,2], we shall wait for 10 min at a set feed pressure, which is far longer than the time required for the passage of water through the membrane pore.

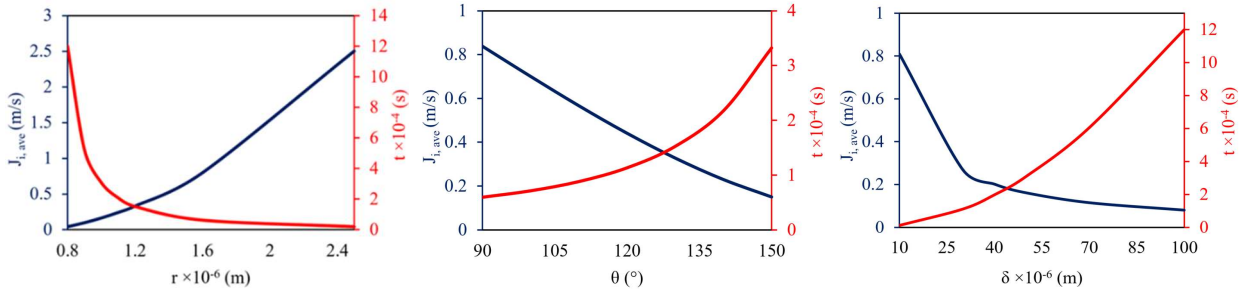

Figure 5-4 Liquid water replaces the air in the pore (contact angle (θ) ≥ 90 °): The influence of A) pore radius (r), B) contact angle (θ), and C) membrane thickness (δ) on average velocity of interface ($J_{i,ave}$) and time required for passing the pore (t_{pass}), [A): θ= 120°, δ = 50×10^{-6} m, p_f=202650 Pa, B): r = 10^{-6} m, δ = 50×10^{-6} m, p_f=253312 Pa, and C): r = 10^{-6} m, θ= 120°, p_f=202650 Pa].

Figure 5-4B shows that $J_{i,ave}$ decreases, whereas t_{pass} increases as θ increases. This is because the capillary force working against the advance of water/air interface increases. Figure 5-4C shows

that $J_{i,ave}$ decreases as δ increases. This is because the flux of both liquid and gas phases is inversely proportional to the length of the corresponding phase (Eqs. 5.10 and 5.12). Moreover, t_{pass} has also an increasing trend due to the increased δ (Eq. 5.20). Increase in time is also intensified due to the decreased average velocity, $1/\int_0^1 \frac{dx}{J_i}$, explained above (Eq. 5.20).

The effects of these effective parameters are summarized with an approximation ($p_i = p_p$) by the following approach. $J_{i,ave}$ can be calculated using Eq. 5.28 as follows:

$$\int_0^1 \frac{dx}{J_i} = \frac{8\eta_l \delta}{\left[(p_f - p_p) + \frac{2\sigma \cos}{r}\right](r^2)} \int_0^1 x\, dx$$

$$= \frac{4\eta_l \delta}{\left[(p_f - p_p) + \frac{2\sigma \cos}{r}\right](r^2)} \tag{5.35}$$

Thus,

$$J_{i,ave} = 1/\int_0^1 \frac{dx}{J_i} = \frac{\left[(p_f - p_p) + \frac{2\sigma \cos\theta}{r}\right](r^2)}{4\eta_l \delta} \tag{5.36}$$

and from Eqs. 5.20 and 5.35:

$$t_{pass} = \delta \times \int_0^1 \frac{dx}{J_i} = \frac{4\eta_l \delta^2}{\left[(p_f - p_p) + \frac{2\sigma \cos\theta}{r}\right](r^2)} \tag{5.37}$$

Eq. 5.36 indicates that $J_{i,ave}$:

1) increases as $(p_f - p_p)$ increases,
2) increases as r increases,
3) decreases as θ increases,
4) decreases as δ increases,

while t_{pass} shows opposite trends (Eq. 5.37).

The results of the rigorous calculation according to the proposed model (Figures 5-4A, B and C) follow the above-mentioned trends faithfully.

Figure 5-5 shows the results of case (2) calculation. From Figure 5-5 (p_i vs. y), p_i is nearly equal to p_f in almost entire pore length. This is again because much less driving force is required to move air. But p_i decreases quickly near the pore exit. Interestingly, the pressure becomes less than the pressure at the pore exit, p_p, which is the atmospheric pressure (101325 Pa). This is because driving force to move water can be positive ($\Delta p_l > 0$) even when $p_i < p_p$ (see Eq. 5.21) as far as $p_i - \frac{2\sigma \cos\theta}{r} > p_p$ is satisfied, which is possible since $\theta = 120^o$. It suggests that the membrane pore may shrink under the vacuum, a phenomenon which has already been observed for hydrophobic membranes [30], although it has not been ascribed to pressure decrease inside the pore. Shrinkage due to the capillary pressure changes has been also observed in other fields. For instance, in fresh cement-based materials subjected to evaporation at an open surface, as water content near the surfaces decreases, a negative capillary pressure occurs which results in shrinkage and probably cracking [31]. Also, *Ji* is very low in most part of the pore but increases quickly at the end of the pore. The linear relationship holds again between $1/J_i$ and y. This is because p_i remains nearly equal to p_f in the most part of the pore. But this time $1/J_i$ decreases with y.

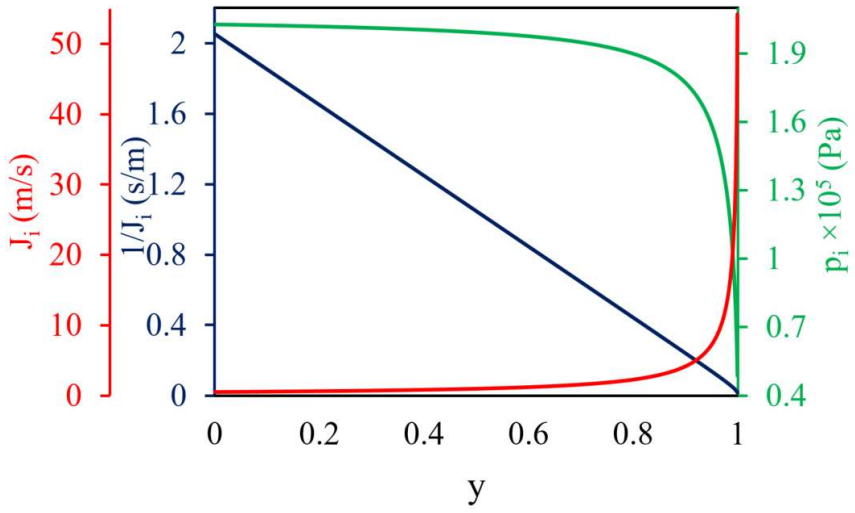

Figure 5-5 Simulation results for case (2), air replaces the liquid water, pore radius (r) = 10^{-6} m, contact angle (θ) = 120°, membrane thickness (δ) = 50×10^{-6} m, and feed pressure (p_f) = 202650 Pa, p_i vs. y, J_i vs. y and $1/J_i$ vs. y.

Since $p_i \cong p_f$ in most parts of the pore, Eq. 5.23 can be approximated by:

$$J_i = \frac{r^2}{8\eta_l \delta_l} \times \left(p_f - p_p - \frac{2\sigma\cos\theta}{r}\right) \tag{5.38}$$

Then,

$$J_{i,ave} = 1/\int_0^1 \frac{dx}{J_i} = \frac{\left[(p_f - p_p) - \frac{2\sigma\cos}{r}\right](r^2)}{4\eta_l \delta} \tag{5.39}$$

And t_{pass} can be estimated by:

$$t_{pass} = \delta \times \int_0^1 \frac{dx}{J_i} = \frac{4\eta_l \delta^2}{\left[(p_f - p_p) - \frac{2\sigma\cos}{r}\right](r^2)} \tag{5.40}$$

Eq. 5.39 indicates that $J_{i,ave}$:

1) increases as $(p_f - p_p)$ increases,

2) increases as r increases,
3) increases as θ increases, because capillary force works for the advance of water/air interface (the effect of θ is now opposite to case 1),
4) decreases as δ increases,

while t_{pass} shows opposite trends (Eq. 5.40).

It should be noted that the effects of the above parameters were also studied without approximation (p_i was not equal to p_f) and the trends were exactly the same as described above with some changes in numerical values.

According to Eq. 5.40, t_{pass} becomes 5×10^{-5} s under the condition given in Figure 5-5 caption. Even when pore radius is reduced ten times, i.e. $r = 10^{-7}$ m, while maintaining other parameters constant, t_{pass} is as small as 0.001 s. In a study carried out to remove water from a wetted hydrophobic membrane, pressurized air was employed to push water through the membrane pores. It was suggested that this method was capable of restoring the membrane to a large extent by forcing trapped water out in several seconds [32]. It should be noted that the tortuosity of the membrane used in the above study was not equal to 1, increasing the time required for restoring the membrane largely.

Figure 5-6 is for case (3) where water replaces air. Note that θ is less than 90° and, unlike case (1), water is drawn into the pore by the capillary force. As well, the feed pressure is 101325 Pa (1 atm) which is the same as the permeate pressure. Due to the quick entry of liquid, Figure 5-6 shows that the interfacial pressure, p_i, becomes higher than the feed pressure, which may lead to the expansion of the pore. But p_i quickly reduces to the permeate pressure, p_p, and as a result, J_i also quickly

approaches an asymptotic value. A linear relationship is also found in $1/J_i$ versus x. Therefore, Eqs. 5.36 and 5.37 are also applicable in case (3).

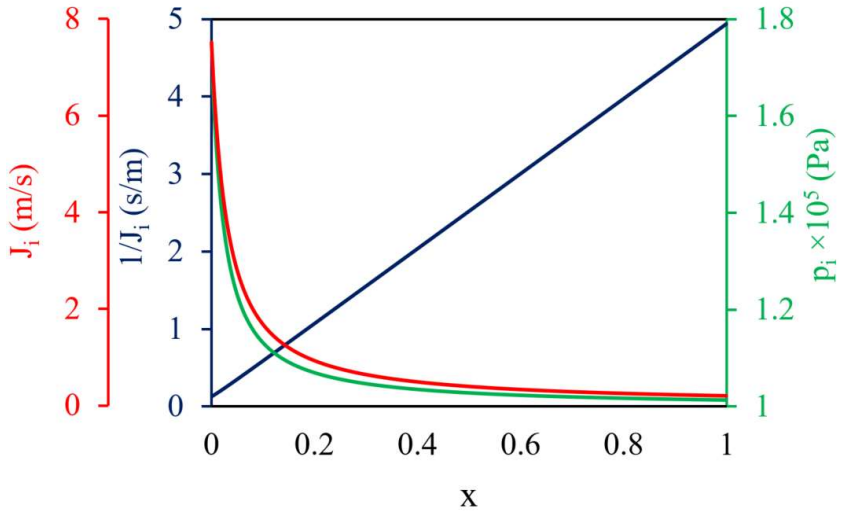

Figure 5-6 Simulation results for case (3), liquid water replaces the air, pore radius (r) = 10^{-6} m, contact angle (θ) = 60°, membrane thickness (δ) = 50×10^{-6} m, and feed pressure (p_f) = 101325 Pa, p_i vs. x, J_i vs. x and $1/J_i$ vs. x.

As mentioned above, pressure build-up occurs for this case, i.e. case (3) (Figure 5-6 (p_i vs. x)), at the interface which might contribute to the swelling phenomena in hydrophilic membranes. For instance, polyvinyl alcohol (PVA) membrane as a hydrophilic polymer is vulnerable to swelling. This drawback can be overcome by crosslinking reactions by consuming some of the OH groups responsible for hydrophilicity [33]. Therefore, the swelling degree is decreased by increasing the hydrophobicity. Herein also the same trend was observed for pressure build-up, i.e. pressure build-up was intensified by decreasing θ (Figure 5-7). Therefore, probably a portion of swelling might be caused by this predicted high interfacial pressure. This theory needs to be investigated more since the displacement of the interface occurs in a fraction of second.

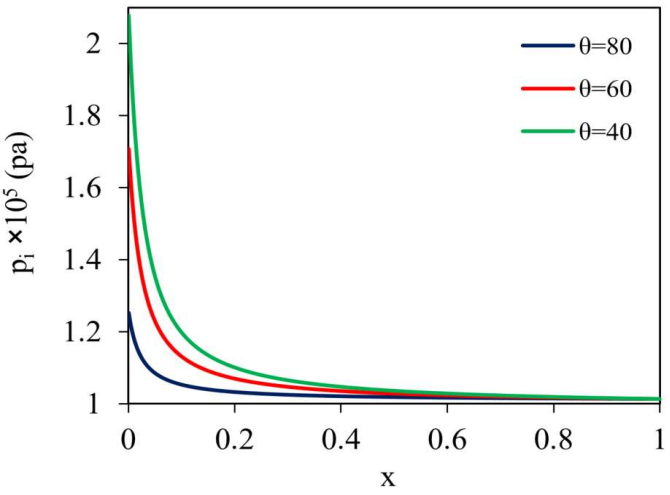

Figure 5-7 Liquid water replaces the air in the pore (contact angle (θ) ≤ 90°): The influence of contact angle (θ) on the interfacial pressure (p_i); pore radius (r) = 10^{-6} m, membrane thickness (δ) = 50×10^{-6} m, and feed pressure (p_f) = 101325 Pa.

Comparing Figure 5-3 (J_i vs. x) of case (1) and Figure 5-6 (J_i vs. x) of case (3), J_i is generally larger in the latter case even though the feed pressure is lower. This is because the effect of the capillary pressure surpasses that of the feed pressure in this case.

Figure 5-8 shows the results of calculation for air replacing water. The membrane is hydrophilic and θ is less than 90°, which is case (4). Figure 5-8 illustrates that p_i remains close to the feed pressure for most of the pore and quickly diminishes near the pore exit. But, unlike Figure 5-5, p_i does not become less than the permeate pressure near the pore exit. In other words, vacuum is not generated in the pore and pore shrinkage is less likely. This is because air should drive water against the capillary pressure that tends to draw water into the pore. J_i tends to increase steeply near the pore exit (Figure 5-8) but compared to Figure 5-5, J_i values are much smaller. Again, a linear relationship is found between 1/ J_i and y, which validates Eqs. 5.39 and 5.40.

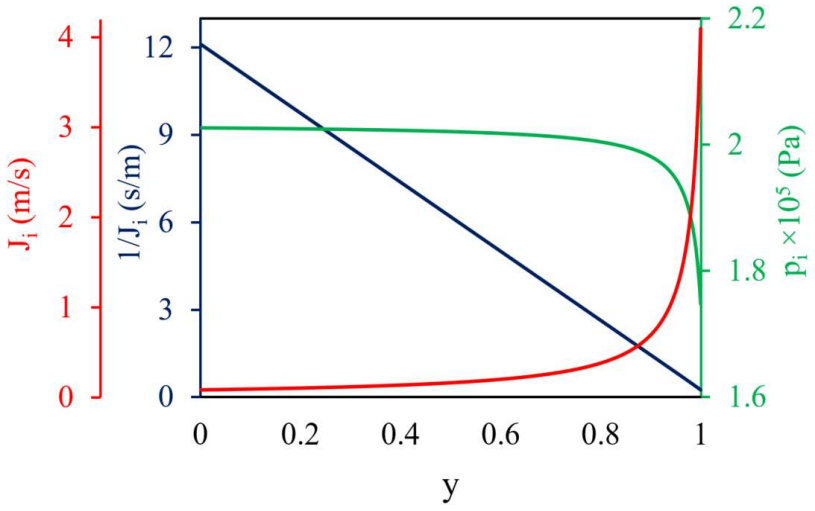

Figure 5-8 Simulation results for case (4), air replaces the liquid water, pore radius (r) = 10^{-6} m, contact angle (θ) = 60°, membrane thickness (δ) = 50×10^{-6} m, and feed pressure (p_f) = 202650 Pa, p_i vs. y, J_i vs. y and $1/J_i$ vs. y.

It should be noted that in this case, a high feed pressure should be applied to drive the air/water interface toward the pore exit and maintain the term $\left(p_f - p_p - \frac{2\sigma\cos\theta}{r}\right)$ in Eq. 5.39 positive. For example, at $r = 10^{-7}$ m and $\theta = 40^o$ feed pressure as high as 12×10^5 Pa should be applied.

5.5. Comparison with experimental data in the literature

Fisher and Lark examined the validity of Washburn's equation by measuring the speed of the movement of cyclohexane and water in horizontal Pyrex glass capillaries of various radii [34]. The experimental results for water flow were summarized in Figure 3 of their work as a straight-line relationship between $\frac{l^2}{t}$ versus r, where l is the distance of water movement in the capillary at time t, which is the same as δ_l of our work. They reported that the slope, $\frac{l^2}{tr}$, obtained from the experimental data was 31.4 m/s, while the theoretical value obtained by Washburn's equation was

36.3 m/s, using $\sigma = 7.27 \times 10^{-2}$ N/m and $\eta_l = 0.001$ Pa s. Thus, the theoretical value was 15 % higher than the experimental one. According to our model calculation (without approximation), t_{pass} for the pore with a radius of 3×10^{-6} m and a length of 50×10^{-6} m is calculated to be 2.33×10^{-5} s. Therefore, the slope of $\frac{l^2}{t}$ versus r will become $\frac{(50\times10^{-6})^2}{(2.33\times10^{-5})\times(3\times10^{-6})} = 35.7$ m/s, which is about 2 % lower than the value calculated by Washburn's equation. Therefore, at least a part of the lowered experimental value can be ascribed to the slower capillary movement of water caused by the interfacial air pressure that is higher than the permeate pressure.

5.6. Conclusion

In this study, model equations for the transport of liquid and gas phases through the membrane pores were derived to track the water/air (or air/water) interface inside the pore. The model could predict the velocity and pressure at the water/air (or air/water) interface inside the hydrophilic or hydrophobic membrane pore under different circumstances, i.e. liquid water replaces air or air replaces liquid water. The model was further compared with the experimental data in the literature and the following conclusions were drawn:

1) The model developed in this work can describe the movement of water/air interface in a capillary.
2) The model allows the calculation of the change of interfacial pressure as the interface moves from the pore entrance to the pore exit.
3) When water replaces air in the air-filled membrane pore, the interfacial pressure is nearly equal to the permeate pressure in most parts of the pore, which justifies the approximation made in the Washburn equation.

4) When air replaces water in the water-filled membrane pore, the interfacial pressure is nearly equal to the feed pressure.
5) When air replaces water in the water-filled pore of hydrophobic membrane, the interfacial pressure may become lower than the permeate pressure near the pore exit.
6) When water replaces air in the air-filled pore of hydrophilic membrane, the interfacial pressure may become higher than the feed pressure near the pore entrance.
7) The time required for the interface to pass the entire pore length of the thin film is at most a fraction of second, which justifies Smolder's method for the measurement of LEP of water for membrane distillation and the bubble point method for the determination of membrane pore size and pore size distribution.

5.7. References

[1] K. Smolders, A.C.M. Franken, Terminology for membrane distillation, Desalination. 72 (1989) 249–262. doi:10.1016/0011-9164(89)80010-4.

[2] G. Rácz, S. Kerker, Z. Kovács, G. Vatai, M. Ebrahimi, P. Czermak, Theoretical and experimental approaches of liquid entry pressure determination in membrane distillation processes, Period. Polytech. Chem. Eng. 58 (2014) 81–91. doi:10.3311/PPch.2179.

[3] Trägårdh G., Characterization methods for ultrafiltration membranes, Desalination 53 (1985) 25-35, doi: 10.1016/0011-9164(85)85050-5.

[4] A. Bottino, G. Capannelli, P. Petit-Bon, N. Cao, M. Pegoraro, G. Zoia, Pore size and pore-size distribution in microfiltration membranes, Sep. Sci. Technol. 26 (1991) 1315–1327. doi:10.1080/01496399108050534.

[5] B.-S. Kim, P. Harriott, Critical entry pressure for liquids in hydrophobic membranes, J. Colloid Interface Sci. 115 (1987) 1–8. doi:10.1016/0021-9797(87)90002-6.

[6] A.T. Servi, J. Kharraz, D. Klee, K. Notarangelo, B. Eyob, E. Guillen-Burrieza, A. Liu, H.A. Arafat, K.K. Gleason, A systematic study of the impact of hydrophobicity on the wetting of MD membranes, J. Membr. Sci. 520 (2016) 850–859. doi:10.1016/J.MEMSCI.2016.08.021.

[7] H. Chamani, P. Yazgan-Birgi, T. Matsuura, D. Rana, M.I. Hassan Ali, H.A. Arafat, C.Q. Lan, CFD-based genetic programming model for liquid entry pressure estimation of hydrophobic membranes, Desalination. 476 (2020) 114231. doi:10.1016/j.desal.2019.114231.

[8] R. Lucas, Ueber das Zeitgesetz des kapillaren Aufstiegs von Flüssigkeiten, Kolloid-Zeitschrift. 23 (1918) 15–22.

[9] Edward W. Washburn, The dynamics of capillary flow, Phys. Rev. 17 (1921) 273–283, doi:10.1103/PhysRev.17.273.

[10] J. Guancheng, Gas Wettability of Reservoir Rock Surfaces with Porous Media, Elsevier, 2018.

[11] H. Bruus, Theoretical Microfluidics, 2006.

[12] K. Li, D. Zhang, H. Bian, C. Meng, Y. Yang, Criteria for applying the Lucas-Washburn law, Sci. Rep. 5 (2015). doi:10.1038/srep14085, 14085.

[13] T. Dang-Vu, J. Hupka, Characterization of porous materials by capillary rise method, Physicochem. Probl. Miner. Process. 39 (2005) 47–65.

[14] W.J. Zhou, C.N. Gao, Y.C. Lu, Z.C. Wang, P.C. Wu, X.F. Li, J.F. Dong, Capillary pressure of a continuous gas–oil–water flow in a horizontal micron capillary, Energy Sources, Part A Recover. Util. Environ. Eff. 38 (2016) 2471–2477. doi:10.1080/15567036.2011.585381.

[15] C.H. Bosanquet, LV. On the flow of liquids into capillary tubes , London, Edinburgh, Dublin Philos. Mag. J. Sci. 45 (1923) 525–531. doi:10.1080/14786442308634144.

[16] C.J. Ridgway, P.A.C. Gane, J. Schoelkopf, Effect of capillary element aspect ratio on the dynamic imbibition within porous networks, J. Colloid Interface Sci. 252 (2002) 373–382. doi:10.1006/jcis.2002.8468.

[17] J. Szekely, A.W. Neumann, Y.K. Chuang, The rate of capillary penetration and the applicability of the washburn equation, J. Colloid Interface Sci. 35 (1971) 273–278. doi:10.1016/0021-9797(71)90120-2.

[18] P. Marchetti, M.F. Jimenez Solomon, G. Szekely, A.G. Livingston, Molecular Separation with Organic Solvent Nanofiltration: A Critical Review, Chem. Rev. 114 (2014) 10735–10806. doi:10.1021/cr500006j.

[19] M.R. Qtaishat, T. Matsuura, Modelling of pore wetting in membrane distillation compared with pervaporation, in: Pervaporation, Vap. Permeat. Membr. Distill., Elsevier, 2015: pp. 385–413. doi:10.1016/B978-1-78242-246-4.00013-1.

[20] H. Chamani, T. Matsuura, D. Rana, C.Q. Lan, Modeling of pore wetting in vacuum membrane distillation, J. Membr. Sci. 572 (2019) 332-342. doi:10.1016/j.memsci.2018.11.018.

[21] H. Huang, Z. Song, N. Wei, L. Shi, Y. Mao, Y. Ying, L. Sun, Z. Xu, X. Peng, Ultrafast viscous water flow through nanostrand-channelled graphene oxide membranes, Nat. Commun. 4 (2013) 2979. doi:10.1038/ncomms3979.

[22] R.H. K. Scott, Industrial Membrane Separation Technology , 1st ed., Springer, 1996.

[23] E. Cha, C. Chiang, J. Enguero, J.J.K. Lee, Effect of temperature and altitude on flying height, IEEE Trans. Magn. 32 (1996) 3729–3731. doi:10.1109/20.538818.

[24] J.D. Current, Physics Related to Anesthesia, 2010.

[25] R. Scardovelli, S. Zaleski, Direct numerical simulation of free-surface and interfacial flow, Annu. Rev. Fluid Mech. 31 (1999) 567–603. doi:10.1146/annurev.fluid.31.1.567.

[26] Estimation of Liquid Dynamic Viscosity, Dortmund Data Bank. http://ddbonline.ddbst.com/VogelCalculation/VogelCalculationCGI.exe.

[27] Estimation of Surface Tension, Dortmund Data Bank. http://ddbonline.ddbst.com/DIPPR106SFTCalculation/DIPPR106SFTCalculationCGI.exe.

[28] G. Abedi, S. Abdollahpour, M.R. Bakhtiari, Aerodynamic properties of potato tubers to airflow separation from stones and clods, Int. J. Veg. Sci. 25 (2019) 87–94. doi:10.1080/19315260.2018.1478920.

[29] J. Schoelkopf, P.A.C. Gane, C.J. Ridgway, G.P. Matthews, Influence of inertia on liquid absorption into paper coating structures, Nord. Pulp Pap. Res. J. 15 (2000) 422–430. doi:10.3183/npprj-2000-15-05-p422-430.

[30] M.R. Bilad, E. Guillen-Burrieza, M.O. Mavukkandy, F.A. Al Marzooqi, H.A. Arafat, Shrinkage, defect and membrane distillation performance of composite PVDF membranes, Desalination. 376 (2015) 62–72. doi:10.1016/j.desal.2015.08.015.

[31] V. Slowik, T. Hübner, M. Schmidt, B. Villmann, Simulation of capillary shrinkage cracking in cement-like materials, Cem. Concr. Compos. 31 (2009) 461–469. doi:10.1016/j.cemconcomp.2009.05.004.

[32] D.M. Warsinger, A. Servi, G.B. Connors, M.O. Mavukkandy, H.A. Arafat, K.K. Gleason, J.H. Lienhard V, Reversing membrane wetting in membrane distillation: comparing dryout to backwashing with pressurized air, Environ. Sci. Water Res. Technol. 3 (2017) 930–939. doi:10.1039/C7EW00085E.

[33] B. Bolto, T. Tran, M. Hoang, Z. Xie, Crosslinked poly(vinyl alcohol) membranes, Prog. Polym. Sci. 34 (2009) 969–981. doi:10.1016/j.progpolymsci.2009.05.003.

[34] L.R. Fisher, P.D. Lark, An experimental study of the washburn equation for liquid flow in very fine capillaries, J. Colloid Interface Sci. 69 (1979) 486–492. doi:10.1016/0021-9797(79)90138-3.

Chapter 6

Modeling of pore wetting in vacuum membrane distillation [1]

[1] The content of this chapter has been published in: Modeling of pore wetting in vacuum membrane distillation, J. Membr. Sci. 572 (2019) 332-342.

6.1. Abstract

In this work, simulation results for the pore wetting of vacuum membrane distillation (VMD) are reported, considering heat and mass balance at liquid/vapor interface when steady state is achieved. Two cases were studied. In case 1, the system is in isothermal condition. In case 2, heat enters only from the pore inlet and is removed at the liquid/vapor interface as liquid vaporizes. The simulation has shown that the liquid/vapor boundary may remain inside the pore at the steady-state condition, which means partial pore wetting is possible. The significant temperature drop from the pore entrance to the liquid/vapor interface has also been predicted. It was found from case 2 simulation that VMD is possible in a wider range of pore radius, r, than the Laplace equation predicts.

6.2. Introduction

Due to the worldwide scarcity of drinking water predicted in the near future, the importance of sea and brackish water desalination is growing. Membrane distillation (MD) is known to be an effective process for desalination of sea and brackish water, as well as treatment of concentrated brine from reverse osmosis (RO) process, etc. [1]. Despite its promising features, MD's full-scale commercialization has not been achieved due to its serious drawback of pore wetting, which causes a significant decrease in MD flux [2-16]. Many attempts have therefore been made to mitigate or, more desirably, completely eliminate the MD pore wetting [17,18]. For example, for recognizing the relationship between the pore wetting and liquid entry pressure (LEP), detailed studies were made to evaluate LEP from the contact angle, pore length, pore entrance sharpness and pore geometry using computational fluid dynamics (CFD) tools [19]. In addition, various models have been presented for estimation of LEP, including Young-Laplace model, Purcell model, etc., which can be found in the literature [20,21]. As well, new devices were designed and constructed to

introduce air bubbles into the feed solution [22] and the pores were dewetted to regenerate and reuse the membrane [18,23].

Among many works on pore wetting, those of Gryta *et al*. seem to be the most insightful [12-14]. Gryta [12], in his comprehensive work of MD by polypropylene (PP) hollow fibers, reported that the flux increased in the very early stage of MD operation from 670 to 715 L/m^2 d. It was ascribed to the partial liquid water intrusion into the pore, which shortened the distance of vapor diffusion that controlled the overall flux. Gryta [14] further reported the possibility of partial pore wetting. He described the pore wetting of direct contact membrane distillation (DCMD) by the following four steps (see Figure 6-1): 1) Non-wetted (Figure 6-1A) 2) Surface-wetted (Figure 6-1B) 3) Partial-wetted (Figure 6-1C) and 4) Wetted (Figure 6-1D). Particularly in 2), as the distance of vapor passage decreases, the membrane flux increases. But Gryta also suggested that the flux might still decrease due to the temperature decrease at the liquid/vapor interface [14].

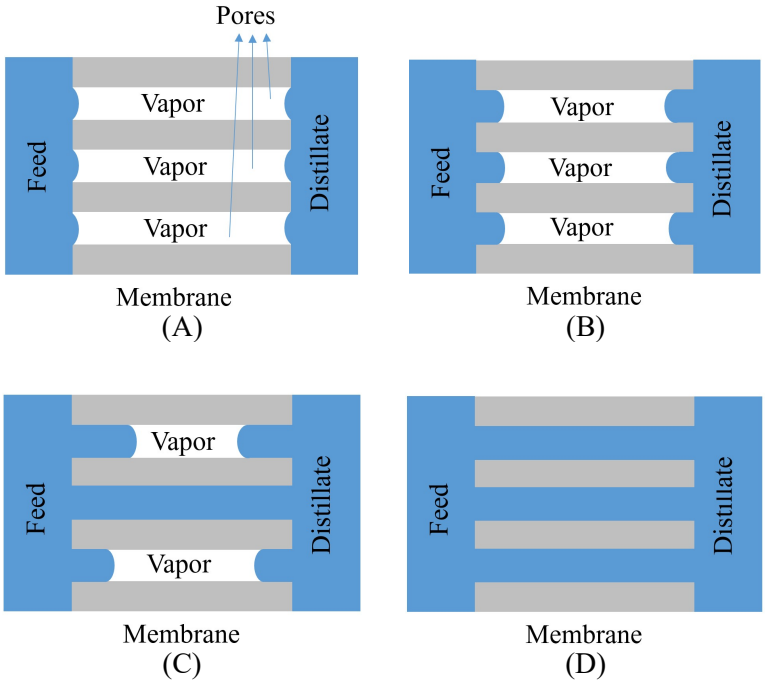

Figure 6-1 A schematic representation of various forms of membrane wettability in MD process: A) Non-wetted, B) Surface-wetted, C) Partial-wetted, and D) Wetted.

Gryta also has given the evidence of partial pore wetting experimentally by showing the concentration profiles of magnesium and calcium in the membrane's depth direction after desalination by MD [14]. Zhu *et al*. also observed the partial pore wetting of the polyvinyl alcohol (PVA)/polyvinylidene fluoride (PVDF) composite hollow fiber membrane used for DCMD by applying scanning electron microscopy (SEM) and energy-dispersive x-ray spectroscopy (EDS or EDX) [24,25]. Thus, some experiments showed that the pore was partially wetted in MD and the salt was deposited not necessarily outside but also inside the pore. It was even suggested that the temperature of water inside the pore would be lower than the feed, even though the temperature in the pore has not been measured by experiments.

In 1996 a recommendation was made by a working party on Membrane Nomenclature to International Union of Pure and Applied Chemistry (IUPAC) [26] about the TERMINOLOGY

FOR MEMBRANES AND MEMBRANE PROCESSES. In the report, “Membrane Distillation” is defined as a “distillation process in which the liquid and gas phases are separated by a porous membrane, the pores of which are not wetted by the liquid phase”.

The above IUPAC definition has clearly made impact on the MD transport theory. In the most popular theory of Schofield *et al.* [27], the concentration polarization is associated only with the hydrodynamic condition of the feed solution [28] and the concentration polarization inside the pore is largely neglected. However, the latter concentration polarization could be much severe due to the absence of liquid turbulence. Moreover, the fast evaporation of water facilitates the increase of salt concentration, which will eventually surpass the solubility limit, resulting in the deposition of salt in the pore.

Similarly, the temperature polarization in the liquid phase has been limited only to the feed and permeate boundary phase. The temperature decrease across the membrane was associated only with the heat conduction in the gas/vapor-filled membrane. The heat transfer via liquid water in the pore was not taken into consideration, even though the temperature at the liquid/vapor interface may become very low due to the slow heat conduction in liquid and fast water evaporation that carries away a large amount of heat, resulting in severe temperature polarization.

Although there are a number of works in which the heat and mass transfer in the capillary has been discussed [29], to the best of our knowledge, none of them have so far dealt with the pore wetting in MD. In other words, curiously enough, no attempts have been made so far to describe this phenomenon by developing a model that includes heat and mass transfer occurring inside the pore, with a notable exception of Qtaishat and Matsuura’s work [30] that predicted unrealistically high flux values.

The objective of this work is to fill the gap between the experimental observation and the partial pore wetting theory by investigating the effect of the presence of water in the pore on the MD flux when the pore is partially wetted with water. To this end, the steady-state MD flux is calculated under various MD conditions taking both heat and mass transfer occurring inside the pore into account. For the first phase of this attempt, vacuum membrane distillation (VMD) of pure water is considered to simplify the simulation procedure.

6.3. Model Development

The VMD transport model in a single pore is developed for the case when the steady-state condition is reached while liquid/vapor phase boundary remains inside the pore (Figure 6-2).

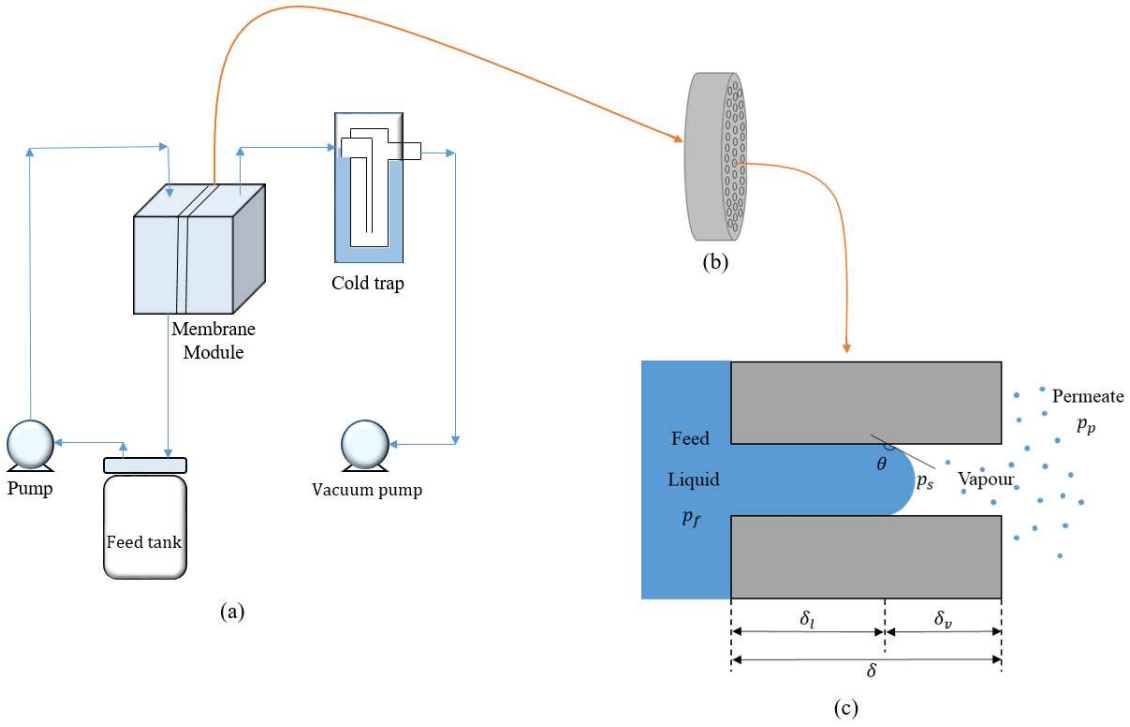

Figure 6-2 A) VMD process, B) Membrane and C) Wetting of a single pore.

The following assumptions are made for model simplification:

- The feed contains a single component.
- The pore is straight and cylindrical.
- The membrane and the mass in the pore are in isothermal condition (case 1).
- The heat enters into the mass inside the pore only from the pore entrance. The heat does not enter through the pore wall (case 2).
- Boundary layer heat transfer resistance of the feed liquid is not considered.
- The liquid mass transfer inside the pore follows the Poiseuille flow.
- The vapor mass transfer inside the pore follows the Knudsen flow.
- The meniscus of liquid/vapor interface does not affect saturation vapor pressure.
- Heat transfer in the x-direction is dominant.
- The liquid is incompressible.
- The conductive heat transfer across the membrane is negligible in VMD, since the permeate side of membrane is vacuum [31].

6.3.1. Mass transfer equation

The weight flow rate (kg/s) of vapor passing through the vapor phase can be calculated using the following equation, assuming that the vapor transport is governed by the Knudsen flow [30]:

$$N_v = \frac{r^3}{\delta_v}\left(\frac{32\pi M}{9R}\right)^{\frac{1}{2}}\Delta p_v \tag{6.1}$$

where r (m) is the pore radius, M (kg/mol) is the molecular weight, R (J/mol K) is the universal gas constant, T (K) is the absolute temperature, and δ_v (m) is the length of the vapor phase. Δp_v (Pa) is the pressure difference between the liquid/vapor interface and the downstream side of the membrane, i.e.

$$\Delta p_v = p_s - p_p \tag{6.2}$$

where p_s (Pa) is the saturation vapor pressure of water and p_p is the permeate side pressure, which is 0 in VMD.

The assumption of the Knudsen flow is justified since the highest temperature used in the model simulation is 353.2 K (=80 ºC), at which the mean free path of water is 0.333×10^{-6} m. The Knudsen number, *Kn*, is more than unity for the pores whose sizes are less than 0.333×10^{-6} m. In fact, the temperature is lower than 80 ºC, and the pressure is below the saturation vapor pressure of water at 80 ºC (=0.47355×10^{5} Pa) in a large part of the pore. Moreover, vacuum is applied on the permeate side. Therefore, the Knudsen diffusion is safely applicable in the range of pore sizes used in this study.

Considering the vapor transport near the pore exit, Eq. 6.1 was modified to [32]:

$$N_v = \frac{3\beta}{8} r^2 \left(\frac{32\pi M}{9RT}\right)^{\frac{1}{2}} \Delta p_v \tag{6.3}$$

where β is given by:

$$\beta = 1 + y^2 - y\sqrt{y^2+1} - \frac{[(2-y^2)\sqrt{y^2+1}+y^3-2]^2}{4.5y\sqrt{y^2+1}-4.5\ln[y+\sqrt{y^2+1}]} \tag{6.4}$$

where y is

$$y = \frac{\delta_v}{2r} \tag{6.5}$$

As for the liquid mass transport, the weight flow rate (kg/s) can be calculated using the following equation based on the assumption of Poiseuille flow [30]:

$$N_l = \frac{\pi\rho r^4}{8\eta\delta_l} \Delta p_l \tag{6.6}$$

where ρ (kg/m^3) is density of liquid, η (Pa s) is viscosity of liquid, δ_l (m) is the length of liquid phase inside the pore and Δp_l (Pa) is the driving force of the liquid movement, given by [30]:

$$\Delta p_l = p_f - p_s + p_c \tag{6.7}$$

In Eq. 6.7, p_f (Pa) is the hydraulic pressure of liquid at the pore entrance and p_c (Pa) is the capillary pressure:

$$p_c = \frac{2\sigma\, cos\theta}{r} \tag{6.8}$$

where σ (N/m) and θ (°) are the liquid surface tension and contact angle, respectively. Thus,

$$\Delta p_l = p_f - p_s + \frac{2\sigma\, cos\theta}{r} \tag{6.9}$$

Poiseuille flow assumption can be justified for the pore radius of above 0.005×10^{-6} m, with which the simulation was carried out. According to Huang *et al*. [33], NSG-GO nanochannels with uniform pore size distribution of 3-5 nm showed a typical viscous flow and obeyed Poiseuille's law.

Moreover, the temperature dependence of the properties of water, such as p_s, ρ, η and σ were considered in the simulation by using the following equations obtained from Dortmund Data Bank [34-37]:

$$p_s = 133.3 \times 10^{8.07131 - \frac{1730.63}{T - 39.7240}} \tag{6.10}$$

$$\rho = \frac{0.14395}{0.0112^{1+(1-\frac{T}{649.727})^{0.05107}}} \tag{6.11}$$

$$\eta = 0.001e^{-3.7188 + \frac{578.919}{-137.546 + T}} \tag{6.12}$$

$$\sigma = 0.13415(1 - T_r)^{1.6146 - 2.035\ r + 1.5598 T_r^2} \quad , \ T_r = \frac{T}{647.3} \tag{6.13}$$

where T (K) is the absolute temperature.

It should be noted that both N_v and N_l are the weight flow rate (kg/s) through a single pore. The membrane flux, J (kg/m^2 h), can be calculated by:

$$J = \frac{3600nN}{\tau} = \frac{3600\varepsilon N}{\pi r^2 \tau} \tag{6.14}$$

where n is the number of pores in 1 m^2 of effective membrane area, τ (-) is tortuosity factor and ε (-) is the porosity.

6.3.2. Heat transfer equation

The following heat transfer equation should be satisfied in the liquid phase when the system is in the steady-state condition:

$$\frac{d^2T}{dx^2} - \frac{u}{\alpha}\frac{dT}{dx} = 0 \tag{6.15}$$

where u (m/s) is velocity and

$$\alpha = \frac{k_l}{\rho c_p} \tag{6.16}$$

In Eq. 6.16, k_l (W/m K) and c_p (J/kg K) are thermal conductivity and heat capacity of water, respectively.

The differential equation (Eq. 6.15) is solved with the following boundary conditions:

at $x = 0$,

$$T = T_f \tag{6.17}$$

and at $x = \delta_l$,

$$\frac{dT}{dx} = \frac{-N_v \Delta H_v}{k_l \pi r^2} \tag{6.18}$$

where T_f (K) is feed temperature and ΔH_v (J/kg) is the heat of vaporization of water, which should be calculated at liquid/vapor interface temperature, T_s (K), by the following equation [38]:

$$\Delta H_v = 8.314 \times 647.3(5.6297\ \tau_r^{\frac{1}{3}} + 13.962\ \tau_r^{\frac{2}{3}} - 11.673\tau_r + 2.1784\ \tau_r^{2} - 0.31666\ \tau_r^{6}) \times 1000/18.02 \tag{6.19}$$

where τ_r is:

$$\tau_r = 1 - \frac{T}{647.3} \tag{6.20}$$

Assuming the properties of the water remain constant at the values corresponding to the average temperature ((T_f+T_s)/2), Eq. 6.15 can be integrated using the boundary conditions, which yields,

$$T(x) = \frac{-N_v \Delta H_v}{k_l \pi r^2} \exp\left(\frac{-u\delta_l}{\alpha}\right) \frac{\alpha}{u} \exp\left(\frac{ux}{\alpha}\right) + T_f + \frac{N_v \Delta H_v}{k_l \pi r^2} \frac{\alpha}{u} \exp\left(\frac{-u\delta_l}{\alpha}\right) \tag{6.21}$$

Since at liquid/vapor interface ($x = \delta_l$) T is equal to T_s, Eq. 6.21 can be rearranged to:

$$T_s = T_f + \left[\frac{N_v \Delta H_v}{k_l \pi r^2} \frac{\alpha}{u}\right] (\exp\left(\frac{-u\delta_l}{\alpha}\right) - 1) \tag{6.22}$$

Furthermore, substituting Eqs. 6.6, 6.16 and the following equation (Eq. 6.23) into Eq. 6.22 and considering steady-state condition ($N_l = N_v$), Eq. 6.24 is yielded.

$$u = \frac{N_l}{\rho \pi r^2} \tag{6.23}$$

$$T_s = T_f + \frac{\Delta H_v}{c_p} (\exp\left(\frac{-\rho r^2 \Delta p_l c_p}{8\eta k_l}\right) - 1) \tag{6.24}$$

6.3.3. Simulation procedure

First, Eq. 6.24 is solved to obtain T_s by iteration. For this purpose, T_s is decreased stepwise from T_f and the properties of water, including ρ , η and σ are calculated by Eqs. 6.11, 6.12 and 6.13, respectively, corresponding to the average temperature ((T_f + T_s)/2), while p_s and ΔH_v are calculated by Eqs. 6.10 and 6.19, respectively, at T_s. The T_s that satisfies Eq. 6.24 is the answer. Once T_s is known, δ_l is obtained from Eqs. 6.3 and 6.6 (N_l =N_v), again considering the temperature dependence of the properties of water. The simulation algorithm is shown in Figure 6-3. The calculation was carried out in MATLAB R2017b environment.

Herein, various scenarios were investigated in which the feed temperature and contact angle varied from 40 ºC up to 80 ºC and 87º up to 93º, respectively. Moreover, feed pressure and pore length were constant in all simulations (101300 Pa and 50×10^{-6} m, respectively). As well, simulations were carried out in the range of pore radii in which partial pore wetting occurred.

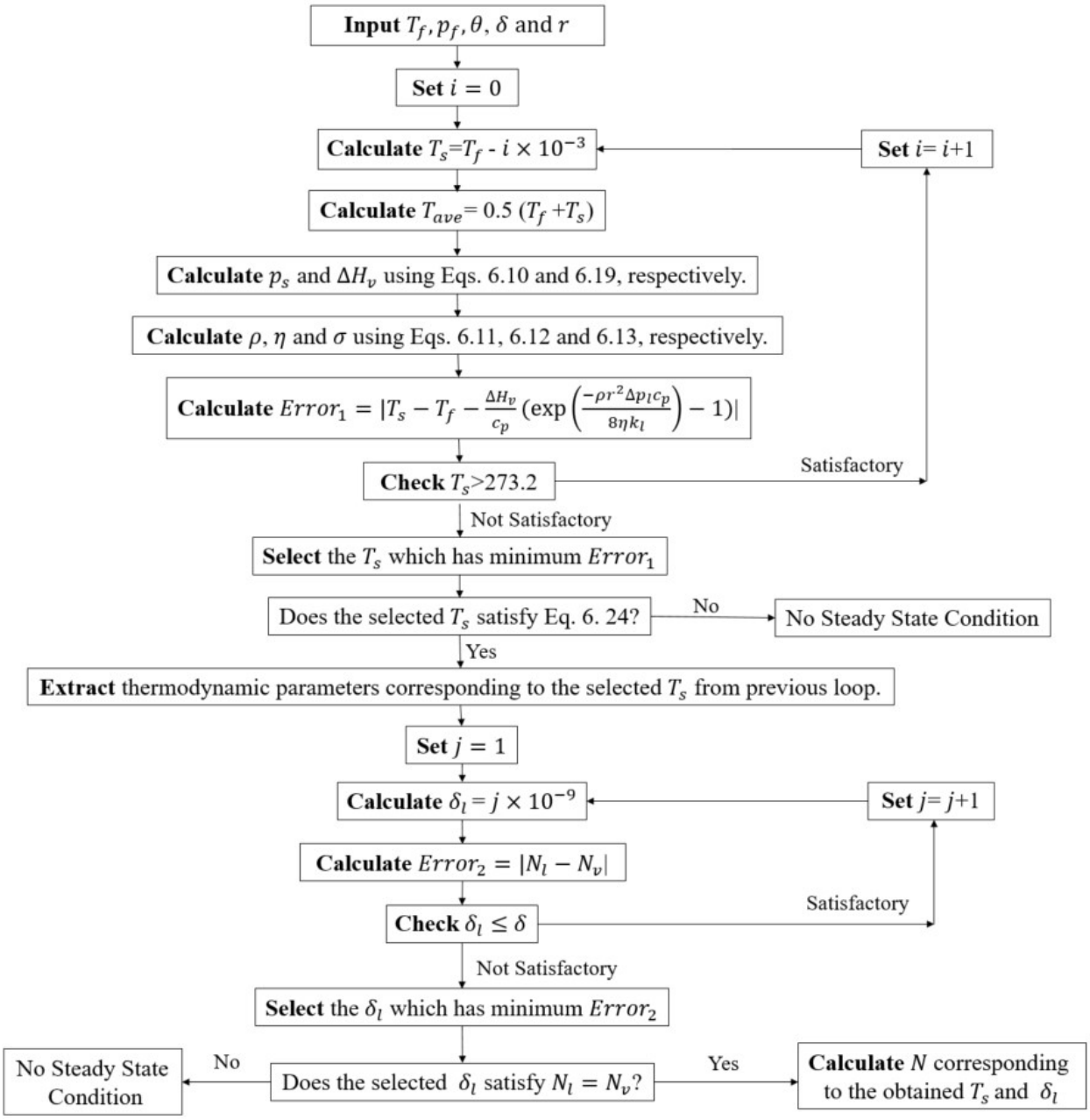

Figure 6-3 The simulation algorithm.

6.4. Results and discussion

6.4.1. The isothermal condition (case 1)

First, the simulation was attempted for the isothermal system (case 1), where T_f, θ and the total pore length, δ, were kept constant at 353.2 K (80 ºC), 93º and 50×10^{-6} m, respectively, while r was changed from about 0.07 to 0.12×10^{-6} m. Since isothermal condition is assumed, T_s is the same as T_f = 353.2 K for any r and p_s at 353.2 K is 47355 Pa. Then, from Eq. 6.7 it is found that Δp_l is negative for any r in its studied range. In other words, there is no driving force for the liquid to enter the pore and the pore is filled with vapor. This is an ordinary VMD and the mass flow rate can be calculated from Eqs. 6.1-6.5, using $\delta_v = \delta = 50\times10^{-6}$ m. The data so obtained are shown in Figure 6-4C as the dashed line.

6.4.2. Heat enters only from the pore inlet and is removed at the liquid/vapor interface (case 2)

Table 6-1 shows all the parameters with which the simulation was made for case 2. Run 1 is under the same condition as case 1 simulation. In Run 1 to 3, T_f was changed from 353.2 to 313.2 K and in Run 1, 4 to 6, θ was changed from 93 to 87º.

Table 6-1 The simulation parameters studied.

Run No.	p_f, Pa	T_f, K	θ, º	$r_{critical}$ $\times10^{-6}$, m
1	101300	353.2	93	0.1210
2	101300	333.2	93	0.0849
3	101300	313.2	93	0.0774
4	101300	353.2	91	0.0404
5	101300	353.2	89	unavailable
6	101300	353.2	87	unavailable

From the case 1 simulation, it was learned that it was important to know the sign of Δp_l because it determines the direction of the liquid movement. The *r* value that makes $\Delta p_l = 0$ is herein called $r_{critical}$, which is calculated for each run and listed in Table 6-1. Depending on $r > r_{critical}$ *or* $r < r_{critical}$ the liquid flows either towards the pore exit or pore entrance, respectively.

It is important to note that according to Eq. 6.9:

$$r_{critical} = \frac{-2\sigma \cos\theta}{p_f - p_s} \tag{6.25}$$

instead of

$$r^L_{critical} = \frac{-2\sigma \cos\theta}{p_f} \tag{6.26}$$

which is obtained by the Laplace equation. Obviously, $r_{critical}$ is larger than $r^L_{critical}$.

As well, since the driving force for the liquid entry into the pore at the pore entrance is no longer p_f but $p_f - p_s$, a higher p_f is required as LEP than what the Laplace equation predicts, and LEP increases with an increase in temperature due to the increase in p_s, which is in accordance with the result of Guillen-Burrieza *et al*. [39].

In Table 6-1 $r_{critical}$ increases with an increase in temperature, which is also obvious from Eq. 6.25 since p_s increases with temperature. It should be noted that $r_{critical}$ in Table 6-1 was obtained using p_s that corresponds to the pore entrance temperature, T_f. As the simulation results will show, T_s can be lower than T_f and hence $r_{critical}$ can be smaller than the value shown in Table 6-1.

6.4.2.1. Effect of change in feed temperature

Figure 6-4 shows the results of the steady state calculation for Run 1. Ts, δ_l and $N=N_l=N_v$ are given as the functions of *r*.

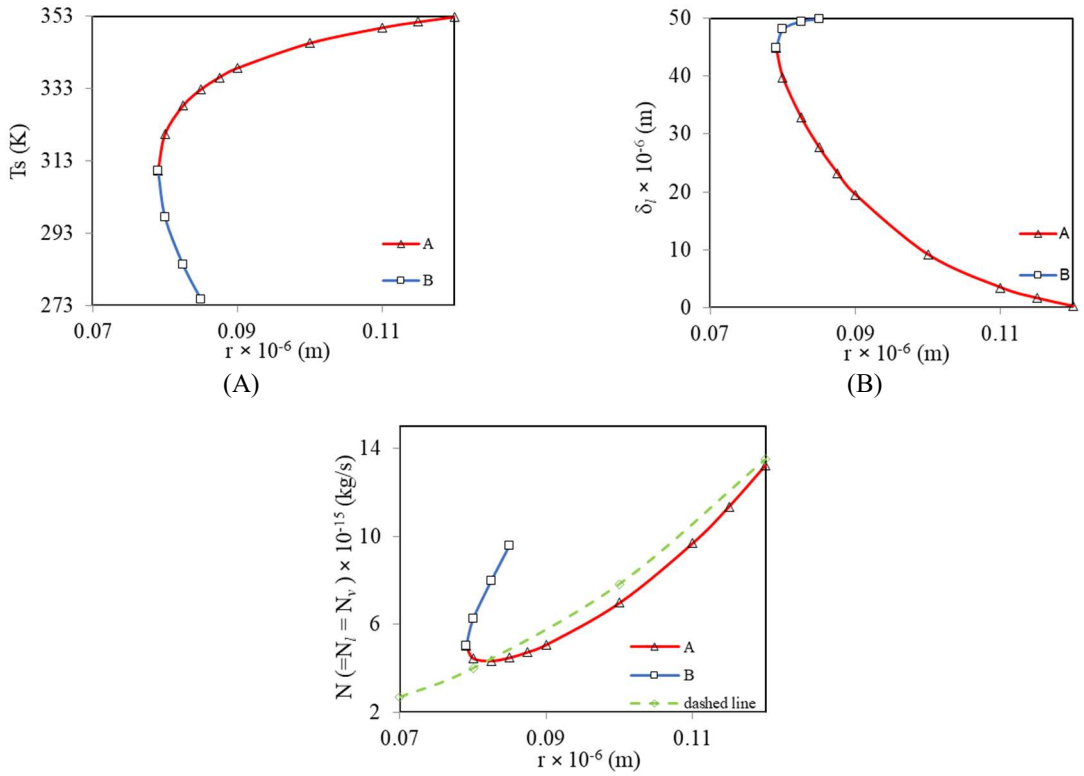

Figure 6-4 Simulation results for Run 1, at T_f = 353.2 K (80 ºC), θ = 93º and the total pore length, $\delta = 50\times10^{-6}$ m, A) T_s vs. r, B) δ_l vs. r and C) N vs. r.

Interestingly, even though r is smaller than $r_{critical}$ given in Table 6-1, δ_l is not equal to zero. This is because T_s is lower than the inlet temperature, T_f, of 353.2 K (see Figure 6-4A) and p_s is lowered and in turn Δp_l becomes positive. Furthermore, there are two solutions, for a given r, one with higher T_s (line A) and the other with lower T_s (line B), which means two T_s values were obtained when Eq. 6.24 was solved.

Both lines start from $r = 0.079\times10^{-6}$ m. The right end of line A is $r = 0.121\times10^{-6}$ m, while line B is much shorter, ending at 0.085×10^{-6} m.

When r increases along line A, T_s increases (Figure 6-4A), δ_l decreases (Figure 6-4B) and N increases (Figure 6-4C). The increase in N is mainly due to the increase of cross-sectional area caused by the increase in r.

Eventually, δ_l becomes nearly equal to zero and the liquid/vapor interface will reach the pore entrance at $r = 0.121\times10^{-6}$ m with T_s which is nearly equal to T_f. When r is beyond this value, $r > r_{critical}$ and liquid is pushed back toward the pore exit until the pore is filled with liquid.

When r increases along line B, on the other hand, T_s decreases (Figure 6-4A), δ_l increases (Figure 6-4B) and N increases (Figure 6-4C). Eventually δ_l becomes close to 50×10^{-6} m, which means the liquid/vapor interface reaches almost the exit of the pore, and N increases due to the decrease in path length of vapor. However, increase in N is not as large as expected from the remarkable decrease in vapor path length since the temperature of the liquid/vapor interface, T_s, drops. The drop in T_s is due to a large amount of heat removed by vaporization of water.

In summary, line A is featured by the high T_s, and therefore the high p_s, with a long path length of vapor transport. In contrast, line B is featured by the low T_s, and therefore the low p_s, with a short path length of vapor transport. In both, the liquid/vapor interface is found in the pore at the steady-state condition.

Let us now examine the difference between the present and conventional approach, based on the Laplace equation, under the conditions of Run 1, i.e. p_f = 101300 Pa, T_f = 353.2 K and θ = 93°. According to the conventional approach, Eq. 6.26 is solved. The result is $r^L_{critical}= 0.0646\times10^{-6}$ m. Depending on r is smaller or larger than $r^L_{critical}$, pore is filled with vapor or with liquid. The flow rate N is then calculated by applying the Knudsen and Poiseuille equation for vapor and liquid

flow, respectively, at 353.2 K, assuming the isothermal condition and the results illustrated in Figure 6-5 where *N* is shown in a logarithmic scale due to the wide range covered by *N*.

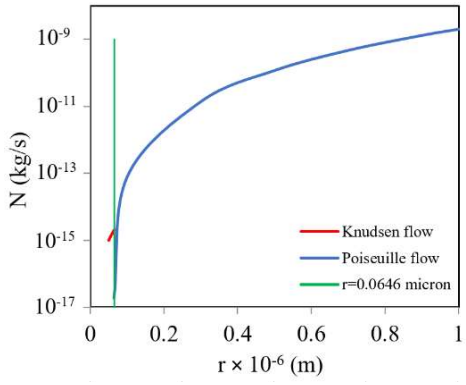

Figure 6-5 Flow rate of conventional approach, Knudsen flow (before $r^L_{critical}$) and Poiseuille flow (after $r^L_{critical}$) (logarithmic scale).

The difference between Figure 6-5 (conventional approach) and Figure 6-4 (current approach) is obvious. The critical pore size has largely shifted from $r^L_{critical}$= 0.0646×10^{-6} m of Figure 6-5 to $r_{critical}$ = 0.121×10^{-6} m and in Figure 6-4 line A and line B appear between $r^L_{critical}$ and $r_{critical}$. In Figure 6-4 the vapor diffusion calculated by the Knudsen equation is extended, as a dashed line, to the region between $r^L_{critical}$ and $r_{critical}$. Interestingly, line A is very close to the extended line, while line B lies far above the line.

Thus, according to the conventional approach based on the IUPAC's definition, *r* should be lower than 0.0646×10^{-6} m for MD to occur but based on the present approach MD may be possible even when *r* is above 0.0646×10^{-6} m.

Further, according to the conventional approach, only the boundary layer in the feed liquid, *outside the membrane*, contributes to the resistance against the heat flow (Figure 6-6A). But according to the current approach, liquid is possible to enter the pore, contributing additional heat transfer

resistance (Figure 6-6B). Thus, the heat transfer resistance in the pore may contribute to the temperature polarization significantly.

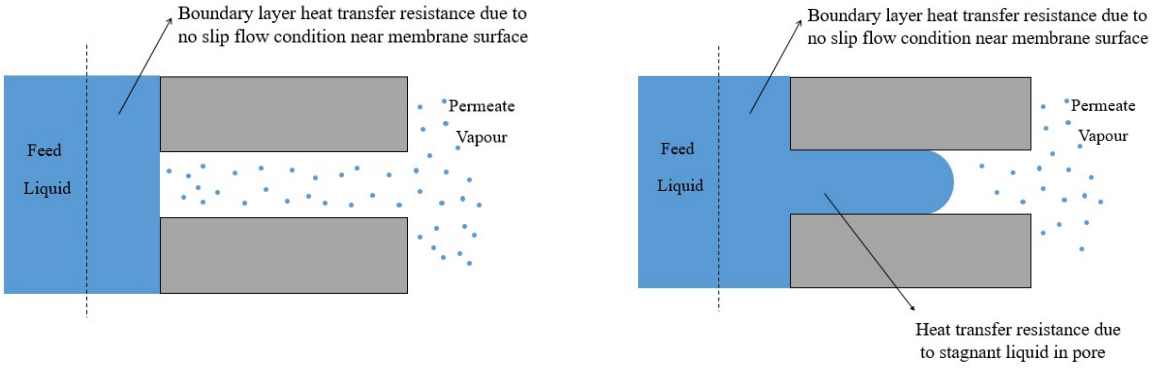

(A) (B)

Figure 6-6 Heat resistance: A) Conventional approach, and B) Current approach.

Moreover, contradictory results were observed or predicted by researchers in terms of increase or decrease in flux during wetting phenomena, e.g. Gilron *et al*. observed a temporary increase in flux due to the shorter diffusion path length [40] which can be justified through line B (Figure 6-4C), as the points on line B have higher values of vapor flow rate than those of dashed line. On the other hand, Gryta predicted permeate flux reduction due to the decrease in temperature of vapor/liquid interface [14] which can be seen using Figure 6-4C, as most of the data on line A are located under the dashed line. Consequently, we can conclude that the proposed model can justify both possible conditions in wetting phenomena.

In order to know precisely which of lines A and B will occur for a given *r*, the unsteady state equations should be solved. But it is speculated that it depends on the initial condition of the unsteady state equation.

Finally, when r is less than 0.079 $\times 10^{-6}$ m, no solution is found for the steady-state equations. Judging from the r value which is much smaller than $r_{critical}$ in Table 6-1, the pore is filled with vapor and the vapor diffusion is governing the mass transport in this region.

Figure 6-7 shows the results for Run 2 where T_f was reduced to 333.2 K. All other simulation parameters are the same as Run 1 for which the results are given in Figure 6-4. The trend found in Figure 6-7C is different from that in Figure 6-4C, i.e. along line A, N decreases as r increases, while the trend is the same along line B.

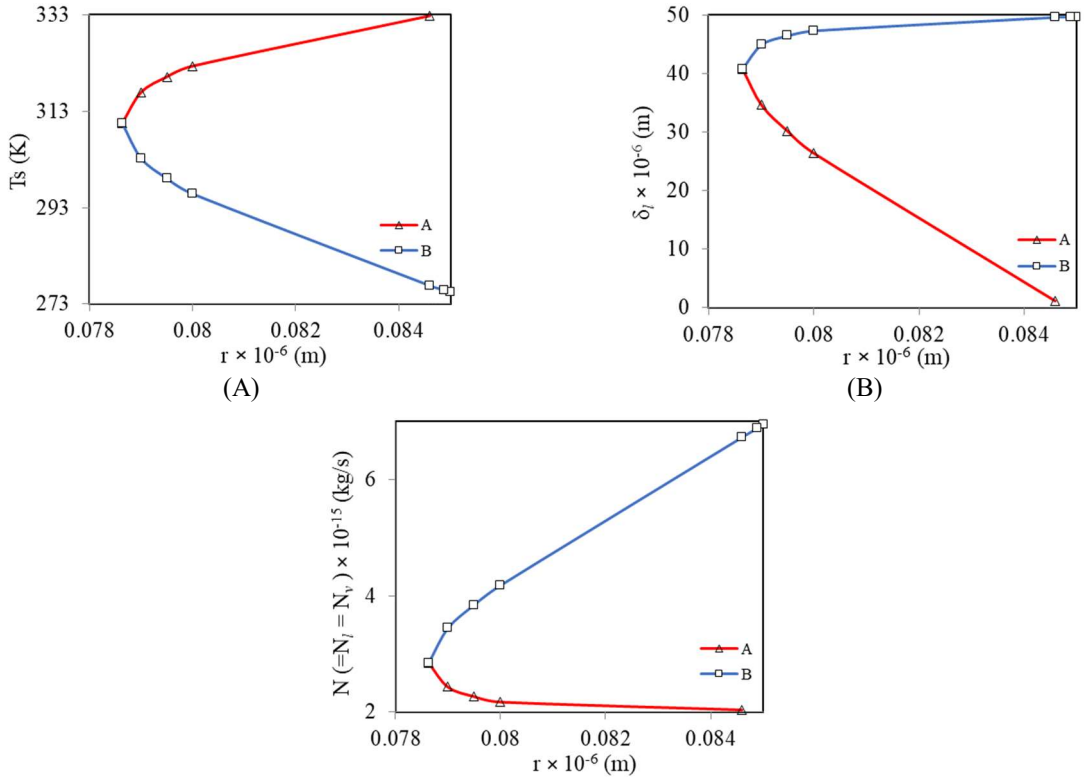

Figure 6-7 Simulation results for Run 2, at T_f = 333.2 K (60 ºC), θ = 93º and the total pore length, $\delta = 50\times10^{-6}$ m, A) T_s vs. r, B) δ_l vs. r and C) N vs. r.

Compared with Figure 6-4, line A is remarkably shorter and at the right end of the line, *r* is much smaller. This is quite expected since $r_{critical}$ of Run 2 is smaller than Run 1.

Figure 6-8 shows the results for Run 3 where T_f = 313.2 K. All other simulation parameters are the same as Run 1. It is noticed that line A has almost disappeared in the studied range of *r* and the reason is that beyond $r_{critical}$ of 0.0774×10^{-6} m, the pore tends to be filled with liquid and the liquid flow will control the transport in the pore.

Regarding line B, there is not much change from Figures 6-4 and 6-8, except for the further decrease in *N*.

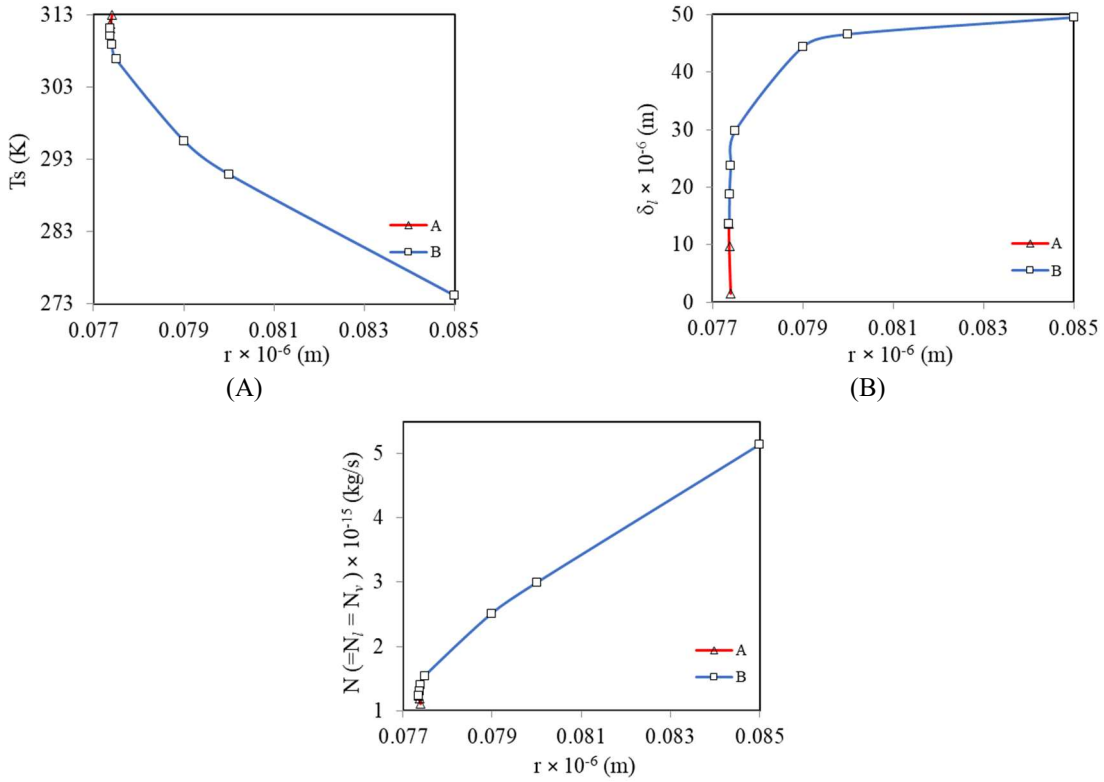

Figure 6-8 Simulation results for Run 3, at T_f = 313.2 K (40 ºC), θ = 93º and the total pore length, $\delta = 50\times10^{-6}$ m, A) T_s vs. r, B) δ_l vs. r and C) N vs. r.

6.4.2.2. Effect of change in contact angle

Figure 6-9 shows the results for Run 4 where θ was reduced to 91º. All other simulation parameters are the same as Run 1 (Figure 6-4). The patterns found for line A and B are the same as Figure 6-4, i.e. along line A, T_s increases, δ_l decreases and N increases as r increases, while along line B, T_s decreases, δ_l increases and N increases. However, both lines appear in much smaller region of r than Run 1. This can be explained again by considering $r_{critical}$ which is even smaller than Run 3. Thus, the pore tends to be filled with liquid at $r > r_{critical}$ =0.0404×10^{-6} m. Interestingly, line B extends to r = 0.047×10^{-6} that is larger than the above $r_{critical}$ but the right end of line B is much smaller than that of Figure 6-4.

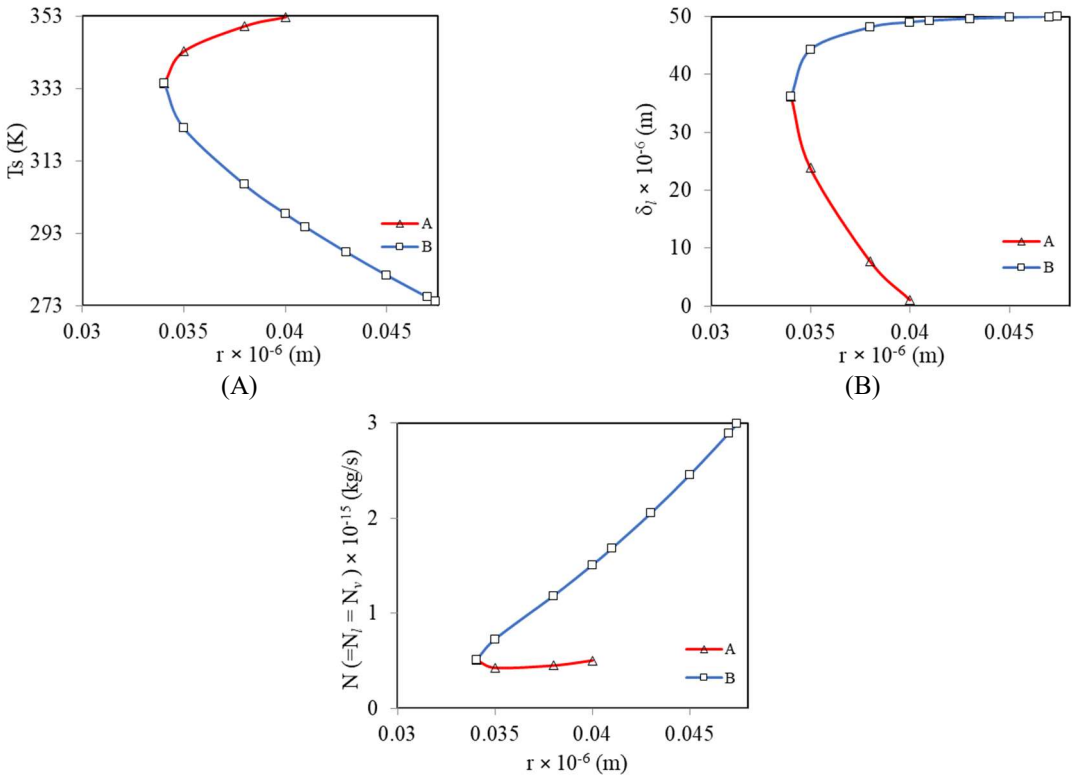

Figure 6-9 Simulation results for Run 4, at T_f= 353.2 K (80 ºC), θ = 91º and the total pore length, $\delta = 50\times10^{-6}$ m, A) T_s vs. r, B) δ_l vs. r and C) N vs. r.

Figure 6-10 shows the results for Run 5, where θ was further reduced to 89º. Now line A disappears completely, and only line B appears. It is interesting to note that no $r_{critical}$ is found for 89º (see Table 6-1) and Δp_l is always positive regardless of r, which means that the pore tends to be filled with liquid water in the entire range of r. Nevertheless, line B still appears, indicating that liquid/vapor interface may exist in the pore and its temperature may go down. As well, the right end of line B was further shifted to the smaller r.

Figure 6-11 shows the results for Run 6 where θ was further decreased to 87º. It is seen that line A has disappeared and the effect of decrease in θ is intensified.

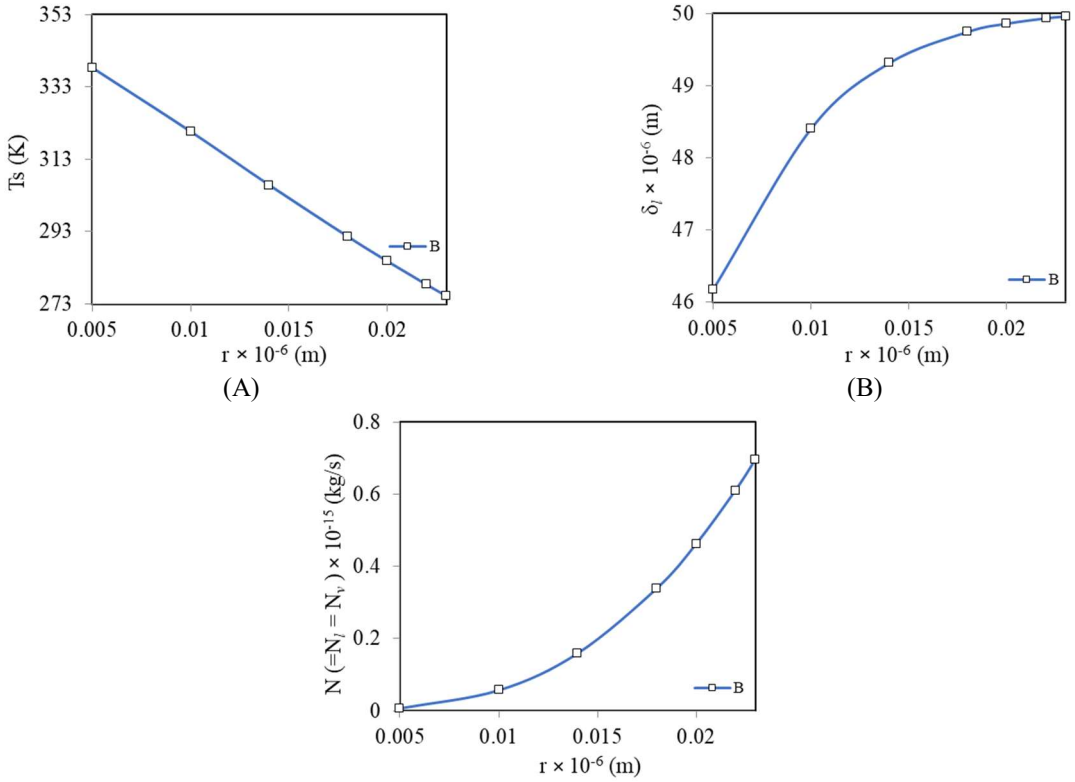

Figure 6-10 Simulation results for Run 5, at T_f= 353.2 K (80 ºC), θ = 89º and the total pore length, $\delta = 50\times10^{-6}$ m, A) T_s vs. r, B) δ_l vs. r and C) N vs. r.

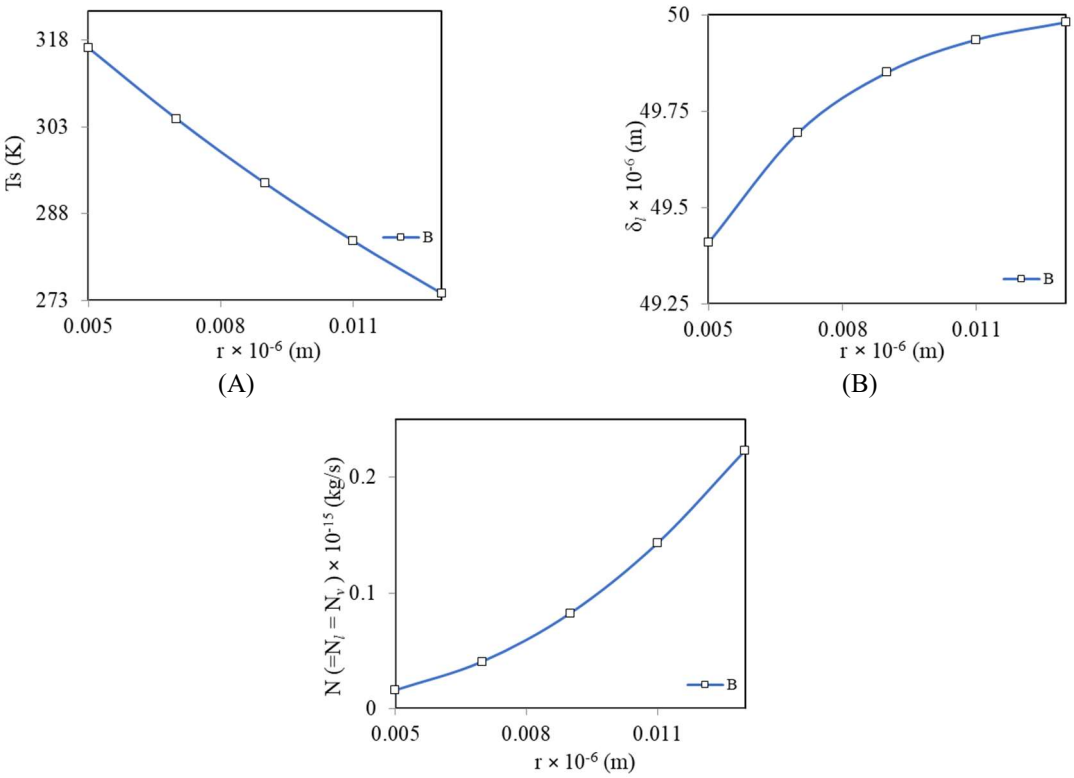

Figure 6-11 Simulation results for Run 6, at T_f= 353.2 K (80 ºC), θ = 87º and the total pore length, $\delta = 50\times10^{-6}$ m, A) T_s vs. r, B) δ_l vs. r and C) N vs. r.

6.4.3. Comparison with the experimental data

Comparison of the simulation results with the experimental VMD values of Alsalhy *et al*. [41] was made. Eq. 6.14 was applied in order to obtain the flux, *J*. Both simulation and experimental values are illustrated in Figure 6-12. This figure shows that the data obtained by simulation is not unreasonable.

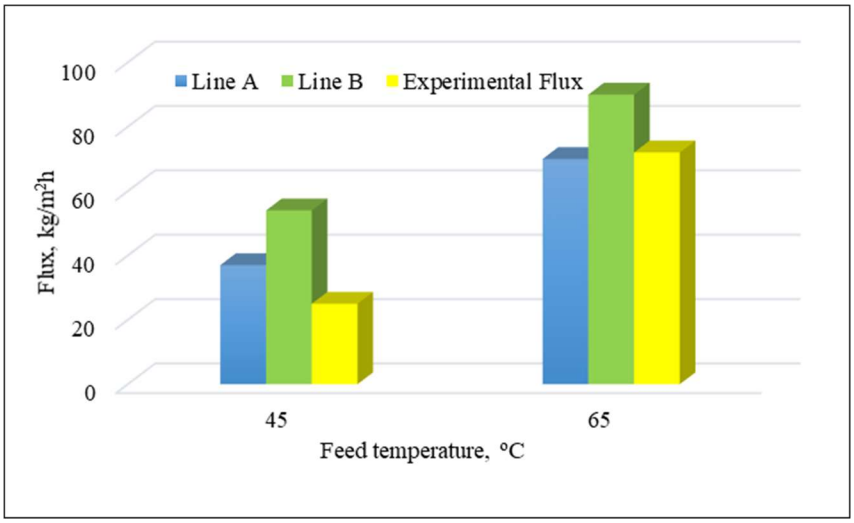

Figure 6-12 Comparison of simulation results with experimental data ($\theta = 103°$, $\delta = 450 \times 10^{-6}$ m, $r = 0.32 \times 10^{-6}$ (simulation), 0.2×10^{-6} (experimental data), $\varepsilon = 0.7$).

6.5. Implications and future research

As already mentioned, the present approach reveals that VMD is possible in a wider range of pore radius, r, than the conventional approach predicts. The flux of line B is consistently higher than line A due to the shorter path length of vapor. In some cases, line A disappears and only line B remains. The occurrence of A or B as an operating line seems to depend on the initial condition. In order to know at which initial condition line B is reached at the steady state, unsteady state equations should be solved. It should be noted that there are two opposing effects of increasing T_s (and p_s). One is decrease in driving force for liquid flow and the other is increase in driving force for vapor diffusion. Therefore, insertion of heating element near the membrane surface [42-44] and adding an optimum amount of heat input (to increase T_s) may be advantageous. Moreover, developing a similar model, considering the presence of salt in water, is recommended.

6.6. References

[1] G. Rácz, S. Kerker, Z. Kovács, G. Vatai, M. Ebrahimi, P. Czermak, Theoretical and experimental approaches of liquid entry pressure determination in membrane distillation processes, Period. Polytech. Chem. Eng. 58 (2014) 81–91. doi:10.3311/PPch.2179.

[2] R.B. Saffarini, B. Mansoor, R. Thomas, H.A. Arafat, Effect of temperature-dependent microstructure evolution on pore wetting in PTFE membranes under membrane distillation conditions, J. Membr. Sci. 429 (2013) 282–294. doi:10.1016/J.MEMSCI.2012.11.049.

[3] L. Camacho, L. Dumée, J. Zhang, J. Li, M. Duke, J. Gomez, S. Gray, Advances in membrane distillation for water desalination and purification applications, Water. 5 (2013) 94–196. doi:10.3390/w5010094.

[4] P. Peng, A.G. Fane, X. Li, Desalination by membrane distillation adopting a hydrophilic membrane, Desalination. 173 (2005) 45–54. doi:10.1016/J.DESAL.2004.06.208.

[5] Y. Peng, Y. Dong, H. Fan, P. Chen, Z. Li, Q. Jiang, Preparation of polysulfone membranes via vapor-induced phase separation and simulation of direct-contact membrane distillation by measuring hydrophobic layer thickness, Desalination. 316 (2013) 53–66. doi:10.1016/J.DESAL.2013.01.021.

[6] M. Qtaishat, M. Khayet, T. Matsuura, Novel porous composite hydrophobic/hydrophilic polysulfone membranes for desalination by direct contact membrane distillation, J. Membr. Sci. 341 (2009) 139–148. doi:10.1016/J.MEMSCI.2009.05.053.

[7] L. Peña, J.M.O. de Zárate, J.I. Mengual, Steady states in membrane distillation: influence of membrane wetting, J. Chem. Soc., Faraday Trans. 89 (1993) 4333–4338. doi:10.1039/FT9938904333.

[8] M. Rezaei, W. Samhaber, Wetting Behaviour of Superhydrophobic Membranes Coated with Nanoparticles in Membrane Distillation, Chem. Eng. Trans. 47 (2016) 373–378. doi:10.3303/CET1647063.

[9] A.M. Alklaibi, N. Lior, Membrane-distillation desalination: Status and potential, Desalination. 171 (2005) 111–131. doi:10.1016/J.DESAL.2004.03.024.

[10] C.M. Tun, A.G. Fane, J.T. Matheickal, R. Sheikholeslami, Membrane distillation crystallization of concentrated salts—flux and crystal formation, J. Membr. Sci. 257 (2005) 144–155. doi:10.1016/J.MEMSCI.2004.09.051.

[11] F. He, J. Gilron, H. Lee, L. Song, K.K. Sirkar, Potential for scaling by sparingly soluble salts in crossflow DCMD, J. Membr. Sci. 311 (2008) 68–80. doi:10.1016/J.MEMSCI.2007.11.056.

[12] M. Gryta, Long-term performance of membrane distillation process, J. Membr. Sci. 265 (2005) 153–159. doi:10.1016/J.MEMSCI.2005.04.049.

[13] K. Karakulski, M. Gryta, Water demineralisation by NF/MD integrated processes, Desalination. 177 (2005) 109–119. doi:10.1016/J.DESAL.2004.11.018.

[14] M. Gryta, Influence of polypropylene membrane surface porosity on the performance of membrane distillation process, J. Membr. Sci. 287 (2007) 67–78. doi:10.1016/J.MEMSCI.2006.10.011.

[15] E. Guillen-Burrieza, R. Thomas, B. Mansoor, D. Johnson, N. Hilal, H. Arafat, Effect of dry-out on the fouling of PVDF and PTFE membranes under conditions simulating intermittent

seawater membrane distillation (SWMD), J. Membr. Sci. 438 (2013) 126–139. doi:10.1016/J.MEMSCI.2013.03.014.

[16] B. Pangarkar, M. Sane, S. Parjane, M. Guddad, Vacuum membrane distillation for desalination of ground water by using flat sheet membrane, Int. Natl. J. Chem. Mol. Eng. 51 (2011) 797–802.

[17] M. Baghbanzadeh, D. Rana, C.Q. Lan, T. Matsuura, Effects of hydrophilic silica nanoparticles and backing material in improving the structure and performance of VMD PVDF membranes, Sep. Purif. Technol. 157 (2016) 60–71. doi:10.1016/J.SEPPUR.2015.11.029.

[18] D.M. Warsinger, A. Servi, G.B. Connors, M.O. Mavukkandy, H.A. Arafat, K.K. Gleason, J.H. Lienhard V, Reversing membrane wetting in membrane distillation: comparing dryout to backwashing with pressurized air, Environ. Sci. Water Res. Technol. 3 (2017) 930–939. doi:10.1039/C7EW00085E.

[19] P. Yazgan-Birgi, M.I. Hassan Ali, H.A. Arafat, Estimation of liquid entry pressure in hydrophobic membranes using CFD tools, J. Membr. Sci. 552 (2018) 68–76. doi:10.1016/J.MEMSCI.2018.01.061.

[20] E. Guillen-Burrieza, A. Servi, B.S. Lalia, H.A. Arafat, Membrane structure and surface morphology impact on the wetting of MD membranes, J. Membr. Sci. 483 (2015) 94–103. doi:10.1016/J.MEMSCI.2015.02.024.

[21] A.T. Servi, J. Kharraz, D. Klee, K. Notarangelo, B. Eyob, E. Guillen-Burrieza, A. Liu, H.A. Arafat, K.K. Gleason, A systematic study of the impact of hydrophobicity on the wetting of MD membranes, J. Membr. Sci. 520 (2016) 850–859. doi:10.1016/J.MEMSCI.2016.08.021.

[22] M. Rezaei, D.M. Warsinger, J.H. Lienhard V, M.C. Duke, T. Matsuura, W.M. Samhaber, Wetting phenomena in membrane distillation: Mechanisms, reversal, and prevention, Water Res. 139 (2018) 329–352. doi:10.1016/J.WATRES.2018.03.058.

[23] Y. Shin, J. Choi, T. Lee, J. Sohn, S. Lee, Optimization of dewetting conditions for hollow fiber membranes in vacuum membrane distillation, Desalin. Water Treat. 57 (2016) 7582–7592. doi:10.1080/19443994.2015.1044266.

[24] J. Zhu, L. Jiang, T. Matsuura, New insights into fabrication of hydrophobic/hydrophilic composite hollow fibers for direct contact membrane distillation, Chem. Eng. Sci. 137 (2015) 79–90. doi:10.1016/J.CES.2015.05.064.

[25] X. Feng, L.Y. Jiang, T. Matsuura, P. Wu, Fabrication of hydrophobic/hydrophilic composite hollow fibers for DCMD: Influence of dope formulation and external coagulant, Desalination. 401 (2017) 53–63. doi:10.1016/J.DESAL.2016.07.026.

[26] J. Koros, Y.H. Ma, T. Shimizu, IUPAC, Pure and Applied Chemistry, 68 (1996) 1479–1489.

[27] R.W. Schofield, A.G. Fane, C.J.D. Fell, Heat and mass transfer in membrane distillation, J. Membr. Sci. 33 (1987) 299–313. doi:10.1016/S0376-7388(00)80287-2.

[28] M.S. Khayet, T. Matsuura, Membrane distillation : principles and applications, Elsevier, Amsterdam, New York, 2011.

[29] A.V. LUIKOV, Heat and Mass Transfer in Capillary-Porous Bodies, Pergamon, London, New York, 1966.

[30] M.R. Qtaishat, T. Matsuura, Modelling of pore wetting in membrane distillation compared with pervaporation, in: Pervaporation, Vap. Permeat. Membr. Distill., Elsevier, 2015: pp. 385–413. doi:10.1016/B978-1-78242-246-4.00013-1.

[31] M.. Izquierdo-Gil, G. Jonsson, Factors affecting flux and ethanol separation performance in vacuum membrane distillation (VMD), J. Membr. Sci. 214 (2003) 113–130. doi:10.1016/S0376-7388(02)00540-9.

[32] J.M. Lafferty, Foundations of vacuum science and technology, John Wiley & Sons, Inc. (US), New York, 1998.

[33] H. Huang, Z. Song, N. Wei, L. Shi, Y. Mao, Y. Ying, L. Sun, Z. Xu, X. Peng, Ultrafast viscous water flow through nanostrand-channelled graphene oxide membranes, Nat. Commun. 4 (2013) 2979. doi:10.1038/ncomms3979.

[34] Estimation of Saturated Vapor Pressure, Dortmund Data Bank. http://ddbonline.ddbst.com/AntoineCalculation/AntoineCalculationCGI.exe.

[35] Estimation of Liquid Density, Dortmund Data Bank. http://ddbonline.ddbst.com/DIPPR105DensityCalculation/DIPPR105CalculationCGI.exe.

[36] Estimation of Liquid Dynamic Viscosity, Dortmund Data Bank. http://ddbonline.ddbst.com/VogelCalculation/VogelCalculationCGI.exe.

[37] Estimation of Surface Tension, Dortmund Data Bank. http://ddbonline.ddbst.com/DIPPR106SFTCalculation/DIPPR106SFTCalculationCGI.exe.

[38] Estimation of Heat of Vaporization, Dortmund Data Bank. http://ddbonline.ddbst.com/PPDS12HVPCalculation/HVP_PPDS12CalculationCGI.exe.

[39] E. Guillen-Burrieza, M.O. Mavukkandy, M.R. Bilad, H.A. Arafat, Understanding wetting phenomena in membrane distillation and how operational parameters can affect it, J. Membr. Sci. 515 (2016) 163–174. doi:10.1016/J.MEMSCI.2016.05.051.

[40] J. Gilron, Y. Ladizansky, E. Korin, Silica fouling in direct contact membrane distillation, Ind. Eng. Chem. Res. 52 (2013) 10521–10529. doi:10.1021/ie400265b.

[41] Q.F. Alsalhy, S.S. Ibrahim, S.R. Khaleel, Performance of vacuum poly(propylene) membrane distillation (VMD) for saline water desalination, Chem. Eng. Process. Process Intensif. 120 (2017) 68–80. doi:10.1016/J.CEP.2017.06.011.

[42] A. V. Dudchenko, C. Chen, A. Cardenas, J. Rolf, D. Jassby, Frequency-dependent stability of CNT Joule heaters in ionizable media and desalination processes, Nat. Nanotechnol. 12 (2017) 557–563. doi:10.1038/nnano.2017.102.

[43] C. Boo, M. Elimelech, Thermal desalination membranes: Carbon nanotubes keep up the heat, Nat. Nanotechnol. 12 (2017) 501–503. doi:10.1038/nnano.2017.114.

[44] Y.Z. Tan, H. Wang, L. Han, M.B. Tanis-Kanbur, M.V. Pranav, J.W. Chew, Photothermal-enhanced and fouling-resistant membrane for solar-assisted membrane distillation, J. Membr. Sci. 565 (2018) 254–265. doi:10.1016/J.MEMSCI.2018.08.032.

Chapter 7

Conclusions

Pore size and PSD are significant parameters affecting membrane performance and efficiency. In filtration processes, larger pore radii result in higher flux and lower rejection. In MD, larger pore radii can result in higher flux and penetration of liquid into the pore and occurrence of pore wetting. There is a trade-off between the occurrence of pore wetting and high flux. Therefore, an optimum pore radius should be selected depending on different parameters such as feed type, temperature, MD configuration, etc. The critical point is that the radius of pores should be distributed in a narrow region around the optimum radius (narrow PSD) because even a small number of large pores may cause pore wetting and consequently reduce flux and/or permeate quality. Hence, estimation of MD membrane PSD is of great importance. Among various available methods, the bubble gas transport method is a common approach for PSD estimation. However, this technique requires many experimental data points. With the proposed model in chapter 3, PSD can be predicted with only four data points, reducing the effort of recording unnecessary data. Unlike the conventional approach, the proposed approach starts from assuming a distribution function for the PSD, according to which a flow rate versus pressure curve is produced. Then, the mean pore size and standard deviation of the mentioned function are optimized by the best fit of the theoretical curve to the experimental data through minimizing an error function using nonlinear regression. Moreover, the developed model considers the nature of flow inside each individual pore depending on the *Kn* number, unlike the conventional approach, which considers a similar flow type inside all pores of a membrane, regardless of the size difference of the pores.

As mentioned in section 2.3.5, in the context of membrane wetting characteristics, LEP is defined as the minimum transmembrane pressure that should be applied to a liquid feed before it overcomes the hydrophobicity of a non-wetted membrane and penetrates the pores. This parameter, i.e. LEP, is the most popular parameter which is used by researchers to show membrane

wettability potential. As already mentioned, exceedance of the LEP is a reason for the occurrence of wetting phenomena, and thus, precise estimation of this parameter is essential. In chapter 4, the penetration of liquid feed in the LEP determination process was modeled by applying the numerical analysis of fluid mechanics and machine learning techniques. In the mentioned study, CFD modeling was employed to model the wetting process inside the pore during the gradual increase in feed pressure at different scenarios (different contact angles, pore radii and membrane thicknesses). Then, GP, as an intelligent technique, was used to produce a computer program estimating LEP in the whole ranges in which CFD modeling was performed. GP is based on the Darwinian natural selection principle. Initially, an equation is produced randomly, and then this equation is improved over generations. The developed equation was validated using the experimental data and could predict LEP in a better agreement in comparison to the Young-Laplace equation. Also, the effect of the membrane thickness was considered in the equation, resulting in a more realistic formula for LEP estimation. This equation could predict non-zero LEP for CA of 90° for small pore radii, unlike the Young-Laplace equation, according to which LEP is equal to zero for CA of 90°, regardless of pore size.

Liquid/gas interface movement inside the pores of a membrane can occur during membrane preparation and characterization processes. Bubble point method, porometry, LEP measurement, etc., are some examples of this kind of flow inside the membrane pore. For instance, during the measurement of LEP, which is a parameter related to wetting characteristics of hydrophobic membranes (as already mentioned), liquid enters the pore and replaces the air. In most of the research conducted in this field, the focus was on the transmembrane pressure required for the liquid entry into the pore, and little attention has been paid to tracking the interface. Unlike the past studies, in chapter 5, the movement of the liquid/gas interface was tracked. Moreover, the

pressure and velocity at the interface were calculated. The model was developed in accordance with the governing equations applicable for liquid and gas flows inside the membrane pore. The agreement of the developed model with the experimental data was better than Washburn's equation (about 2 %) due to the slower capillary movement of water caused by the interfacial air pressure that is higher than the permeate pressure.

In accordance with a literature review, three models had been presented for pore wetting in MD, none of which investigated the temperature decrease within the pore. In chapter 6, an alternative model for pore wetting in VMD considering heat and mass balances at the vapor/liquid interface at steady state was presented. This model assumes that heat only enters the pore inlet and is removed due to liquid vaporization at the vapor-liquid interface, with heat transfer through the pore wall neglected. This model showed that partial pore wetting is possible since the vapor/liquid interface might remain within the pore at steady state. Further, this model predicts a significant decrease in temperature from the pore inlet to the vapor/liquid interface.

For future research, the following projects are recommended:

- A similar model can be developed for other systems of PSD determination, including liquid-liquid systems.
- Verifying the applicability of the proposed PSD model for other distributions such as multimodal distributions.
- An equation can be developed using the combination of CFD and GP to estimate dynamic LEP.
- Combination of CFD and GP tools seems to be a powerful method for other chemical engineering processes since with which a complicated CFD model can be delivered to other researchers and users through an explicit formula.

- Developing a model for pore wetting that captures the progression of the vapor/liquid interface at unsteady state conditions (considering the presence of salt in water).
- Pore wetting model development for other configurations of MD process, such as DCMD.
- Insertion of heating element near the membrane surface and adding an optimum amount of heat input is suggested as the liquid temperature within the pore significantly affects the efficiency of MD process.